Analysis of energy cascade in wall-bounded turbulent flows

Rakesh Yuvaraj

CENTRALE LILLE

THESE

Presentée en vue
d'obtenir le grade de

DOCTEUR

En

Spécialité : Mécanique

Par

Rakesh YUVARAJ

DOCTORAT DELIVRE PAR CENTRALE LILLE

Titre de la thèse:

Analyse de la cascade d'énergie dans une couche limite turbulente

---

Soutenue le 06 Juillet 2021 devant le jury d'examen:

Président	**Luminita DANAILA**	Professeur, Université de Rouen
Rapporteur	**Laurent DAVID**	Professeur, Université de Poitiers
Rapporteur	**Elisabetta DE ANGELIS**	Maître de Conférences, Cardiff University
Examinateur	**Christos VASSILICOS**	Directeur de Recherche, CNRS, LMFL, Lille
Examinateur	**Jean-Philippe LAVAL**	Directeur de Recherche, CNRS, LMFL, Lille
Directeur de thèse	**Jean-Marc FOUCAUT**	Professeur, École Centrale de Lille

Thèse préparée au Laboratoire de Mécanique des Fluids de Lille - Kampé de Fériet

École Doctorale SPI 072 (Lille, Artois, ULCO, UVHC, Centrale Lille, IMT Lille Douai)

centralelille

CENTRALE LILLE

THESIS

Presented to
obtain the grade of

DOCTOR

In

Specialisation : Mechanics

By

Rakesh YUVARAJ

DOCTORATE DELIVERED BY CENTRALE LILLE

Title of the thesis:

Analysis of energy cascade in wall-bounded turbulent flows

Defended on 06 July 2021 before the members of jury:

President	**Luminita DANAILA**	Professor, Université de Rouen
Reviewer	**Laurent DAVID**	Professor, Université de Poitiers
Reviewer	**Elisabetta DE ANGELIS**	Assosciate Professor, Cardiff University
Examiner	**Christos VASSILICOS**	Senior Researcher, CNRS, LMFL, Lille
Examiner	**Jean-Philippe LAVAL**	Senior Researcher, CNRS, LMFL, Lille
Supervisor	**Jean-Marc FOUCAUT**	Professor, École Centrale de Lille

PhD Thesis prepared at Lille Laboratory of Fluid Mechanics - Kampé de Fériet

Doctoral School SPI 072 (Lille, Artois, ULCO, UVHC, Centrale Lille, IMT Lille Douai)

centralelille

Résumé

Introduction

Les écoulements turbulents sont résolus à l'aide de l'équation de Navier-Stokes, et la complexité de l'écoulement implique que la simplification de l'écoulement entraîne une perte significative de physique. Ceci est dû aux non-linéarités associées à l'écoulement, en plus de la physique qui dépend des différentes échelles de mouvement. Cette nature multi-échelle des écoulements turbulents a été étudiée par Richardson [97] dans le cadre de la turbulence isotrope, décrite dans ce célèbre poème : 'Big whirls have little whirls .... and so on to viscosity'. Selon son modèle, l'énergie est injectée aux grandes échelles et s'écoule vers le bas de l'échelle jusqu'à ce qu'elle atteigne la plus petite échelle où elle est dissipée en raison de la viscosité. Et la viscosité et la dissipation sont confinées aux plus petites échelles du flux, et la cascade d'énergie peut se produire entre des échelles de taille similaire et est toujours une cascade d'énergie vers l'avant, c'est-à-dire des plus grandes aux plus petites échelles.

Cette théorie est suivie par celle de Kolmogorov [67, 68, 69], également connue sous le nom de théorie K41, et Oboukhov [89] a postulé l'hypothèse de l'universalité qui se produit à la limite des grands nombres de Reynolds où la plage d'inertie séparant les échelles intégrales et les échelles dissipatives est si grande que les petites échelles se découplent entièrement des grandes échelles et présentent une isotropie. Les résultats du passé ont montré quelques résultats importants sur l'écoulement turbulent qui est homogène et isotrope. En réalité, les écoulements turbulents présentent une inhomogénéité ou une anisotropie dans certaines directions, ce qui rend l'applicabilité des études du passé plus restrictive. De Karman and Howarth [31] ont utilisé le coefficient de corrélation entre deux points pour étudier les statistiques multipoints. Avec l'introduction de la fonction de structure de second ordre par Kolmogorov, il est devenu possible d'étudier le phénomène de cascade énergétique dans l'espace physique et dans l'espace des échelles. Ce phénomène est largement connu sous le nom de loi 4/5e qui peut s'écrire comme suit

$$-\langle(\delta u_1)^3\rangle + 6\nu\frac{d}{dr}\langle(\delta u_1)^2\rangle = \frac{4}{5}\langle\epsilon'\rangle r \tag{1}$$

où ϵ' est le taux de dissipation moyen de l'énergie cinétique turbulente, ν est la viscosité cinématique du fluide et les parenthèses angulaires représentent les moyennes d'ensemble.

Hill[54] a dérivé l'équation exacte pour le bilan énergétique échelle par échelle directement de l'équation de Navier-Stokes sans aucune moyenne ou hypothèse sur l'isotropie/homogénéité de l'écoulement. Cette équation de Kolmogorov généralisée, également connue sous le nom d'équation de Kármán-Howarth-Monin-Hill (KHMH), est une équation d'évolution de l'énergie cinétique turbulente locale et instantanée relative à un vecteur de séparation donné (δu^2) qui quantifie les différents processus associés au transfert d'énergie à la fois dans l'espace physique et dans l'espace des échelles et peut être appliquée à tous les écoulements turbulents numériques et expérimentaux. Elle est donnée par

$$\begin{aligned}&\underbrace{\frac{\partial}{\partial t}(\delta \boldsymbol{u_i'})^2}_{A_t}+\underbrace{\delta \boldsymbol{u_j'}\frac{\partial}{\partial r_j}(\delta \boldsymbol{u_i'})^2}_{\Pi}+\underbrace{2\delta \boldsymbol{u_j'}\delta \boldsymbol{u_i'}\frac{\partial}{\partial r_j}(\delta \overline{\boldsymbol{u_i}})}_{P_r}+\underbrace{\overline{\boldsymbol{u_j^*}}\frac{\partial}{\partial X_j}(\delta \boldsymbol{u_i'})^2}_{A}+\underbrace{\boldsymbol{u_j'^*}\frac{\partial}{\partial X_j}(\delta \boldsymbol{u_i'})^2}_{T_u}\\&=\underbrace{-\frac{2}{\rho}\delta \boldsymbol{u_i'}\frac{\partial}{\partial X_i}(\delta p)}_{T_p}+\underbrace{2\nu\frac{\partial^2}{\partial r_j^2}(\delta \overline{\boldsymbol{u_i}})^2}_{D_{r1}}+\underbrace{2\nu\frac{\partial^2}{\partial r_j^2}(\delta \boldsymbol{u_i'})^2}_{D_{r2}}+\underbrace{4\nu\frac{\partial^2}{\partial r_j^2}(\delta \overline{\boldsymbol{u_i}}\delta \boldsymbol{u_i'})^2}_{D_{r3}}+\underbrace{\frac{\nu}{2}\frac{\partial^2}{\partial X_j^2}(\delta \boldsymbol{u_i'})^2}_{D_x}-\epsilon\end{aligned}\tag{2}$$

L'équation de Kármán-Howarth-Monin-Hill a ouvert la possibilité d'étudier le bilan énergétique échelle par échelle dans la plupart des écoulements turbulents complexes. Cela a donné lieu à une multitude de recherches dans différents écoulements turbulents. Voici les différentes études qui ont résulté de l'équation KHMH dans les simulations numériques, y compris les simulations numériques directes (DNS) et les simulations de grands tourbillons (LES). Marati et al.[81] ont étudié la cascade d'énergie et le flux spatial dans la TCF et ont détaillé le comportement du transfert, de la production et de la dissipation inter-échelle dans différentes régions de la turbulence délimitée par des murs. De cette manière, la double nature des écoulements turbulents, à savoir la dynamique à petite échelle définie dans l'espace des échelles d'une part et la physique à proximité de la paroi définie dans l'espace physique, est abordée en même temps. Cimarelli et al.[22] ont analysé les chemins de la cascade d'énergie dans le TCF à partir de la production de la couche tampon vers la paroi et l'écoulement extérieur et souligne l'importance de la cascade d'énergie inverse dans de tels processus. Cimarelli and De Angelis[21] ont discuté des problèmes de modélisation dans LES de la rétrodiffusion qui est prévalente dans les petites échelles 23des flux turbulents de paroi. Cimarelli et al.[23] ont décrit les deux mécanismes d'entraînement, à savoir (a) une source d'énergie à forte échelle dans la couche tampon concernant le cycle proche de la paroi (b) une source extérieure associée à un cycle turbulent extérieur en suivant les termes spécifiques de l'équation KHMH représentant le processus de cascade énergétique. Alves Portela et al.[4] ont étudié la cascade de turbulence sur la ligne centrale du sillage turbulent créé par un prisme carré en utilisant l'équation KHMH. Il existe une région éloignée du prisme mais dans le champ proche du sillage où le terme de cascade inter-échelle moyenné sur l'orientation est à peu près égal au taux de dissipation même si les processus liés à l'inhomogénéité sont importants. Mollicone et al.[83] ont analysé le bilan échelle par échelle dans la dynamique de la couche de cisaillement dans une région séparée derrière une bosse dans l'écoulement du

canal, où l'équation KHMH est résolue en cinq dimensions comprenant trois coordonnées d'espace d'échelle et deux coordonnées physiques dans la direction du courant et de la paroi normale pour relier à la fois la physique dans l'espace physique et l'espace d'échelle. Le présent travail vise à étudier le bilan énergétique échelle par échelle en utilisant l'équation KHMH afin de répondre aux questions suivantes.

- Il est connu que l'écoulement turbulent en canal et l'écoulement turbulent en couche limite sont similaires l'un à l'autre et qu'ils sont limités à certaines distances aux parois. Ainsi, les résultats obtenus à partir des termes de l'équation KHMH moyenne sont également les mêmes entre les deux écoulements lorsqu'ils sont normalisés avec les paramètres appropriés ? La forme instantanée des termes KHMH se comporte-t-elle de la même manière entre les deux flux ?

- Considérant que les résultats de l'équation KHMH instantanée reposent sur une estimation précise des fluctuations des différents termes, est-il possible d'obtenir les mêmes résultats à partir des ensembles de données DNS avec des expériences (PIV) qui permettent d'obtenir des résultats à un nombre de Reynolds plus élevé (Re_τ) que le DNS ?

- Yasuda and Vassilicos [137] ont proposé d'étudier l'équation KHMH au sens instantané pour obtenir le bilan énergétique échelle par échelle dans une turbulence isotrope. La même idée mise en œuvre dans des écoulements turbulents limités par des murs permet-elle de découvrir de nouvelles informations sur la physique de la cascade énergétique ?

- Marati et al. [81] ont utilisé l'équation KHMH pour la fluctuation de la vitesse pour étudier le comportement des différents termes en moyenne sur un plan dans le sens du courant et de l'envergure. Bien qu'il s'agisse de directions homogènes, l'étude de la physique de l'écoulement dans le sens de l'écoulement et dans le sens de l'envergure séparément révèle-t-elle plus d'informations ?

- Saikrishnan et al. [99] ont découvert que dans la région logarithmique, le transfert d'énergie inter-échelle de l'équation KHMH moyennée varie avec le nombre de Reynolds. L'influence du nombre de Reynolds est-elle uniquement visible dans la région logarithmique, même avec les statistiques instantanées ?

- Casciola et al. [19] introduisent l'échelle de croisement l_c^+ , qui sépare les régimes dominés par le transfert et les régimes dominés par la production. Existe-t-il une autre échelle qui correspond au comportement de certains termes de l'équation KHMH ?

Résumé des Résultats

Résultats des ensembles de données DNS

Le présent travail permet de tirer diverses conclusions sur la physique des écoulements Turbulents limités par des parois, sur la base des valeurs moyennes et instantanées des termes de l'équation KHMH et de leur évolution en fonction de la distance aux parois. Les principales conclusions sont les suivantes.

Moyenne Spatio-Temporelle des Termes de l'équation KHMH

Les valeurs moyennes spatio-temporelles des termes de l'équation de KHMH dans les écoulements TCF et TBL avec des moyennes nulles ou négligeables sont -$\langle A_t \rangle$, -$\langle A \rangle$, $\langle T_p \rangle$ et $\langle D_x \rangle$. Et les termes dominants sont $\langle D_{r2} \rangle$ près de l'échelle de Kolmogorov, -$\langle \Pi \rangle$ dans les multiples plages d'échelles dépendant de la distance aux parois, -$\langle P_r \rangle$ au-delà de l'échelle intégrale, -$\langle T_u \rangle$ près de la ligne centrale de l'écoulement du canal et du bord de la couche limite turbulente, et les termes de dissipation (ϵ'^*) dans toutes les échelles à toutes les distances aux parois. De plus, près du bord de la couche limite, -$\langle A \rangle$ et $\langle T_p \rangle$ i sont dominants dans le TBL550.

Le -$\langle \Pi \rangle$ est dominant seulement aux plus petites échelles dans la couche tampon. Avec l'augmentation de la distance aux parois, -$\langle \Pi \rangle$ est dominant à des échelles plus grandes. Au niveau de l'axe du canal et du bord de l'épaisseur de la couche limite, -$\langle \Pi \rangle$ est non nul même à des échelles supérieures à δ. Dans TCF3000, -$\langle \Pi \rangle$ est approximativement égal à $0{,}5\langle \epsilon'^* \rangle$ à $r_x = 9\delta$. Une décomposition rapide de ce terme a révélé que la dominance de ce terme aux très grandes échelles est due à ce terme $u_1' u_2' \frac{\partial u_1'}{\partial x_2}$, qui est dû à la corrélation entre les grandes et petites échelles de l'écoulement.

Les valeurs moyennes spatio-temporelles des termes de l'équation KHMH sont différentes entre la direction du courant et celle de l'envergure. Ceci est principalement observé entre -$\langle \Pi \rangle$ et -$\langle P_r \rangle$. A partir de la couche tampon, il y a quelques échelles dans lesquelles la production dépasse le $\langle \epsilon'^* \rangle$ et ce pic positif de -$\langle P_r \rangle$ coïncide avec le pic négatif de -$\langle \Pi \rangle$. L'échelle à laquelle ce pic se produit augmente progressivement avec l'in l'augmentation de la distance de la paroi de la même manière dans les trois ensembles de données DNS lorsque la distance de la paroi est normalisée par δ. Cimarelli et al. 23 ont observé ce comportement de $\langle \Pi \rangle$ dans un DNS de TCF, pour conclure que cela est dû à la cascade spatiale inversée où l'énergie énergie monte vers la ligne centrale du canal en ligne droite dans l'espace (r_y, r_z, y).

Une micro-échelle de Taylor modifiée, dérivée pour des écoulements turbulents limités par des parois, séparément dans le sens de l'écoulement et dans le sens de l'envergure, permet de mettre à l'échelle le pic de -$\langle \Pi \rangle$ depuis l'extérieur de la couche tampon jusqu'au voisinage de la ligne centrale de l'écoulement du canal.

Termes instantanés de l'équation KHMH

Les résultats du comportement instantané de l'équation KHMH révèle d'autres aspects de différents termes qui étaient masqués dans les moyennes. Les termes dominants dans l'équation l'analyse de l'équation KHMH instantanée sont $A_t + A$, T_p , Π, T_u . Et les fluctuations de ces termes dominants sont au moins d'un ordre de grandeur supérieur à celui des termes fluctuation du terme de dissipation (ϵ'^*), et elle tend à augmenter avec la distance de la paroi. La dominance de $A_t + A$, Π et T_u peut être expliquée par l'anti-alignement des termes d'accélération locale et convective. les termes d'accélération locale et convective des écoulements turbulents en canal. Lorsque les Lorsque l'écart-type des termes est normalisé par l'écart-type de Π, l'ampleur de l'écart-type des termes de l'accélération locale et de l'accélération convective est plus importante. l'ampleur de l'écart-type de tous les termes est la même entre le TCF à différents différents nombres de Reynolds et l'écoulement TBL.

Un coefficient de corrélation élevé entre $A_t + A$ et (Π, T_u) de l'ordre de -0.5 de $y^+ = 12$ à $\frac{y}{\delta} = 1$ est observé dans TCF550 et TBL550. Et le coefficient de corrélation avec $A_t + A$ est compris entre 0,65 et 0,8 avec $\Pi + T_u$ de $y^+ = 12$ à $\frac{y}{\delta} = 1$. dans TCF550 et TBL550. A proximité du mur, cela s'explique par le fait que $A_t + A$ équilibre la valeur de $\Pi + T_u$, et loin du mur, cela pourrait être dû au fait que les structures à grande échelle balayant les structures de petite échelle (hypothèse de décorrélation par balayage). Un coefficient de corrélation élevé est observé entre $A_t + A$ et T_p uniquement à proximité de la paroi, de l'ordre de 0,3 dans les trois ensembles de données DNS. Un coefficient de corrélation de l'ordre de de 0,35-0,45 est observé entre T_p et les deux termes de transfert d'énergie (Π, T_u). Le coefficient de corrélation de coefficient de corrélation entre T_p et $\Pi + T_u$ est de l'ordre de 0,5 à 0,65. Ce haut coefficient de corrélation élevé des deux termes de transfert d'énergie avec $A_t + A$ et T_p reflète la relation entre le terme non linéaire et le terme de transfert d'énergie. la relation entre le terme non linéaire et le terme dérivé du temps, et le terme non linéaire et le terme de pression dans l'équation de Navier-Stokes. Cet argument selon lequel le terme non linéaire est à l'origine de ce coefficient de corrélation est renforcé par le fait que le coefficient de corrélation entre $A_t + A$ et T_p est négligeable sauf près de la paroi.

L'augmentation du nombre de Reynolds augmente le coefficient de corrélation entre $A_t + A$ et $\Pi + T_u$, ce qui est perceptible de $y^+ = 12$ jusqu'à la ligne centrale du canal. D'autre part, l'augmentation du nombre de Reynolds entraîne une réduction du coefficient de corrélation entre T_p et $\Pi + T_u$. coefficient de corrélation entre T_p et $\Pi + T_u$ lorsque $y^+ > 100$. Le coefficient de corrélation élevé de -0.5 est observé entre $A_t + A$ et les deux termes de transfert d'énergie s'étend à des échelles de l'ordre de 9δ dans la DNS de TCF à $Re_\tau = 3000$. La décomposition des deux termes de transfert d'énergie révèle que les termes δu_1 et $\frac{\partial \delta u_1}{\partial x_j}$ contribuent le plus, notamment le $\delta u_1 \frac{\partial \delta u_1}{\partial x_1}$, au coefficient de corrélation entre Π et $A_t + A$, et entre Π et T_p.

Cascade d'énergie échelle par échelle

En observant la composante radiale du terme de transfert d'énergie inter-échelle (Π_ρ) et le flux d'énergie d'échelle ($\delta u_\rho \delta u_i^2$), il est révélé qu'il existe une cascade d'énergie inverse dans la couche tampon à $y^+ = 12$. la couche tampon à $y^+ = 12$, ce qui coïncide approximativement avec l'observation de Cimarelli et al.[22] comme source d'énergie d'échelle, où la production surpasse la dissipation. Avec l'augmentation de la distance aux parois, la cascade inverse se déplace vers des échelles plus élevées dans le sens de l'envergure dans les trois ensembles de données DNS. Ceci est suivi par la valeur négative du pic de -$\langle\Pi\rangle$ dans la direction r_z à différentes distances de la paroi. Ce pic négatif de -$\langle\Pi\rangle$ coïncide approximativement coïncide approximativement avec le pic positif de -$\langle P_r\rangle$. La tendance des deux pics en r_z/δ est linéaire en $\frac{y}{\delta}$. linéaire en $\frac{y}{\delta}$. Il n'y a pas d'effet de Re_τ , de $\frac{y}{\delta} = 0{,}01$ à 0,1 dans la position des deux pics, ce qui suggère qu'il s'agit d'un effet de l'environnement deux pics, ce qui suggère que cela se situe dans la gamme des structures de la couche tampon. Dans la plage 0,1< $\frac{y}{\delta}$ <0,4, les pics de la TCF et de la TBL à $Re_\tau = 550$ sont ensemble, et le pic de la TCF3000 suit une trajectoire de plus en plus longue. TCF3000 suit une courbe différente, et ceci est dans la gamme des structures autosimilaires attachées au mur (WCF). structures autosimilaires (WASS).

Résultats des expériences de PIV

Incertitude de mesure

Les variances et les covariances des ensembles de données de PIV concordent bien avec celles des DNS de Re_τ similaires lorsque $y^+ > 20$ et $y^+ > 40$ pour la PIV avec $Re_\tau = 2220$ et 3840 respectivement. L'incertitude de mesure pour les deux ensembles de données de PIV est inférieure à 1% de la vitesse du flux libre pour les deux ensembles de données de PIV. La valeur du bruit associé aux fluctuations de la vitesse dans le sens de l'écoulement est de l'ordre de 0,03-0,06 pixels et de 0,04-0,08 pixels pour l'ensemble de données de PIV avec Re_τ = 2220 et 3840 respectivement.

Calcul de la dissipation

Le taux de dissipation normalisé D^+ calculé avec l'ensemble de données de PIV avec Re_τ = 2220, en remplaçant les dérivées manquantes par l'hypothèse d'axisymétrie[43] s'accorde bien avec celui de l'ensemble de données TBL DNS $Re_\tau = 1989$ lorsque $y^+ > 25$. Ceci est vérifié pour le calcul à partir de l'utilisation du système 1 de S-PIV, du système 2 et d'une combinaison de deux systèmes (système$_{1|2}$), et ils tendent tous à être en bon accord avec les ensembles de données DNS quand $y^+ > 25$.

Le taux de dissipation normalisé D^+ calculé avec l'ensemble de données PIV avec Re_τ = 3840 ne correspond pas à celui de l'ensemble de données DNS lorsque $y^+ < 200$. Ceci est

attribué à la résolution spatiale limitée qui est de l'ordre de 4.6η - 5.6η. Avec la PIV à Re_τ = 2220, la résolution spatiale est de l'ordre de 2.3η-2.8η, ce qui a aidé au calcul qui concorde avec les jeux de données DNS.

Équation KHMH moyenne spatio-temporelle

La moyenne spatio-temporelle des termes de l'équation KHMH obtenue à partir des deux ensembles de données de PIV, a révélé que -$\langle \Pi \rangle$ est qualitativement le même entre les ensembles de données DNS et PIV. Cependant, leur valeur maximale est plus élevée dans les deux ensembles de données de PIV par rapport aux ensembles de données DNS. -$\langle P_r \rangle$ des deux ensembles de données de PIV dépasse ϵ'^* à peu près à la même échelle, et il augmente avec la distance de la paroi. En comparaison, -$\langle P_r \rangle$ est toujours inférieur à ϵ'^* pour toutes les valeurs r_x^+ considérées dans la présente analyse des ensembles de données DNS dans la présente analyse. L'utilisation de deux systèmes S-PIV dans le calcul entraîne une erreur de biais pour -$\langle A_t \rangle$ et $\langle A \rangle$, mais le terme -$\langle A_t + A \rangle$ est approximativement le même quel que soit le système utilisé pour le calcul quel que soit le système utilisé pour le calcul dans la PIV avec Re_τ = 2220. Le site Le calcul avec le PIV à Re_τ = 3840 a une valeur plus élevée pour -$\langle A_t + A \rangle$ que tous les autres ensembles de données. autres ensembles de données. La micro-échelle de Taylor modifiée ne met pas exactement à l'échelle le pic dans les données PIV et DNS. dans les ensembles de données de PIV et de DNS lorsqu'elle est considérée comme ayant des termes uniquement dans le plan XY. cela pourrait être dû à l'absence de $\frac{\partial u_1}{\partial x_3}$ et $\frac{\partial u_2}{\partial x_3}$ termes.

Termes de l'équation KHMH instantanée

L'écart type de Π et T_u est du même ordre dans les ensembles de données PIV et DNS et donc ces termes ont le moins d'effet de bruit. P_r n'est pas affecté par le le bruit en moyenne, cependant, son écart type à $y^+ = 40$ n'est pas comparable à celui des ensembles de données DNS. À $y^+ = 100$ et 140, l'écart type de P_r est approximativement le même entre la PIV et les ensembles de données DNS. $A_t + A$ est le terme le plus affecté par le bruit des ensembles de données de PIV. L'utilisation de deux systèmes S-PIV a permis de réduire cet écart type, mais il reste plus élevé dans les deux ensembles de données PIV que dans l'ensemble de données DNS.

Le coefficient de corrélation entre $A_t + A$ et Π, T_u s'améliore lorsque deux systèmes S-PIV sont utilisés. Cela peut s'expliquer par l'écart type plus faible du terme $A_t + A$ lorsque deux systèmes S-PIV sont utilisés. À $y^+ = 40$, ce coefficient de corrélation de la PIV à Re_τ = 2220 est approximativement le même que celui des ensembles de données DNS. Cependant, avec l'augmentation de la distance à la paroi, ce coefficient de corrélation augmente en valeur absolue dans le DNS, et il reste le même dans la PIV avec Re_τ = 2220. La PIV avec Re_τ = 3840 présente le coefficient de corrélation le plus faible des trois ensembles de données. Cela

pourrait être attribué à la résolution spatiale limitée de l'ensemble de données.

L'effet du bruit dans le signal instantané est simulé avec l'ensemble de données DNS par l'ajout de bruit blanc gaussien additif (AGWN) de différents niveaux de rapport signal/bruit (SNB). Il a été constaté que lorsque le SNB=150, les résultats du coefficient de corrélation du DNS est approximativement égal à celui de la PIV à $Re_\tau = 2220$. De plus, la valeur absolue réduite du coefficient de corrélation entre $A_t + A$ et T_u est produite dans l'ensemble de données DNS avec l'ajout de l'AGWN, ce qui montre l'effet du bruit dans les petites échelles.

Acknowledgement

Foremost, I wish to express my gratitude to Prof. Jean-Marc Foucaut who provided me with this great opportunity to perfom research with him. The guidance, support and patience he provided always helped me immensely during the research and also with the writing. I am particularly grateful to him for sharing his knowledge in fluid mechanics, turbulent flows, his endless love to do experimental studies and that his curiosity to answer my questions even after-work hours and during vacations.

Many words of gratitude to Dr. Jean-Philippe Laval, who has always been there to help me without the slightest of hesitation. The numerical data provided by you hugely helped me to have an idea about the flow before embarking on the experiment and I am really thankful for your suggestions and ideas to help me out with the research. I would like to thank Tai Wada for his code which helped me to start processing the DNS data.

I am hugely indebted to Prof. Christos Vassilicos who really helped to shape the theoretical part of the thesis, with his visionary ideas to explain the physics behind the turbulent flows. Your ideas and suggestions really opened up a new perspective in my understanding of turbulence.

A very special gratitude to Dr. Christophe Cuvier to have provided me his insight about turbulence, fluid mechanics problems, PIV experiments and also with teaching duties. I am grateful to you and Dr. Yashar Ostovan for helping out with the PIV experiment and its processing.

I am thankful to all my colleagues at LMFL (Ilkay, Sri, Florian, Nathaniel, Hussein, Tarek, Adam, Oguzhan, Yashar..) for providing an invaluable set of resources both inside and outside the lab. I would also like to thank Nathalie Labaeye, Emanuelle Wingfield, Isabelle Flament for their unfailing support and assistance.

My friends outside lab Abhishek, Siva, Manasi, Phallyka, Morgane, Dorian, James, Miho, Gauthier, Rémi, Antoine, Hubert and many others : It really made my life in Lille an enjoyable and a memorable experience. I would like to extend my sincere thanks to my family for providing me the support over my decisions and for everything else in my life.

I would like to thank Centrale Lille, and the region Hauts-de-France for their financial support that made the study possible. This work was given access to HPC resources of IDRIS to perform the post processing of both numerical and experimental datasets.

Contents

Nomenclature

Abbreviations

2D	Two dimensional
3D	Three dimensional
2D2C	Two dimensions, two components
2D3C	Two dimensions, three components
DNS	Direct Numerical Simulations
FOV	Field-Of-View
HWA	Hot-Wire Anemometry
KHMH	Kármán-Howarth-Monin-Hill
L_{11}	Integral scale with streamise velocity in streamwise direction
L_{13}	Integral scale with streamise velocity in spanwise direction
LES	Large Eddy Simulations
LS	Least-Square method
LSM	Large Scale Motions
M	Magnification factor
PIV	Particle Image Velocimetry
RANS	Reynolds Averaged Navier Stokes
RMS	Root-Mean Square value
SNR	Signal-to-Noise Ratio
S-PIV	Stereoscopic PIV
PTV	Particle Tracking Velocimetry
Tomo PIV	Tompgraphic PIV
TBL	Turbulent Boundary Layer flow
TBL550	DNS of TBL dataset at $Re_\tau = 550$
TCF	Turbulent Channel Flow
TCF550	DNS of TCF dataset at $Re_\tau = 550$
TCF3000	DNS of TCF dataset at $Re_\tau = 3000$
TKE	Turbulent Kinetic Energy
WASS	Wall-Attached Self Similar structures
ZPG	Zero Pressure Gradient

Greek symbols

δ	Boundary layer thickness / Channel half-width
δ^*	Displacement thickness
$\delta\mathbf{u}^2$	Second-order structure function
ϵ	Dissipation based on the total velocity $\mathbf{u}$
ϵ'	Dissipation based on the fluctuation of velocity $\boldsymbol{u'}$
$\tilde{\epsilon}$	Pseudo-dissipation
λ	Taylor microscale
λ_x	Modified Taylor microscale in x- direction
λ_z	Modified Taylor microscale in z- direction
ρ	Density of the fluid
u_τ	Friction velocity
η	Kolmogorov length scale
μ	Dynamic viscosity of the fluid
$\nabla(.)$	Gradient of quantity
ϕ_d	Diameter of the particle
ν	Kinematic viscosity of the fluid
$\sigma_{(.)}$	Standard deviation
τ	Kolmogorov time scale
τ_w	Wall shear stress
θ	Momentum thickness
υ	Kolmogorov velocity scale

Latin symbols

A	Advection term in KHMH equation
A_t	Time derivative of second-order structure function
$A_t + A$	Sum of time derivative and advection terms
$\tilde{C}_{direct}$	Direct cascade of energy
$\tilde{C}_{inverse}$	Inverse cascade of energy
c_f	Skin friction coefficient
corr(.,.)	Correlation coefficient between two quantities
D_r	Diffusion in scale space
D_{x1}, D_{x2}, D_{x3}	Diffusion in physical space
H	Shape factor
f	Focal length of the lens
$f_\#$	Aperture size of the lens

f_s	Sampling frequency
k	Turbulent Kinetic Energy
u, v, w	Streamwise, wall-normal, spanwise total velocities. Alternatively u_1, u_2, u_3
$\overline{u}, \overline{v}, \overline{w}$	Streamwise, wall-normal, spanwise mean velocities. Alternatively $\overline{u_1}, \overline{u_2}, \overline{u_3}$
u', v', w'	Streamwise, wall-normal, spanwise velocity fluctuations. Alternatively u'_1, u'_2, u'_3
$\overline{\boldsymbol{u'_i u'_j}}$	Reynolds stress tensor
P_r	Production term
p	pressure
Π	Interscale energy transfer term
T_p	Pressure velocity correlation term
Re_τ	Reynolds number based friction velocity
$r_{(.)}$	Separation co-ordinate
T_u	Energy transfer in physical space
$\Pi + T_u$	Sum of energy transfer terms in both physical space and space of scales
U_∞	Free-stream velocity of the flow
U_e	Local free-stream velocity of the flow
$X_{(.)}$	Mid-point co-ordinate
x	Streamwise direction. Alternatively x_1
y	Wall-normal direction. Alternatively x_2
z	Spanwise direction. Alternatively x_3

Others

$(.)^+$	Wall units (u_τ, ν)
$\overline{(.)}$,$\langle . \rangle$	Mean

List of Figures

List of Tables

Part I

Introduction, Literature review and Overview of Kármán-Howarth-Monin-Hill equation

Chapter 1

Introduction

Turbulence is the most important unsolved problem of classical physics.

Richard P. Feynman

Turbulent flows present a challenging front in fluid mechanics research for more than a century. Its ubiquitous presence in natural and engineering flows including the flow of gulf streams, ocean currents, rivers, canals, etc for the former and the flow around aircraft, ships, cars, buildings, wind farms for the latter making it more relevant in the modern-day life. One of the first studies involved includes the classification of flow into laminar and turbulent states and was performed by Hagen [49]. This is followed by Reynolds [95] who studied laminar and turbulent flow in a pipe by performing a coloured filament experiment at different velocities. He experimented with different velocities, pipe diameters, and viscosities and found that the transition roughly happened at the same value of a dimensionless number, which is since addressed by his name Reynolds number, $\mathrm{Re} = \frac{Vd}{\nu}$.

Turbulence has inspired artists to make interesting works that date back to 15^{th}-century artwork by Leonardo da Vinci (1507), who painted the water flowing into a reservoir with attention to different scales of motions present in it. Three centuries later Vincent Van Gogh depicted turbulence in many of his paintings, notably *The Starry Night* [127] had much more detailing and has led to some researchers who then concluded that the paintings follow the turbulence theories [6, 11] that came decades later.

Turbulent flows are solved using the Navier-Stokes' equation, and the complexity of the flow implies that simplifying the flow results in a significant loss of physics. This is due to the non-linearities associated with flow, in addition to the physics that

depends on different scales of motion. This multi-scale nature of turbulent flows was studied in isotropic turbulence by Richardson [97], which is described in this famous poem, 'Big whirls have little whirls .... and so on to viscosity'. According to his model, the energy is injected at large scales and it flows down the scale until it reaches the smallest scale where it is dissipated due to viscosity. And viscosity and dissipation are confined to the smallest scales of the flow, and the energy cascade can occur between scales of similar size and is always a forward cascade of energy, meaning larger to smaller scales.

This is followed by Kolmogorov [67, 68, 69], alternatively known as the K41 theory, and Oboukhov [89] postulated the universality hypothesis that occurs at large Reynolds number limit where the inertial range separating the integral scales and the dissipative scales are so large that the small scales decouple entirely from large scales and exhibit isotropy. Based on this hypothesis, Kolmogorov argued that the dynamics of small scales are entirely governed by the mean dissipation of energy $\langle \epsilon' \rangle$ and viscosity ν, and therefore proposed length ($\eta = (\frac{\nu^3}{\epsilon})^{1/4}$), time ($\tau = (\nu/\epsilon)^{1/2}$) and velocity ($\upsilon = (\nu\epsilon)^{1/4}$) at those scales. He continued by stating that scales larger than the viscous scales thus discussed, will be free from the effect of viscosity and hence be governed by mean dissipation of energy alone. This gave rise to the famous 'two-thirds law' and 'five-thirds law', which states that the mean square of the velocity structure-function (δu^2) is equal to $C(\bar{\epsilon}r)^{2/3}$ in the real space and equal to $C_1(\bar{\epsilon})^{2/3}k^{-5/3}$ in the Fourier space, provided the 'r' and 'k' corresponds to the scale and wavenumber in the inertial subrange. The year 1961 produced further refinement to the existing hypothesis surrounding local the structure of turbulent flow at the limit of large Reynolds number by including the effect of intermittency of dissipation field. This essentially means that the K41 hypothesis is valid on the constancy of the mean rate of dissipation of kinetic energy $\langle \epsilon' \rangle$, and it does undergo highly disordered fluctuations and this only increases with the Reynolds number. This lead to corrections of the 'two-thirds law' and 'five-thirds law' which made them agree with the experimental and numerical data in the present day. Kolmogorov theory and its interpretation does go beyond the scope of the thesis and the interested reader may refer to Frisch and Kolmogorov [40] for a complete review.

The results from the past have shown some important results about the turbulent flow which is homogeneous and isotropic. In reality, turbulent flows are present with inhomogeneity or anisotropy in some directions which makes the applicability of the studies from the past to be more restrictive. De Karman and Howarth [31] used the correlation coefficient between two points to study the multi-point statistics. With

the introduction of the second-order structure-function by Kolmogorov became possible to study the energy cascade phenomenon in both physical space and space of scales. This is widely known as the $4/5^{th}$ law which can be written as

$$-\langle(\delta u_1)^3\rangle + 6\nu\frac{d}{dr}\langle(\delta u_1)^2\rangle = \frac{4}{5}\langle\epsilon'\rangle r \tag{1.1}$$

where $\langle\epsilon'\rangle$ is the mean dissipation rate of the turbulent kinetic energy, ν is the kinematic viscosity of the fluid and the angular brackets represent the ensemble averages. The derivation for the above can be found in Batchelor [10], Landau and Lifshitz [72]. Monin and Yaglom [84] derived what was called the Kolmogorov structure function equation or alternatively known as the Kármán-Howarth-Monin (KHM) equation without the assumption of global isotropy and had dropped the pressure term stating that velocity differences are uncorrelated with the difference of any scalar in isotropic turbulence. Frisch and Kolmogorov [40] generalised this Kármán-Howarth-Monin equation by adding the driving force for the turbulence which acts only on large scale, is steady in time, is homogenous in space. In turn, he was able to derive the four-fifths law from the energy flux equation. Lindborg [74] argued that in the Kármán-Howarth-Monin equation, pressure terms are made zero by erroneous arguments about local isotropy and this restricts it from obtaining the proper physics behind pressure velocity correlation in the inertial range. Hill [53] resolved the problem of neglecting pressure term on this basis of local isotropy and has provided derivations that show how different conditions such as local/global, isotropy/homogeneity, etc will result in pressure term becoming zero. Antonia et al. [5] derived the equation for $\delta u_1(\delta u_i)^2$ which appears similar to Yaglom's equation for $\delta u_1(\delta\theta)^2$ and is valid for relatively small scales and when the Reynolds number is moderate. The advantage is that this equation extends the Kolmogorov equation for all velocity components. Looking at the fact that limitation of Kolmogorov equation to apply for grid-generated decaying turbulent flow which is isotropic, Danaila et al. [29] reiterated the hypotheses involved in the derivation of the equation and derived an exact equation that contained a new term reflecting the non-stationarity or a rather large scale non-homogeneity along the streamwise direction. This increased the applicability of the Kolmogorov equation but is limited to decaying turbulence only. Lindborg [75] arrived at generalising the Kolmogorov equation by adding the time derivative term and estimated the new term using k - $\langle\epsilon\rangle$ model. Danaila et al. [28] derived the Kolmogorov equation for nearly homogeneous sheared turbulence by incorporating the shear effect in the outer region of the wall and also the non-homogeneity of large scales along the direction of the wall, which has good agreement with Hot-Wire Anemometry (HWA) data.

Hill[54] derived the exact equation for the scale-by-scale energy budget directly from Navier-Stokes' equation without any averages or assumptions about the isotropy/ homogeneity of the flow. This generalised Kolmogorov equation alternatively known as Kármán-Howarth-Monin-Hill (KHMH) equation, is an evolution equation for local and instantaneous Turbulent Kinetic Energy relating to a given separation vector ($\delta\mathbf{u}^2$) which quantifies the different processes associated with the energy transfer in both physical space and the space of scales and is possible to apply to all numerical and experimental turbulent flows. This equation is derived in different forms such as second-order structure-function for total velocity[137], velocity fluctuations[81,30,23], velocity decomposed into mean and fluctuations[125,4,46].

Kármán-Howarth-Monin-Hill equation opened up the possibility to study the scale-by-scale energy budget in most complex turbulent flows. This has resulted in a multitude of research in different turbulent flows. The following are the different studies that resulted from the KHMH equation in numerical simulations including Direct Numerical Simulations (DNS) and Large Eddy Simulations (LES). Marati et al.[81] studied the energy cascade and spatial flux in TCF and detailed the behaviour of the interscale transfer, production and dissipation in different regions in the wall-bounded turbulence. This way the dual nature of turbulent flows which is the small scale dynamics defined in the space of scales on the one hand and the near-wall physics which is defined in the physical space is addressed at the same time. This work was extended to higher Reynolds numbers by Saikrishnan et al.[99], who discovered the regimes with specific properties as a function of newly defined cross-over length scale which was not possible with the previous study. Cimarelli et al.[22] analysed the paths of energy cascade in TCF from the production from the buffer layer to the wall and the outer flow and emphasises the importance of inverse energy cascade in such processes. Cimarelli and De Angelis[21] discussed the modelling issues in LES of the backscatter which is prevalent in the small scales of wall-turbulent flows. Cimarelli et al.[23] described the two driving mechanisms namely, (a) a strong scale energy source in buffer layer concerning the near-wall cycle (b) an outer source associated with an outer turbulent cycle by following specific terms of the KHMH equation representing the energy cascade process. Alves Portela et al.[4] studied the turbulence cascade on the centerline of turbulent wake created by square prism using the KHMH equation. There exists a region far from the prism but within the near field of wake where the orientation averaged interscale cascade term is roughly equal to the dissipation rate even though the processes related to inhomogeneity are significant. Mollicone et al.[83] analysed the scale-by-scale budget in the dynamics of the shear layer in a separated region behind a bump in the chan-

nel flow, where the KHMH equation is solved in five dimensions comprising three scale-space coordinates and two physical co-ordinates in streamwise and wall-normal direction to link both the physics in both physical and scale space.

The following studies involve the use of the KHMH equation to study the scale-by-scale budget using experimental methods Particle Image Velocimetry (PIV) and Hot-wire Anemometry (HWA). Thiesset et al. [122] studied the central region of the wake behind a cylinder using the scale-by-scale budget in the context of isotropic and general frameworks. Danaila et al. [30] applied the KHMH equation in a different form to study the kinetic energy budget in the impact region of two opposed jets to conclude that the energy transfer occurs mostly in planes perpendicular to the axisymmetry axis and is strongly inhibited along the axisymmetry direction. Valente and Vassilicos [125] investigated the grid-generated turbulence to study the behaviour of different physical processes corresponding to different terms of KHMH equation such as energy transfer, dissipation, advection, production and transport at different distances from the grid. Gomes-Fernandes et al. [46] performed a PIV experiment behind grid-generated turbulence to study the energy cascade process using the KHMH equation to conclude that both forward and inverse cascade coexist instantaneously but only forward cascade on average. They also pointed out that well-defined 5/3 power law is obtained in the streamwise direction which is at a small angle to the inverse cascade region.

Objectives

The present work is perfomed in Labarotoire de Mécanique des Fluides de Lille - Kampé de Fériet (LMFL). The research in this group is mainly focused on understanding and explaining the physics of wall turbulence, by using both numerical simulations and experiments. Earlier and ongoing works by researchers in this group include the characterisation of high Reynolds number in decelerating TBL [27], the study of near-wall reverse flow event [134] on the PIV experiments side. Analysis of TBL flows using DNS to apply the skeletonization method to obtain detailed statistics on coherent structures [113], on the numerical side.

The present work aims to study the scale-by-scale energy budget using the KHMH equation to answer the following questions.

- It is known that the Turbulent Channel Flow and Turbulent Boundary Layer flows are similar to each other and it is restricted to certain wall-distances. Thus, the results obtained from the terms of mean KHMH equation terms

are also the same between the two flows when normalised with the proper parameters? Does the instantaneous form of KHMH terms behave the same between the two flows?

- Considering that the results from instantaneous KHMH equation rely on accurate estimation of fluctuations of different terms, is it possible to realise the same results from DNS datasets with experiments (PIV) which allows obtaining results at a higher Reynolds number (Re_τ) than DNS?
- Yasuda and Vassilicos [137] proposed studying the KHMH equation in the instantaneous sense to obtain the scale-by-scale energy budget in isotropic turbulence. Does the same idea implemented in wall-bounded turbulent flows enables to uncover new pieces of information about the energy cascade physics?
- Marati et al. [81] used the KHMH equation for the fluctuation of velocity to study the behaviour of different terms in average over a streamwise and spanwise plane. Despite being homogeneous directions, does studying the flow physics with streamwise and spanwise directions separately reveals more information?
- Saikrishnan et al. [99] found that in the logarithmic region, the interscale energy transfer of averaged KHMH equation varies with the Reynolds number. Is the influence of Reynolds number only visible in the logarithmic region even with the instantaneous statistics?
- Casciola et al. [19] introduces cross-over scale l_c^+, which separates the transfer dominated regimes and the production dominated regimes. Is there any other scale that corresponds to the behaviour of certain terms in the KHMH equation?

Approach

The primary goal is to solve the KHMH equation to obtain information about the scale-by-scale energy budget in the wall-bounded turbulent flows. There were different KHMH equations used in the past, and each has its own sets of advantages and disadvantages. For the present work, it was decided to use the KHMH equation written for total velocity [137], in which the velocity decomposition is performed to separate the influence of mean and turbulent fluctuations separately. For the present study, the values of $r_y = 0$ is used. This condition results in a lot of terms becoming identically equal to zero. Then the non-zero terms are computed and averaged with

the DNS of a TCF at $Re_\tau = 550$. This DNS is chosen because it is closer to some related studies in the past[81,99], thereby validating the codes used for computation.

This is followed by the use of the instantaneous KHMH equation to understand the physics associated with the fluctuations of each term. Computation of the KHMH equation as they appeared, resulted in a high residue in the balance of the left-hand and the right-hand sides of the equation. Thus it is necessary to obtain the correct balance to move forward. This is performed by switching back to original coordinates for the computation of the KHMH terms[41]. This method of computation resulted in negligible balance, which in turn allowed to perform the analysis in the instantaneous KHMH equation

The instantaneous behaviour of all the terms was quantified by visualising the standard deviation of all the terms. This is followed by the computation correlation coefficient between the different terms of the KHMH equation. Since each term corresponds to a physical process in the energy cascade, any significant value of correlation coefficient between certain terms essentially reveals the correlation between physical processes associated with them.

After analysing the terms with the TCF at $Re_\tau = 550$, the next step was to study the effect of the Reynolds number. And so the same analysis is performed on a DNS of TCF at $Re_\tau = 3000$. The different results so obtained from this flow is then compared with that of the previous DNS, by normalising the parameters accordingly ie., using wall units and channel half-width.

This is followed by performing the same analysis on ZPG TBL at $Re_\tau = 550$ and is compared with the results of TCF at the same Reynolds number. This is to identify the differences or similarities that occur between the two canonical wall-bounded turbulent flows.

The results obtained so far forms the base on which the PIV experiment on the ZPG TBL in LMFL is planned. With the results of the DNS of ZPG-TBL, it became possible to identify the type of experiments and to adjust the different parameters to obtain comparable results. The DNS data also allowed to choose the plane (XY-plane) for the two sets of independent stereoscopic PIV experiments overlooking the same field of view. The PIV experiment of ZPG-TBL is at $Re_\tau = 2272, 3840$, which is much higher than that of DNS of ZPG-TBL, and so the results of TCF at $Re_\tau = 3000$ so analysed previously gives the proper idea of what to expect from the experiments. The results from the PIV are obtained by the right use of the data

from the two independent stereoscopic PIV systems, to make the data free from noise.

The PIV dataset is then used to do the KHMH equation analysis with both averaged and the instantaneous sense. Since the PIV experiment is performed on an XY-plane, some spanwise derivatives ($\frac{\partial u_1}{\partial x_3}, \frac{\partial u_2}{\partial x_3}$) are not available for the computation of KHMH equation terms. Thus the DNS datasets are re-analysed by removing the missing derivatives so that the results correspond to that of PIV datasets which are plotted side-by-side for comparison.

Contents and Organisation of the thesis

The present work is organised into four parts which are further divided into eight chapters. Two appendices present the different computations and results involved in the present work. The parts are presented in an order that makes it easier for the reader to follow the introduction, motivations, methodology and results, which is the direct reflection of the work performed for the past three years.

Part I is the introduction of the document. Chapter 1 starts with the introduction of turbulence in general and is followed by the objectives and the research approach. Chapter 2 presents the relevant literature review of the wall-bounded turbulent flows. Chapter 3 explains the different parts of the KHMH equation used in the present work.

The three DNS datasets, which compares the effect of an increase of Reynolds number, and the differences between Turbulent Channel Flow and Turbulent Boundary Layer flow at the same Reynolds number is reported in Part II. Chapter 4 shows the parameters of the three DNS datasets used in the present work. Chapter 5 presents the results of the analysis of the KHMH equation with all three DNS datasets.

The two system S-PIV experiment performed as a part of the present work is explained in detail in Part III. Chapter 6 shows the various computation of multiple parameters used to design the PIV experiments. Chapter 7 presents the results of KHMH equation analysis with PIV experiment datasets and are then compared with corresponding results of the DNS datasets.

Part IV is the conclusion of the document. Chapter 8 presents the summaries of the conclusions of the results presented in the previous chapters. It also presents the possible perspectives for the KHMH equation analysis in general and to the DNS datasets and the PIV experiment datasets.

Publications and Communications

Conference participation

[1] (2019). *Energy budget in wall-bounded turbulent flows*, Turin, Italy, September 2-6, 2019. The 17th European Turbulence Conference

Chapter 2

Wall turbulence

Wall-bounded flows are one of the first flows where the turbulence was formally recognised[49,95]. In this case, vorticity is usually generated by an incoming flow which is bought to rest instantly by the presence of the wall. This is called the no-slip condition and it ensures that the tangential velocity of the fluid at the wall is equal to the tangential velocity of the wall. If the wall is at rest, then the no-slip condition requires the tangential velocity of the fluid at the wall to be identically zero. The vorticity thus generated is diffused, amplified or transported. The flow may develop in the absence of walls such as the free shear flows. On the other hand, wall-bounded turbulent flows are attached to the flow surface and evolve continuously under the influence of the wall.

In addition to the presence of a wall, turbulence usually requires the flow to be at a high Reynolds number (Re). In the definition of Reynolds number, viscous forces are in the denominator and hence high Re meant the flow was approximated to be inviscid. This led to the famous D'Alembert's paradox of no drag (viscous drag) in such inviscid flows. In reality, whenever flow happens around an object, there is always drag in addition to that as the velocity increased flow tends to separate, produces wakes and so on. Prandtl recognised the importance of viscous no-slip condition and proposed that at least one viscous term must be present in the high Reynolds number limit.

The equations used to solve the turbulent flows are the continuity equation also known as the conservation of mass equation and the Navier-Stokes' equation also known as the conservation of momentum equation. In the present work, the fluid flow is considered to be incompressible and isothermal, which implies that there is no change in density or temperature during the process. The governing equations

are given by :

$$\nabla.\boldsymbol{u} = 0 \tag{2.1}$$

$$\frac{\partial \boldsymbol{u}}{\partial t} + \boldsymbol{u}.\nabla\boldsymbol{u} = -\frac{1}{\rho}\frac{\partial p}{\partial x} + \nu\nabla^2\boldsymbol{u} + \boldsymbol{g} \tag{2.2}$$

where t is the time, $\mathbf{u}$ is the velocity vector, p is the pressure, ρ is the density of the fluid and ν is the kinematic viscosity of the fluid. External forces such as body forces (gravity, magnetic forces) are given by g.

Reynolds [96] introduced the decomposition of instantaneous velocity components into their mean and fluctuation parts, which is given by

$$\boldsymbol{u} = \overline{\boldsymbol{u}} + \boldsymbol{u'} \quad and \quad p = \overline{p} + p' \tag{2.3}$$

where the overbar denotes the mean component and the prime denotes the fluctuation component of the quantity.

Applying the Reynolds decomposition to the governing equations, we get the Reynolds Averaged Navier-Stokes' (RANS) equation, given by :

$$\frac{d\overline{\boldsymbol{u_i}}}{dx_i} = 0 \tag{2.4}$$

$$\rho\left(\frac{\partial\overline{\boldsymbol{u_i}}}{\partial t} + \overline{\boldsymbol{u_j}}\frac{\partial\overline{\boldsymbol{u_i}}}{\partial x_j}\right) = \frac{\partial\overline{p}}{\partial x_i} + \mu\frac{\partial^2\overline{\boldsymbol{u_i}}}{\partial x_j^2} - \rho\frac{\partial\overline{\boldsymbol{u_i'u_j'}}}{\partial x_j} \tag{2.5}$$

where $\overline{\boldsymbol{u_i'u_j'}}$ is the Reynolds stress tensor. The Reynolds Stress transport equation is obtained by subtracting Equation 2.5 from Equation 2.2, and then multiplying the result with $\boldsymbol{u_k'}$ and this is given by :

$$\begin{aligned}\frac{\partial}{\partial t}\overline{\boldsymbol{u_i'u_k'}} + \overline{\boldsymbol{u_j}}\frac{\partial}{\partial x_j}\overline{\boldsymbol{u_i'u_k'}} =& \overline{\frac{p'}{\rho}\left[\frac{\partial\boldsymbol{u_i'}}{\partial x_k} + \frac{\partial\boldsymbol{u_k'}}{\partial x_i}\right]} + \frac{\partial}{\partial x_j}\Bigg[-\frac{1}{\rho}\left(\overline{p'\boldsymbol{u_k'}}\delta_{ij} + \overline{p'\boldsymbol{u_i'}}\right) - \overline{\boldsymbol{u_i'u_j'u_k'}} \\ &+ 2\nu\left(\overline{s_{ij}\boldsymbol{u_k'}} + \overline{s_{kj}\boldsymbol{u_i'}}\right)\Bigg] - \left[\overline{\boldsymbol{u_i'u_j'}}\frac{\partial}{\partial x_j}\overline{\boldsymbol{u_k}} + \overline{\boldsymbol{u_k'u_i'}}\frac{\partial}{\partial x_j}\overline{\boldsymbol{u_i}}\right] \\ &- 2\nu\left[\overline{s_{ij}\frac{\partial\boldsymbol{u_k'}}{\partial x_j}} + \overline{s_{kj}\frac{\partial\boldsymbol{u_i'}}{\partial x_j}}\right]\end{aligned} \tag{2.6}$$

where s_{ij} is the strain rate tensor, which is defined by

$$s_{ij} \equiv \frac{1}{2}\left[\frac{\partial\boldsymbol{u_i}}{\partial x_j} + \frac{\partial\boldsymbol{u_j}}{\partial x_i}\right]$$

The Reynolds stress tensor is symmetric whose trace is equal to twice the turbulent kinetic energy, which is given by :

$$k = \frac{1}{2}\overline{\boldsymbol{u_i' u_i'}}$$

The equation for turbulent kinetic energy is obtained by contracting the free indices. For steady flows with constant physical properties, it is given by [45]

$$\begin{aligned}\left[\frac{\partial}{\partial t} + \overline{\boldsymbol{u_j}}\frac{\partial}{\partial x_j}\right]k =& \frac{\partial}{\partial x_j}\left[-\frac{1}{\rho}\left(\overline{p'\boldsymbol{u_i'}}\delta_{ij}\right) - \frac{1}{2}\overline{q^2\boldsymbol{u_j'}} + 2\nu\overline{\boldsymbol{s_{ij}u_i'}}\right] \\ &- \overline{\boldsymbol{u_i'u_j'}}\frac{\partial}{\partial x_j}\overline{\boldsymbol{u_i}} - 2\nu\overline{\boldsymbol{s_{ij}s_{ij}}}\end{aligned} \tag{2.7}$$

where $q^2 \equiv u_i u_i$, and is related to k which is given by:

$$k = \frac{1}{2}\overline{q^2}$$

In the above equation, each term corresponds to a different process concerning the turbulent kinetic energy fluctuations which are described in Schlichting and Gersten [105]. The first term on the left-hand side corresponds to the rate of change of kinetic energy due to convection. The second term on the left-hand side is the rate of change of the kinetic energy through advection of mean flow through an inhomogeneous fluid. The first term on the right-hand side corresponds to the transport of kinetic energy in an inhomogeneous fluid by the action of pressure fluctuations, turbulence fluctuations and viscous stresses respectively. This is followed by the rate of production of turbulent kinetic energy from the mean velocity gradient, which represents the flow of energy from the mean flow towards the turbulent fluctuations. The last term on the right-hand side represents the viscous dissipation term which is always positive. And the negative sign preceding the term makes it an "energy sink". When the production and dissipation are greater than all the other terms of the equation, both of them tend to balance each other and this represents the so-called "equilibrium region".

2.1 Turbulent Boundary Layer theory

In wall-bounded flows, a boundary layer is formed at the region close to the wall where the effect of viscosity is dominant and influences the dynamics of the flow. At the start of the development of the boundary layer, it is laminar and with an increase

of Reynolds number, the boundary layer eventually transitions to be fully turbulent. In an ideal fluid, the flow field is composed of a viscous boundary layer close to the wall and an inviscid outer flow which exhibits no fluctuations of velocity. In practice however, the outer flow is not free from turbulence. The turbulence intensity[105] is given by

$$Turbulence\ intensity = \frac{\sqrt{\frac{1}{3}(\overline{u'^2} + \overline{v'^2} + \overline{w'^2})}}{U_\infty} = \frac{\sqrt{2k/3}}{U_\infty} \tag{2.8}$$

The laminar-turbulent transition in a flow is dependent on the turbulence intensity. In addition, the development of turbulent boundary layer, point of separation and heat transfer are all influenced by the turbulence intensity of the outer flow.

The edge of the turbulent boundary layer is characterised by the transition from irrotational outer flow to the rotational turbulent boundary-layer flow. The thickness of the turbulent boundary layer (δ) is taken as the point at which the velocity of the flow (u) attains 0.99 times the freestream velocity of the flow (U_e). This quantity δ is not an absolute one, since the boundary layer exhibits strong fluctuation spatially and temporally. However, the boundary layer characteristics can be explained by displacement thickness (δ^*) and momentum thickness (θ), which has definite physical meaning. They are given by:

$$\delta^* = \int_0^\infty \left[1 - \frac{\overline{u}(y)}{U_e}\right] dy \tag{2.9}$$

and

$$\theta = \int_0^\infty \frac{\overline{u}(y)}{U_e}\left[1 - \frac{\overline{u}(y)}{U_e}\right] dy \tag{2.10}$$

The displacement thickness (δ^*) is defined as the distance through which the flow must be displaced outwards to the loss of velocity in the boundary layer due to friction. The momentum thickness (θ) defines as the thickness of an imaginary layer in fluid flow whose momentum is equal to the loss of momentum per unit time to the real fluid in the turbulent boundary layer. A quantity relating the two thicknesses is the shape factor (H), which is the ratio of displacement thickness to momentum thickness

$$H = \frac{\delta^*}{\theta} \tag{2.11}$$

In wall-bounded turbulent flows, it is important to study the physics that defines the wall itself. One such quantity is the wall shear stress, which is defined by

$$\tau_w = \nu\left(\left.\frac{\partial \overline{u}}{\partial y}\right|_w\right) \tag{2.12}$$

where the subscript 'w' denotes the value of the quantity at the wall. A non-dimensional quantity that defines this wall shear stress is the skin-friction coefficient

$$c_f = \frac{\tau_w(x)}{\frac{1}{2}\rho U_e^2} \tag{2.13}$$

The normalisation based on wall viscous length scale is given by $\delta_\nu = \frac{\nu}{u_\tau}$ and on the friction velocity scale is $u_\tau = \sqrt{\frac{\tau_w}{\rho}}$. The Reynolds number based on this friction velocity is given $Re_\tau = \frac{u_\tau \delta}{\nu}$. Another equally used Reynolds number is based on the momentum thickness, given by $Re_\theta = \frac{U_e \theta}{\nu}$

2.2 Boundary-Layer Equations for Plane Flows

The fundamental equations given in Equations 2.4, 2.5 are simplified using the two-dimensional boundary layer approximations ($\overline{w} \equiv 0$) which hold for $Re \to \infty$, given by:

- $\delta << \mathrm{L}$
- $\frac{\partial}{\partial x} << \frac{\partial}{\partial y}$
- $\overline{v} << U_e$

where δ is the thickness of the boundary layer, L is the length scale in the streamwise direction of the flow and $\overline{v}$ is the mean velocity in the wall-normal direction and U_e is the free-stream velocity outside the turbulent boundary layer. Applying the boundary layer approximations to the equation 2.5 in the y-direction results in :

$$0 = \frac{\partial \overline{p}}{\partial y} - \frac{\partial \rho \overline{v'^2}}{\partial y} \tag{2.14}$$

Integrating the equation over the boundary layer thickness gives

$$\overline{p} + \rho \overline{v'^2} = \overline{p_w} = p_e \tag{2.15}$$

Here, the outer layer is assumed to be free from turbulence and so the pressure is p_e. Since the velocity fluctuations are zero at the wall, the pressure at wall $\overline{p_w} = p_e$. However, in the turbulent flow between the wall and the outer layer, the pressure $\overline{p}$

is not a constant but $\overline{p} + \rho\overline{v'^2}$ is a constant.
The x- momentum equation 2.5 after boundary layer approximation is given by

$$\rho\left(\overline{u}\frac{\partial\overline{u}}{\partial x} + \overline{v}\frac{\partial\overline{u}}{\partial y}\right) = -\frac{d\overline{p}}{dx} + \frac{\partial}{\partial y}\left(\mu\frac{\partial\overline{u}}{\partial y} - \rho\overline{u'v'}\right) \tag{2.16}$$

$$\frac{\partial\overline{u}}{\partial x} + \frac{\partial\overline{v}}{\partial y} = 0 \tag{2.17}$$

The equation of kinetic energy of turbulent fluctuations after boundary layer approximations is given by:

$$\rho\left(\overline{u}\frac{\partial k}{\partial x} + \overline{v}\frac{\partial k}{\partial y}\right) = \mu\frac{\partial^2 k}{\partial y^2} - \frac{\partial}{\partial y}\left[\overline{v'\left(p' + \frac{\rho}{2}q^2\right)}\right] - \rho\overline{u'v'}\frac{\partial\overline{u}}{\partial y} - \rho(\overline{u'^2} - \overline{v'^2})\frac{\partial\overline{u}}{\partial x} - \rho\epsilon' \tag{2.18}$$

where ϵ' is the pseudo-dissipation[92]

Boundary layers are classified into three categories based on how the pressure varies downstream. They are : (a) Zero Pressure Gradient (ZPG) which implies the mean pressure doesn't vary as the flow travels downstream ($\frac{\partial p}{\partial x} = 0$), (b) Favourable Pressure Gradient (FPG) which implies the mean pressure decreases as the flow travels downstream ($\frac{\partial p}{\partial x} < 0$), (c) Adverse Pressure Gradient (APG) which implies that the mean pressure increases as the flow travels downstream ($\frac{\partial p}{\partial x} > 0$).

2.3 ZPG Turbulent Boundary Layer

ZPG Turbulent Boundary Layer occurs in the canonical wall-bounded turbulent flows like fully developed turbulent pipe flow, channel flow and ZPG turbulent boundary layer flow. In these flows, at sufficiently high Reynolds number two distinct regions exist, which are the inner region and the outer region.

The inner region encompasses the flow between the wall and $y^+ = 0.1\delta$, where δ is the thickness of turbulent boundary layer[92]. This is analogous to the thin wall-layer in the two-layer structure in which Schlichting and Gersten[105] explains that both turbulent and molecular momentum transfer co-exist to define the dynamics of the flow. Equation 2.16 for ZPG are obtained by neglecting the convective terms ($\overline{u} << U$) and substituting the pressure gradient term to zero *i.e.*, $\frac{\partial P}{\partial x} = 0$. This is given by :

$$\underbrace{\mu\frac{\partial^2\overline{u}}{\partial y^2}}_{\overline{\tau_v}} - \underbrace{\rho\frac{\partial\overline{u'v'}}{\partial y}}_{\overline{\tau_t}} = 0 \tag{2.19}$$

There are two ways by which the momentum is transferred between the wall and the rest of the flow. They are momentum transfer due to viscosity ($\overline{\tau_v}$ and momentum transfer due to turbulent fluctuations ($\overline{\tau_t}$). Integrating the above equation in the wall-normal direction till the wall, we get

$$\tau = \mu\frac{\partial u}{\partial y} - \rho\overline{u'v'} = \tau_w = \rho u_\tau^2 \tag{2.20}$$

The above equation can be rearranged by the following

$$\tau_w = \rho u_\tau^2 = \mu\frac{\partial \overline{u}}{\partial y}\bigg|_{y=0} = constant \tag{2.21}$$

Integrating the equation gives

$$\overline{u}(y) = y\frac{u_\tau^2}{\nu} \tag{2.22}$$

$$\overline{u}^+ = f(y^+) \tag{2.23}$$

The inner layer is further divided into a viscous sublayer, buffer layer and an overlap layer. The viscous sublayer is also known as the linear sublayer where the viscosity effect dominates and the Reynolds stress is negligible. This is followed by the buffer layer, where both viscous and Reynolds stresses are comparable. In the overlap region, the Reynolds stress term dominates the viscous stress term. This is summarised in Table 2.1.

Region	Location	Defining property	Equation
Viscous sublayer	$y^+ < 5$	$\mu\frac{\partial \overline{u}}{\partial y} >> \rho\overline{u'v'}$	$\overline{u}^+ = y^+$
Buffer layer	$5 < y^+ < 30$	$\mu\frac{\partial \overline{u}}{\partial y} \sim \rho\overline{u'v'}$	$\frac{\partial \overline{u}^+}{\partial y^+} - \overline{u'v'}^+ = constant$
Overlap Layer	$y^+ > 50$, $y/\delta < 0.1$	$\mu\frac{\partial \overline{u}}{\partial y} << \rho\overline{u'v'}$	$\overline{u}^+ = \frac{1}{\kappa}ln(y^+) + c$

Table 2.1: Different layers of inner regions with defining properties, reproduced from Pope[92]

The outer region or core region is where the direct effect of viscosity is negligible. This found approximately at $y^+ > 50$. Tennekes et al.[119] explains that the Reynolds stresses scales with u_τ^2 and so the mean velocity gradient in the wall-normal direction dU/dy will scale with u_τ/h. Hence :

$$\frac{dU}{dy} = \frac{u_\tau}{\delta}\frac{dF}{d\eta} \tag{2.24}$$

where $\eta = \frac{y}{\delta}$, and F is an unknown function with $\frac{dF}{d\eta}$ of order 1. Integrating the above equation from till the edge of the boundary layer,

$$\frac{U_e - \overline{u}}{u_\tau} = F(\eta) \tag{2.25}$$

The overlap region is a region where the scaling laws for both the inner region and the outer region holds good. This is derived by matching equations for inner and outer regions and was proposed by Millikan [82]. Starting with Equation 2.23

$$\overline{u}^+ = f(y^+) \tag{2.26}$$

This gives

$$\frac{d\overline{u}^+}{dy} = \frac{u_\tau^2}{\nu}\frac{df}{dy^+} \tag{2.27}$$

In the core region, Equation 2.24 is valid. Equating them both gives:

$$\frac{u_\tau}{\delta}\frac{dF}{d\eta} = \frac{u_\tau^2}{\nu}\frac{df}{dy^+} \tag{2.28}$$

Multiplying y/u_τ gives

$$\eta\frac{dF}{d\eta} = y^+\frac{df}{dy^+} = \frac{1}{\kappa} \tag{2.29}$$

This results in :

$$F(\eta) = \frac{U_e - \overline{u}}{u_\tau} = \frac{1}{\kappa}ln(\eta) + constant \tag{2.30}$$

$$f(y^+) = \frac{\overline{u}}{u_\tau} = \frac{1}{\kappa}ln(y^+) + constant \tag{2.31}$$

Both the equations above are valid only if $\eta << 1$ and $y^+ >> 1$. The constant κ in the above equations is called the von Kármán constant, since Von Kármán [128] derived this logarithmic profile using similarity arguments. The value of κ is much debated from the second half of the last century to even today. For ZPG turbulent boundary layers, an accepted value of κ is 0.41 [26]. This logarithmic region is also valid for fully developed channel flows, pipe flows in which the corresponding length scale must be used in the derivation.

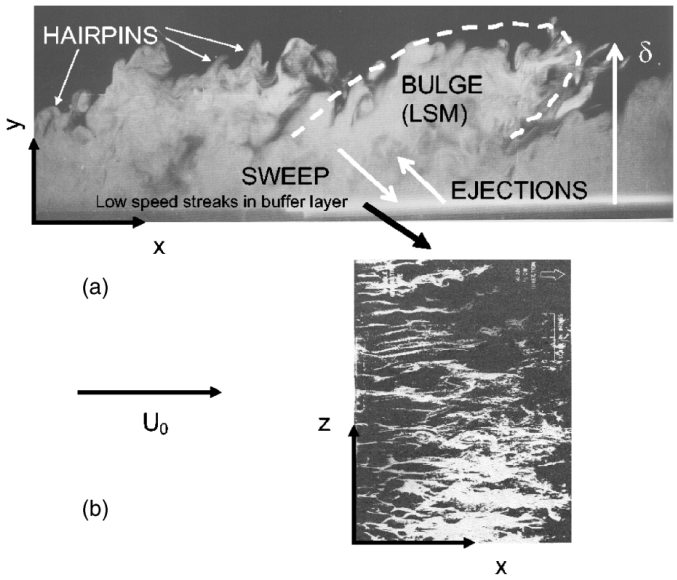

Figure 2.1: (a) Smoke visualisation of the streamwise-wall-normal plane in a turbulent boundary layer (from Falco[37]) (b) H_2 visualisation of low-speed streaks in the streamwise-spanwise plane (from Kline et al.[66]). Figure and captions reproduced from Adrian[1].

2.4 Coherent Structures

It is well known that turbulent flows are random, complex, most importantly multi-scaled in nature. The need for a better understanding of the flow, such as finding order in the random flow, explaining the different mechanisms in the flow *etc*, motivates the study of so-called *eddies*[123] or *coherent structures*[17]. These structures are entities in the fluid flow that tends to possess temporal coherence, in addition to the spatial coherence which is an inherent part of fluid continuity. Thus the coherent structures tend to have time scales that are much larger than the smallest scales of turbulent flow and/or contributes significantly to the averaged statistics of the flow[1].

A brief account of the coherent structures in the canonical wall-bounded turbulent flow which includes the steady, fully developed, smooth-walled channel and pipe flow and the zero pressure gradient turbulent boundary layer is presented in this literature review.

Starting with the well-known smoke visualisation of a low Reynolds number turbulent boundary layer flow in Figure 2.1(a) shows the many different known types of coherent structures. Near the outer edge between the smoke-filled regions and clear

regions are large-scale motions (LSMs) or *turbulent bulges* which is of the order of $2-3\delta$. There is the presence of hairpin vortices above the LSMs, which are similar to the *horseshoe vortex* proposed by Theodorsen [121]. The horseshoe vortices are vortex elements that are oriented in the spanwise direction and are slightly perturbed above the wall. Later investigations have shown this structure to be a hairpin with a pair of counter-rotating vortices oriented along the streamwise direction [98]. In addition to the horseshoe vortex structures, other types of vortical structures that appeared in the literature such as hairpin vortices [50], counter-rotating eddy pair of elongated streamwise extent [9], canes [48].

The characteristics of the vortex structure such as the shape and size are dependent on the Reynolds number [50], and studies have shown that they are inclined downstream at about 42^o-46^o, which indicates that on average it is about 45^o with the wall. Figure 2.1(b) shows the long streamwise low-speed streaks of H_2 bubbles reported by Kline et al. [66] near the wall. The streaks are observed in the buffer layer and are observed to have a mean spanwise spacing of about 100 wall units, which is widely accepted in studies of wall-bounded turbulence [1]. Robinson [98] reports that these low-speed streaks associates with the quasi-streamwise vortices and are responsible for the lift-up of the viscously retarded fluid from regions near the wall. Studies have also shown that in which the streaks wavered vertically with high amplitudes and eventually becomes detached from the wall in a chaotic motion sequence of events which is termed as *bursting*.

It is well-known that in the Turbulent Kinetic Energy Equation 2.7, the production term contains the product of the Reynolds stress and the mean velocity gradient. It is also known that the net Reynolds force retards the mean velocity in the core of the flow and accelerates it near the wall. Corino and Brodkey [24] with their experiment on moving frame-of-reference found out the connected regions of near flow erupted away from the wall due to the near-wall deceleration in a process of ejection. In addition, Corino and Brodkey [24] estimated that in a pipe flow of $Re_d = 20000$, the ejections accounted for 70% of the Reynolds shear stress while occurring only about 18% of the time. Shortly after, in the pursuit of understanding more about the role of the Reynolds stresses in the turbulent flow, Wallace et al. [130] introduced the concept of quadrant analysis which is the decomposition of velocity fluctuations contributing to Reynolds stress term $\overline{u'v'}$ into four parts, and therefore the name quadrant analysis. This is achieved by classifying the product of the velocity fluctuations into Q1(+u,+v) events correspond to outward interaction, Q2(-u,+v) events correspond to ejection, Q3(-u,-v) events corresponds to inward interaction

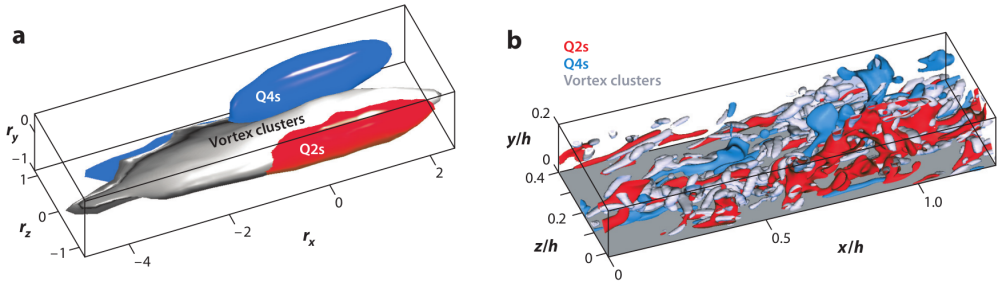

Figure 2.2: (a) PDFs of scales that have Q2 (green), Q4 (blue) and vortex clusters (grey). Instantaneous snapshot of the distribution of Q2, Q4 and vortex clusters with the same colour code as of (a). The results are of Lozano-Durán et al. [76] and are adapted and reproduced from Wallace [129].

and Q4(+u,-v) events corresponds to sweep.

Kim and Moin [65] used quadrant analysis with two conditions : (a) local and instantaneous Q2 and $u'v'$ product values above a specific threshold value, the ensemble-averaged vorticity lines resembled hairpins, (b) the same with Q4 events, they resembled inverted hairpins. Adrian and Moin [2] obtained linear mean-square stochastic estimation with $u'v'$ as event vector conditions which are from the values from the Q2 and Q4 peak values covariance integrand plots. This methodology enabled to obtain the hairpin and the inverted hairpin structures in the flow which agreed with similar results were found by Kim and Moin [65] in the DNS of channel flow. Bernard and Handler [12] used Lagrangian particle tracking that passes through a fixed Eulerian location in a DNS of turbulent channel flow, to explain the existence of Q1 and Q3 type events and serves as a redirection of particles to the wall before passing into the Q2 and Q4 type events, in agreement with the results of Brodkey et al. [14]. In addition, the Lagrangian particle tracking enabled to obtain the result that at $y^+ = 12$, all particles contributing to Q2 events do not originate from $y^+ < 12$.

Lozano-Durán et al. [76] extended the quadrant analysis by considering three-dimensional connected structures in the logarithmic and outer layers in DNS of turbulent channel flow. They obtained two types of structures namely, wall-attached and wall-detached structures based on the definition of hole Reynolds-stress $u'v'$ magnitude filtering by Willmarth and Lu [136]. The properties of the wall-detached structures include small, isotropically oriented and are revealed not to have any contribution towards the mean shear stress. Thus all the contributions to mean Reynolds stress is mainly from the wall-attached structures which are larger than the wall-detached structures. The author also shows that despite the complex instantaneous structures dis-

tribution (Figure 2.2(b)) in the logarithmic layer, the dominant ensemble-averaged structure is a quasi-streamwise vortex separating the Q2 and Q4 events on the side given by Figure 2.2(a). Lozano-Durán and Jiménez[77] extended this analysis at a higher Reynolds number to conclude that the large attached structures which are found to extend from the wall to the logarithmic layer tend to contribute most to the vertical momentum flux and also has long lifespans.

Chapter 3

Kármán-Howarth-Monin-Hill equation

3.1 The KHMH equation with full velocity

The KHMH equation which was introduced in the previous chapters was originally derived by Hill [54] from Navier-Stokes' equation. It follows different processes associated with the evolution of $(\delta\mathbf{u})^2$, which when derived in its general sense, contains no velocity decomposition, no assumption and also no averages. In this form, it is possible to extract the basic underlying physics behind each process in the energy cascade.

$$\frac{\partial}{\partial t}(\boldsymbol{u_i}) + \boldsymbol{u_j}\frac{\partial}{\partial x_j}(\boldsymbol{u_i}) = -\frac{1}{\rho}\frac{\partial}{\partial x_i}(p) + \nu\frac{\partial^2}{\partial x_j^2}(\boldsymbol{u_i}) \tag{3.1}$$

The KHMH equation based on total velocity (mean+fluctuation) is derived by applying the Navier-Stokes' equation (given by Equation 3.1) at two points separated by distance 'r'. This results in two equations, which are then subtracted to obtain the equation in terms of the increment of velocity 'δu_i'. The resulting equation is then converted from the co-ordinates based on two points to co-ordinates based on midpoint (X) and separation distance (r), by the following equations :

$$\frac{\partial\phi}{\partial X_j} = \frac{\partial\phi}{\partial x_j}\bigg|_1 + \frac{\partial\phi}{\partial x_j}\bigg|_2$$

$$\frac{\partial\phi}{\partial r_j} = \frac{1}{2}\left[\frac{\partial\phi}{\partial x_j}\bigg|_2 - \frac{\partial\phi}{\partial x_j}\bigg|_1\right]$$

$$\frac{\partial^2\phi}{\partial X_j^2} = \frac{\partial^2\phi}{\partial x_j^2}\bigg|_1 + \frac{\partial^2\phi}{\partial x_j^2}\bigg|_2 + 2\frac{\partial}{\partial x_j}\left(\frac{\partial\phi}{\partial x_j}\bigg|_2\right)\bigg|_1 \tag{3.2}$$

$$\frac{\partial^2\phi}{\partial r_j^2} = \frac{1}{4}\left[\left.\frac{\partial^2\phi}{\partial x_j^2}\right|_1 + \left.\frac{\partial^2\phi}{\partial x_j^2}\right|_2 - \frac{1}{2}\frac{\partial}{\partial x_j}\left(\left.\frac{\partial\phi}{\partial x_j}\right|_2\right)\right|_1\Bigg]$$

This equation is then multiplied by an increment of another component of velocity to get an equation for '$\delta\boldsymbol{u_i}\delta\boldsymbol{u_k}$'. And another equation is written with 'i' and 'k' reversed to obtain it in terms of '$\delta\boldsymbol{u_k}\delta\boldsymbol{u_i}$', which is then added together with the previous equation. The trace of that resulting equation gives an equation for '$\delta\boldsymbol{u_i}^2$', which is called the local and instantaneous TKE relating to a given separation vector.

$$\begin{aligned}\frac{\partial}{\partial t}(\delta\boldsymbol{u_i})^2 + \delta\boldsymbol{u_j}\frac{\partial}{\partial r_j}(\delta\boldsymbol{u_i})^2 + \boldsymbol{u_j^*}\frac{\partial}{\partial X_j}(\delta\boldsymbol{u_i})^2 = &-\frac{2}{\rho}\delta\boldsymbol{u_i}\frac{\partial}{\partial X_i}(\delta p) + 2\nu\frac{\partial^2}{\partial r_j^2}(\delta\boldsymbol{u_i})^2 + \frac{\nu}{2}\frac{\partial^2}{\partial X_j^2}(\delta\boldsymbol{u_i})^2 \\ &- 2\nu\left[\left(\left.\frac{\partial\boldsymbol{u_i}}{\partial x_j}\right|_1\right)^2 + \left(\left.\frac{\partial\boldsymbol{u_i}}{\partial x_j}\right|_2\right)^2\right]\end{aligned} \tag{3.3}$$

where ν is the kinematic viscosity, ρ is the fluid density.

The equation above is the KHMH equation which quantifies the energy cascade in space of scales and the physical space. The seven different terms in the equation 3.3, defines seven different processes related to energy cascade in the flow, given by:

- $\frac{\partial}{\partial t}(\delta\boldsymbol{u_i})^2$ is the time-derivative term
- $\delta\boldsymbol{u_j}\frac{\partial}{\partial r_j}(\delta\boldsymbol{u_i})^2$ is the interscale energy cascade term
- $\boldsymbol{u_j^*}\frac{\partial}{\partial X_j}(\delta\boldsymbol{u_i})^2$ is the energy transfer term in physical space
- $\frac{2}{\rho}\delta\boldsymbol{u_i}\frac{\partial}{\partial X_i}(\delta p)$ is the pressure-velocity term
- $2\nu\frac{\partial^2}{\partial r_j^2}(\delta\boldsymbol{u_i})^2$ is the diffusion in scale space
- $\frac{\nu}{2}\frac{\partial^2}{\partial X_j^2}(\delta\boldsymbol{u_i})^2$ is the diffusion in physical space
- $2\nu\left[\left(\left.\frac{\partial\boldsymbol{u_i}}{\partial x_j}\right|_1\right)^2 + \left(\left.\frac{\partial\boldsymbol{u_i}}{\partial x_j}\right|_2\right)^2\right]$ is the dissipation term

3.2 The KHMH equation with velocity decomposition

The KHMH equation based on full velocity is used to study the scale-by-scale energy budget in flows with no mean flow, such as the periodic box simulations. This way the Equation 3.3 enables to study the dynamics of the flow due to the fluctuation

of velocity. In the current study on wall-bounded turbulent flows in which there is mean flow, it becomes necessary to decompose the velocity into its mean and fluctuation components. The resulting equation consists of a lot of terms containing both mean and fluctuation terms of structure functions. In the present study, it is then simplified by studying the behaviour of the terms only along the streamwise (r_x) and spanwise direction (r_z) in the scale space, i.e., $r_y = 0$. In fully developed canonical wall-bounded turbulent flow such as the channel flow, the mean flow velocity varies only in the wall-normal direction (y-direction). If the y-direction scale space (r_y) is kept at zero, then this will eliminate all the structure-function quantity which contains the mean velocities, i.e., $\delta\overline{\boldsymbol{u_i}} = 0$. This is explained for all terms.

Substituting $\delta\boldsymbol{u_i} = \delta\overline{\boldsymbol{u_i}} + \boldsymbol{u_i'}$

The time derivative is given by

$$\frac{\partial}{\partial t}(\delta\overline{\boldsymbol{u_i}} + \delta\boldsymbol{u_i'})^2 = \underbrace{\frac{\partial}{\partial t}(\delta\boldsymbol{u_i'})^2}_{A_t} + \underbrace{\left[\frac{\partial}{\partial t}(\delta\overline{\boldsymbol{u_i}})^2 + 2\delta\boldsymbol{u_i'}\frac{\partial}{\partial t}(\delta\overline{\boldsymbol{u_i}}) + 2\delta\overline{\boldsymbol{u_i}}\frac{\partial}{\partial t}(\delta\boldsymbol{u_i'})\right]}_{\text{zero terms when } r_y=0} \tag{3.4}$$

The interscale energy transfer is given by

$$\begin{aligned}(\delta\overline{\boldsymbol{u_j}} + \delta\boldsymbol{u_j'})\frac{\partial}{\partial r_j}(\delta\overline{\boldsymbol{u_i}} + \delta\boldsymbol{u_i'})^2 = &\underbrace{\delta\boldsymbol{u_j'}\frac{\partial}{\partial r_j}(\delta\boldsymbol{u_i'})^2}_{\Pi} + \underbrace{2\delta\boldsymbol{u_j'}\delta\boldsymbol{u_i'}\frac{\partial}{\partial r_j}(\delta\overline{\boldsymbol{u_i}})}_{P_r} \\ &+ \underbrace{\delta\overline{\boldsymbol{u_j}}\frac{\partial}{\partial r_j}(\delta\overline{\boldsymbol{u_i}})^2 + \delta\overline{\boldsymbol{u_j}}\frac{\partial}{\partial r_j}(\delta\boldsymbol{u_i'})^2 + \delta\overline{\boldsymbol{u_j}}\delta\overline{\boldsymbol{u_i}}\frac{\partial}{\partial r_j}(\delta\boldsymbol{u_i'})}_{\text{zero terms when } r_y=0} \\ &+ \underbrace{2\delta\overline{\boldsymbol{u_j}}\delta\boldsymbol{u_i'}\frac{\partial}{\partial r_j}(\delta\overline{\boldsymbol{u_i}}) + 2\delta\boldsymbol{u_j'}\delta\overline{\boldsymbol{u_i}}\frac{\partial}{\partial r_j}(\delta\overline{\boldsymbol{u_i}}) + 2\delta\boldsymbol{u_j'}\delta\overline{\boldsymbol{u_i}}\frac{\partial}{\partial r_j}(\delta\boldsymbol{u_i'})}_{\text{zero terms when } r_y=0}\end{aligned} \tag{3.5}$$

The energy transfer in physical space is given by

$$\begin{aligned}(\overline{\boldsymbol{u_j^*}} + \boldsymbol{u_j^{*\prime}})\frac{\partial}{\partial X_j}(\delta\overline{\boldsymbol{u_i}} + \delta\boldsymbol{u_i'})^2 = &\underbrace{\overline{\boldsymbol{u_j^*}}\frac{\partial}{\partial X_j}(\delta\boldsymbol{u_i'})^2}_{A} + \underbrace{\boldsymbol{u_j^{*\prime}}\frac{\partial}{\partial X_j}(\delta\boldsymbol{u_i'})^2}_{T_u} \\ &+ \underbrace{\overline{\boldsymbol{u_j^*}}\frac{\partial}{\partial X_j}(\delta\overline{\boldsymbol{u_i}})^2 + 2\overline{\boldsymbol{u_j^*}}\delta\overline{\boldsymbol{u_i}}\frac{\partial}{\partial X_j}(\delta\boldsymbol{u_i'}) + 2\overline{\boldsymbol{u_j^*}}\delta\boldsymbol{u_i'}\frac{\partial}{\partial X_j}(\delta\overline{\boldsymbol{u_i}})}_{\text{zero terms when } r_y=0} \\ &+ \underbrace{\boldsymbol{u_j^{*\prime}}\frac{\partial}{\partial X_j}(\delta\overline{\boldsymbol{u_i}})^2 + 2\boldsymbol{u_j^{*\prime}}\delta\overline{\boldsymbol{u_i}}\frac{\partial}{\partial X_j}(\delta\boldsymbol{u_i'}) + 2\boldsymbol{u_j^{*\prime}}\delta\boldsymbol{u_i'}\frac{\partial}{\partial X_j}(\delta\overline{\boldsymbol{u_i}})}_{\text{zero terms when } r_y=0}\end{aligned} \tag{3.6}$$

The pressure term is given by

$$-\frac{2}{\rho}(\delta\overline{\boldsymbol{u_i}}+\delta\boldsymbol{u_i'})\frac{\partial}{\partial X_i}(\delta p) = \underbrace{-\frac{2}{\rho}(\delta\boldsymbol{u_i'})\frac{\partial}{\partial X_i}(\delta p)}_{T_p} \underbrace{-\frac{2}{\rho}\delta\overline{\boldsymbol{u_i}}\frac{\partial}{\partial X_i}(\delta p)}_{\text{zero term when } r_y=0} \tag{3.7}$$

The interscale diffusion term is given by

$$2\nu\frac{\partial^2}{\partial r_j^2}(\delta\overline{\boldsymbol{u_i}}+\delta\boldsymbol{u_i'})^2 = \underbrace{2\nu\frac{\partial^2}{\partial r_j^2}(\delta\overline{\boldsymbol{u_i}})^2}_{D_{r1}} + \underbrace{2\nu\frac{\partial^2}{\partial r_j^2}(\delta\boldsymbol{u_i'})^2}_{D_{r2}} + \underbrace{2\nu\frac{\partial^2}{\partial r_j^2}(2\delta\overline{\boldsymbol{u_i}}\delta\boldsymbol{u_i'})}_{D_{r3}} \tag{3.8}$$

The diffusion in physical space term (D_x) is given by

$$\frac{\nu}{2}\frac{\partial^2}{\partial X_j^2}(\delta\overline{\boldsymbol{u_i}}+\delta\boldsymbol{u_i'})^2 = \underbrace{\frac{\nu}{2}\frac{\partial^2}{\partial X_j^2}(\delta\boldsymbol{u_i'})^2}_{D_x} + \underbrace{\frac{\nu}{2}\frac{\partial^2}{\partial X_j^2}(\delta\overline{\boldsymbol{u_i}}^2) + \frac{\nu}{2}\frac{\partial^2}{\partial X_j^2}(2\delta\overline{\boldsymbol{u_i}}\delta\boldsymbol{u_i'})}_{\text{zero terms when } r_y=0} \tag{3.9}$$

The dissipation term (ϵ) is considered as an entire term, i.e., without velocity decompositions. This is given by the last term in Equation 3.3. However, there is another form of dissipation based on the derivative of velocity fluctuations, which is also used in the present study. This is given by

$$\epsilon' = 2\nu\left[\left(\frac{\partial\boldsymbol{u_i'}}{\partial x_j}\bigg|_1\right)^2 + \left(\frac{\partial\boldsymbol{u_i'}}{\partial x_j}\bigg|_2\right)^2\right] \tag{3.10}$$

Thus the remaining terms of the velocity decomposed KHMH equation with $r_y = 0$ is given by:

$$\begin{aligned}
&\underbrace{\frac{\partial}{\partial t}(\delta\boldsymbol{u_i'})^2}_{A_t} + \underbrace{\delta\boldsymbol{u_j'}\frac{\partial}{\partial r_j}(\delta\boldsymbol{u_i'})^2}_{\Pi} + \underbrace{2\delta\boldsymbol{u_j'}\delta\boldsymbol{u_i'}\frac{\partial}{\partial r_j}(\delta\overline{\boldsymbol{u_i}})}_{P_r} + \underbrace{\overline{\boldsymbol{u_j^*}}\frac{\partial}{\partial X_j}(\delta\boldsymbol{u_i'})^2}_{A} + \underbrace{\boldsymbol{u_j'^*}\frac{\partial}{\partial X_j}(\delta\boldsymbol{u_i'})^2}_{T_u} \\
&= \underbrace{-\frac{2}{\rho}\delta\boldsymbol{u_i'}\frac{\partial}{\partial X_i}(\delta p)}_{T_p} + \underbrace{2\nu\frac{\partial^2}{\partial r_j^2}(\delta\overline{\boldsymbol{u_i}})^2}_{D_{r1}} + \underbrace{2\nu\frac{\partial^2}{\partial r_j^2}(\delta\boldsymbol{u_i'})^2}_{D_{r2}} + \underbrace{4\nu\frac{\partial^2}{\partial r_j^2}(\delta\overline{\boldsymbol{u_i}}\delta\boldsymbol{u_i'})^2}_{D_{r3}} + \underbrace{\frac{\nu}{2}\frac{\partial^2}{\partial X_j^2}(\delta\boldsymbol{u_i'})^2}_{D_x} - \epsilon
\end{aligned} \tag{3.11}$$

Each term in the equation corresponds to a different process contributing to the evolution of $\delta\mathbf{u}^2$ in physical space and the space of scales.

- $A_t = \frac{\partial}{\partial t}(\delta\boldsymbol{u_i'})^2$ represents the rate of change of $\delta\boldsymbol{u_i'^2}$ at every physical point and the separation distance. In the present study, the turbulent boundary layer

datasets (both DNS and experiment) contained the time derivative of Navier Stokes' equation, from which A_t is computed. For the DNS of Turbulent Channel Flow, the time derivative term was obtained by computing all the other terms of the Navier Stokes' equation, from which A_t is computed.

- $\Pi = \delta \boldsymbol{u'_j} \frac{\partial}{\partial r_j} (\delta \boldsymbol{u'_i})^2$ represents the interscale energy transfer between the fluctuation of velocity. This term accounts for non-linear interactions in the redistribution of $\delta \boldsymbol{u'^2_i}$ in the space of scales by the fluctuation of velocity. Thus this term is central to all the studies of scale-by-scale energy budget and is one of the three terms in the Kolmogorov equation for scale-energy balance.

- $P_r = 2\delta \boldsymbol{u'_j} \delta \boldsymbol{u'_i} \frac{\partial}{\partial r_j} (\delta \overline{\boldsymbol{u_i}})$ term, which when transformed back to the two-point physical co-ordinate system gives $\delta \boldsymbol{u'_j} \delta \boldsymbol{u'_i} (\frac{\partial \overline{\boldsymbol{u_i}}}{\partial x_j}\big|_2 + \frac{\partial \overline{\boldsymbol{u_i}}}{\partial x_j}\big|_1)$. The two terms when averaged, results in the production term of one point turbulent kinetic energy equation. Thereby P_r represents the production $\delta \boldsymbol{u'^2_i}$ through the gradient of mean velocity. In addition, the equation for $\delta \overline{\boldsymbol{u_i}}$ has the same term with an opposite sign similar to the production term in one-point kinetic energy equation[4].

- $A = \overline{\boldsymbol{u^*_j}} \frac{\partial}{\partial X_j} (\delta \boldsymbol{u'_i})^2$ is the advection term, which represents the transport of $\delta \boldsymbol{u'^2_i}$ by the mean flow in the physical space.

- $T_u = \boldsymbol{u'^*_j} \frac{\partial}{\partial X_j} (\delta \boldsymbol{u'_i})^2$ is the transport of $\delta \boldsymbol{u'^2_i}$ by the fluctuation of velocity. This is the physical space counterpart of interscale energy transfer term Π.

- $T_p = \frac{2}{\rho} \delta \boldsymbol{u'_i} \frac{\partial}{\partial X_i} (\delta p)$ is the pressure velocity term, which accounts for the effect of pressure in the dynamics of the flow.

- $D_{r2} = 2\nu \frac{\partial^2}{\partial r_j^2} (\delta \boldsymbol{u'_i})^2$ is the diffusion of $\delta \boldsymbol{u'^2}$ in the space of scales. When the two points for the computation of structure-function coincide, this is the only non-zero term that compensates dissipation. This is a dominant term close to the wall. Away from the wall and at higher separation, its contribution is negligible. The other terms D_{r1} and D_{r3} has negligible contribution to the dynamics of the flow.

- $D_x = \frac{\nu}{2} \frac{\partial^2}{\partial X_j^2} (\delta \boldsymbol{u'_i})^2$ is the diffusion of $\delta \boldsymbol{u'^2_i}$ in the physical space, which is analogous to the diffusion term in the one-point turbulent kinetic energy equation, whose contribution is appreciable very close to the wall.

- ϵ^*, ϵ'^* represents the sum of energy dissipation rate at the two points based on total velocity and fluctuation of velocity respectively.

3.3 KHMH equation based on fluctuations of velocity

The KHMH equation has been used to study different processes associated with scale-by-scale energy budget in different turbulent flow fields. This meant that the equation has been derived in many forms for various studies. One of the widely used forms of the KHMH equation is by deriving it for the velocity fluctuations[81]. The equation is given by:

$$\begin{aligned}
&\underbrace{\frac{\partial}{\partial t}(\delta \boldsymbol{u'}^2)}_{A_t} + \underbrace{\frac{\partial}{\partial X_j}(\delta \boldsymbol{u'}^2 \boldsymbol{u'^*_j})}_{T_u} + \underbrace{\frac{\partial}{\partial r_j}(\delta \boldsymbol{u'}^2 \delta \boldsymbol{u'_j})}_{\Pi} + \underbrace{\frac{\partial}{\partial X_j}(\delta \boldsymbol{u'}^2 \overline{\boldsymbol{u^*_j}})}_{A} + \frac{\partial}{\partial r_j}(\delta \boldsymbol{u'}^2 \delta \overline{\boldsymbol{u_j}}) \\
&+ 2\delta \boldsymbol{u'_i} \boldsymbol{u'^*_j} \frac{\partial}{\partial X_j} \overline{\delta \boldsymbol{u_i}} + \underbrace{2\delta \boldsymbol{u'_i} \delta \boldsymbol{u'_j} \frac{\partial}{\partial r_j} \overline{\delta \boldsymbol{u_i}}}_{P_r} + 2\delta \boldsymbol{u_i} \frac{\partial \overline{\boldsymbol{u'_i} \boldsymbol{u'_j}}}{\partial x_j}\Big|_2 - 2\delta \boldsymbol{u_i} \frac{\partial \overline{\boldsymbol{u'_i} \boldsymbol{u'_j}}}{\partial x_j}\Big|_1 \qquad (3.12) \\
&= \underbrace{-\frac{2}{\rho} \delta \boldsymbol{u'_i} \frac{\partial}{\partial X_i}(\delta p)}_{T_p} + \underbrace{\frac{\nu}{2} \frac{\partial^2 (\delta \boldsymbol{u'}^2)}{\partial {X_j}^2}}_{D_x} + \underbrace{2\nu \frac{\partial^2}{\partial {r_j}^2}(\delta \boldsymbol{u'_i}^2)}_{D_{r2}} - 2\epsilon'^*
\end{aligned}$$

In comparison between Equations 3.12 with that derived with velocity decomposition given by Equation 3.11, the common terms between the equations are named accordingly. The last two terms on the left-hand side of the present equation are the Reynolds stress terms, which aren't found in Equation 3.11. This is because, to obtain the equation for fluctuation of velocity, the Reynolds Averaged Navier Stokes' equation is subtracted from the Navier Stokes' equation for full velocity, and this resulted in the two Reynolds stress terms. However, in the derivation of Equation 3.11, the mean equation was not subtracted. And the terms which are not named were equal to zero when $r_y = 0$.

3.4 Computation of KHMH equation terms

The terms of the KHMH equation when computed in the way they appear in Equations 3.11 didn't exactly balance the terms of the left-hand and right-hand sides of the equation. To understand the reason behind this problem, the KHMH equation was solved at every step of its derivation. Starting with Navier-Stokes' equation which produced the difference between left-hand and right-hand sides of the order of zero of the computer. While tracking the error at every step, it was found that the step where the conversion of coordinates from $(x_j\big|_1, x_j\big|_2)$ to the mid-point and

separation vector coordinates (X_j, r_j), is where the error increased. However, if this step is avoided then the final equation will not have terms that are in space of scales. Instead, all terms of that equation will have a dependence on physical space and the difference between the left-hand side and the right-hand side still stays close to computer zero.

To have the KHMH equation whose terms depend on both physical space and scale space and to correctly compute the terms, it was decided to take the final form of KHMH equation terms and compute them by transforming them back to $(x_j\big|_1, x_j\big|_2)$. The transformation of KHMH equation terms from (X_j, r_j) co-ordinates to $(x_j\big|_1, x_j\big|_2)$ is given by Equation 3.2. More detail on how each term is transformed is given in Appendix A.3.

Part II

Overviews of the DNS datasets and its analysis with KHMH equation

Chapter 4

DNS datasets

4.1 Assessment of DNS datasets

This chapter focuses on providing the details of the three DNS datasets used in the present work, which is the Turbulent Channel flow at $Re_\tau = 550, 3000$ and Zero-Pressure-Gradient Turbulent Boundary Layer at $Re_\tau = 550$. The parameters of the channel flow DNS datasets are given in Table 4.1, and that of the turbulent boundary layer is given in table 4.2.

Dataset	Re_τ	L_x/δ	L_y/δ	L_z/δ	$N_x \times N_y \times N_z$	Δx^+	Δz^+
TCF	550	2π	2	π	$576 \times 257 \times 288$	5^+	5^+
TCF	3000	6π	2	1.5π	$5120 \times 2048 \times 768$	11^+	7^+

Table 4.1: Parameters of TCF DNS datasets, where the channel half-width is δ. L_x, L_y, L_z are the sizes of the domain and N_x, N_y, N_z are the corresponding resolution in all three directions respectively

The DNS of TCF550 is performed with the code that solves for incompressible three-dimensional Navier Stokes' equation, which is made dimensionless using channel half-width h as the reference length, the maximum velocity at inlet U_{max} as the reference velocity. The spatial resolution is given by Figure 4.1, which shows that DNS is well-resolved in the wall-normal direction close to the wall and it increases close to 1.8η away from the wall, where $\eta = (\nu^3/\epsilon)^{1/4}$ is the local isotropic Kolmogorov scale. In the streamwise and spanwise directions, the spatial resolution is close to 4η close to the wall and becomes close to 1.7η away from the wall.

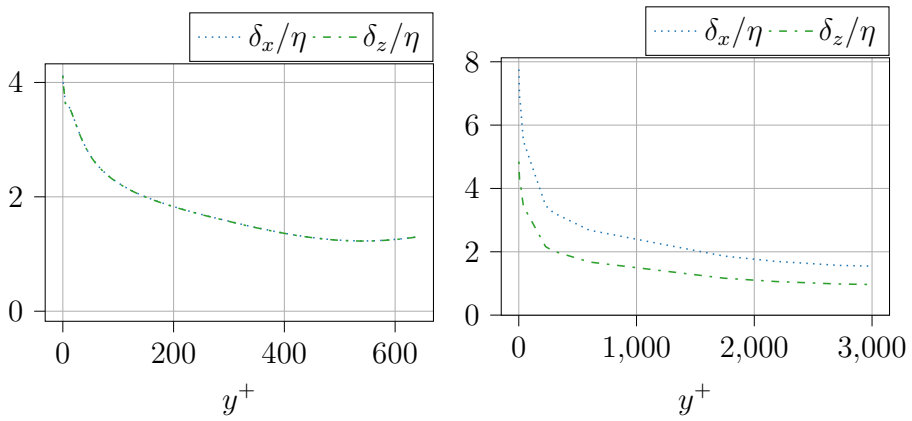

Figure 4.1: Spatial resolution of DNS of TCF in streamwise and spanwise directions at $Re_\tau = 550$ (left) and $Re_\tau = 3000$ (right)

The time-step is kept constant at a value of 4.0×10^{-4}, which corresponds to a CFL number of approximately 0.15. The three-dimensional Navier-Stokes' equations are discretised using fourth and eighth order centred finite differences in the streamwise direction, pseudo-spectral Chebyshev collocation method in wall-normal direction, and spectral Fourier expansion which is assumed periodic in the spanwise direction. The non-linear coupling terms being computed using the conventional de-aliasing technique (3/2-rule). The resulting Poisson equations are solved in parallel using the MPI library. Implicit second-order backward Euler finite difference method is used for time-integration, whereas the non-linear terms are evaluated using an explicit second-order Adams-Bashforth scheme. The fractional-step method has been adapted to the present formulation of the Navier-Stokes' system to ensure a divergence-free velocity field. The simulation was initialised using 128 IBM SP4 processors at IDRIS (CNRS computing facilities) and followed with 128 IBM SP5 processors at CRIHAN (Center of Computing Resources at Haute-Normandie, France)

The DNS of TCF3000 is performed by L.Thais and co-workers, which solves for Newtonian or viscous turbulent channel flow using a massively parallelised code. The spatial discretisation used is the sixth-order compact finite difference scheme for the wall-normal direction and Fourier modes in the streamwise and spanwise directions. The grid is stretched in the wall-normal direction such that the first grid point is at $y^+ = 0.5$ from each wall and up to 18 points are used to discretize till $y^+ = 10$. The simulation was performed on the IBM Blue Gene/Q computer running at the IDRIS/CNRS computing centre, Orsay, France. Interested readers could refer to Thais et al. [120], for more details about the simulation.

Dataset	Re_θ	L_x/δ	L_y/δ	L_z/δ	$N_x \times N_y \times N_z$	Δx^+	Δz^+
TBL	250-2500	53.19	4.72	2.36	$6401 \times 321 \times 448$	8.27^+	3.94^+

Table 4.2: Parameters of TBL DNS datasets at $Re_\theta = 2068$, where the boundary layer thickness $\delta = 8.46\delta_o$, δ_o being the laminar boundary layer thickness at the inlet. For the definition of Reynolds number and grid resolution in wall-unit, the value of friction velocity u_τ and momentum thickness θ are used at this streamwise position. L_x, L_y, L_z are the sizes of the domain and N_x, N_y, N_z are the corresponding resolution in all three directions respectively

The DNS of TBL is performed with the code of Incompact3d[71], which is a massively parallelised code written in FORTRAN solving the incompressible Navier-Stokes' equation. Sixth order compact finite difference schemes are used for spatial discretization. The tripping mechanism uses the wall-normal momentum equation with a source term in a constrained volume near the lower wall as proposed by Schlatter and Örlü[104]. The DNS is performed with a domain size $L_x = 600\delta_o$, $L_y = 40\delta_o$, $L_z = 20\delta_o$, where δ_o is the laminar boundary layer thickness at the inlet. The grid is only stretched in the wall-normal direction such that the first grid point is at $y^+ = 1$ at the streamwise position for which the $Re_\theta = 2068$. The DNS of the turbulent boundary layer is integrated for more than 15 characteristic times, $\tau = \frac{Tu_\tau}{\delta}$, based on the boundary layer parameters at 75% of the domain length. Interested readers could refer to Solak[113], for more details about the simulation.

4.1.1 Processing of DNS datasets

The three DNS datasets used in the present work had to be pre-processed to compute the scale-by-scale energy budget. The issues to be addressed were (a) the spatial derivatives of both velocity and pressure fields weren't available for all three DNS datasets, (b) time-derivative of velocities were available only for TBL550 datasets and not for the TCF550 and TCF3000 datasets.

The first issue is solved by the computation of spatial derivatives of the fields in all directions, which is performed by obtaining the cubic spline of each field in the corresponding direction and computing their derivatives. The second issue which is the computation of time derivative for the TCF datasets is solved by obtaining all the terms of Navier-Stokes' equation except the time derivative term. The time

derivative is then calculated from the sum of all the other terms with the proper sign.

4.1.2 Spatio-temporal averaging of DNS datasets

The KHMH equation is an energy budget equation in both physical space and space of scales. Hence the equation has three coordinates in the physical space defined by the three cartesian coordinates and coordinates system of space of scales in all three axes: The x-axis is along the streamwise velocity direction, the y-axis is along the wall-normal velocity direction and the z-axis is along the spanwise velocity direction. In addition, each DNS dataset contains the velocity field in multiple time-steps, which makes the variable dependent on time. Thus each variable used in the computation of KHMH equation terms is of the form $\boldsymbol{a(t, x, y, z, r_x, r_y, r_z)}$.

With the three DNS datasets being steady, the average is performed along the time-steps. For the two channel flows, the streamwise and spanwise directions are homogeneous directions with periodic boundary conditions and so for both the channel flows the averaging is performed on the x- and z-directions. For the TBL, the homogeneous direction is only in the spanwise direction. And the streamwise extent of 6δ is assumed to be homogeneous, which then allows averaging in the x-direction for this region in addition to the z-direction. Thus the spatio-temporally averaged variable in the computation of KHMH equation terms is of the form $\langle \boldsymbol{a(y, r_x, r_y, r_z)} \rangle$.

To understand the behaviours of the KHMH equation terms in the present work, it is plotted at a certain wall distance (y^+) and along either r_x or r_z direction. So, when the results are plotted along r_x direction, the other values $r_y = r_z = 0$ such that it becomes $\langle \boldsymbol{a(y^+, r_x, r_y = 0, r_z = 0)} \rangle$, and when the results are plotted along the r_z direction, and the other values $r_y = r_z = 0$, such that it becomes $\langle \boldsymbol{a(y^+, r_x = 0, r_y = 0, r_z)} \rangle$.

4.1.3 Convergence of the DNS datasets

It is important to discuss the level of convergence obtained by the datasets before understanding the results. To be relevant to the present study, the time derivative of the KHMH equation ($\langle A_t \rangle$) is chosen as the quantity to determine the convergence of the results. And this particular term is chosen to display the convergence of the results because this term has the highest amount of fluctuation and the present flows under consideration are steady flows and so the average value of the time derivative

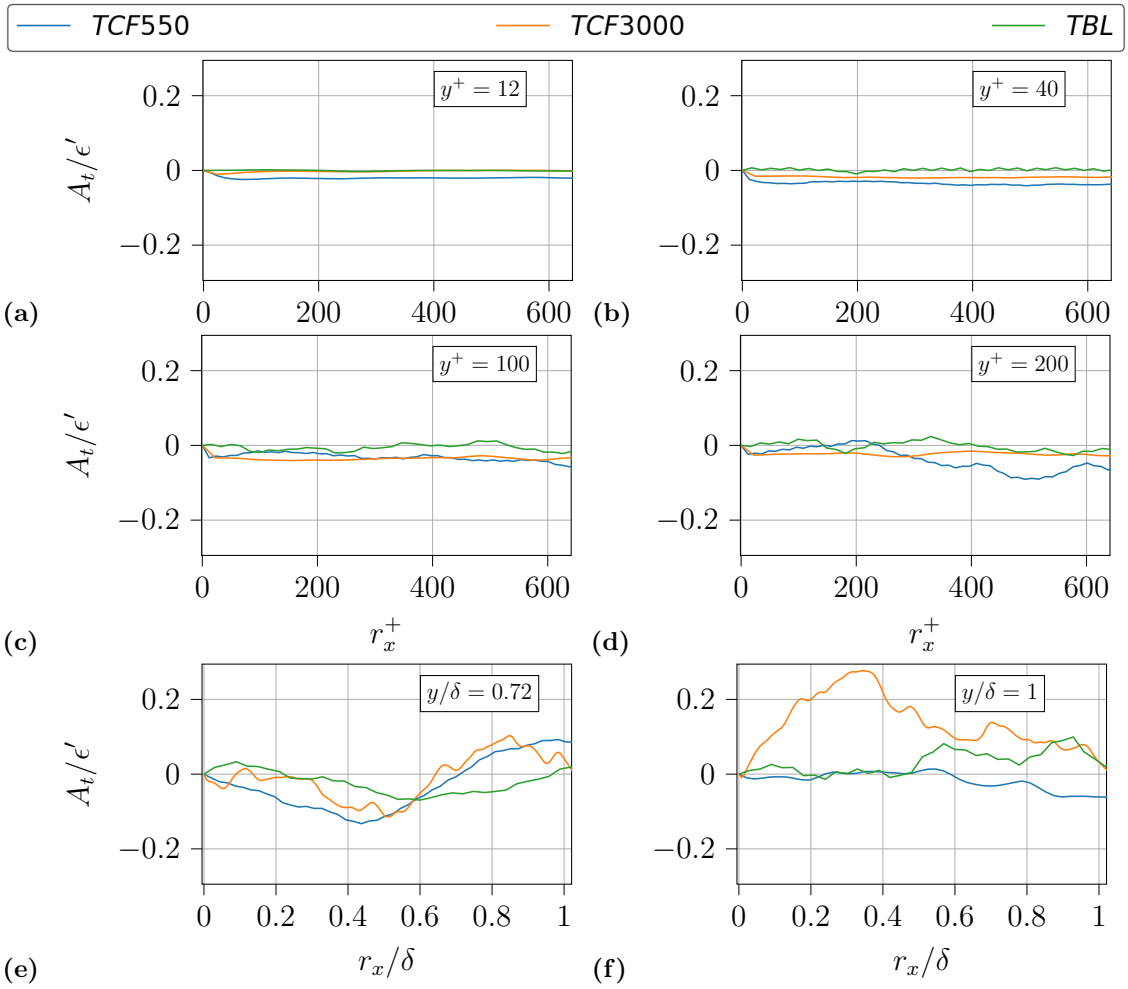

Figure 4.2: Computation of Spatio-temporal average of normalised time derivative term ($\langle A_t \rangle / \langle \epsilon'^* \rangle$) in the streamwise direction separation for the three DNS datasets at various wall distances. The x-axis and the wall distances are normalised by wall units from **(a)** to **(d)**, and by channel half-width or boundary layer thickness (δ) from **(e)** to **(f)**

is equal to zero. This means that averaging time derivative and subtracting its ideal value (which is equal to zero), gives the error associated with the convergence. This term is computed with all three DNS datasets (two TCF and one TBL) and has been spatio-temporally averaged in the way discussed in the previous subsection.

For each dataset and each of the wall distances considered, the time derivative values at all the grid points of the datasets are considered. Since the three datasets have a different number of points to perform the Spatio-temporal average, and the datasets converge differently. The results presented are normalised using the absolute value

of dissipation based on fluctuations ($\langle \epsilon'^* \rangle$).

Figure 4.2 shows the convergence value of the computation of A_t term with all three DNS datasets at different wall distances. It is observed that near the wall, the error stays well below $0.1\langle \epsilon'^* \rangle$, and this value grows as the wall distance is increased. This is due to the presence of a large scale correlation of velocity fluctuations, which results in less number of uncorrelated samples compared to the near-wall region or the log layer. At δ, each dataset has the highest value of error due to convergence, and this value is of the order of $0.1\langle \epsilon'^* \rangle$ for TCF550 and TBL550, and of the order of $0.3\langle \epsilon'^* \rangle$ for TCF3000.

Chapter 5

Results: DNS

5.1 Introduction

The study aims to use the KHMH equation in its general sense to study the behaviour of KHMH equation terms at different parts of the flow field. This is to extract the physics underlying the cascade of energy in both physical space and the space of scales. This chapter focuses on obtaining the results from Direct Numerical Simulation (DNS) of Turbulent Channel Flow (TCF) and Turbulent Boundary Layer (TBL) to understand the energy budget in both wall-bounded turbulent flow configurations.

This chapter is organised as follows. Following the introduction, Section 5.2 explains the analysis of KHMH equation terms computed from the DNS of Turbulent Channel Flow at $Re_\tau = 550$, henceforward this flow will be addressed as TCF550. It shows the results of the behaviour of the terms of the KHMH equation in average and instantaneous form, before proceeding to discuss the correlation coefficient between different terms of the KHMH equation. These results are then compared with Turbulent Channel Flow at $Re_\tau = 3000$, henceforward this flow will be addressed as TCF3000. In Section 5.3 the same analyses as with the previous flows are performed on Zero Pressure Gradient Turbulent Boundary Layer (ZPG-TBL) at $Re_\tau = 550$, henceforward this flow will be addressed as TBL550, which is then compared with the corresponding results of TCF550. Section 5.4 shows the results of the energy cascade in the streamwise-spanwise plane in all three DNS datasets at different wall distances. This is followed by section 5.5, where the results of the wall-attached eddies are discussed in all three DNS datasets.

5.2 Scale-by-scale energy budget with DNS of Turbulent Channel Flows

This section begins with understanding the behaviour of different terms of the KHMH equation in its averaged form from the studies in the past and continues towards the present work, which is the analysis of average values of KHMH equation on Turbulent Channel Flows and the influence of an increase in Reynolds number. This is followed by the results concerning the instantaneous part of the terms of the KHMH equation terms, which is made possible by considering the equation without averages. Then the correlation coefficient of different terms are computed to understand the physics underlying the cascade of energy.

5.2.1 Spatio-temporal average values of the KHMH equation terms

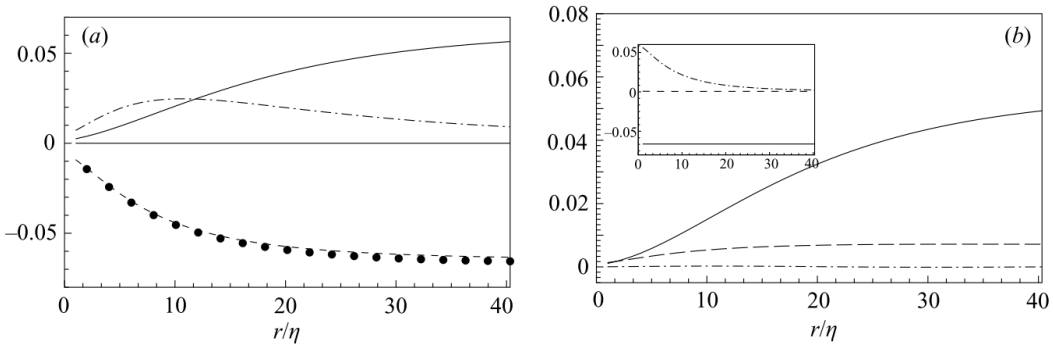

Figure 5.1: Detailed balance of terms of KHMH equation 3.12 at $y^+ = 80$ in channel flow at $Re_\tau = 180$. (a) The behaviour of a group of terms in space of scales. The sum of all terms except diffusion and dissipation terms are given by filled circles, the sum of diffusion and dissipation terms are given by dashed lines. The dashed-dotted line corresponds to interscale energy transfer, the solid lines comprise of energy transfer in physical space, production, pressure terms. (b) Behaviour of individual terms in the space of scales. Here production (solid line), energy transfer in physical space (dashed line), pressure term (dashed-dotted line); the sign of each of these terms are changed. In the inset, dissipation (solid line), diffusion in scale space (dash-dotted line) and physical space (dashed line), respectively. Figure and caption reproduced from Marati et al. [81]

Studies of the scale-by-scale energy budget in channel flows using the KHMH equation include Marati et al.[81], who solved the KHMH equation for fluctuations of velocity (Equation 3.12) to understand the behaviour of each term of the equation in the space of scales and physical space at different wall distances. Figure 5.1 (b) shows the behaviour of individual terms contributing to effective production, energy transfer in physical space, pressure, diffusion and dissipation of KHMH equation at $y^+ = 80$. It is observed that the energy transfer in physical space and pressure terms are negligible on average at all scales. The production term starts at zero at the small scales and increases with the scale and becomes approximately the value of dissipation at large scales. The diffusion in physical space is negligible on average at all scales. At $r = 0$, the diffusion in scale space is equal to dissipation and becomes negligible at large scales.

Figure 5.1 (a) shows the behaviour of all these terms when they are combined under three groups : (i) interscale transfer, (ii) effective production terms, (iii) dissipation and diffusion terms. The behaviour of individual terms of the effective production, dissipation and diffusion terms are discussed previously. The interscale energy transfer starts at zero and increases with the scale to attain a peak and decreases thereafter as the scale increases.

At this wall distance, Marati et al.[81] conclude that the scales at which production term dominates, is approximately equal to the dissipation and this is essentially the condition for the locally homogeneous shear. Below the production dominated regime, the interscale energy transfer dominates the dynamics of the flow in which the effect of shear and viscosity are negligible and it follows the result of the classical Richardson cascade ends at the local dissipative scale by diffusion.

Continuing in this direction, this subsection focuses on the behaviour of the KHMH equation 3.11 terms in average at different wall distances from TCF550. Henceforth unless mentioned otherwise, the KHMH equation always refers to Equation 3.11. This is then compared with the results of the behaviour of the KHMH equation terms on average at different wall distances with Turbulent Channel Flow at $Re_\tau = 3000$ (TCF3000). This serves as a way to understand the effect of Reynolds number in the present analysis of KHMH equation terms in wall-bounded turbulent flows. Saikrishnan et al.[99] studied the effect of Reynolds number by analysing DNS of Turbulent Channel Flow at $Re_\tau = 300, 590, 934$ and compared it with the results of Marati et al.[81] who had the results of Turbulent Channel Flow at $Re_\tau = 180$. The main conclusion from their study includes that the results in the viscous sublayer and buffer regions were found to not influence the Reynolds number. The Reynolds

number influence was observed in the logarithmic region where the transfer of energy across scales increased with Re_τ, keeping production at a constant value. To maintain the balance between the different processes, the dissipation of Turbulent Kinetic Energy increased with the Reynolds number.

The objective here is to understand the average dynamics of different processes at various regions of the wall-bounded turbulent flow. In this regard, various wall distances are studied and compared between the two flows, at $y^+ = 12$, 25, 40, 100, 200, 320 and at $y/\delta = 0.07, 0.18, 0.58, 0.72, 1$. These wall distances are chosen so as to include the near-wall region, logarithmic region, turbulent core and along the centre-line of the channel.

Format of the plots

For the results to be comparable between the two channel flows at different Reynolds numbers. The left column of each figure is the result from TCF550 and its corresponding comparison with TCF3000 is present on the right column. When there is a result of a KHMH term given by $\boldsymbol{a(r_x^+, r_y^+, r_z^+, y^+)}$ is presented in one direction, the indices of other variables are zero. Thus, when the results are presented along r_x direction for a particular wall distance y^+, the other scale variables are considered to be zero, for example in the r_x direction the results would correspond to $\boldsymbol{a(r_x^+, r_y^+ = 0, r_z^+ = 0, y^+)}$. Similarly for the results in r_z direction, it is $\boldsymbol{a(r_x^+ = 0, r_y^+ = 0, r_z^+, y^+)}$.

All KHMH terms in the figures are normalised by the absolute value of $\langle \epsilon'^* \rangle$. The vertical dash-dotted lines in each plot give the Kolmogorov micro-scale (coral), modified Taylor micro-scale (dim grey) and integral scale (crimson). The modified Taylor microscale is derived for the wall-bounded turbulent flow for both streamwise and spanwise directions separately. More detail about the modified Taylor microscale for each direction is explained later in this subsection. The integral scale plotted along the r_x direction corresponds to u' along the streamwise direction L_{11}, and along the r_z direction corresponds to u' in the spanwise direction L_{13}. More detail about the computation of integral scales is given in Appendix B.1.

5.2.2 Normalisation of the results

In the comparison of the two channel flows at different Reynolds numbers, two different normalisations are used. To observe the limits of each normalisation, the comparison is made for both types from near the wall to the turbulent core in both r_x and r_z directions. The wall-units normalisation is plotted for results from

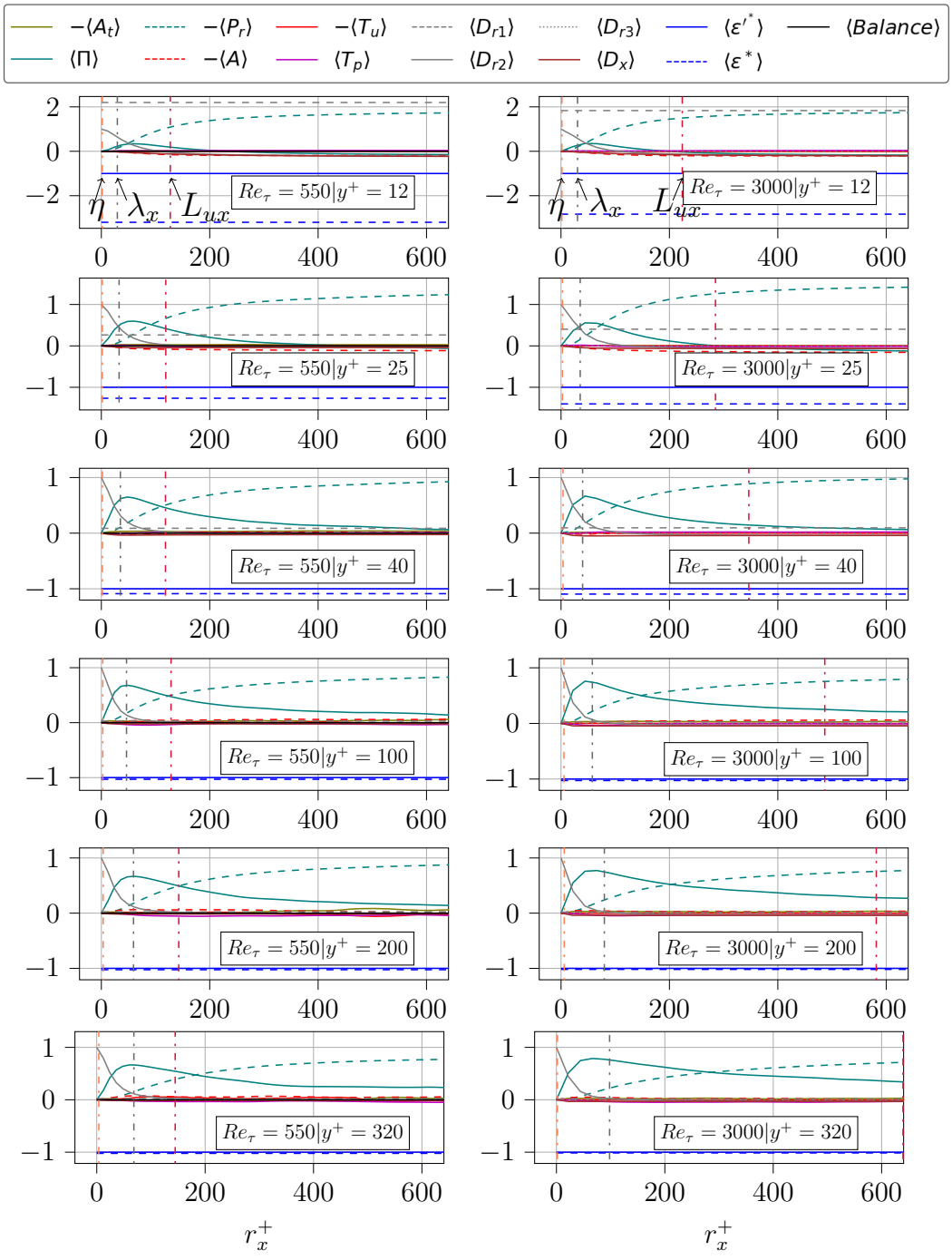

Figure 5.2: Spatio-temporal averaged values of all KHMH equation terms normalised by the absolute value of $\langle \epsilon'^* \rangle$ in streamwise direction separation in TCF550 (left) and TCF3000 (right) at various wall distances. The wall distances and the x-axes are normalised by wall-units

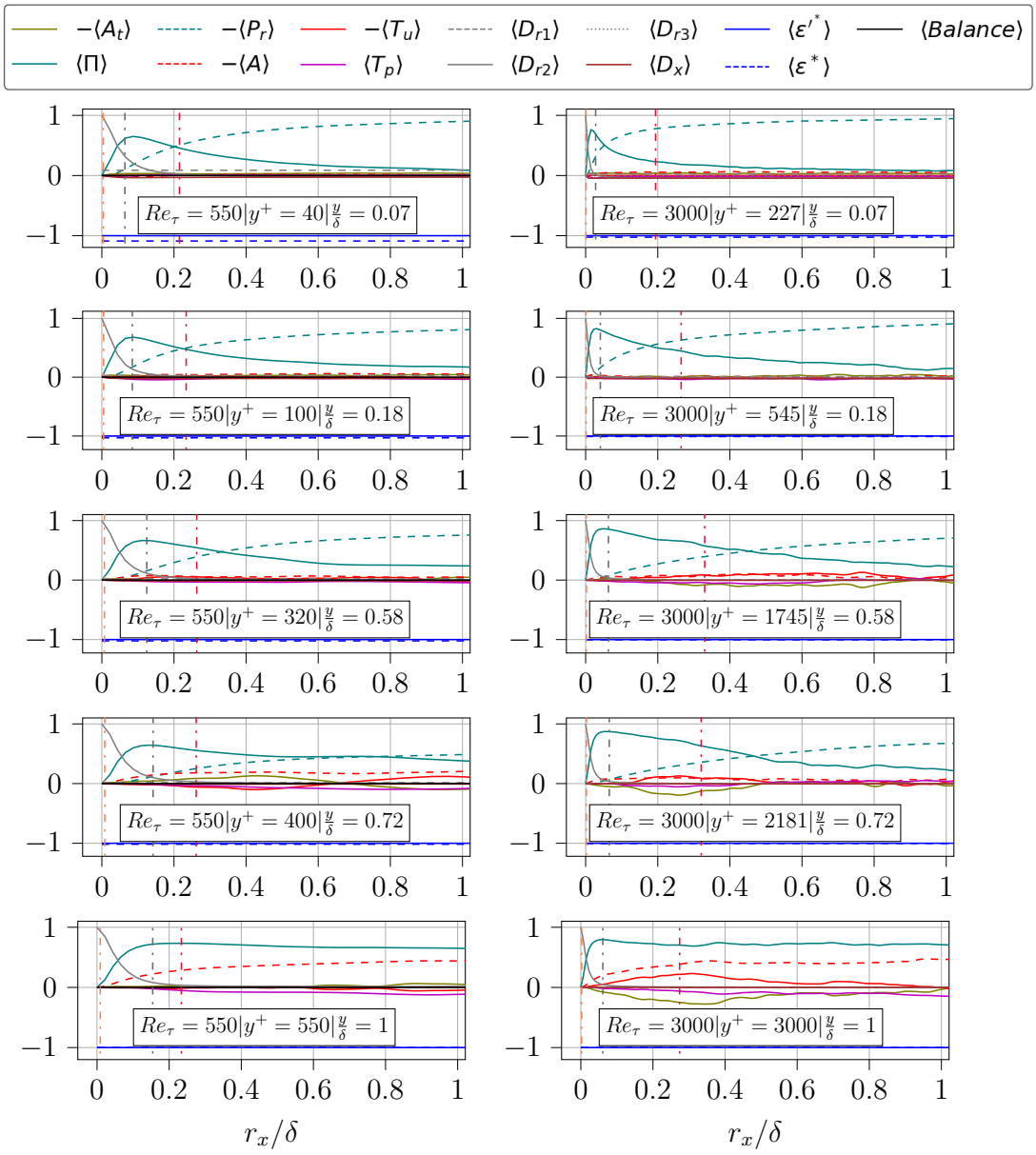

Figure 5.3: Spatio-temporal averaged values of all KHMH equation terms normalised by the absolute value of $\langle \epsilon'^* \rangle$ in streamwise direction separation in TCF550 (left) and TCF3000 (right) at various wall distances. The wall distances and x-axes are normalised by the channel half-width

$y^+ = 12$ to $y^+ = 320$, and the normalisation by channel half-width δ is plotted from $y/\delta = 0.07$ to $y/\delta = 1$.

In both the r_x an r_z direction, it is observed that the results between the flows at two different Re_τ have similar results from $y^+ = 12$ till $y^+ = 100$. It starts to differ

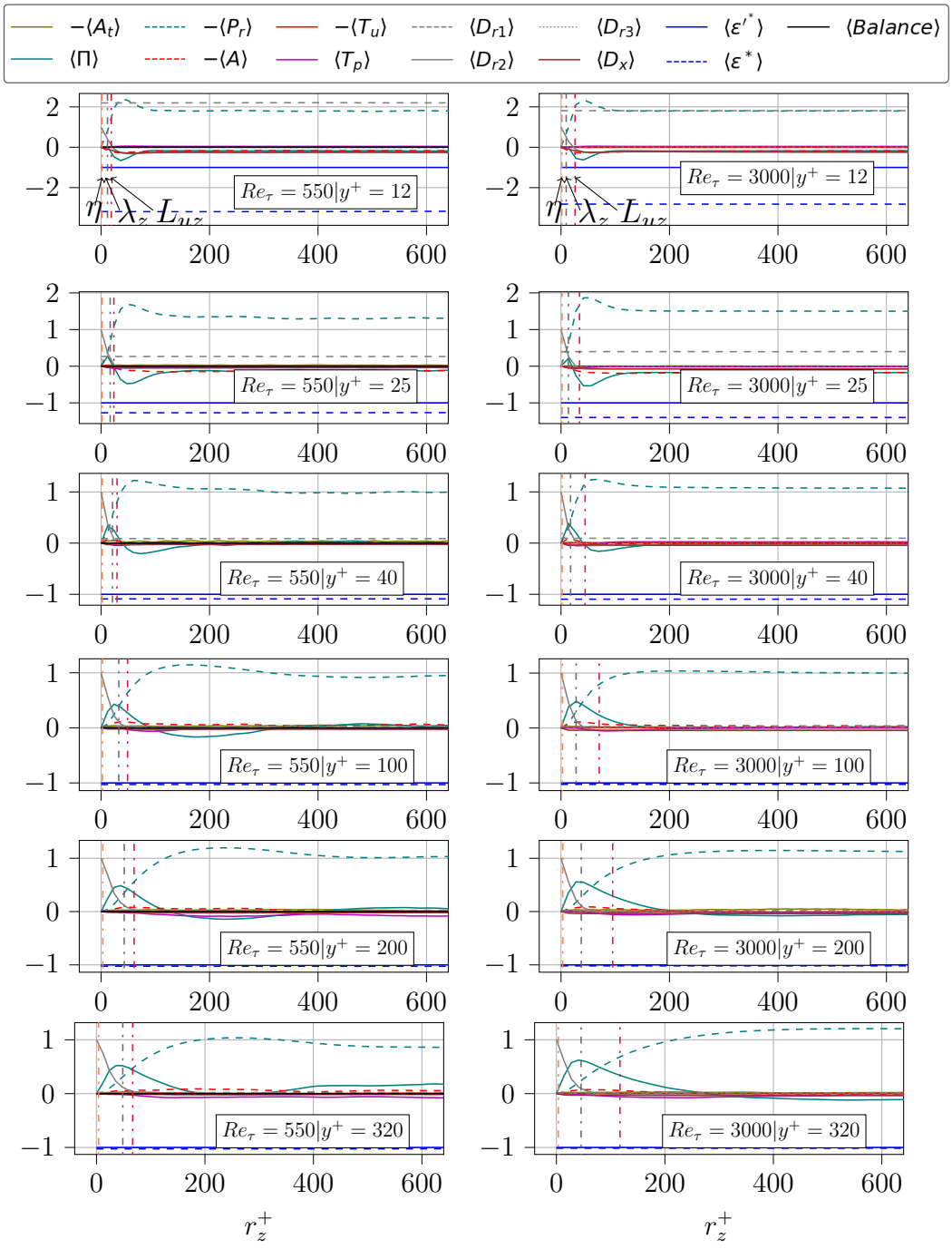

Figure 5.4: Spatio-temporal averaged values of all KHMH equation terms normalised by the absolute value of $\langle \epsilon'^* \rangle$ in spanwise direction separation in TCF550 (left) and TCF3000 (right) at various wall distances. The wall distances and the x-axes are normalised by wall-units

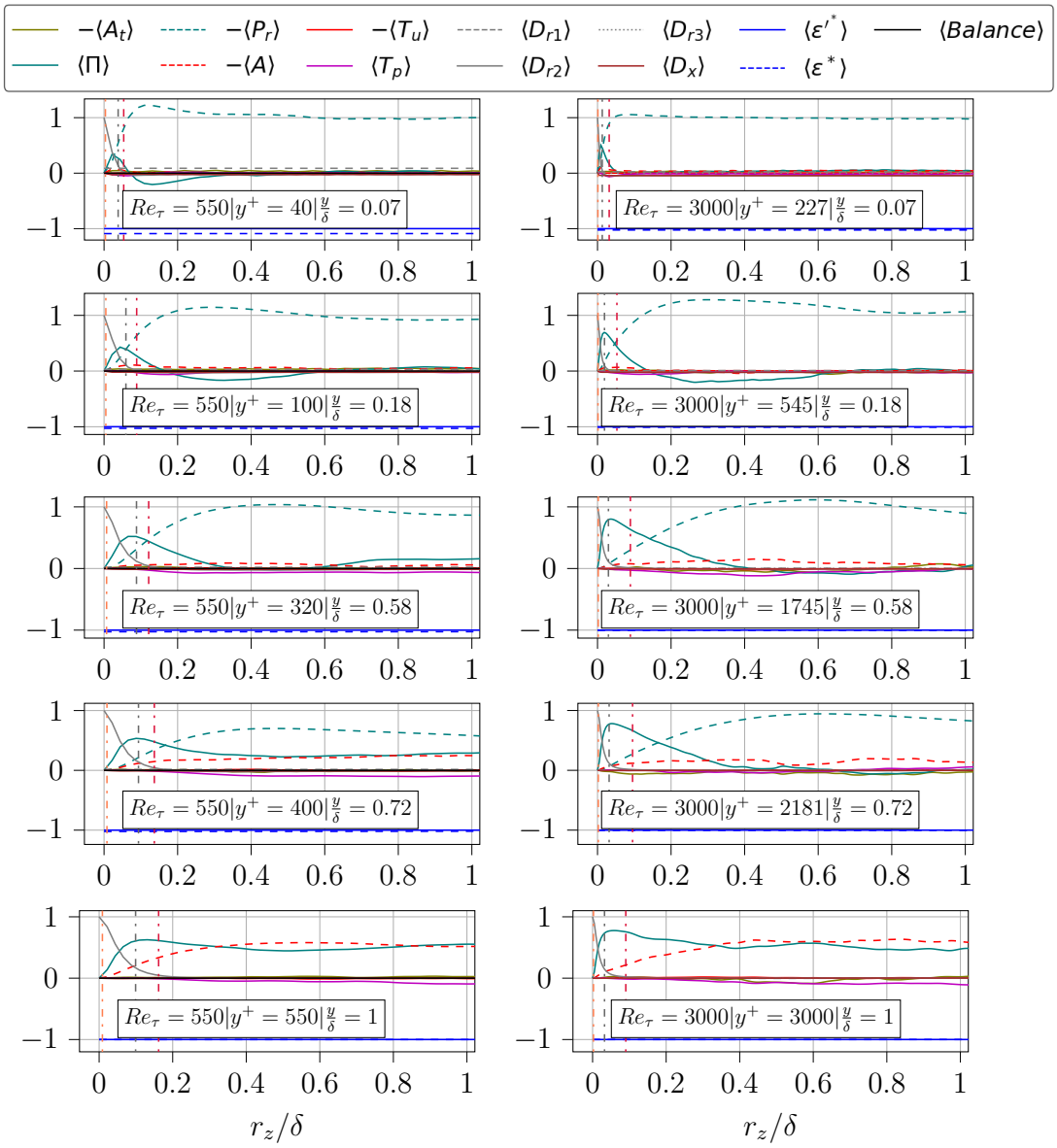

Figure 5.5: Spatio-temporal averaged values of all KHMH equation terms normalised by the absolute value of $\langle \epsilon'^* \rangle$ in spanwise direction separation in TCF550 (left) and TCF3000 (right) at various wall distances. The wall distances and x-axes normalised by the channel half-width

between the two at $y^+ = 200$ and diverges further at $y^+ = 320$. On the other hand, the normalisation with channel half-width between two flows have similar results at the centre-line, and the difference starts to appear as the y/δ is reduced. Thus based on the observation, it can be concluded that the comparison between the two flows with wall-unit normalisation holds good until $y^+ = 200$, and thereafter the

results are better normalised with the channel half-width.

Observation

Figures 5.2, 5.3, 5.4 and 5.5 show the averaged value of all the terms of the KHMH equation in the r_x and r_z direction at different wall distances from the DNS of both TCF550 and TCF3000. The sign of all the terms on the left-hand side of the KHMH equation (A_t, Π, P_r, A, T_u) is inverted so that the sum of all terms will be equal to zero. This sum is given by the 'Balance' term. The balance is close to the zero of the computer at all wall distances. This is due to two reasons: (a) the computation of the terms in their original coordinates[41], (b) the computation of time derivative by decomposing the Navier-Stokes' equation.

The terms of the KHMH equation have different behaviours depending on the wall distance considered, and so the observation will be based on looking at each term separately and how it evolves as the wall distance is increased, and as well as the influence of the Reynolds number. Starting with the time derivative term $-\langle A_t \rangle$, it is well-known that this term is zero on average when the flow is statistically steady such as the Turbulent Channel Flow studied in this subsection. This is discussed in the previous chapter, where it was pointed out that the residual value that appears at higher wall distances correspond to the limits of convergence of the current dataset at those high wall distances. This is attributed to the increase of correlation that exists when moving away from the wall, which would require more uncorrelated samples to converge the dataset. The advection term $-\langle A \rangle$ and the pressure term $\langle T_p \rangle$ tends to be negligible on average at all wall distances and all scales considered in the analysis.

The interscale energy transfer term $-\langle \Pi \rangle$ in TCF550 at $y^+ = 12$ in r_x and r_z directions, starts at zero and increases to reach a peak, then decreases until the integral scale and becomes negligible thereafter as the scale separation increases. In addition in the r_z direction, there is a negative peak for the $-\langle \Pi \rangle$ after the first positive peak. The negative values observed only in the r_z direction suggests a possibility of inverse energy cascade, which will be discussed later in this section. As the wall distance is increased, the negative peak value tends to move to higher scales. Also with an increase of wall distance, $-\langle \Pi \rangle$ tends to be significant at scales much larger than the integral scale. At the channel centre-line, this term is the most dominant at all scales till $r^+ = \delta$, except at very small scales.

With a higher Reynolds number in TCF3000, $-\langle \Pi \rangle$ behaves qualitatively the same

way between the two channel flows at all wall distances when normalised accordingly discussed previously in this subsection in both r_x and r_z directions. And the peak value of this term tends to be larger in TCF3000 than in TCF550 indicating an effect of Reynolds number in the average, as observed in Saikrishnan et al. [99].

The production term $-\langle P_r \rangle$ in TCF550 increases from zero at $r_x^+ = 0$ to approximately 1.8 times the value of $\langle \epsilon'^* \rangle$ at large scales at $y^+ = 12$. When the wall distance is increased, the behaviour of $-\langle P_r \rangle$ remains approximately the same, except its value at large scales which reduces with increased wall distance. Beyond $y^+ = 25$ it tends to attain approximately the value of $\langle \epsilon'^* \rangle$. $-\langle P_r \rangle$ in the r_z direction starts from zero at $r_z^+ = 0$, and increases to have a positive peak at approximately the same scale as the previously mentioned negative peak of $-\langle \Pi \rangle$ above $2\langle \epsilon'^* \rangle$, and at scales thereafter it reduces to approximately 1.8-1.9$\langle \epsilon'^* \rangle$. With the increase of wall distance, $-\langle P_r \rangle$ at large scales approaches $\langle \epsilon'^* \rangle$ similar to that in r_x direction. However, the positive peak of $-\langle P_r \rangle$ in the r_z direction is always higher than $\langle \epsilon'^* \rangle$ up to $y^+ = 320$. Beyond $y^+ = 320$, the dominance of this term reduces with the further increase of wall distance, and it becomes negligible at the centre-line of the channel flow in both r_x and r_z directions.

When the Reynolds number is increased, $-\langle P_r \rangle$ has the same behaviour in both TCF550 and TCF3000 in the r_x direction, when the x-axis is normalised using wall-units till $y^+ = 320$ and thereafter using the channel half-width. In the r_z direction however, the positive peak compares well between the two flows with the x-axis normalised by wall-units up to $y^+ = 40$, and thereafter it agrees well when the x-axis is normalised by the channel half-width δ.

The energy transfer in physical space $\langle T_u \rangle$ is negligible at all wall distances until $y/\delta = 0.72$. Beyond $y/\delta = 0.72$, the contribution of this term to the average increases from $0.25\langle \epsilon'^* \rangle$ at $y/\delta = 0.72$ to approximately $0.5\langle \epsilon'^* \rangle$ along the centre-line of the channel flow. The increase of $\langle T_u \rangle$ approximately coincides with the reduction value of the production term at $y/\delta > 0.72$. There is no influence of Reynolds number in the behaviour of this term.

The diffusion in scale space due to velocity fluctuations $\langle D_{r2} \rangle$ is always equal to $\langle \epsilon'^* \rangle$ when the two points of the structure-function coincide *i.e.,* $r = 0$, in both r_x and r_z directions at all wall distances. Beyond $r = 0$, the influence of this term is shown to be negligible above the Taylor microscale in the context of grid generated turbulence by Valente and Vassilicos [125]. Although the present study uses a modified Taylor microscale, the result still holds good. The other diffusion terms $\langle D_{r1} \rangle$, $\langle D_{r3} \rangle$ and

$\langle D_x \rangle$ are negligible at all wall distances and scales.

Discussion

Starting the discussion near the wall at $y^+ = 12$, it is well known from single point turbulent kinetic in the buffer layer, the production $-\langle P_r \rangle$ exceeds dissipation and this can be concluded by the fact that the production term being approximately 1.6-1.8$\langle \epsilon'^* \rangle$ at large scales. $-\langle \Pi \rangle$ dominates between the modified Taylor microscale and the integral scale in the r_x direction. In the r_z direction, the positive peak of $-\langle P_r \rangle$ coinciding at the same scale at which $-\langle \Pi \rangle$ has its negative peak. This could be due to the presence of the inverse cascade in this direction, and this is discussed in section 5.5.

Above the buffer layer, from $y^+ = 25$ to $y^+ = 320$, there are three distinct ranges of scales observed in the average dynamics of KHMH equation terms. The first range of scales in both r_x and r_z direction is characterised by the domination of $\langle D_{r2} \rangle$ which is valid from $r^+ = 0$ till the modified Taylor microscale. The next range of scales is characterised by the dominant $-\langle \Pi \rangle$ between Taylor microscale and the integral scales. $-\langle \Pi \rangle$ term tends to be positive in r_x direction, suggesting the classical Richardson cascade. However, there is a range of r_z values, for which the $-\langle \Pi \rangle$ is negative, which suggests a mix of both forward and inverse cascade in this direction. The forward and reverse cascade events are discussed for each flow in section 5.4. The third range of scales corresponds to where $-\langle P_r \rangle$ tends to equal to $\langle \epsilon'^* \rangle$ with the increase of scales, thereby reproducing the equilibrium assumption in this region.

Moving from the bulk region of the flow from $y/\delta = 0.72$ to the centre-line of the channel flow at $y/\delta = 1$, the role of the $\langle P_r \rangle$ starts to diminish compared to the previous wall distance. At the centre-line of the channel flow, $\langle P_r \rangle$ vanishes entirely from the dynamics of the flow, which is known previously due to the zero value of $\frac{d\overline{u}}{dy}$. In the bulk region of the flow, the interscale energy transfer term $-\langle \Pi \rangle$ is dominant from modified Taylor microscale to scales larger than the integral scale. At the centre-line, this term is dominant from modified Taylor microscale to even scales of the order of δ, and this is investigated later in the subsection. In the bulk region, the reduction of the $-\langle P_r \rangle$ coincides exactly with the increase of $-\langle T_u \rangle$. Along the centre-line, this term is dominant in large scales and contributes equally to the dynamics of the flow as $\langle \Pi \rangle$. Thus in the bulk and the centre-line, the process of transfer of energy in both physical-space and the scale-space dominates the entire dynamics of the flow. The dynamics of the flow in the r_x and r_z direction are similar

only as the centre-line is reached, despite both streamwise and spanwise being both homogeneous directions.

Modified Taylor microscale

The Taylor microscale λ is defined for the isotropic turbulence by the following equation

$$\langle \epsilon' \rangle = 15\nu \frac{\langle u'^2 \rangle}{\lambda^2} \tag{5.1}$$

where $\langle \epsilon' \rangle$ is the dissipation based on fluctuation of velocity, u'^2 is defined as $\frac{1}{3}\langle u'_i u'_i \rangle$ which is equal to $\langle u'^2_1 \rangle$ in the isotropic turbulence. The Taylor microscale is also associated with the curvature of the spatial velocity autocorrelation function. Lundgren [78] showed that for the compensated third-order structure-function, the peak occurred at 1.5λ. This is quantitatively verified by Obligado and Vassilicos [88] who observed in decaying turbulence which is nearly isotropic, that the compensated the third-order structure-function has its peak at $r \approx 1.5\lambda$.

In the context of wall-bounded turbulence which is anisotropic, a length scale based on the Taylor microscale is introduced in the present work. This modified Taylor microscale is defined separately for the streamwise and the spanwise directions. This modified Taylor microscale in r_x direction is λ_x is obtained by the use of only $\langle u'^2 \rangle$ instead of all the velocity components, and given by :

$$\lambda_x = \sqrt{15 \frac{\nu}{\epsilon'} \langle u'^2 \rangle} \tag{5.2}$$

And in the r_z direction, λ_z is obtained by the use of $\langle w'^2 \rangle$, and $\frac{15}{2}$ is used as the coefficient instead of 15. This is given by :

$$\lambda_z = \sqrt{\frac{15}{2} \frac{\nu}{\epsilon'} \langle w'^2 \rangle} \tag{5.3}$$

Figures 5.6 and 5.7 show $-\langle \Pi \rangle$ normalised by the absolute value of $\langle \epsilon'^* \rangle$ along with the separation distance r_x and r_z normalised by Taylor micro-scale λ_x and λ_z respectively for DNS of TCF550 and TCF3000. The top two plots in each figure, show the full extent of $-\langle \Pi \rangle$ term normalised by the absolute value of $\langle \epsilon'^* \rangle$. The bottom two plots in each figure, show the plot near $r = \lambda$ in the respective direction, which helps to visualise the peak of Π term at the modified Taylor microscale.

It is observed that in TCF550 in the r_x direction, the positive peak of $-\langle \Pi \rangle$ coincides with the λ_x in the range $0.1 < y/\delta < 1$. In the r_z direction, the positive

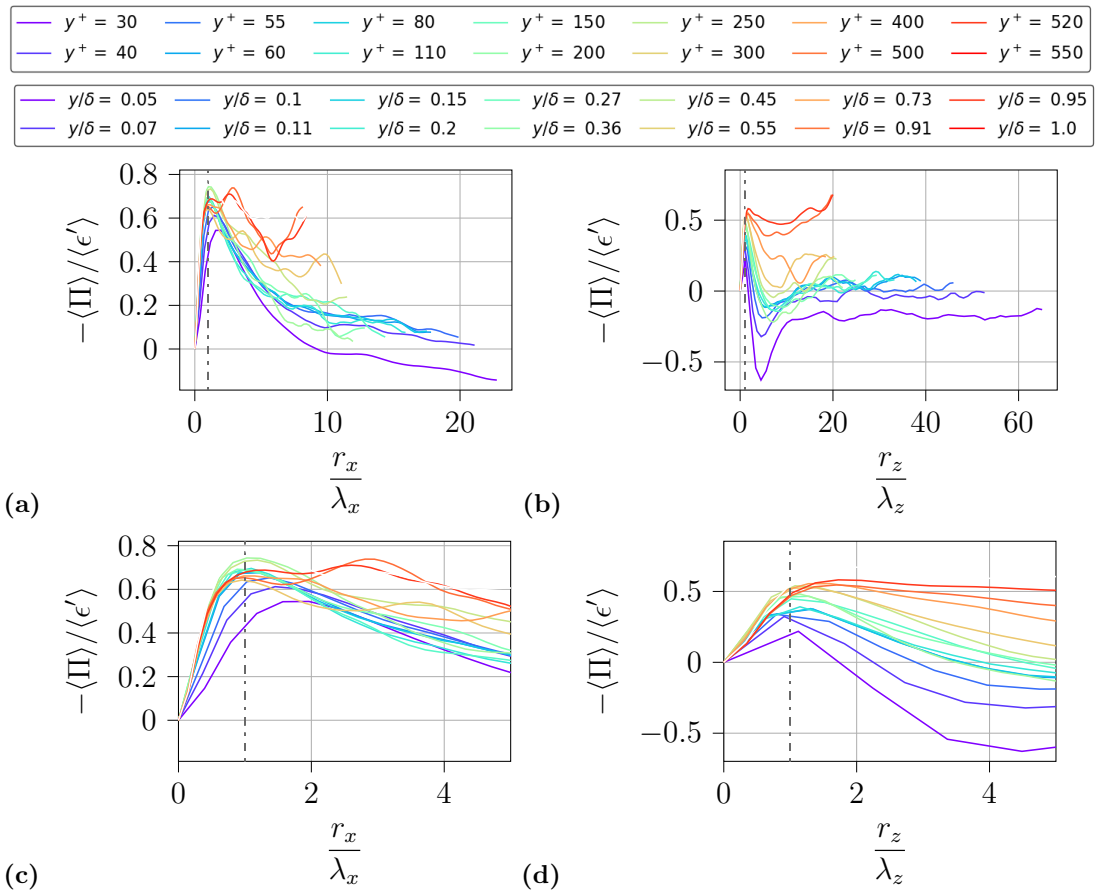

Figure 5.6: Spatio-temporal average of interscale energy transfer term normalised by the absolute value of $\langle\epsilon'^*\rangle$ at different wall distances for TCF550 **(a)** in the streamwise direction, **(b)** in the spanwise direction. **(c),(d)** Same as (a),(b) but the x-axis zoomed in the region near $r_x = \lambda_x$ and $r_z = \lambda_z$ respectively

peak of $-\langle\Pi\rangle$ coincides with λ_z in the range $0.1 < y/\delta < 0.9$. With the increase of Reynolds number in TCF3000 in the r_x direction, the positive peak of $-\langle\Pi\rangle$ coincides approximately with λ_x in the range $0.1 < y/\delta < 1$, and in the r_z direction the positive peak of $-\langle\Pi\rangle$ coincides with λ_z in the range $0.01 < y/\delta < 1$.

From the previous studies in isotropic turbulence, it is known that the Taylor microscale scales the peak of the third-order structure-function. In the present study of the anisotropic flow, it is observed that the modified Taylor microscale scales the peak of $-\langle\Pi\rangle$, which is the derivative in scale space of the third-order structure-function. Similar to the $-\langle\Pi\rangle$, the $-\langle T_u\rangle$ is also a derivative of the third-order structure-function, but in physical space. And the modified Taylor microscale

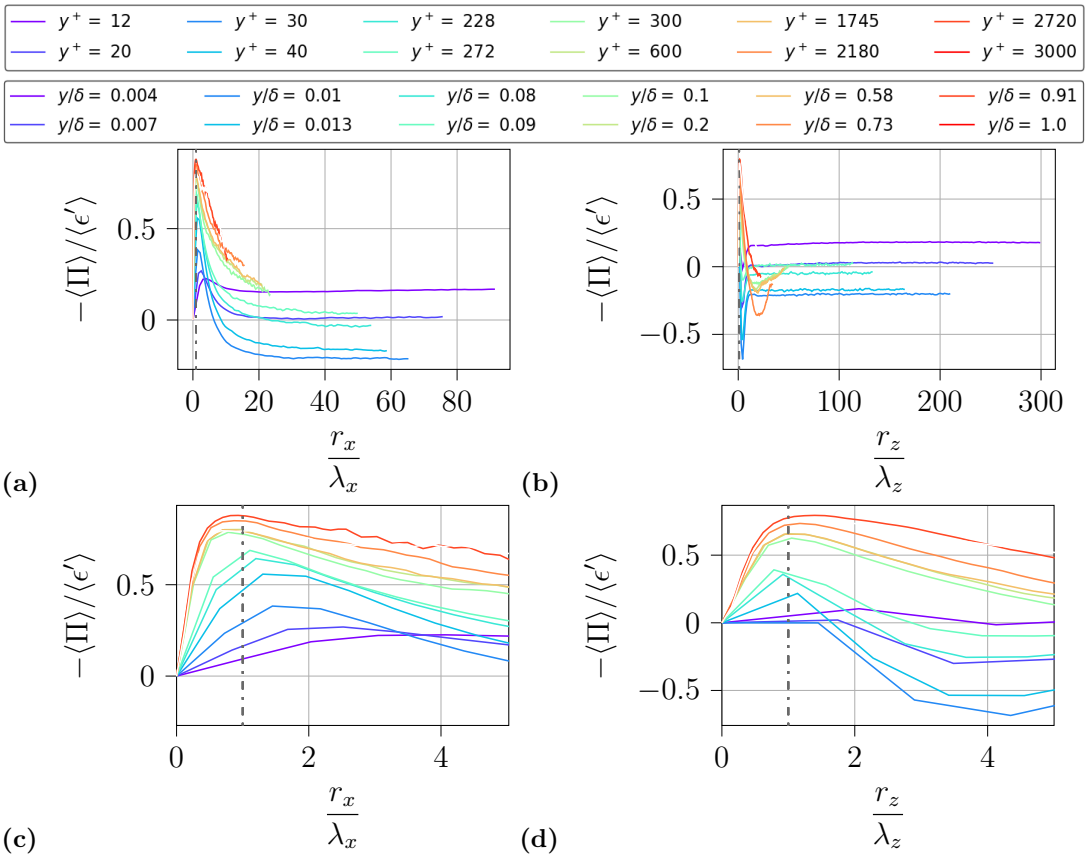

Figure 5.7: Same as Figure 5.6, but for TCF3000

doesn't scale $-\langle T_u \rangle$ term at any wall distance, which proves the importance of this modified Taylor microscale in the scale-dependent physics of turbulent flows.

Average value of Interscale energy transfer at large scales

The $-\langle\Pi\rangle$ is dominant between the Kolmogorov scales and the integral scales near the wall in both r_x and r_z direction. As the wall distance is increased, the scales at which $-\langle\Pi\rangle$ is significant also increases. And as the centre-line is reached, $-\langle\Pi\rangle$ remained close to $0.5\langle\epsilon'^*\rangle$ even at $r_x = \delta$. This prompted the question about whether $-\langle\Pi\rangle$ remains the same even beyond $r_x = \delta$. If there is a significant average at large values of r_x, it is necessary to decompose $-\langle\Pi\rangle$ to observe the contribution of each

of the individual terms. The Π term is decomposed as :

$$
\begin{aligned}
\Pi &= \delta u_j' \frac{\partial (\delta u_i')^2}{\partial r_j} \\
&= \delta u_i' \delta u_j' \left[\frac{\partial u_i'}{\partial x_j}\bigg|_b + \frac{\partial u_i'}{\partial x_j}\bigg|_a \right] \\
&= \underbrace{\delta u_1' \delta u_1' \left[\frac{\partial u_1'}{\partial x_1}\bigg|_b + \frac{\partial u_1'}{\partial x_1}\bigg|_a \right]}_{a_{11}} + \underbrace{\delta u_2' \delta u_1' \left[\frac{\partial u_2'}{\partial x_1}\bigg|_b + \frac{\partial u_2'}{\partial x_1}\bigg|_a \right]}_{a_{12}} + \underbrace{\delta u_3' \delta u_1' \left[\frac{\partial u_3'}{\partial x_1}\bigg|_b + \frac{\partial u_3'}{\partial x_1}\bigg|_a \right]}_{a_{13}} \\
&+ \underbrace{\delta u_1' \delta u_2' \left[\frac{\partial u_1'}{\partial x_2}\bigg|_b + \frac{\partial u_1'}{\partial x_2}\bigg|_a \right]}_{a_{21}} + \underbrace{\delta u_2' \delta u_2' \left[\frac{\partial u_2'}{\partial x_2}\bigg|_b + \frac{\partial u_2'}{\partial x_2}\bigg|_a \right]}_{a_{22}} + \underbrace{\delta u_3' \delta u_2' \left[\frac{\partial u_3'}{\partial x_2}\bigg|_b + \frac{\partial u_3'}{\partial x_2}\bigg|_a \right]}_{a_{23}} \\
&+ \underbrace{\delta u_1' \delta u_3' \left[\frac{\partial u_1'}{\partial x_3}\bigg|_b + \frac{\partial u_1'}{\partial x_3}\bigg|_a \right]}_{a_{31}} + \underbrace{\delta u_2' \delta u_3' \left[\frac{\partial u_2'}{\partial x_3}\bigg|_b + \frac{\partial u_2'}{\partial x_3}\bigg|_a \right]}_{a_{32}} + \underbrace{\delta u_3' \delta u_3' \left[\frac{\partial u_3'}{\partial x_3}\bigg|_b + \frac{\partial u_3'}{\partial x_3}\bigg|_a \right]}_{a_{33}}
\end{aligned}
\tag{5.4}
$$

Figure 5.8 shows $-\langle \Pi \rangle$ and its decomposed terms at large scales till $r_x = 9\delta$. For this analysis, only the results away from the wall is used because the value of $-\langle \Pi \rangle$ becomes negligible at small values of r_x/δ, near the wall.

It is observed that along the centre-line, $\langle \Pi \rangle$ at scales as large as 9δ is still approximately $0.5\langle \epsilon'^{*} \rangle$. Thus this signifies a very large scale correlation between some terms that contribute to $-\langle \Pi \rangle$. It is also observed that a_{21} which is due to the wall-normal derivative of the streamwise velocity is the main contribution to $-\langle \Pi \rangle$ at all scales along the centre-line. When a_{21} is negative or negligible at $y^+ = 270, 600$, $\langle \Pi \rangle$ becomes negligible even at scales less than δ. This term a_{21} is given by:

$$
\begin{aligned}
a_{21} &= \langle \delta u_1' \delta u_2' \left[\frac{\partial u_1'}{\partial x_2}\bigg|_b + \frac{\partial u_1'}{\partial x_2}\bigg|_a \right] \rangle = \langle (u_1'\big|_b - u_1'\big|_a)(u_2'\big|_b - u_2'\big|_a) \left[\frac{\partial u_1'}{\partial x_2}\bigg|_b + \frac{\partial u_1'}{\partial x_2}\bigg|_a \right] \rangle \\
&= \langle \Big((u_1'\big|_b u_2'\big|_b) - (u_1'\big|_b u_2'\big|_a) - (u_1'\big|_a u_2'\big|_b) + (u_1'\big|_a u_2'\big|_a) \Big) \left[\frac{\partial u_1'}{\partial x_2}\bigg|_b + \frac{\partial u_1'}{\partial x_2}\bigg|_a \right] \rangle
\end{aligned}
\tag{5.5}
$$

For long values of r, this reduces to

$$
\lim_{r \to \infty} a_{21} = 4 \langle u_1' u_2' \frac{\partial u_1'}{\partial x_2} \rangle \tag{5.6}
$$

Kholmyansky and Tsinober[64] makes a point about the small, but significant correlation coefficient between the vorticity and velocity fluctuations to imply the correlation between large and small scales of the flow. Along the same way, that a_{21} being

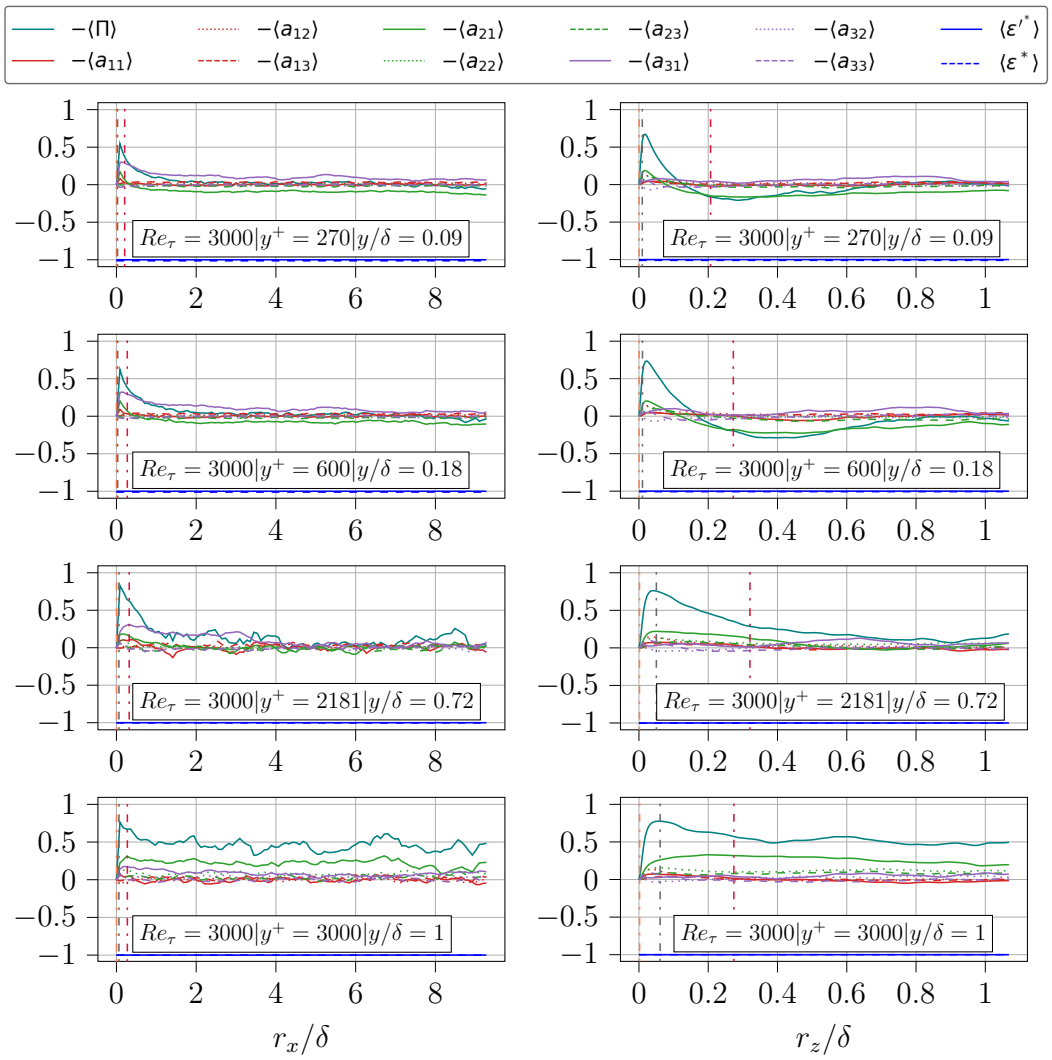

Figure 5.8: Spatio-temporal average value of $-\Pi$ and its decomposed terms shown in Equation 5.4 normalised by the absolute value of $\langle \epsilon'^{*} \rangle$. This is presented along the streamwise separation direction (left) and spanwise separation direction (right), normalised by the channel half-width

non-zero for scales as large as 9δ extends the result that the product of two velocity fluctuations $\langle u_1' u_2' \rangle$ and a velocity derivative $\frac{\partial u_1'}{\partial x_2}$ to a significant correlation between the large and the small scales of the flow. With the present results, it can be shown that such correlation between large and small scales of the flow is responsible for high values of interscale energy transfer near the centre-line of the flow.

Conclusion

In this subsection, the Spatio-temporal average behaviour of individual terms of the KHMH equation at different wall distances is discussed in detail. The terms that have zero or negligible average and thereby don't contribute to the average dynamics of the flow at all wall distances are A_t, A, T_p, D_x.

The interscale diffusion term $\langle D_{r2} \rangle$, is equal to $\langle \epsilon'^* \rangle$ at $r = 0$, and reduces with increase of scale and becomes negligible beyond the modified Taylor micro-scale in both r_x and r_z directions at all wall distance away from the wall.

The interscale energy transfer term $-\langle \Pi \rangle$ at $y^+ = 12$, starts at zero at $r^+ = 0$, and reaches its peak and reduces thereafter to becomes negligible after the integral scales. This is by observation of energy spectrum, where there are three distinct ranges, in which the energy cascade process occurs in the inertial subrange which is situated between the viscous effects dominated Kolmogorov scale and the energy-containing integral scales. However, as the wall distance is increased, this term starts to become relevant well beyond the integral scales, and along the centre-line of the channel it reaches close to $0.5\langle \epsilon'^* \rangle$ at scales $r^+ = 9\delta$. This pointed out the long-range correlation between some velocity and vorticity components, which symbolises the correlation between the large and small scales of the flow. In addition, the increase of Reynolds number manifests as a higher peak value of this term.

The modified Taylor microscale derived for the channel flow in r_x and r_z directions separately, scales the positive peak of $-\langle \Pi \rangle$ in the range $0.1 < y/\delta < 1$ in the r_x direction, and the range $0.1 < y/\delta < 0.9$ in the r_z direction. In isotropic turbulence, the Taylor microscale is observed to scale the peak of the third-order structure-function. And in the present flow, modified Taylor microscale which is a similar parameter is observed to scale only the peak of $-\langle \Pi \rangle$ which is the scale derivative of the third-order structure-function.

The production term starts dominating the flow dynamics beyond the integral scales at all wall distances. At $y^+ = 12$, which is the buffer layer, the production exceeds $\langle \epsilon'^* \rangle$ in both r_x and r_z directions at all scales beyond the integral scale. Beyond the buffer layer in the r_x direction, it never exceeds $\langle \epsilon'^* \rangle$. On the other hand, there is a positive peak of production term where it exceeds $\langle \epsilon'^* \rangle$ at all wall distances till $y/\delta = 0.58$. This peak of production term coincides with the negative peak of $-\langle \Pi \rangle$. Cimarelli et al.[23] explain that this is an inverse energy cascade and ascends to the centre-line of the channel flow moving through a straight line in the spanwise-wall-normal separation plane. As the wall distances approach the centre-line, the

influence of the production term starts to reduce and it becomes negligible at the centre-line of the channel flow. Here, the energy transfer in physical space dominates the flow dynamics, and so at the centre-line of the channel both the energy transfer terms (physical and scale) mostly balance the dissipation term.

5.2.3 Instantaneous KHMH equation terms

It is a well-known fact that intermittency is an integral part of the turbulent flow. And an averaged value of quantities only provides part of the information. Despite the knowledge that the turbulent energy cascade is forward on average i.e., large to small scales, there have been multiple studies in the past that shows the evidence of inverse energy cascade i.e., small to large scales, in free shear-flows [15], in wall-turbulence [60]. This will also be discussed in the present work in section 5.4.

Yasuda and Vassilicos [137] discovered that in DNS of periodic box simulations, the fluctuating part of KHMH equation terms presents a completely different picture than what was observed in their average. This is because there are terms with huge fluctuations, but with negligible or zero average. To expand that idea in wall-bounded turbulence, this subsection focuses on the implementation of the analysis of instantaneous behaviour of KHMH equation terms.

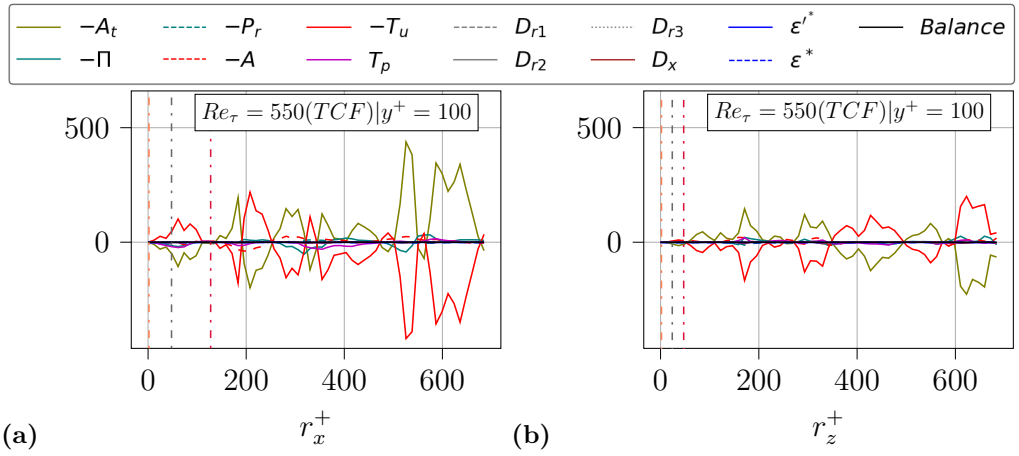

Figure 5.9: Instantaneous values of all KHMH equation terms, normalised by the absolute value of $\langle \epsilon'^* \rangle$. This is presented in **(a)** streamwise direction separation and **(b)** spanwise direction separation normalised by wall-units

Figure 5.9 shows the instantaneous behaviour of all the terms of KHMH Equation 3.11 at $y^+ = 100$ in TCF550, normalised by absolute value of ϵ'^*. The dominant terms are A_t and A, and they both seem to be anti-correlated. Their magnitude

seems to be close to 400-450 times the value of ϵ'^*. On the other hand, from the last subsection where the average value of the KHMH equation terms is studied, it was observed that both of these terms attains zero or negligible value on average. On a closer inspection, it appears that the terms $A_t = \frac{\partial}{\partial t}(\delta u_i')^2$ and $A = \overline{u_j^*}\frac{\partial}{\partial X_j}(\delta u_i')^2$ when added together results in a much smaller value than the individual terms and this is explained by the Taylor hypothesis. So the resulting anti-correlation between terms A_t and A, can be explained based on the frozen turbulence hypothesis. To look further this anti-correlation, it was decided to add these two terms, since in the KHMH equation they are added. This added term $A_t + A$ is the Lagrangian time derivative of $\delta(u_i'^*)^2$ following the mean flow.

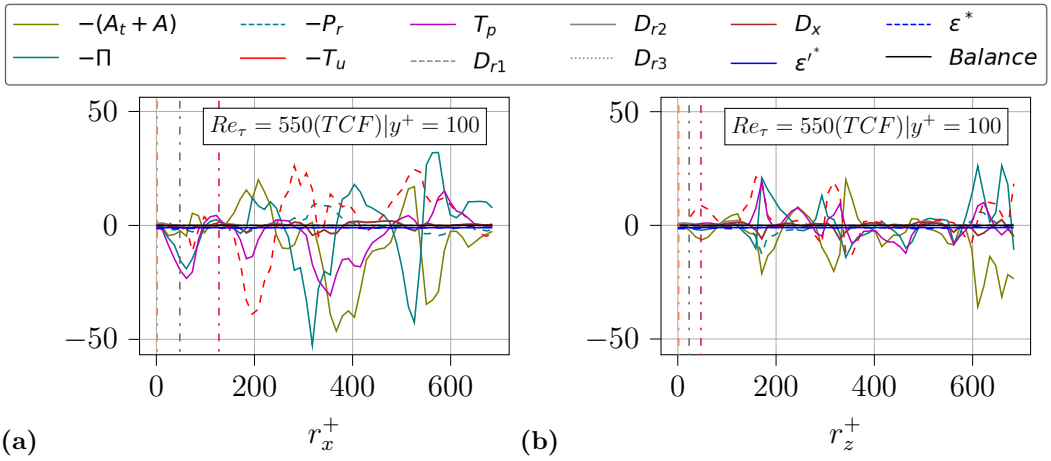

Figure 5.10: Instantaneous values of all KHMH equation terms excluding the A_t and A terms and including $A_t + A$ term, normalised by the absolute value of ϵ'^*. This is presented in **(a)** streamwise direction separation and **(b)** spanwise direction separation normalised by wall-units

Figure 5.10 shows the instantaneous behaviour of all the terms of the KHMH equation plus the $-(A_t + A)$ term and excluding the individual $-A_t$ and $-A$ term. It is observed that the dominant terms are the $-(A_t + A)$, $-\Pi$, $-T_u$ and T_p, all of which fluctuate close to 40-50 times the value of ϵ'^*. This result shows the importance of the dynamics of terms that have negligible or zero average but has their influence instantaneously. This result although being interesting doesn't reveal the entire picture, because this instantaneous behaviour of the terms are dependent on the position in the flow at which the analysis is performed. To understand the instantaneous fluctuations further, it is decided to obtain the standard deviation of each of the terms, which will then make it easier to understand the results between r_x and r_z directions at different wall distances. This would also serve as a reference

for future studies on the relevance of different terms in the dynamics of different regions of the flow.

Normalisation of standard deviation

The results of the Spatio-temporal averaged value of KHMH equation terms were normalised by the absolute value of $\langle \epsilon'^* \rangle$. However when the absolute value of $\langle \epsilon'^* \rangle$ is used to normalise standard deviation datasets, it became difficult to compare between the two channel flows. Other quantities like $\frac{u_\tau^4}{\nu}$ near the wall and $\frac{U_{max}^3}{\delta}$ near the centre-line of the channel flow also made it difficult to compare, and this is presented in Appendix B.4.1. This problem is solved when the KHMH equation terms were normalised with the standard deviation of Π, which is one of the leading terms at all wall distances from $y^+ = 12$ till the centre-line of the channel flow. The wall distance and x-axes are normalised by the wall-units till $y^+ = 100$, and thereafter by the channel half-width δ until the centre-line of the channel flow.

Observation

Figure 5.11 and 5.12 shows the standard deviation of all the terms of KHMH equation at different wall distances in r_x and r_z directions. It is observed that the diffusion and dissipation terms have considerable values close to the wall at $y^+ = 12$, and they are negligible for the standard deviation of Π at all wall distances thereafter till the centre-line of the channel flow. Between the Kolmogorov scales and the modified Taylor microscale, the diffusion and dissipation terms are observed to be dominant at all wall distances. The small-scale values of the diffusion and dissipation terms were quite high that it became difficult to observe the orders of the other terms and so the plot is cropped. The full plot is given in Appendix B.4.1. At $y^+ = 12$, the standard deviation of ϵ^* is higher than that of ϵ'^*, and with the increase of y^+, they become approximately of the same order.

The production term P_r is dominant at all scales in both the channel flows in both r_x and r_z directions and is of the order of standard deviation of Π at $y^+ = 12$. With the increase of y^+, the standard deviation of P_r reduces and it becomes negligible at the centre-line of the channel flow in both r_x and r_z directions. The standard deviation of $A_t + A$, T_u and T_p are all dominant from $y^+ = 12$ till the centre-line of channel flow in both r_x and r_z directions and is of the order of standard deviation of Π. The instantaneous behaviours of the KHMH equation terms are not influenced by the increase of Reynolds number when normalised by the standard deviation of Π.

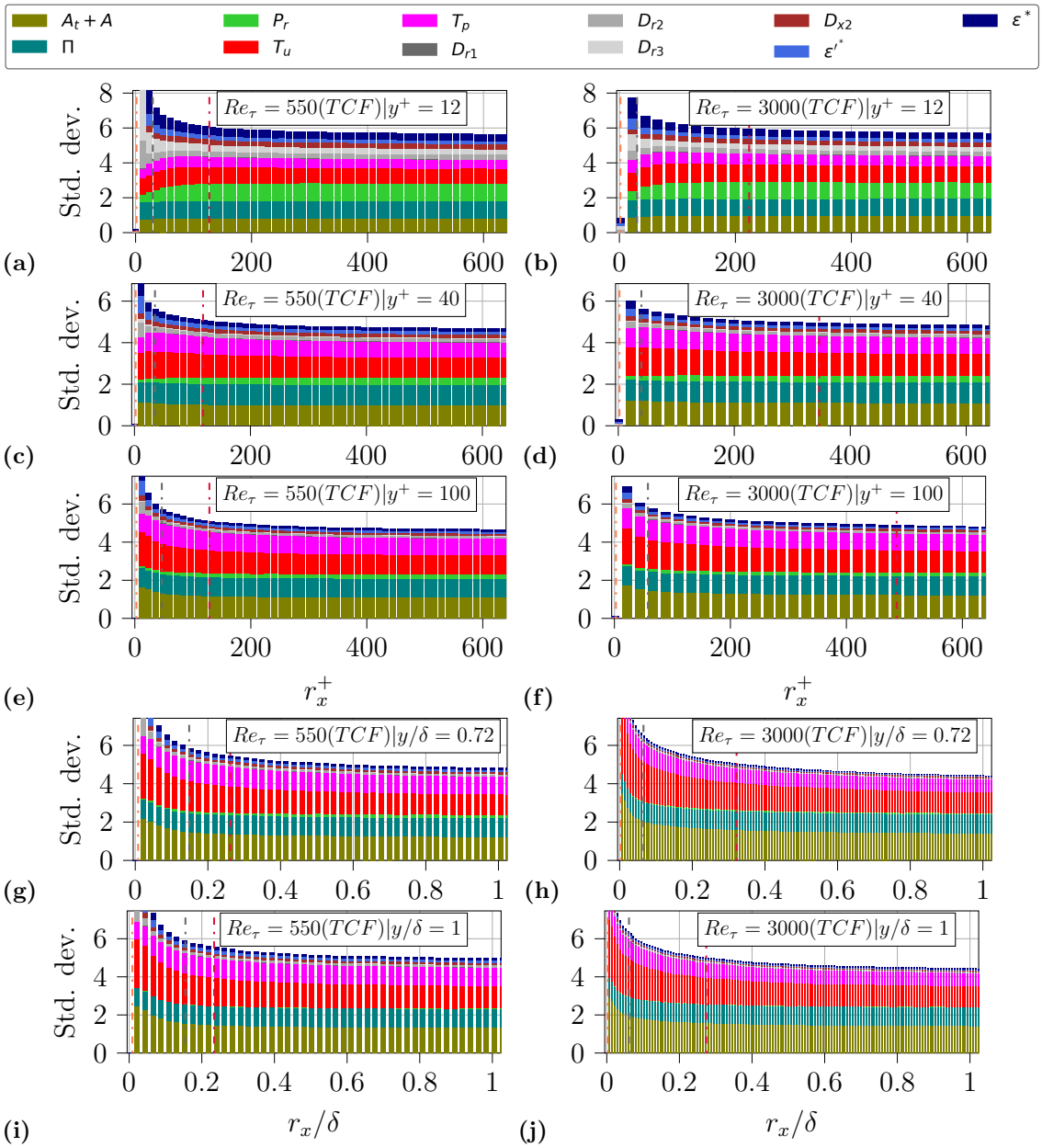

Figure 5.11: Standard deviation of all KHMH terms of TCF at $Re_\tau = 550$ (left) and TCF at $Re_\tau = 3000$ (right). This is presented in the streamwise direction separation, where the x-axis and the wall distances are normalised by the wall-units between **(a)** and **(f)**, and by the channel half-width between **(g)** and **(j)**

Discussion

The near-wall dynamics of the KHMH equation terms is dominated by the diffusion and the dissipation process. It is also true that the diffusion processes are dominant

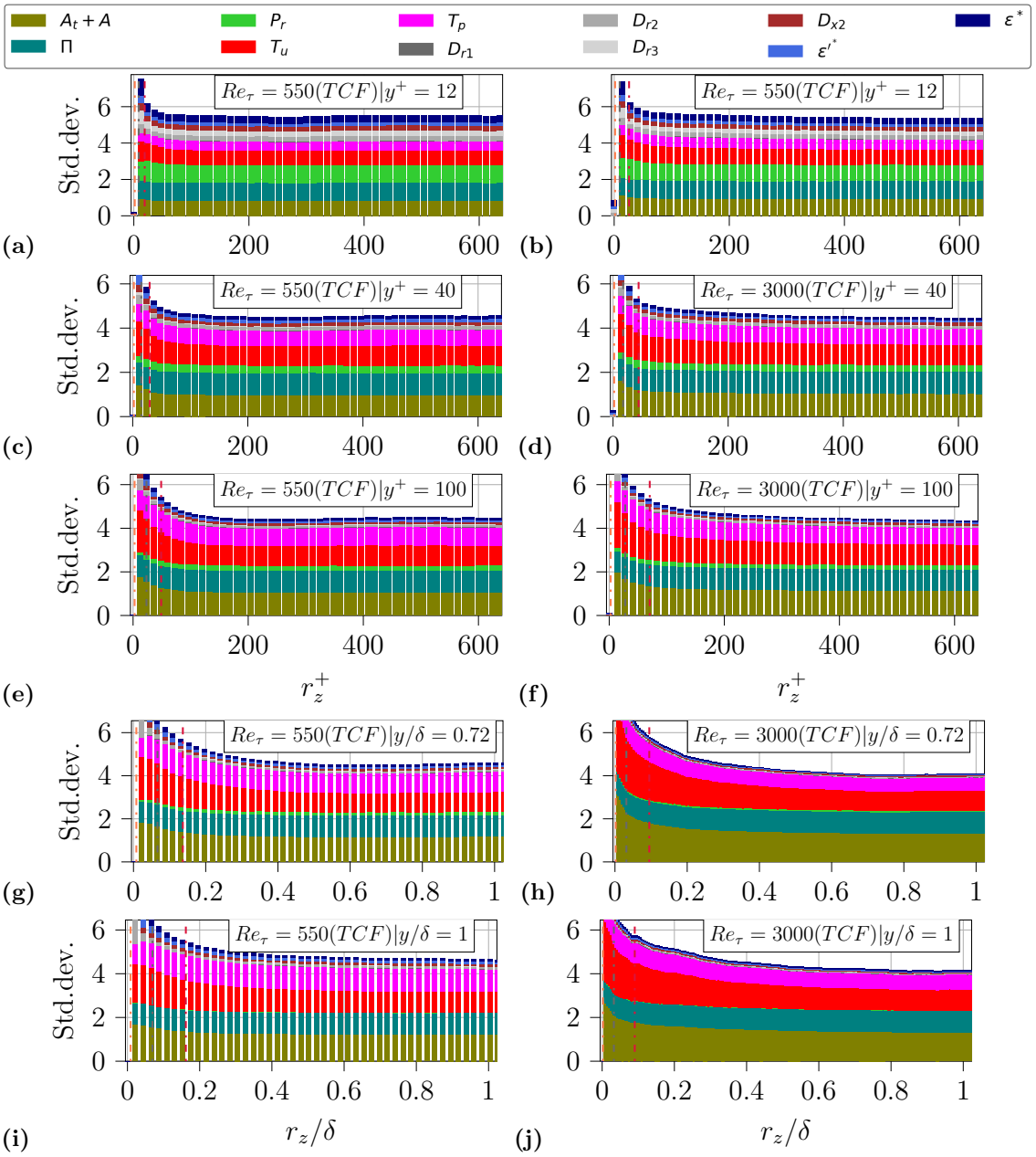

Figure 5.12: Standard deviation of all KHMH terms of TCF at $Re_\tau = 550$ (left) and TCF at $Re_\tau = 3000$ (right). This is presented in the spanwise separation direction, where the x-axis and the wall distances are normalised by the wall-units between **(a)** and **(f)**, and by the channel half-width between **(g)** and **(j)**

at small scales and this was also observed with the average results, where $\langle D_{r1} \rangle$ balances the $\langle \epsilon'^* \rangle$ at $r^+ = 0$. In addition, this high value of dissipation and diffusion

terms at such small scales could be due to small values of the standard deviation of interscale energy transfer at those small scales. The standard deviation of ϵ^* greater than that of ϵ'^* could be explained by the higher value of mean velocity derivatives compared to the derivatives of fluctuations of velocity near the wall at $y^+ = 12$.

The dominance of the production term at $y^+ = 12$ is explained by the fact that this region is the buffer layer which is considered to be the engine of turbulent fluctuations in wall-bounded turbulent flows. The negligible value of the standard deviation of P_r at the centre-line is explained by the fact that the mean velocity gradient in the wall-normal direction is zero at the centre-line of the channel flow, and this particular result is also reflected in $-\langle P_r \rangle$ in the last subsection. However, the decreasing influence of instantaneous dynamics of P_r with the increase of wall distance between the buffer layer and the centre-line of the channel flow is not captured by the average value of this term.

The terms $A_t + A$, Π, T_u and T_p have approximately the same order at all wall distances and so contribute equally to the dynamics of the flow. However, the average value of all terms except for Π is either zero or negligible compared to ϵ'^*. Chen et al. [20] showed that in a turbulent channel flow, the local ($\frac{\partial \boldsymbol{u'}}{\partial t}$) and convective ($\boldsymbol{u'}.\nabla \boldsymbol{u'}$) accelerations tend to anti-align each other. With local acceleration partly in A_t and the convective acceleration is present in Π and T_u, it is clear that these terms (A_t, Π, T_u) are of the same order. The standard deviation of T_p being of the same order of the other terms implies that there is some contribution from the pressure term in the energy transfer processes in the flow and this will be discussed in the upcoming subsection.

Conclusion

The instantaneous part of the terms helped to observe the full contribution of each term beyond their averages. This is especially important for the terms with negligible or zero average like A_t, A and T_p. Thus it also helped to identify the dominant terms at different wall distances which gives more information about the dynamics of the flow. The increase of Reynolds number doesn't produce any change in the standard deviation of the KHMH terms when normalised by the standard deviation of Π.

The near-wall dynamics and the small-scale dynamics at all wall distances are dominated by the diffusion and dissipation terms. The production term is dominant at the buffer layer and gradually decreases with an increase of wall distance and

becomes negligible at the centre-line of the channel flow. The terms $A_t + A$, Π, T_u and T_p are dominant at all wall distances from $y^+ = 12$ till the centre-line of the channel flow. The dominance of the $A_t + A$, Π and T_u are explained by the anti-alignment of local and convective accelerations in channel flow. The T_p having a similar standard deviation as the acceleration terms may imply the involvement of pressure term in the energy transfer dynamics.

5.2.4 Correlation coefficient of KHMH equation terms

In the previous subsections, starting with average values of KHMH equation terms and discussing the results, and moving towards the instantaneous behaviour of KHMH equation terms, some correlation between KHMH terms are identified and that the instantaneous contribution of each term is completely different from its average contribution to the dynamics of the flow.

To study the correlation between different terms of KHMH equation, Pearson's correlation coefficient is used and is given by:

$$corr(Q_1, Q_2) = \frac{\langle Q_1 - \langle Q_1 \rangle \rangle \langle Q_2 - \langle Q_2 \rangle \rangle}{\sigma_{Q_1} \sigma_{Q_2}} \tag{5.7}$$

where Q_1 and Q_2 are the terms for which the correlation coefficient is computed, σ_{Q_1} and σ_{Q_2} is the standard deviation of the terms Q_1 and Q_2 respectively. The angular brackets $\langle . \rangle$ represent the Spatio-temporal averaging which is obtained over time, streamwise and spanwise directions such that the correlation coefficient is a function of the three scale-space variables and the wall distance (r_x, r_y, r_z, y).

The most interesting correlation-coefficient occured between :

- $Q_1 = A_t + A$ and $Q_2 = \Pi, T_u$
- $Q_1 = T_p$ and $Q_2 = \Pi, T_u, P_r$

Thus the correlation coefficients are studied with only the following six KHMH equation terms: $A_t + A$, P_r, T_p, Π, T_u, and the sum of two energy transfer terms $\Pi + T_u$. It is also known that the standard deviations of all the above terms are non-negligible at the wall distances from $y^+ = 12$ till $y/\delta = 1$. And so the correlation-coefficient of these terms is analysed at all the wall distances as in the previous subsection *i.e.*, $y^+ = 12, 40, 100; y/\delta = 0.72, 1$.

Observation with $A_t + A$ term

Figure 5.13 and 5.14 shows the correlation coefficient of $A_t + A$ term with the other KHMH terms under consideration. The correlation coefficient of T_p and $A_t + A$ is

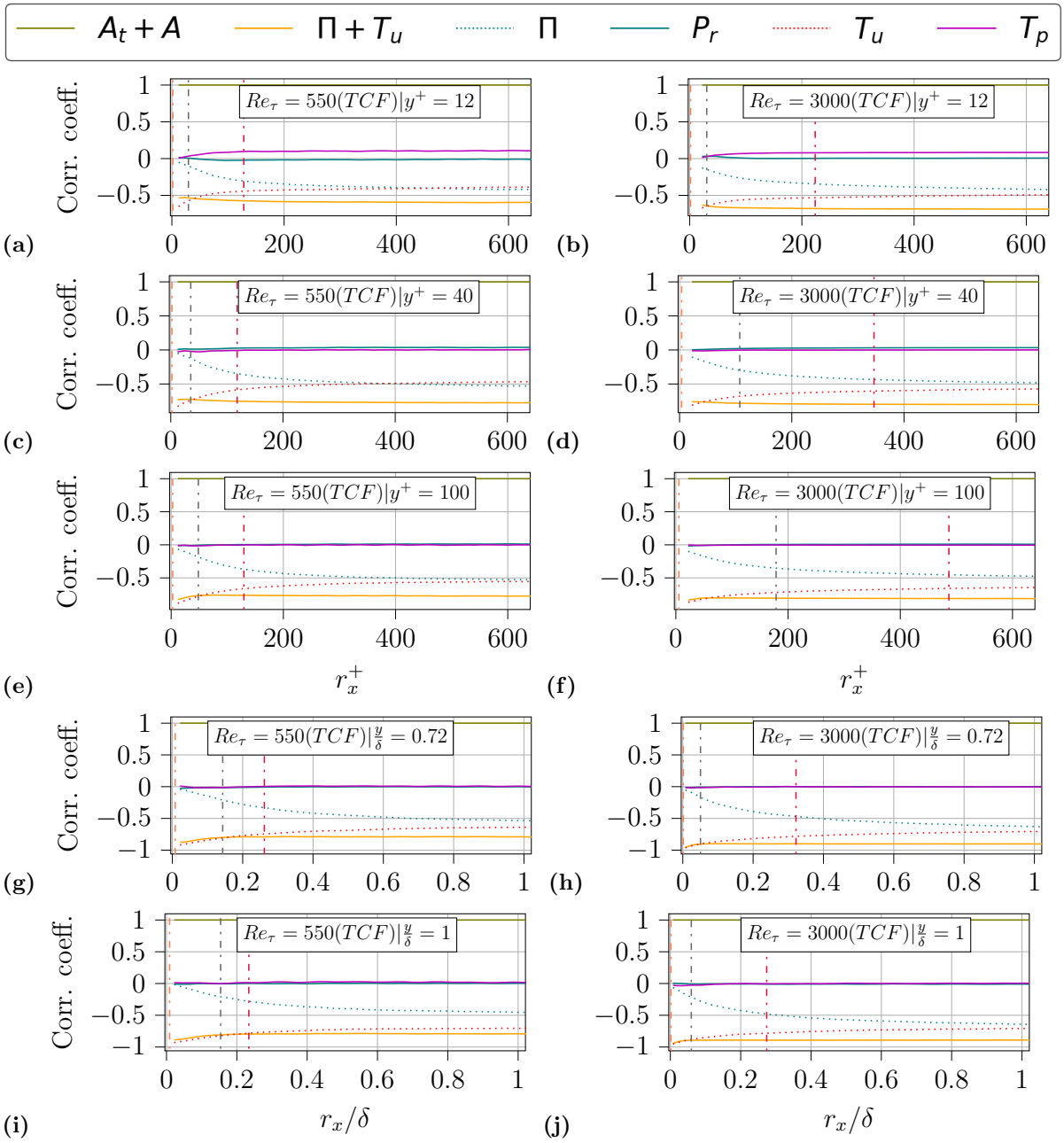

Figure 5.13: Correlation coefficient of the KHMH equation terms with $A_t + A$ in streamwise direction separation of TCF at $Re_\tau = 550$ (left) and TCF at $Re_\tau = 3000$ (right). This is presented at various wall distances, where the x-axis and wall distances are normalised by wall-units between **(a)** to **(f)**, and by channel half-width from **(g)** to **(j)**

of the order of 0.1 at $y^+ = 12$ and becomes negligible beyond that wall distance.

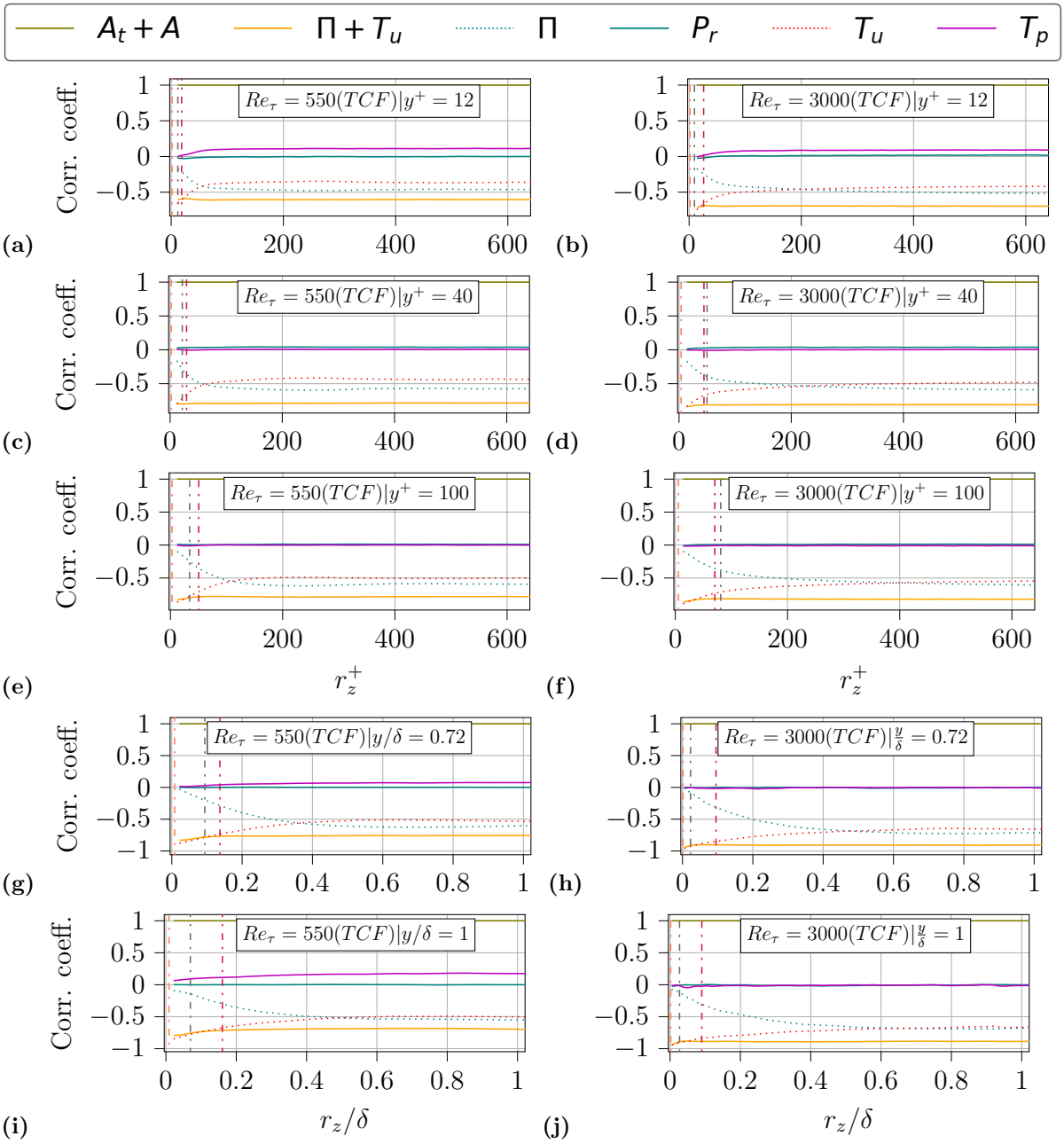

Figure 5.14: Correlation coefficient of the KHMH equation terms with A_t+A in spanwise direction separation of TCF at $Re_\tau = 550$ (left) and TCF at $Re_\tau = 3000$ (right). this is presented at various wall distances, where the x-axis and wall distances are normalised by wall-units between **(a)** to **(f)**, and by channel half-width from **(g)** to **(j)**

The correlation coefficient of $A_t + A$ and Π term approximately has correlation coefficient of -0.4 to -0.5 after the integral scale and remains in this value thereafter.

With the increase of wall distance, the correlation coefficient between $A_t + A$ and Π remains close to -0.5 at large scales in both r_x and r_z directions. However between $A_t + A$ and T_u, it increases until approximately to -0.75 at the centre-line of the channel flow in the r_x direction. In the r_z direction, the correlation coefficients between $A_t + A$ and both the energy transfer terms remains approximately the same from $y^+ = 12$ till the centre-line of the channel flow. The correlation coefficient of $A_t + A$ and T_u also reaches the value to close to -0.5 at scales larger than integral scales. As the scales reduce smaller than integral scales, the correlation coefficient between $A_t + A$ term and T_u increases, whereas the same with Π decreases. When the two energy transfer terms were considered together as $\Pi + T_u$, the correlation coefficient of this term with $A_t + A$ is higher than the correlation coefficient with the individual terms (Π, T_u). The correlation coefficient between $A_t + A$ and $\Pi + T_u$ is a constant value at all scales, and it is approximately -0.55 at $y^+ = 12$ and reaches a value of approximately -0.8 to -0.85 at the centre-line of the channel flow.

The increase of Reynolds number increased the correlation coefficient between $A_t + A$ and Π, T_u, $\Pi + T_u$, with the most difference in $\Pi + T_u$ which is between -0.55 to -0.7 for TCF550 and between -0.65 to -0.9 for TCF3000.

A small correlation coefficient exists between T_p and $A_t + A$, and it starts at $y/\delta = 0.72$ and it increases when the wall distance is increased in TCF550. On the other hand, this correlation coefficient is not observed in the TCF3000. This is not observed in the r_x direction of both the flows. Hence it could be concluded that it is an artefact of the particular simulation at high values of wall distance in the spanwise direction.

Observation with T_p term

Figures 5.15 and 5.16 shows the correlation coefficient of T_p with other terms of the KHMH equation. Similar to the previous analysis, the study is performed at $y^+ = 12, 40, 100$; $y/\delta = 0.72, 1$, to understand the correlation coefficient between the terms from near the wall to the centre-line of the channel.

The correlation coefficient between T_p and $A_t + A$ observed here is the same as what was observed previously, about 0.1 correlation near the wall which becomes negligible after $y^+ = 12$. The correlation coefficient between P_r and T_p is approximately 0.35-0.37 at $y^+ = 12$, and it reduces to approximately 0.2 at $y^+ = 100$ and stays at the same value until $y/\delta = 0.72$. This correlation coefficient becomes negligible at the centre-line of the channel.

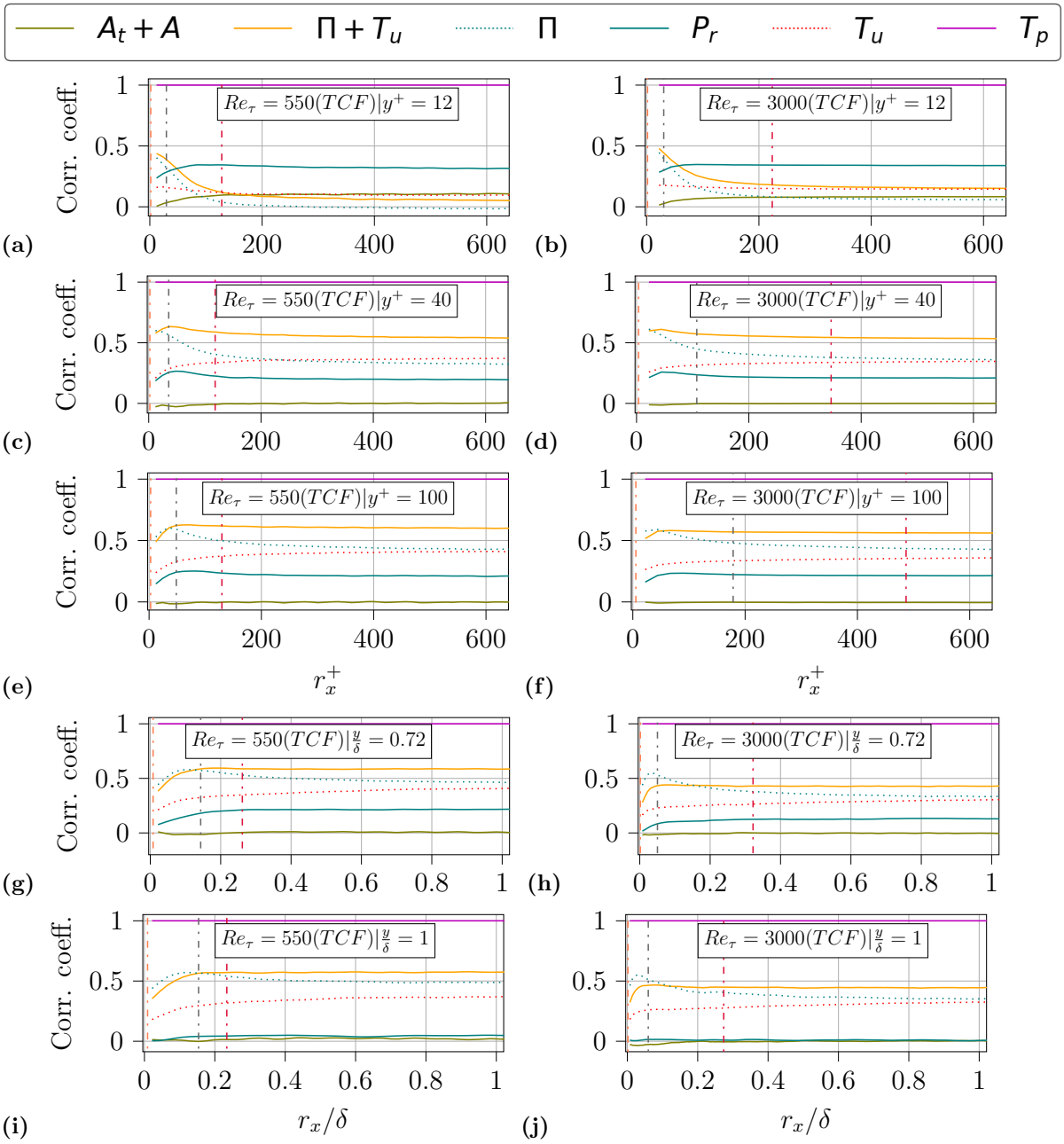

Figure 5.15: Correlation coefficient of KHMH equation terms with T_p in streamwise direction separation of TCF at $Re_\tau = 550$ (left) and TCF at $Re_\tau = 3000$ (right). This is presented at various wall distances, where the x-axis and wall distances are normalised by wall-units between (a) to **(f)**, and by channel half-width from **(g)** to **(j)**

The correlation coefficient between T_p and Π has a negligible value near the wall at $y^+ = 12$. At $y^+ = 40$, this correlation coefficient between T_p and Π has its

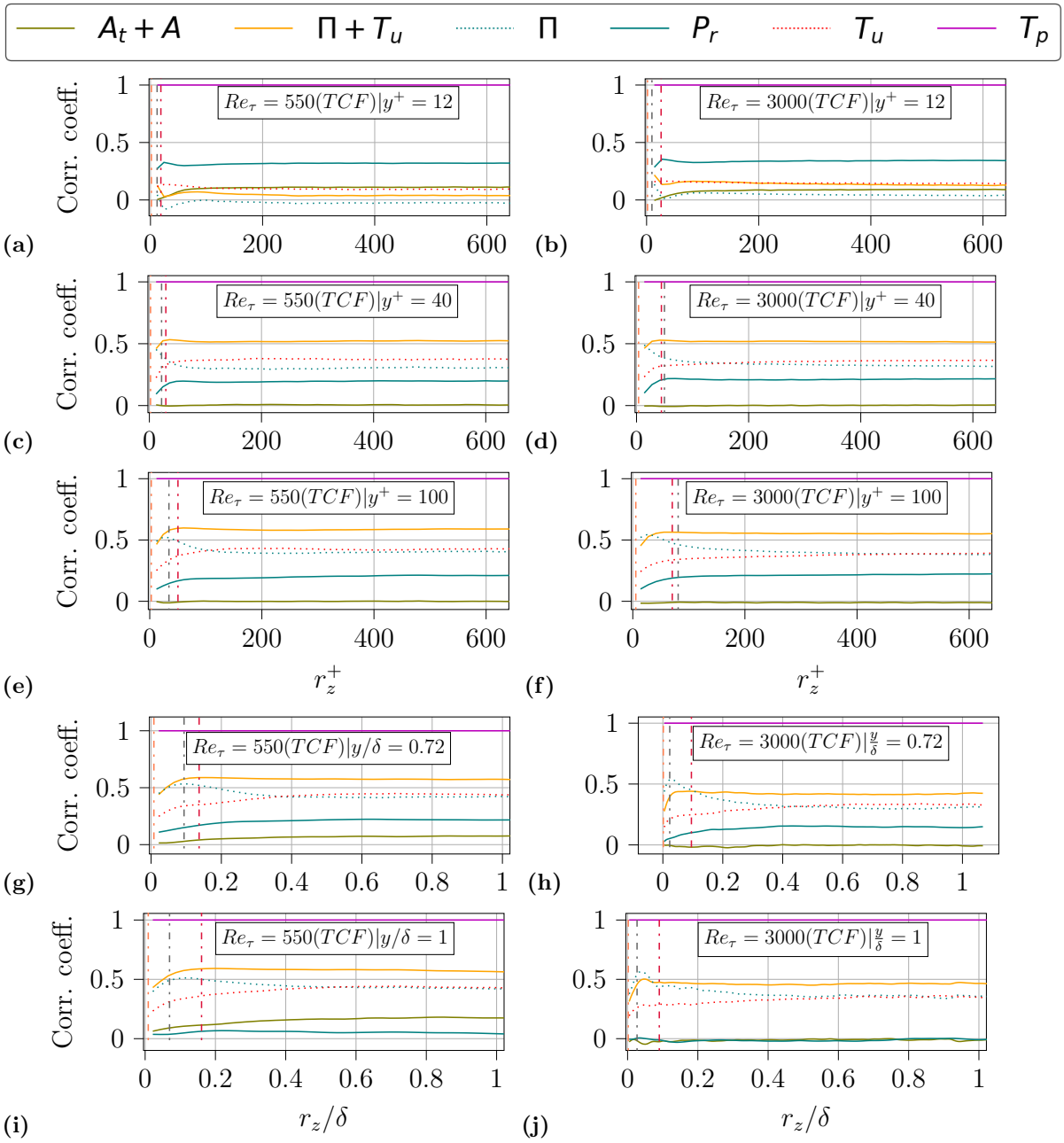

Figure 5.16: Correlation coefficient of KHMH equation terms with T_p in spanwise direction separation of TCF at $Re_\tau = 550$ (left) and TCF at $Re_\tau = 3000$ (right). This is presented at various wall distances, where the x-axis and wall distances are normalised by wall-units between **(a)** to **(f)**, and by channel half-width from **(g)** to **(j)**

peak value close to 0.5 at a small scale and it reduces thereafter to approximately 0.4 at large scales. Moving away from the wall, the correlation coefficient at large

scales between T_p and Π increase to approximately 0.45. The correlation coefficient between T_p and T_u is also non-negligible after $y^+ = 40$, with values approximately 0.4-0.45 at all wall distances thereafter till the centre-line. As the scales reduce, the correlation coefficient of T_p term increases with Π and decreases with T_u. And the correlation coefficient between the pressure term T_p and the sum of the two energy transfer terms $(\Pi + T_u)$ tends to have a correlation coefficient of about 0.55 at all scales from $y^+ = 40$ till the centre-line of the channel, which is higher than the correlation coefficient of the individual terms. All the above observations are valid in both r_x and r_z directions.

With the increase of Reynolds number, the correlation coefficient between T_p and P_r stays the same from $y^+ = 12$ to $y^+ = 100$, whereas it decreases its value from 0.2 in TCF550 to 0.15 in TCF3000. The correlation coefficient between T_p and Π, T_u, $\Pi + T_u$ approximately remain the same between the two flows from $y^+ = 12$ to $y^+ = 100$. With further increase in wall distance, the correlation coefficient between T_p and $\Pi + T_u$ reduce from 0.55 in TCF550 to 0.45 in TCF3000 till the centre-line.

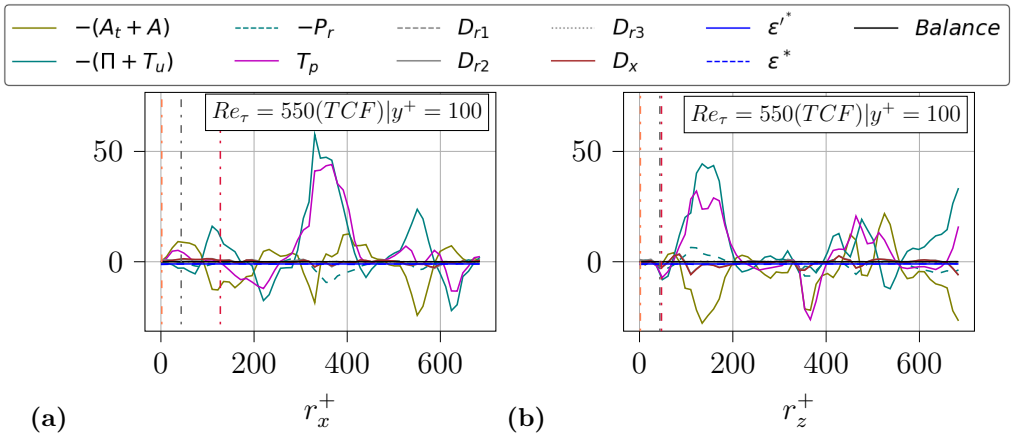

Figure 5.17: Instantaneous values of all KHMH equation terms excluding A_t, A, Π, T_u terms and including $A_t + A$ and $\Pi + T_u$ terms in **(a)** streamwise direction separation and **(b)** spanwise direction separation in DNS of TCF550 at $y^+ = 100$

Discussion

This result between the $A_t + A$ and $\Pi + T_u$ could be partially explained by the sweeping decorrelation hypothesis first proposed by Tennekes [118], by stating that *at high Reynolds number turbulence, the dissipative eddies flow past an Eulerian observer in a time frame much shorter than the time scale which characterises their*

dynamics. Tsinober et al.[124] explained how the hypothesis means the local $\frac{\partial}{\partial t}\boldsymbol{u'}$ and convective acceleration term $\boldsymbol{u'}.\nabla\boldsymbol{u'}$ of Navier-Stokes' equation tend to anti-align with the increase of Reynolds number and thereby cancel most of each other. This results in the sum of the two acceleration terms tend to be much smaller and scales very differently to the individual acceleration terms[20]. In the current study, the local acceleration can be thought of as $A_t + A$ because A_t is from the time-derivative term of Navier-Stokes' equation. The Π and T_u terms are obtained from the convective acceleration term $(\boldsymbol{u'}.\nabla\boldsymbol{u'})$ of Navier-Stokes' equation. Figure 5.17 shows the instantaneous value of $A_t + A$ and $\Pi + T_u$ to reinforce the point that these two terms arising from time derivative and the non-linear term of Navier-Stokes' equation approximately cancels each other.

This results of the correlation coefficient between $A_t + A$ and the two energy transfer terms $\Pi + T_u$ obtained so far, are very different from what has been observed in the previous subsections, because the correlation coefficient between the terms remains the same from near the wall at $y^+ = 12$ till the centre-line of the channel flow at $y/\delta = 1$. This is completely unusual because the dynamics in these regions close to the wall and away from the wall are different from each other. This difference is the reason behind dividing the wall-bounded turbulence into many different layers within the outer and inner layer classification.

The sweeping decorrelation hypothesis states that the dissipative eddies being swept by the large scales works for the dynamics far from the wall. And so for the results obtained from the correlation coefficient, it could have been easier to explain the phenomenon in the region away from the wall. However, the result is the same even close to the wall making it difficult to understand the flow dynamics with this physical explanation. Thus the present results are not fully explained by the sweeping decorrelation hypothesis in the near-wall dynamics of the flowfield.

It is known that the Navier-Stokes' equation, at the wall, reduces to pressure term balancing the diffusion term. And when the wall distance increases, the total velocity becomes non-zero and so the other terms of Navier-Stokes' equation which starts to contribute to the dynamics of the flow. Thus near the wall, the time derivative term, advection term starts to increase faster than the convective acceleration $(u'.\nabla u')$ term. However, the sum of time derivative and advection term scales like the non-linear terms. This could be an explanation for the correlation coefficient between the $A_t + A$ term and the two energy transfer terms $\Pi + T_u$. In addition, this could be the reason for T_p not correlating with the two energy transfer terms very near the wall.

Correlation coefficient of interscale energy transfer at large scales

In the previous analysis of correlation coefficients, it is observed that at large scales (r larger than Integral scales), the correlation coefficient between both the energy transfer terms Π and T_u tends to have approximately a constant value of -0.5 with $A_t + A$ and 0.35-0.45 with T_p, up to $r = \delta$. That observation prompted the curiosity to perform the analysis to verify the limits of 'r' values at which this correlation coefficient tends to decrease. The present simulation of TCF3000 is available for approximately $6\pi\delta$ and so the analysis is performed for scales up to the order of 9δ, because of the periodicity in the streamwise direction.

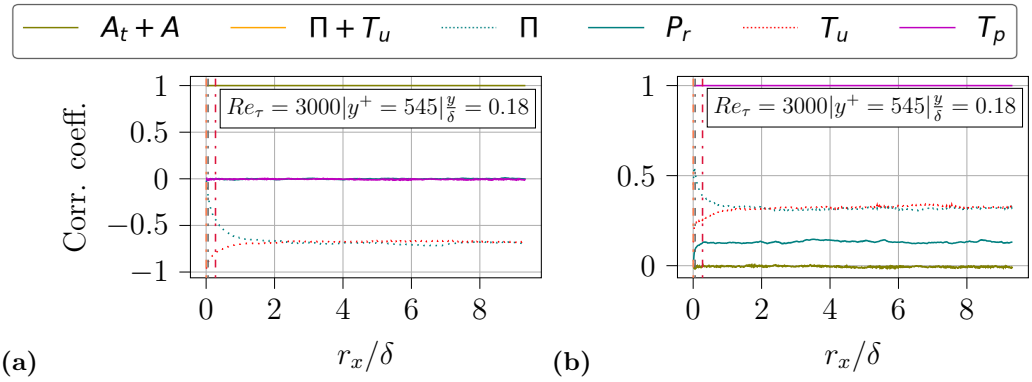

Figure 5.18: Correlation coefficient of KHMH equation terms with **(a)** A_t+A and **(b)** T_p in TCF3000 at $y^+ = 545$ in the streamwise direction.

Figure 5.18 shows the correlation coefficient of $A_t + A$ and T_p respectively, at $y^+ = 100$ with other KHMH terms at scales till $r = 9\delta$ in the streamwise direction. As the observation is similar between the r_x and r_z directions at all wall distances, the result is only presented in r_x direction for one wall distance. The main observation is that the correlation coefficient of Π and T_u with $A_t + A$ stays approximately -0.65 to -0.7 respectively till $r_x = 9\delta$. The correlation coefficient of the same terms with T_p is approximately constant and equal to 0.35 till $r_x = 9\delta$.

It is shown in the previous subsection that the energy transfer terms can be decomposed into 9 terms given by Equation 5.4, for which the correlation coefficients can be computed. For example, the correlation coefficient computation for a_{11} and $A_t + A$ is given by:

$$corr(a_{11}, A_t + A) = \frac{\langle (a_{11} - \langle a_{11} \rangle)(A_t + A - \langle A_t + A \rangle) \rangle}{\sigma_\Pi \sigma_{A_t + A}} \tag{5.8}$$

This way, the correlation coefficient for all the decomposed terms can be computed, and the sum $corr(a_{ij}, A_t + A)$ will be equal to $corr(\Pi, A_t + A)$. This method helps to

determine which terms, thereby which processes are contributing to this high value of correlation coefficient between Π and $A_t + A$. The results are presented for all the correlation coefficients at large scales in Table 5.1, with significant correlation shown in bold numbers. This is also extended to the computation of correlation coefficient of a_{11} to a_{33} with T_p, which is presented in Table 5.2.

$A_t + A$				Π			r_x direction			
y^+	Full	a_{11}	a_{12}	a_{13}	a_{21}	a_{22}	a_{23}	a_{31}	a_{32}	a_{33}
12	-0.58	**-0.28**	0	-0.018	**-0.11**	0.003	-0.001	**-0.18**	0.001	0.003
30	-0.51	**-0.21**	-0.0055	0.001	-0.073	0.004	-0.002	**-0.2**	0.004	-0.002
40	-0.54	**-0.25**	0.0005	-0.006	-0.08	0.005	-0.0045	**-0.18**	-0.004	-0.027
227	-0.57	**-0.27**	-0.0026	-0.014	**-0.1**	0.0062	-0.0097	**-0.14**	-0.01	-0.032
599	-0.64	**-0.26**	-0.063	-0.071	-0.067	-0.004	-0.03	-0.07	-0.027	-0.04
2178	-0.66	**-0.28**	-0.072	-0.076	-0.07	-0.005	-0.029	-0.066	-0.027	-0.032
3000	-0.7	**-0.24**	-0.096	-0.078	-0.088	-0.024	-0.037	-0.067	-0.03	-0.025

Table 5.1: Large scale correlation coefficient of $A_t + A$ with Π and its decomposed terms ($a_{11} - a_{33}$) in the streamwise direction

T_p				Π			r_x direction			
y^+	Full	a_{11}	a_{12}	a_{13}	a_{21}	a_{22}	a_{23}	a_{31}	a_{32}	a_{33}
30	0.034	-0.048	0.0052	0.022	-0.043	0.0065	0.03	0.007	0.0047	0.05
40	0.157	-0.017	0.009	0.022	-0.001	0.0072	0.039	0.031	0.009	0.057
227	0.26	0.017	0.011	0.021	0.032	0.011	0.043	0.05	0.013	0.058
599	0.35	**0.087**	0.008	0.016	**0.066**	0.016	0.03	**0.066**	0.022	0.037
2178	0.32	**0.08**	0.007	0.013	**0.065**	0.018	0.026	**0.062**	0.02	0.03
3000	0.32	**0.07**	0.012	0.014	**0.058**	0.026	0.024	**0.056**	0.025	0.03

Table 5.2: Large scale correlation coefficient of T_p with Π and its decomposed terms ($a_{11} - a_{33}$) in the streamwise direction

It is observed that the correlation coefficient between Π and $A_t + A$ is mainly due to the term a_{11} at all wall distances. There is an additional contribution from the terms a_{21} and a_{31} till $y^+ = 227$. Thus the correlation coefficient can be attributed to δu_1 and $\frac{\partial u_1}{\partial x_j}$, where j=1,2,3. This implies that Π contributes to the dynamics of different processes through the product of the streamwise velocity with its derivatives in all three directions.

The correlation coefficient of T_p and Π doesn't show a strong value of any individual term up to $y^+ = 100$. Beyond that wall distance, there is a higher contribution of correlation coefficient from the terms a_{11}, a_{21} and a_{31}, but this contribution is limited to less than 0.1 from each of the decomposed terms. Thus it is not possible to conclude that this correlation coefficient contribution is due to the physics in the streamwise direction.

A similar analysis was performed on the correlation coefficient of energy transfer in physical space term T_u with both $A_t + A$ and T_p terms and didn't return any conclusive results.

Conclusion

It is observed that the $A_t + A$ has approximately -0.5 correlation with Π and T_u, and -0.6 to -0.7 correlation coefficient with $\Pi + T_u$ from near the wall at $y^+ = 12$ till $y/\delta = 1$. This is explained by the mathematical formulation of the sweeping decorrelation hypothesis which is explained by the anti-alignment of the local and convective acceleration terms in the channel flows. However, the physical explanation of the sweeping decorrelation hypothesis involving large scale structures and small scale structures is reasonable away from the wall. Near the wall, it is mostly due to the $A_t + A$ balancing the $\Pi + T_u$ resulting in the high correlation coefficient between them.

T_p has a correlation coefficient of 0.35 with P_r at $y^+ = 12$ and it reduces to 0.2 with the increase of wall distance and becomes negligible at the centre-line of the channel. T_p has approximately 0.4-0.45 correlation with $\Pi + T_u$ from $y^+ = 40$ till the centre-line of the channel at $y/\delta = 1$.

The increase of Reynolds number resulted in the increase of correlation coefficient between $A_t + A$ and $\Pi + T_u$, which is noticeable from $y^+ = 12$ till the centre-line of the channel. On the other hand, the increase of Reynolds number results in the reduction of the correlation coefficient between T_p and $\Pi + T_u$ when $y^+ > 100$.

At small scales, the $A_t + A$ has a high correlation coefficient with T_u and T_p has a high correlation coefficient with Π. As the scale increases and reaches the integral scales, the correlation coefficient of both the energy transfer terms Π and T_u, with $A_t + A$ becomes approximately equal. This is also the same observation between T_p and both the energy transfer terms. And the sum of two energy transfer terms $\Pi + T_u$ has an even higher correlation with $A_t + A$ and T_p, than the individual terms Π and T_u separately. This high correlation coefficient of both the energy

transfer terms with $A_t + A$ and T_p reflects the relation between the non-linear term and time derivative term, and non-linear term and the pressure term in the Navier-Stokes' equation. This argument that the non-linear term is causing this correlation coefficient is solidified by the fact that the correlation coefficient between $A_t + A$ and T_p is negligible at all wall distances except near the wall.

When the correlation coefficient is computed for very large scales ($r = 9\delta$), the correlation coefficient results of both the energy transfer terms with $A_t + A$ and T_p remained the same, despite the length scale being several orders of magnitude higher than the integral scales. This is investigated further by decomposing Π to find that the correlation coefficient between Π and $A_t + A$. The result of the correlation coefficient is mainly due to the δu_1 and $\frac{\partial}{\partial x_j}(\delta u_1)$ which needs further investigation. The investigation of decomposing Π and T_p did result in showing that the terms involving δu_1 and $\frac{\partial}{\partial x_j}(\delta u_1)$ are dominant, but with correlation coefficient is not significant enough to make a reasonable conclusion. Thus the interscale energy cascade depends mainly on the δu_1 and $\frac{\partial}{\partial x_j}(\delta u_1)$ for its instantaneous dynamics in the flow.

5.3 Scale-by-scale energy budget with TBL550

The objective of the present work includes studying the behaviour of the KHMH equation terms in Turbulent Boundary Layer (TBL) using PIV experiments at high Reynolds numbers, $Re_\tau = 2272$ and 3840. In that regard, the results from the previous sections have given the basic idea of what to expect from the wall-bounded turbulent flows, specifically for turbulent channel flows. To proceed towards the experiment, it is necessary to know the behaviour of KHMH equation terms specifically with ZPG-TBL flows. To facilitate the comparison with the results of turbulent channel flow, the $Re_\tau = 550$ is chosen to study the DNS of TBL flow.

5.3.1 Spatio-temporal average values of KHMH equation terms

The first step in the process of comparing in the present analysis is to compare the average value of KHMH equation terms between TCF550 and TBL550. Since the two flows are at the same Reynolds number Re_τ, it is decided to compare them in terms of distances normalised by wall-units. Five wall distances, $y^+ = 12, 40, 100, 400, 550$ are chosen for the comparison between the two flows. And all the averaged values of terms of the KHMH equation are normalised by the absolute

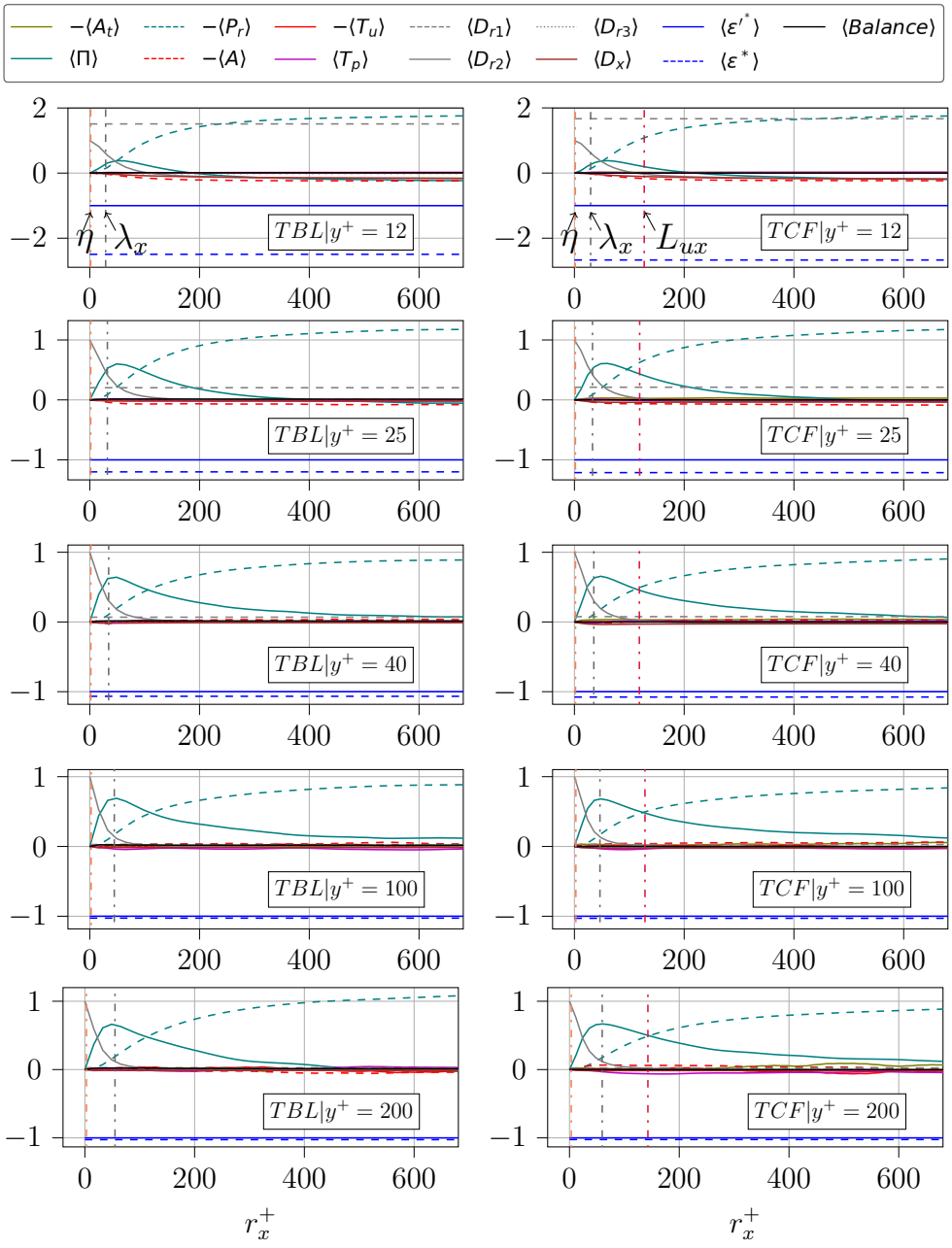

Figure 5.19: Spatio-temporal averaged values of all KHMH equation terms normalised by the absolute value of $\langle \epsilon'^* \rangle$ in the streamwise direction in TBL550 (left) and TCF550 (right) at various wall distances. The wall distances and the x-axes are normalised by wall-units

value of $\langle \epsilon'^* \rangle$.

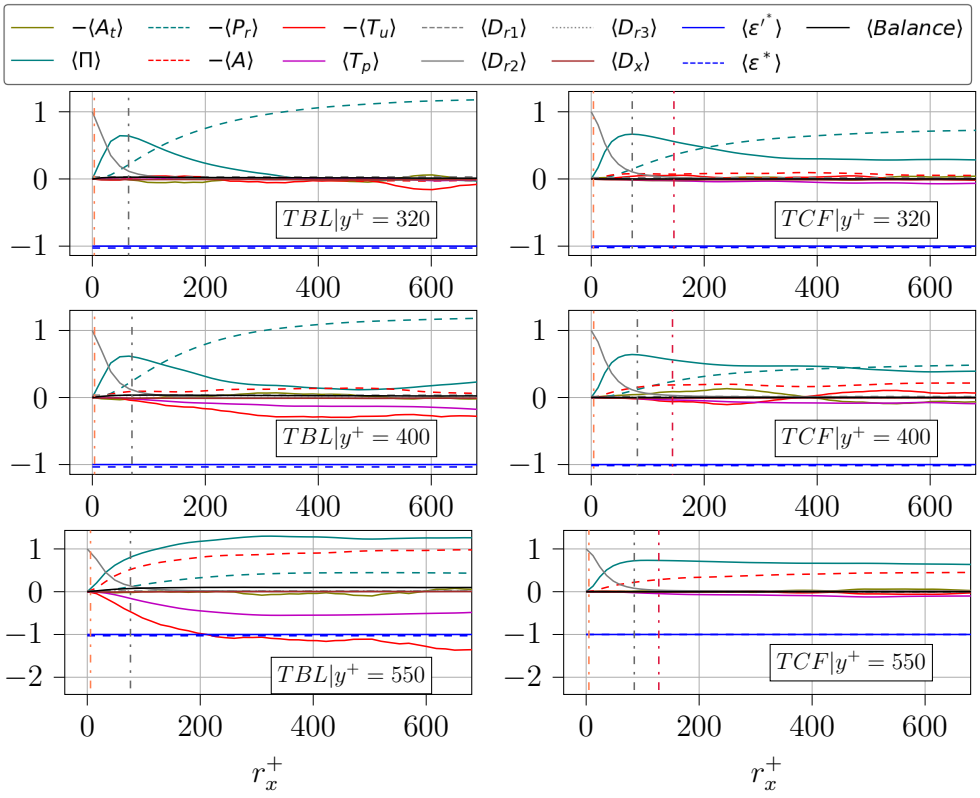

Figure 5.20: Spatio-temporal averaged values of all KHMH equation terms normalised by the absolute value of $\langle \epsilon'^{*} \rangle$ in the streamwise direction in TBL550 (left) and TCF550 (right) at various wall distances. The wall distances and the x-axes are normalised by wall-units

Observation

Figure 5.19, 5.20, 5.21 and 5.22 shows the average behaviour of KHMH equation terms compared between TBL550 and TCF550 in the streamwise and spanwise direction. The behaviours of each of the terms of the KHMH equation in both r_x and r_z directions are similar between the two flows from $y^+ = 12$ till $y^+ = 100$. This includes negligible or zero $-\langle A_t \rangle$, $-\langle A \rangle$, $-\langle T_u \rangle$, $\langle D_x \rangle$ and $\langle T_p \rangle$. This is followed by dominant values of $-\langle \Pi \rangle$, $-\langle P_r \rangle$, $\langle \epsilon^{*} \rangle$ and $\langle \epsilon'^{*} \rangle$, with the addition of $\langle D_{r2} \rangle$ at only small scales away from the wall.

Between $y^+ = 400$ and $y^+ = 500$, there is a difference in the behaviours of the KHMH equation terms in the two flows. In TCF550 in both r_x and r_z directions, $-\langle P_r \rangle$ do start from zero and attains a peak value as the scale increases and decrease thereafter with further increase of scales. However with TBL550, $-\langle P_r \rangle$ stay higher than $\langle \epsilon'^{*} \rangle$ at all scales larger than 300^+ for r_x direction, and 100^+ for r_z direction.

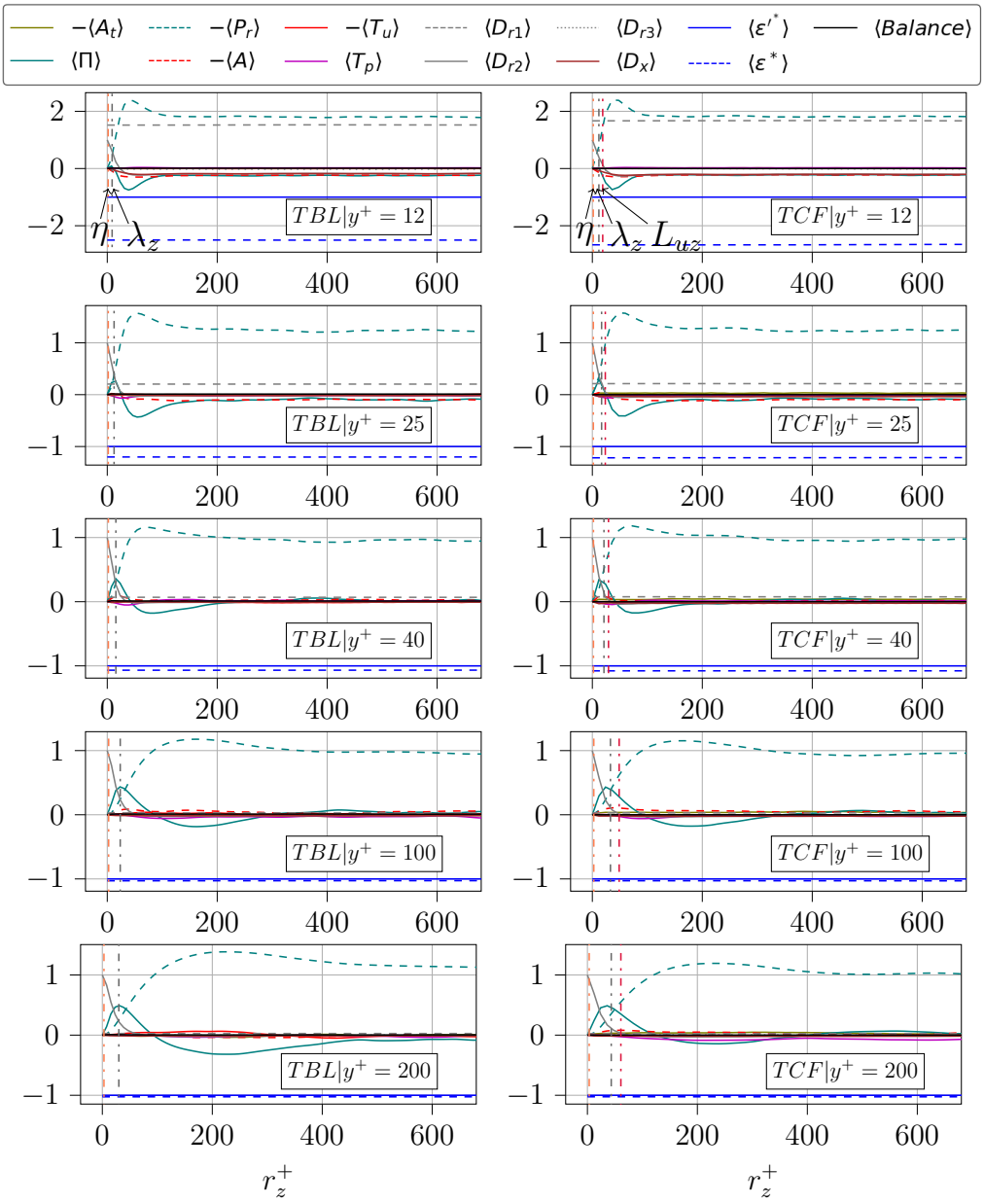

Figure 5.21: Spatio-temporal averaged values of all KHMH equation terms normalised by the absolute value of $\langle \epsilon'^* \rangle$ in the spanwise direction separation in TBL550 (left) and TCF550 (right) at various wall distances. The wall distances and the x-axes are normalised by wall-units

At $y^+ = 550$, the production term has negligible average for TCF550. However for TBL550 $y^+ = 550$, and $-\langle P_r \rangle$ has a non-zero average.

The interscale energy transfer term $-\langle \Pi \rangle$ behaves similarly between TCF550 and

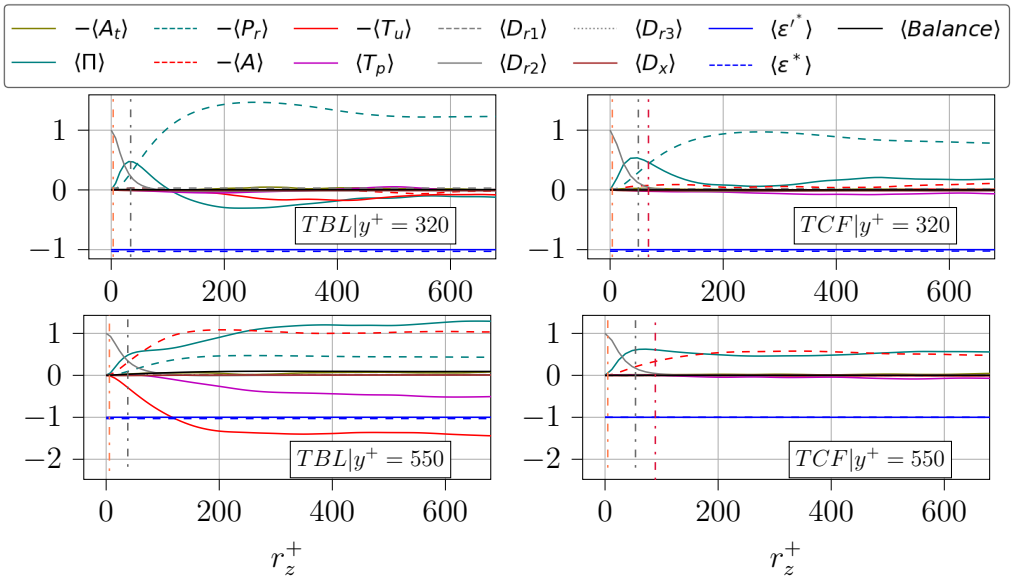

Figure 5.22: Spatio-temporal averaged values of all KHMH equation terms normalised by the absolute value of $\langle \epsilon'^* \rangle$ in the spanwise direction separation in TBL550 (left) and TCF550 (right) at various wall distances. The wall distances and x-axes are normalised by wall-units

TBL550 from near the wall till approximately $y^+ = 200$. $-\langle \Pi \rangle$ in TCF550 at $y^+ = 400$ is dominant from modified Taylor microscale till $r^+ = \delta$ in both directions. However for TBL550 at $y^+ = 400$, $-\langle \Pi \rangle$ after being dominant near modified Taylor microscale becomes negligible thereafter the scale increases in both r_x and r_z directions. At $y^+ = 550$, $-\langle \Pi \rangle$ even surpasses $\langle \epsilon'^* \rangle$ in both r_x and r_z directions in TBL550, but it stays approximately $0.5\langle \epsilon'^* \rangle$ for TCF550 at large scales.

At $y^+ = 550$, $-\langle A \rangle$ surpasses $\langle \epsilon'^* \rangle$ at large scales in TBL550. In addition, $-T_p$ reaches approximately $0.5\langle \epsilon'^* \rangle$ at large scales in TBL550. Both of these terms have a negligible Spatio-temporal average in TCF550 at all wall distances considered. $-\langle T_u \rangle$ is non-negligible at large scales from $y^+ = 400$ and reaches approximately -0.5ϵ'^* in the centre-line of the channel. In TBL550 $-\langle T_u \rangle$ tends to be approximately to $\langle \epsilon'^* \rangle$ at large scales in TBL550.

Discussion

The behaviours of the KHMH equation terms in TCF550 and TBL550 are approximately the same from $y^+ = 12$ till $y^+ = 100$. $-\langle P_r \rangle$ surpasses $\langle \epsilon'^* \rangle$ in the buffer layer where there is an excess of production. With the increase of wall distance, $-\langle P_r \rangle$ becomes approximately equal to $\langle \epsilon'^* \rangle$ at large scales. However at $y^+ = 400$,

$-\langle P_r \rangle$ again surpasses $\langle \epsilon'^* \rangle$. This sudden increase of $-\langle P_r \rangle$ meant that the energy transfer terms $-\langle \Pi \rangle$ and $-\langle T_u \rangle$ are negligible at larger scales at this wall distance to balance the KHMH equation for $\langle \epsilon'^* \rangle$. In addition in the r_z direction, there is a presence of negative values of $-\langle \Pi \rangle$ term till $y^+ = 320$, which in continuation with the explanation from the previous section shows the path in which the excess energy from the buffer layer reaches the larger scales with the increase of wall distance.

At $y^+ = 550$ in TBL550, multiple KHMH terms contribute to the dynamics of the turbulent flow. Both the energy transfer terms are dominant at large scales reach approximately equal to $\langle \epsilon'^* \rangle$. In addition, there is a high contribution from $\langle T_p \rangle$ and $\langle A \rangle$, which were negligible at all wall distances in both the channel flows.

Interscale energy transfer scaling with modified Taylor microscale

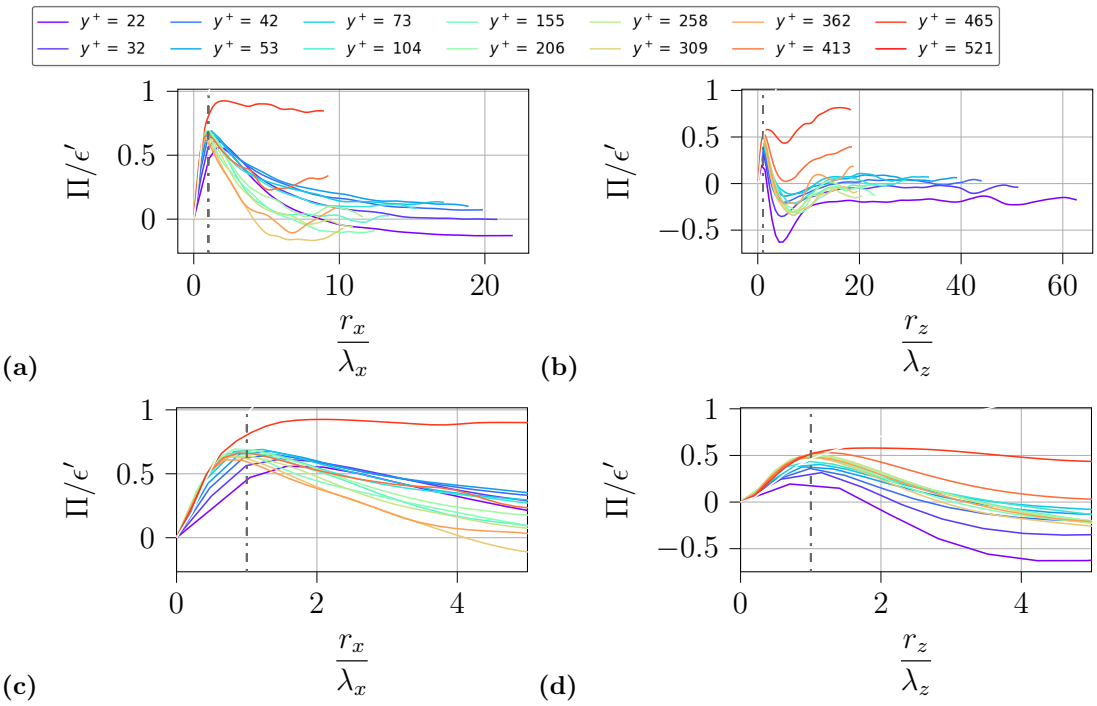

Figure 5.23: Spatio-temporal average of interscale energy transfer term normalised by the absolute value of $\langle \epsilon'^* \rangle$ at different wall distances for TBL550 **(a)** in the streamwise direction, **(b)** in the spanwise direction. **(c)**,**(d)** Same as (a),(b) but x-axis zoomed in the region near $r_x = \lambda_x$ and $r_z = \lambda_z$ respectively

In the previous section with the results of two channel flows, it is observed that the positive peak value of $-\langle \Pi \rangle$ coincides with the modified Taylor microscale

computed at that wall distance corresponding to each direction. This subsection focuses on the modified Taylor microscale with $-\langle\Pi\rangle$ in TBL550.

Figure 5.23 shows the behaviour of $-\langle\Pi\rangle$ normalised by the absolute value of $\langle\epsilon'^*\rangle$, with the x-axis being the scale-space separation normalised by the modified Taylor microscale at each wall distance. The top plots show the full extent of the term in both r_x and r_z directions and the bottom plots are a zoom near the modified Taylor microscale in both directions. In the streamwise direction, the positive peak of $-\langle\Pi\rangle$ coincides with λ_x in the range $42 < y^+ < 465$, and in the spanwise direction, it is in the range $22 < y^+ < 465$. This is approximately the same observation in the channel flows.

Conclusion

The conclusions in this subsection are as follows. The TCF550 and TBL550 are part of the family of canonical wall-bounded turbulent flows which tend to have the same behaviour for the terms of the KHMH equation until $y^+ < 100$. As the wall distance is increased further, $-\langle P_r\rangle$ surpasses $\langle\epsilon'^*\rangle$ at $200 < y^+ < 400$ at large scales in TBL550, however, $\langle P_r\rangle$ always stays lower than $\langle\epsilon'^*\rangle$ at all scales in TCF550 when $y^+ > 100$. In the spanwise direction, for some scales $-\langle\Pi\rangle$ is negative in the same region as the production surpasses dissipation, which is similar between the TCF and TBL flows. This could be explained by the transfer of excess production towards the large scales away from the wall.

At $y^+ = 550$, $-\langle\Pi\rangle$ and $-\langle T_u\rangle$ attain approximately equal or higher than $\langle\epsilon'^*\rangle$ in TBL550, whereas $-\langle\Pi\rangle$ and $-\langle T_u\rangle$ attain approximately $0.5\langle\epsilon'^*\rangle$ in TCF550. In addition, there is a high contribution from the $\langle T_p\rangle$ and $\langle A\rangle$ from $y^+ = 400$ to $y^+ = 550$ in TBL550, and they are both negligible in TCF550 at $y^+ = 550$. These are explained by the difference in flow physics between TCF and TBL flows at $y/\delta = 1$.

The modified Taylor microscale does scale the peak of $-\langle\Pi\rangle$ in the range $40 < y^+ < 465$ in the r_x direction, and it is in the range $22 < y^+ < 465$ in the r_z direction, which is similar to what was observed from the channel flows.

5.3.2 Instantaneous KHMH equation

With the average behaviour of KHMH equation terms discussed in the previous subsection, the next step in this process is to discuss the instantaneous behaviour of the KHMH terms. This subsection presents the results of the standard deviation

of KHMH equation terms in TBL550 and is then compared with that of TCF550. The same wall distances as the previous subsection will be used for the comparison.

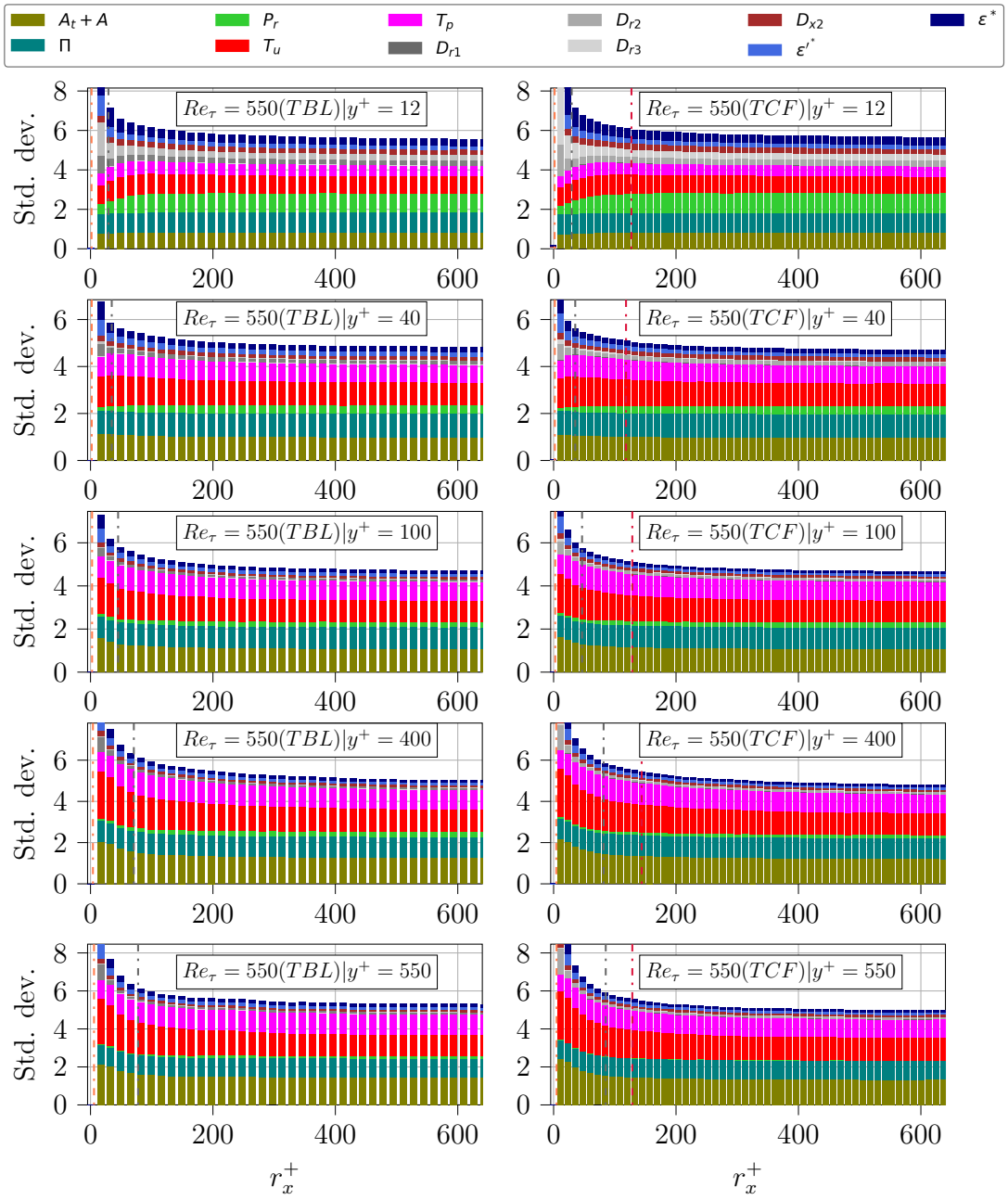

Figure 5.24: Standard deviation of all KHMH terms of TBL550 (left) and TCF550 (right). This is presented in the streamwise direction separation, where the x-axis and the wall distances are normalised by the wall-units

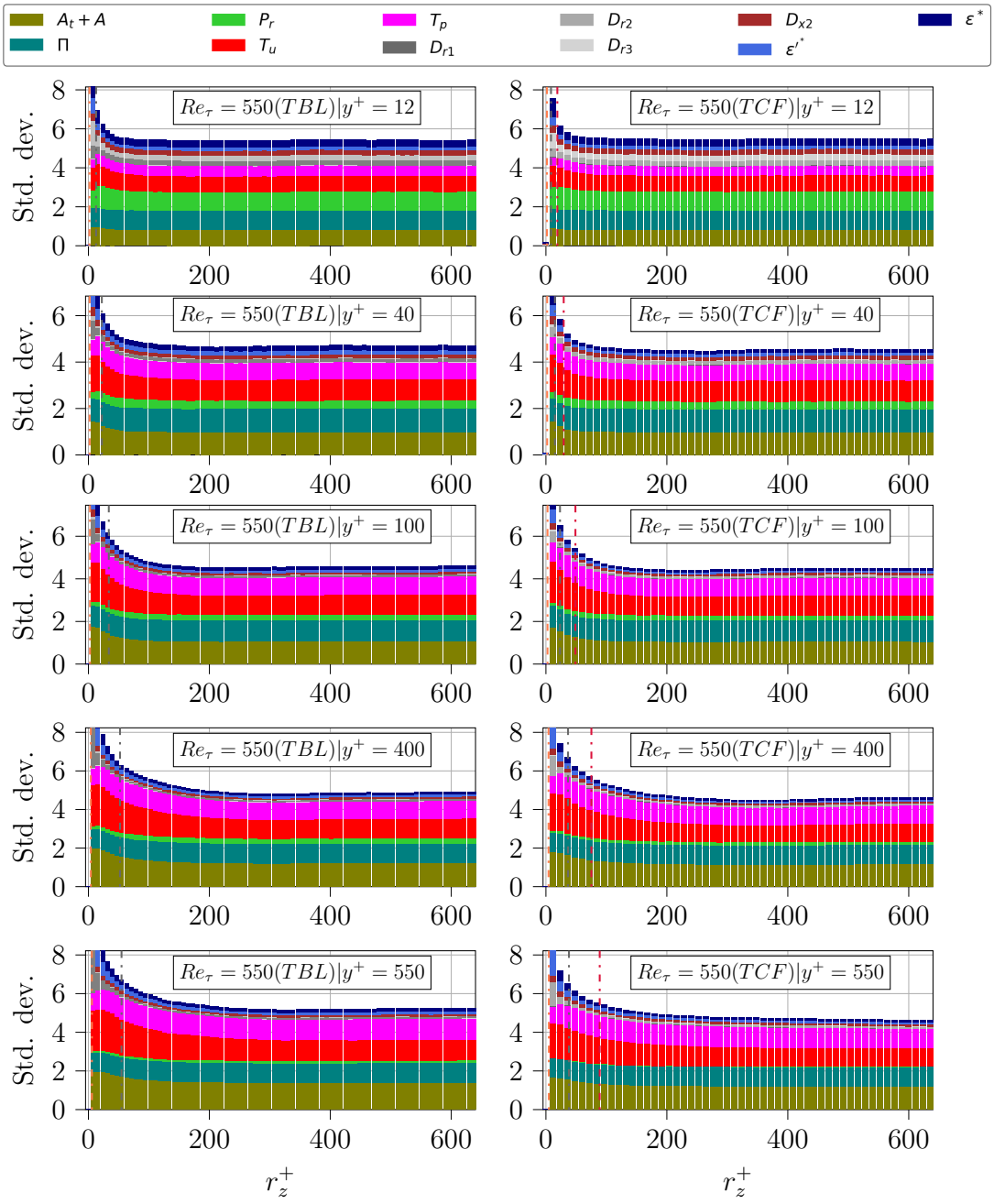

Figure 5.25: Standard deviation of all KHMH terms of TCF at $Re_\tau = 550$ (left) and TBL at $Re_\tau = 550$ (right). This is presented in the spanwise direction separation, where the x-axis and the wall distances are normalised by the wall-units

Observation

Figure 5.24 and 5.25 shows the standard deviation of all the terms of the KHMH equation in both TBL550 and TCF550, in the streamwise and spanwise direction separation respectively. The standard deviation of each of the terms is normalised by the standard deviation of the interscale energy transfer term, similar to the corresponding results from the previous section.

In both the flows, the diffusion and the dissipation have considerable standard deviation near the wall at approximately all the scales. These terms are also dominant between the Kolmogorov scale and the modified Taylor microscale at all wall distances. The standard deviation of ϵ^* is higher than ϵ'^* at $y^+ = 12$.

P_r term is dominant at $y^+ = 12$ in both TBL550 and TCF550. With the increase of wall distance, the standard deviation of P_r reduces and it becomes negligible at the centre-line of the channel for TCF550. However, in TBL550 the standard deviation of P_r is not entirely negligible at the edge of the boundary layer. The standard deviation of $A_t + A$, Π, T_u and T_p are all dominant from $y^+ = 12$ till the centre-line for the TCF550 and the edge of the boundary layer for TBL550. All the observations are valid in both r_x and r_z directions.

Discussion

It is already discussed in the previous section about the near-wall dynamics at all scales, and small scale dynamics at all wall distances being dominated by the diffusion and the dissipation terms in the two channel flows at different Re_τ. The explanation that the diffusion and dissipation terms balance each other at small scales at all wall distances is equally valid for the turbulent boundary layer flows. In addition, the smaller value of the standard deviation of Π at small scales could also contribute to the high values of the standard deviation of these terms at all wall distances.

The same reason as the buffer layer being considered the engine of turbulent fluctuations is valid for both Turbulent Channel Flows and Turbulent Boundary Layer flows at $y^+ = 12$. The reduction of the standard deviation of production term thereafter with the increase of the wall distance is explained by the mean velocity gradient in the wall-normal direction. However, this standard deviation is zero for the TCF550 at $y^+ = 550$, whereas it is non-zero for TBL550 could be explained by the difference of physics of both these flows at that wall distance. For channel flows, at the centre-line the mean velocity is at its maximum and is symmetric from

both top and the bottom wall, thereby resulting in a zero mean velocity gradient in the wall-normal direction. For TBL flows, $y^+ = 550$ is approximately the turbulent extent of the flow in the wall-normal direction. It is not a strict boundary and therefore it fluctuates during the flow, and there are interactions between the outer laminar flow and turbulent part. This results in some evolution of mean velocity in the wall-normal direction at that wall distance, which could therefore explain the non-zero standard deviation of P_r.

The dominance of the standard deviation of $A_t + A$, Π, T_u and T_p follows the same explanation from the discussion in the previous section, which points out the anti-alignment of local and the convective acceleration in the channel flows[20]. The standard deviation of the pressure term being of the order of local and convective acceleration could have resulted in the correlation coefficient between T_p and $\Pi + T_u$ observed in the last section, however, more investigation is required in this direction to explain this observation.

Conclusion

In concluding this subsection, the instantaneous behaviour of the KHMH equation terms is mostly the same between the TCF550 and TBL550 at the same wall distance. This includes the behaviour of the diffusion and dissipation terms near the wall at all scales and in small scales at all wall distances. P_r has the same behaviour between the two flows from $y^+ = 12$ and it reduces similarly in both the flows when the wall distance is increased. At $y^+ = 550$ however, it becomes zero for TCF550 and it stays non-zero for TBL550. This is explained by the difference of physics of both the flows at that wall distance. The standard deviation of $A_t + A$, Π, T_u and T_p are dominant at all wall distances is partially explained by the anti-alignment of local and convective acceleration in these flows, and the dominance of pressure term needs further explanation.

5.3.3 Correlation coefficient of KHMH terms

With the average and the instantaneous behaviours of the KHMH equation discussed in the previous subsections, the next step in the present study is to compute the correlation coefficient of the KHMH equation terms with $A_t + A$ and T_p with TBL550. The results are then compared with the corresponding results of TCF550. This study is performed in the same wall distances as it was in the results in previous subsections.

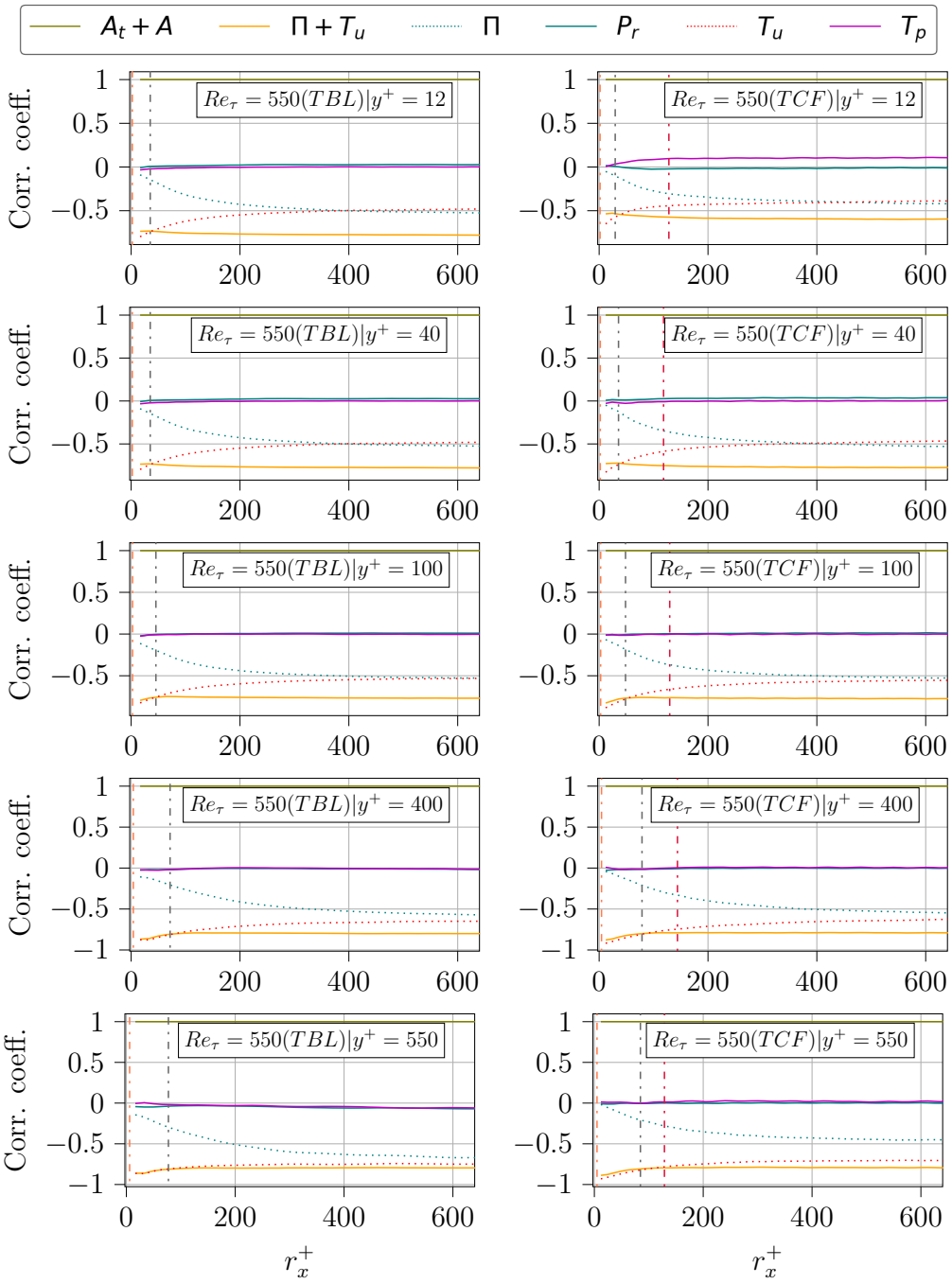

Figure 5.26: Correlation coefficient of the six KHMH terms with $A_t + A$ in the streamwise direction separation of TBL at $Re_\tau = 550$ (left) and TCF at $Re_\tau = 550$ (right). This is presented at various wall distances, where the x-axis and wall distances are normalised by wall-units

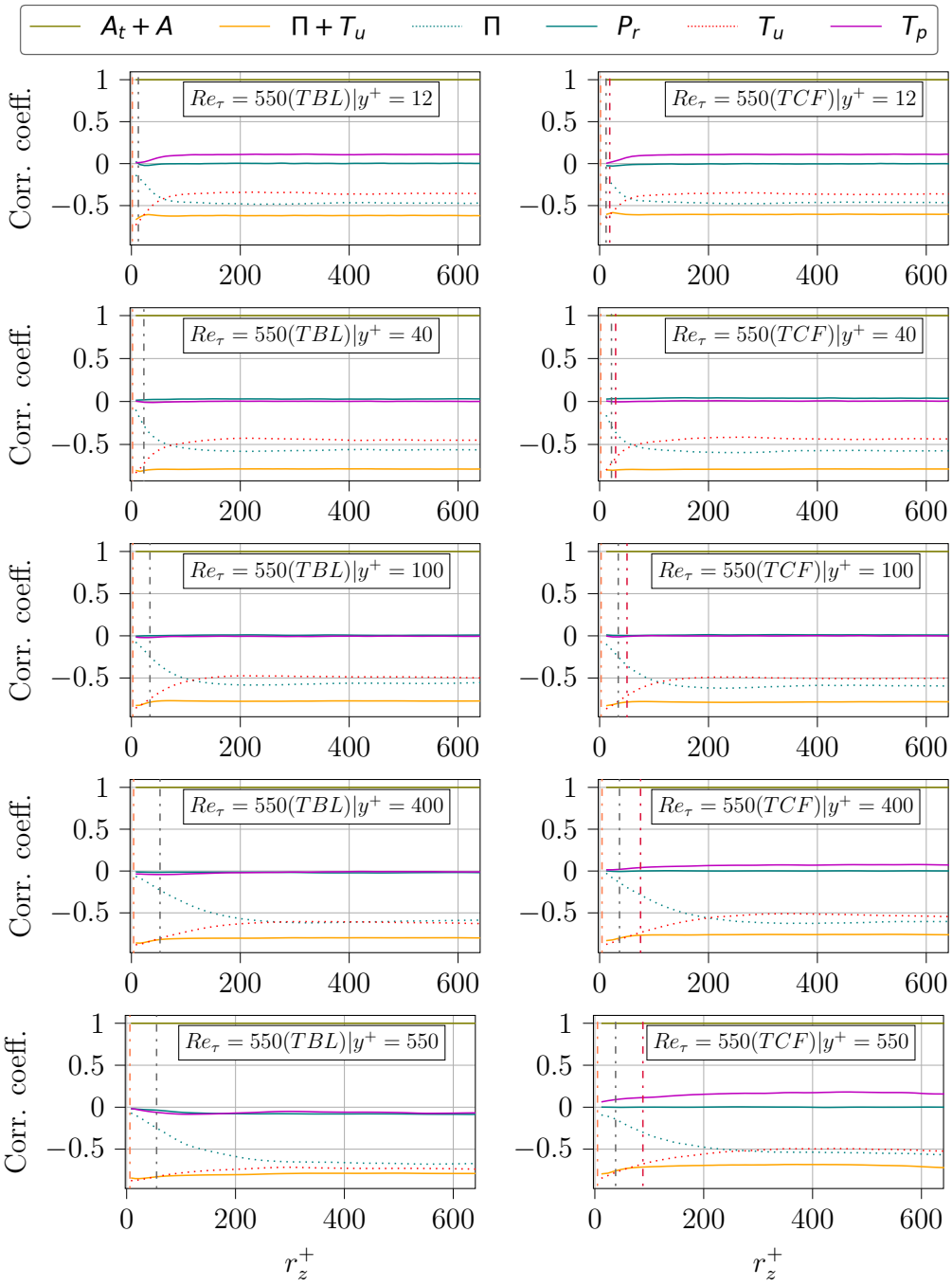

Figure 5.27: Correlation coefficient of the six KHMH terms with $A_t + A$ in the spanwise direction separation of TBL at $Re_\tau = 550$ (left) and TCF at $Re_\tau = 550$ (right). This is presented at various wall distances, where the x-axis and wall distances are normalised by wall-units

Observation : $A_t + A$ term

Figure 5.26 and 5.27 shows the correlation coefficient of $A_t + A$ term with other terms of KHMH equation between the two flows in r_x and r_z direction respectively. $T_p$has approximately 0.1 correlation with $A_t + A$ term at $y^+ = 12$. This becomes negligible with the increase of wall distance.

The correlation coefficient of Π with $A_t + A$ is zero at $r^+ = 0$ and tends to increase to reach -0.4 to -0.45 at large scales. This large scale correlation coefficient between Π and $A_t + A$ tends to increase with the increase of wall distance and reaches -0.6 to -0.65 at $y^+ = 550$. The correlation coefficient of T_u and $A_t + A$ starts around -0.6 at $r^+ = 0$ and decreases with 'r' to reach almost the same correlation coefficient as Π with $A_t + A$ at large scales. With the increase of wall distance, the correlation coefficient of T_u with $A_t + A$ at $r^+ = 0$ tends to reach approximately -0.8, and the large scale value reaches approximately -0.7 at $y^+ = 550$. The correlation coefficient of $A_t + A$ and the sum of two energy transfers $\Pi + T_u$ has a higher correlation coefficient of -0.5 to -0.8 at all scales and all wall distances in both the flows. All the above observations are similar between the r_x and r_z directions.

Observation: T_p term

Figures 5.28 and 5.29 shows the correlation coefficient of KHMH terms with T_p between the two flows in the streamwise and spanwise directions respectively. T_p has approximately 0.35-0.4 correlation with P_r at $y^+ = 12$, and this correlation coefficient tends to reduce with the increase of wall distance to 0.2 until $y^+ = 400$. At $y^+ = 550$, the correlation coefficient between T_p and P_r reach about 0.4 at large scales.

The correlation coefficient of T_p with Π around 0.45-0.5 at $r^+ = 0$ and has a peak at small scales and reduces its value as the scale increases to reach a value of 0.35-0.4 at large scales. With the increase of wall distance, this large scale correlation coefficient value increases to 0.55-0.6 at $y^+ = 550$. The correlation coefficient of T_p with T_u starts around 0.3 at $r^+ = 0$ and tends to increase with scale and reaches 0.35-0.4 at large scales. With the increase of wall distance, the large scale correlation coefficient reaches 0.5 at $y^+ = 550$. The correlation coefficient of T_p with the sum of two energy transfers $\Pi + T_u$ is approximately 0.55 at all scales above $y^+ = 40$ till $y^+ = 550$. All the observations are similar between the r_x and r_z directions.

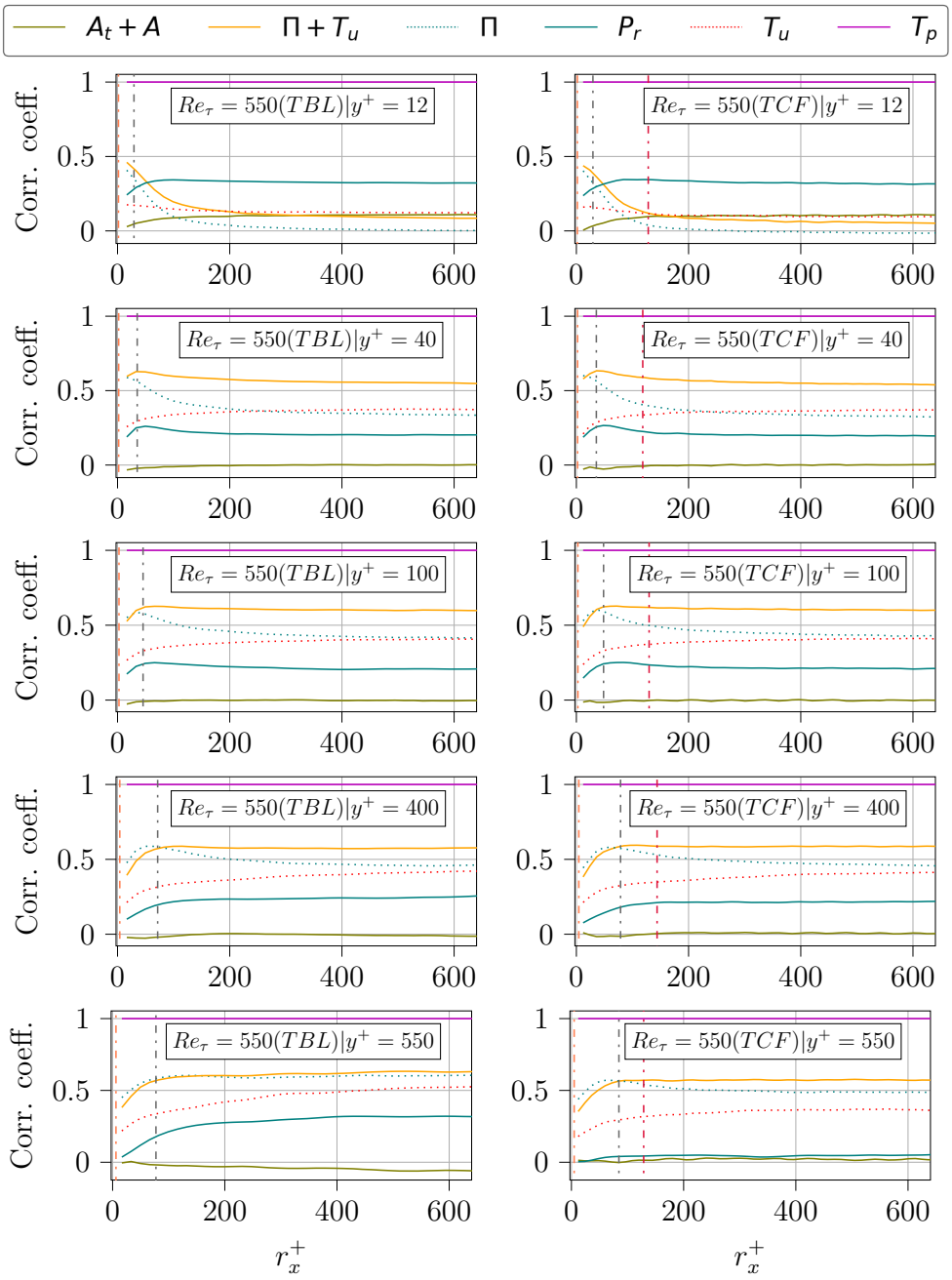

Figure 5.28: Correlation coefficient of the six KHMH terms with T_p in the streamwise direction separation of TBL at $Re_\tau = 550$ (left) and TCF at $Re_\tau = 550$ (right). This is presented at various wall distances, where the x-axis and wall distances are normalised by wall-units

Discussion

The correlation coefficient between the two energy transfer terms Π, T_u and the $A_t + A$ terms behave the same way between the TCF550 and TBL550 at all wall

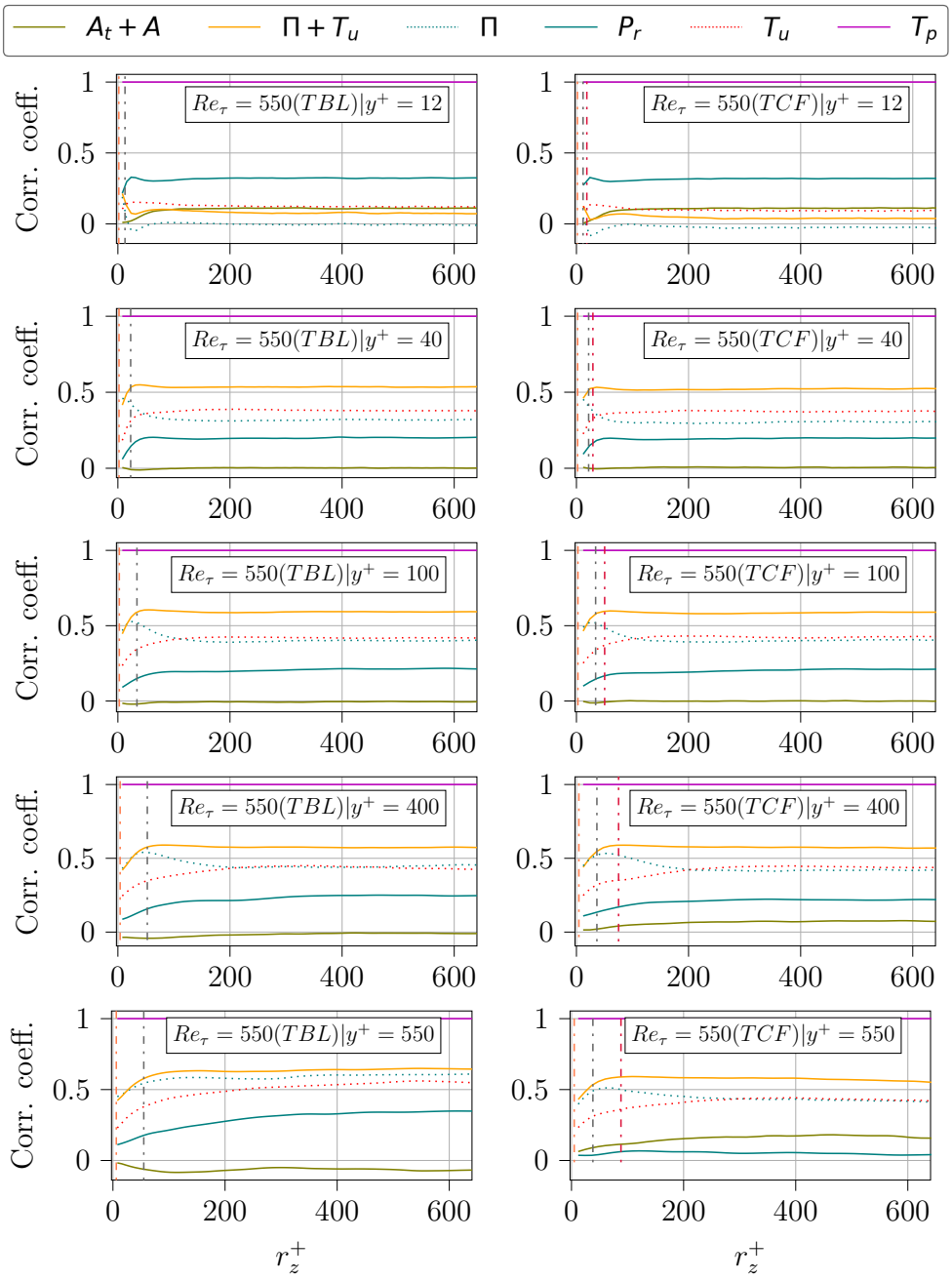

Figure 5.29: Correlation coefficient of the six KHMH terms with T_p in the spanwise direction separation of TBL at $Re_\tau = 550$ (left) and TCF at $Re_\tau = 550$ (right). This is presented at various wall distances, where the x-axis and wall distances are normalised by wall-units

distances from $y^+ = 12$ till $y^+ = 400$. At $y^+ = 550$, these correlation coefficients are higher in TBL550 than in TCF550. The results although with a small difference

still show the presence of the sweeping decorrelation hypothesis in both the flows. The high value of correlation coefficient at $y^+ = 550$ for both the energy transfer terms with $A_t + A$ in TBL550 could be explained by the fact that the average value of both Π and T_u are of the order of ϵ'^*. This shows the dominance of both the energy transfer terms at the edge of the boundary layer. By contrast, in channel flows, both the energy transfer terms never surpass or become equal to ϵ'^* at any scales or any wall distances considered in the present analysis. Despite the difference of flow physics at higher wall distances, the correlation coefficient between $A_t + A$ and $\Pi + T_u$ remains the same between the two flows at all wall distances in both r_x and r_z directions.

The correlation coefficient between T_p and the two energy transfer terms Π and T_u has a significant value from $y^+ = 40$ till the edge of the boundary layer. And the correlation coefficient values are similar between TCF550 and TBL550 from $y^+ = 12$ till $y^+ = 400$. At $y^+ = 550$, the correlation coefficient of both the energy transfer terms with T_p is above 0.5 at large scales. In the average value of the KHMH equation terms in TBL550, it is observed $-\langle P_r \rangle$ starts to become significant from $y^+ = 400$ in TBL550, and the average value of pressure term also reaches about the value of ϵ'^*, which could be attributed to the high correlation coefficient between the energy transfer terms and the pressure term. By contrast, the pressure term never had a significant average value at any scale and any wall distance considered in the present analysis in TCF550. The correlation coefficient between T_p and $\Pi + T_u$ also remains the same above $y^+ = 40$ till $y^+ = 550$ in both the flows, despite the difference in flow physics at higher wall distances.

The increase of correlation coefficient between the pressure term and the $A_t + A$ term in TCF550 only in r_z direction at $y^+ = 550$ is not observed in the TBL550 and TCF3000. So it could be termed as the artefact of the particular TCF550 simulation.

Conclusion

The correlation coefficients of both the energy transfer terms show the presence of the sweeping decorrelation hypothesis at all wall distances considered in the present analysis in TBL550, which is the same as TCF550. The correlation coefficient of both the energy transfer terms have significant values with the pressure term from $y^+ = 40$ till $y^+ = 550$ in both TCF550 and TBL550 flows. Thus the causal relationship between both the energy transfer terms and the $A_t + A$ term and T_p term is valid in TBL550 as it was valid in TCF550.

The correlation coefficient between $A_t + A$ and the energy transfer terms (Π, T_u) is higher in TBL550 than TCF550 at $y^+ = 550$. This is the same between T_p and the two energy transfer terms Π, T_u. This is explained by the difference in dynamics of the two flows at higher wall distances. Despite the change in flow physics at higher wall distances between the two flows, the large scale correlation coefficient of $\Pi + T_u$ with $A_t + A$, and $\Pi + T_u$ with T_p terms are approximately the same between TBL550 and TCF550.

5.4 Cascade of Energy

This section focuses on the different types of energy cascade that occurs in wall-bounded turbulent flows. This concept of energy cascade is central to the theory of turbulence, which started with the work of Richardson who proposed an energy cascade that is purely forward i.e., from large scales to small scales. In recent years, there have been hypotheses and also proofs based on the existence of inverse energy cascade, where the energy flows from small to large scales in some regions of the turbulent flows.

In both the channel flows and the turbulent boundary layer flow, $-\langle\Pi\rangle$ has a negative peak in the r_z direction, after the first positive peak at λ_z. This negative peak of $-\langle\Pi\rangle$ is observed between $y^+ = 12$ till approximately $y/\delta = 0.6$. This suggests that there is a possibility of an inverse energy cascade. Cimarelli et al. [22] discovered this behaviour of interscale energy transfer term average value of $\langle\Pi\rangle$ with the turbulent channel flow in the r_z direction for different wall distances. Cimarelli et al. [23] followed this up by explaining how the transfer of energy happens from the source to the sink in the turbulent channel flow with scale energy flux term $(\delta u_k(\delta u_i)^2)$ and proposed two sets of energy cascade : (a) attached reverse cascade and (b) detached forward cascade and divided the wall distances into different regions. This is followed by Alves Portela et al. [4] who showed that the necessary conditions to conclude the presence of inverse energy cascade are:

- positive value of scale energy flux in the radial direction (in cylindrical coordinates)
- positive value of interscale energy transfer term in the radial direction (in cylindrical coordinates)

The scale energy flux in the radial direction (in cylindrical coordinates) is given by:

$$\frac{\delta\vec{u}.\vec{\rho}}{|\vec{\rho}|}(\delta u_i^2) = \frac{1}{|\vec{\rho}|}(\delta u_\rho(\delta u_i^2)) \tag{5.9}$$

where δu_ρ is the structure-function in the radial direction The divergence of a function ϕ from cartesian coordinates to cylindrical coordinates is given by:

$$\frac{\partial \phi_x}{\partial x} + \frac{\partial \phi_y}{\partial y} + \frac{\partial \phi_z}{\partial z} = \frac{1}{\rho}\frac{\partial(\rho\phi_\rho)}{\partial \rho} + \frac{1}{\rho}\frac{\partial \phi_\theta}{\partial \theta} + \frac{\partial \phi_z}{\partial z} \tag{5.10}$$

The radial component is given by the first term on the right-hand side. The interscale energy transfer term in the radial direction is given by:

$$\begin{aligned} \frac{\partial}{\partial r_j}(\delta u_j(\delta u_i^2))\bigg|_{radial} &= \frac{1}{\rho}\frac{\partial}{\partial \rho}((\rho)(\delta u_\rho \delta u_i^2)) \\ &= \frac{\partial(\delta u_\rho \delta u_i^2)}{\partial \rho} + \frac{1}{\rho}(\delta u_\rho \delta u_i^2) \end{aligned} \tag{5.11}$$

To visualise the energy cascades at different wall distances, it was decided to multiply both the interscale energy transfer rate in the radial direction Π_r and the scale energy flux in the radial direction $\delta u_r(\delta u_i)^2$, such that the result is positive, when the two individual terms are positive: This conditional average for the cascade of energy is given by :

$$\tilde{C}_{inverse} = \begin{cases} \langle \Pi_\rho \rangle & \text{if } \Pi_\rho > 0 \text{ and } \delta u_\rho(\delta u_i)^2 > 0 \\ 0 & \text{otherwise} \end{cases} \tag{5.12}$$

$$\tilde{C}_{direct} = \begin{cases} \langle \Pi_\rho \rangle & \text{if } \Pi_\rho < 0 \text{ and } \delta u_\rho(\delta u_i)^2 < 0 \\ 0 & \text{otherwise} \end{cases} \tag{5.13}$$

Observation

Figure 5.30, 5.31 shows the normalised conditional Spatio-temporal average of interscale energy cascade in radial direction $\langle \Pi \rangle / \langle \epsilon'^* \rangle$ for the three DNS datasets (TCF550,TCF3000 and TBL550) in $r_x - r_z$ plane for multiple wall distances from $y^+ = 12$ to $y^+ = 300$. Figure 5.32 shows the same for the three DNS datasets, but at $y/\delta = 0.72$ and $y/\delta = 1$. The present result concerns the scales at which direct and inverse cascade occurs. Since each cascade occurs in certain scales and we are interested in finding the scales at which inverse cascade occurs to explain other results, the observation is made only for scales at which inverse cascade happens. And the energy cascade is direct in all the remaining scales.

It is observed that in all the three DNS datasets, there is a region of inverse cascade in the small scale values of both r_x and r_z. As the wall distance increases at $y^+ = 25, 40$, the extent of the inverse cascade region grows in r_z direction, with TCF3000 having a larger range of all the datasets and it is restricted to small values

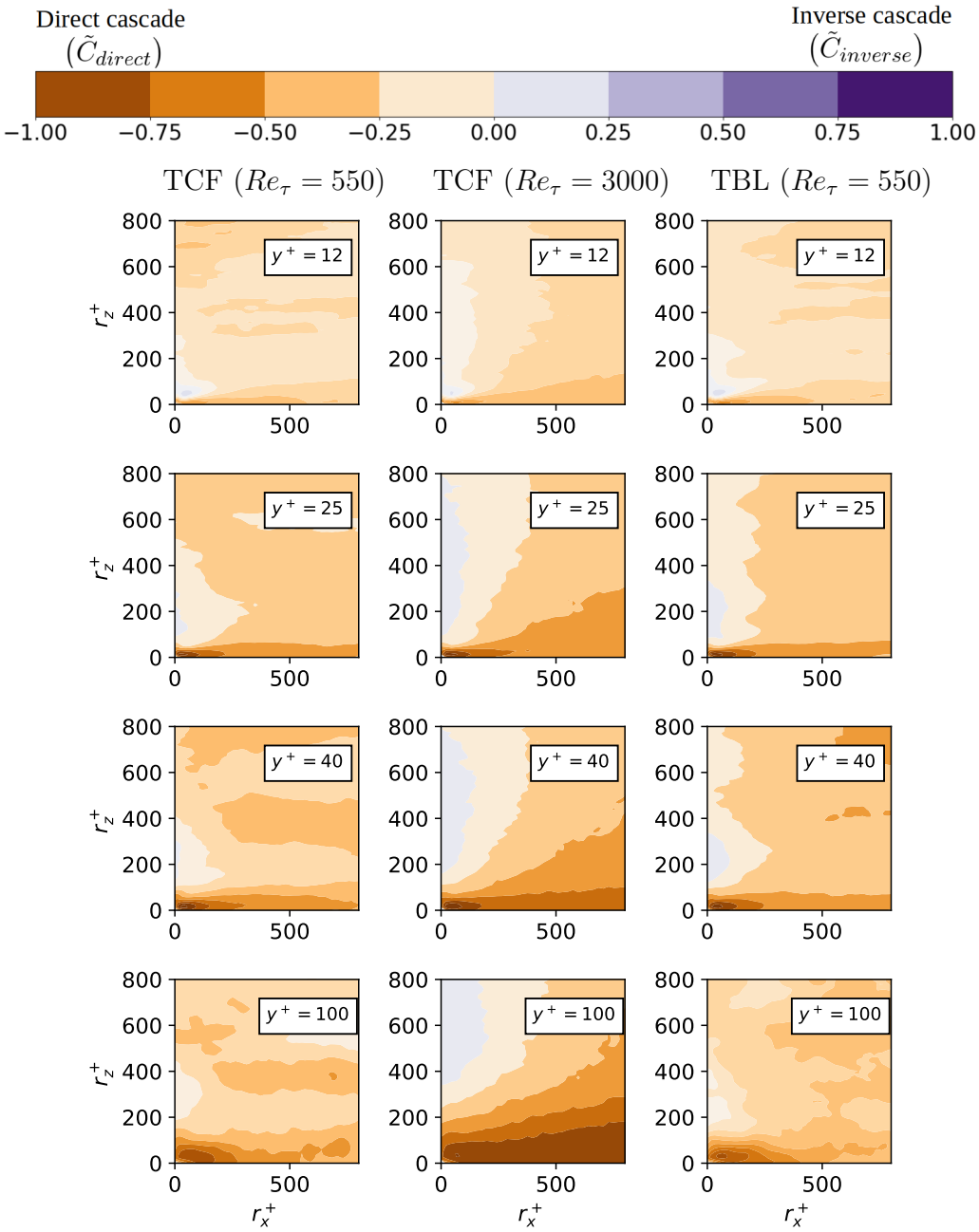

Figure 5.30: Direct and inverse cascade values in TCF550 (left), TCF3000 (middle) and TBL550 (right) in the streamwise-spanwise direction planes. The result is presented at different wall distances, where the x-axis and the wall distances are normalised by wall-units. $(\langle \Pi_\rho \rangle / abs(\langle \epsilon'^* \rangle)) > 0$: Inverse cascade. $(\langle \Pi_\rho \rangle / abs(\langle \epsilon'^* \rangle)) < 0$: Direct cascade.

of r_x. At $y^+ = 100$, the inverse cascade diminishes in both TCF550 and TBL550,

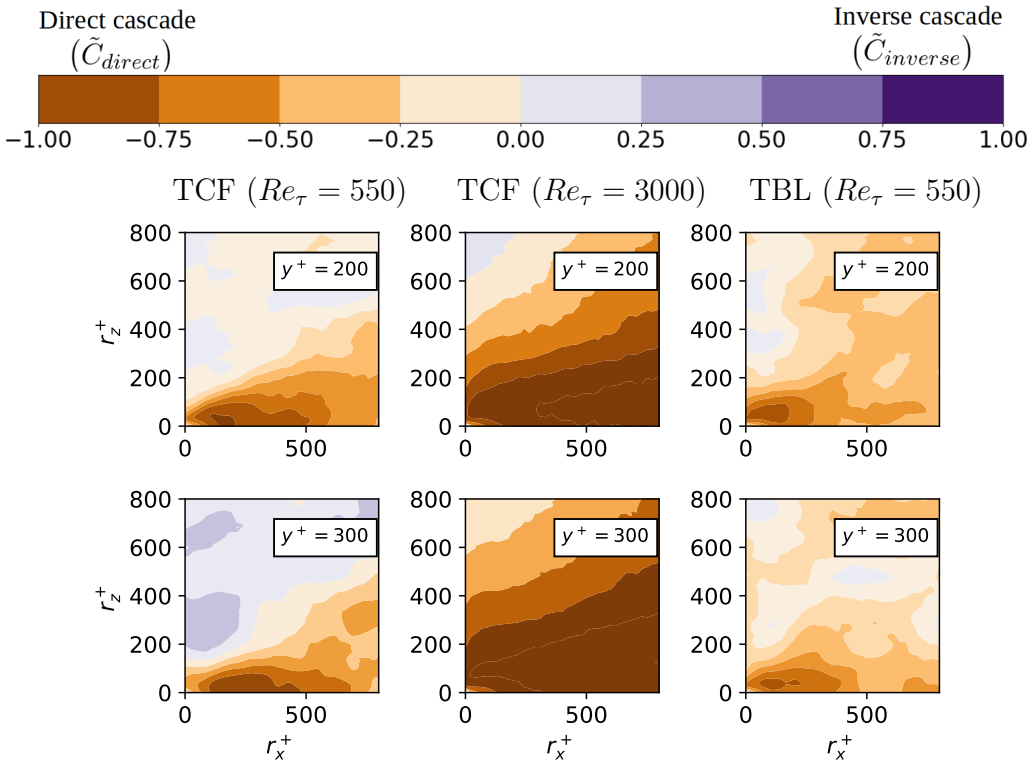

Figure 5.31: Direct and inverse cascade values in TCF550 (left), TCF3000 (middle) and TBL550 (right) in the streamwise-spanwise direction planes. The result is presented at different wall distances, where the x-axis and the wall distances are normalised by wall-units. $(\langle \Pi_\rho \rangle / abs(\langle \epsilon'^* \rangle)) > 0$: Inverse cascade. $(\langle \Pi_\rho \rangle / abs(\langle \epsilon'^* \rangle)) < 0$: Direct cascade.

on the other hand, it increases to higher r_z values in TCF3000. At $y^+ = 200$, the inverse cascade is found at higher values of r_z than it was in the previous wall distances in all three DNS datasets. In addition, the plots start to differ between the two Re_τ for the three flows, and so the remaining wall distances will be normalised by δ. At $y/\delta = 0.72$ and $y/\delta = 1$, the scales of forward and inverse cascade don't resemble the same between the three flows.

Discussion

From the results of the scales at which inverse cascade occurs, it is restricted to small values of r_x and r_z at the buffer layer in all three DNS datasets. This has been identified in the past as the scale energy source[22] in the buffer layer of the flow. With the increase of wall distance, the inverse cascade moves to higher scales in the spanwise direction, whereas it doesn't change appreciably in the streamwise

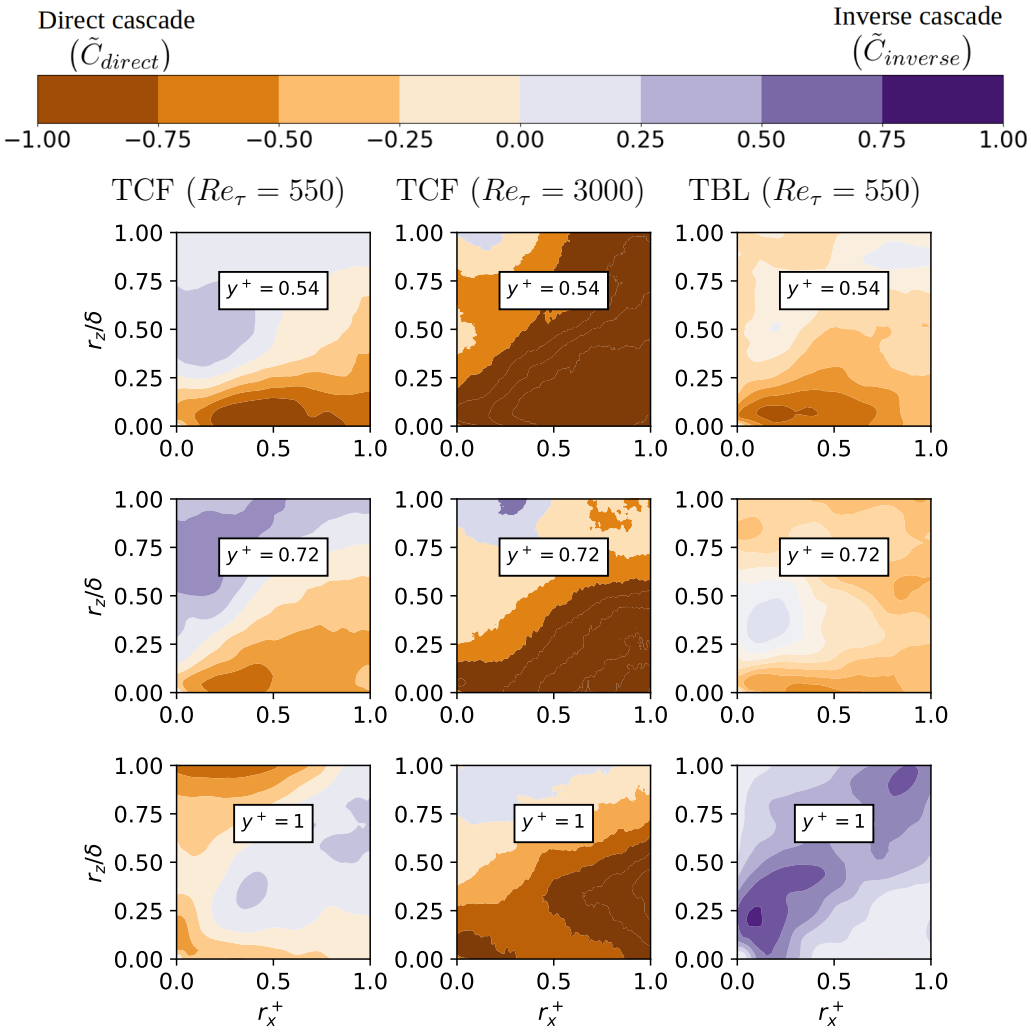

Figure 5.32: Direct and inverse cascade values in TCF550 (left), TCF3000 (middle) and TBL550 (right) in the streamwise-spanwise direction planes. The result is presented at different wall distances, where the x-axis and the wall distances are normalised by channel half-width or the boundary layer thickness. $(\langle \Pi_\rho \rangle / abs(\langle \epsilon'^* \rangle)) > 0$: Inverse cascade. $(\langle \Pi_\rho \rangle / abs(\langle \epsilon'^* \rangle)) < 0$: Direct cascade.

direction in all three flows. At $y^+ = 100, 200$, the scales of inverse and forward cascades are comparable between TCF and TBL at $Re_\tau = 550$, however it is not the same in TCF3000. Normalising the axes and the wall distance by δ for higher wall distances, the results are further different between the two flows.

Conclusion

The observation of inverse energy cascade points to the fact that the excess of energy from the buffer layer moves towards higher wall distances through increasing values of r_z, and this is observed to be similar between the three flows near the wall. There is an influence of the Reynolds number at $y^+ = 100, 200$ in the results.

5.5 Wall-attached eddies

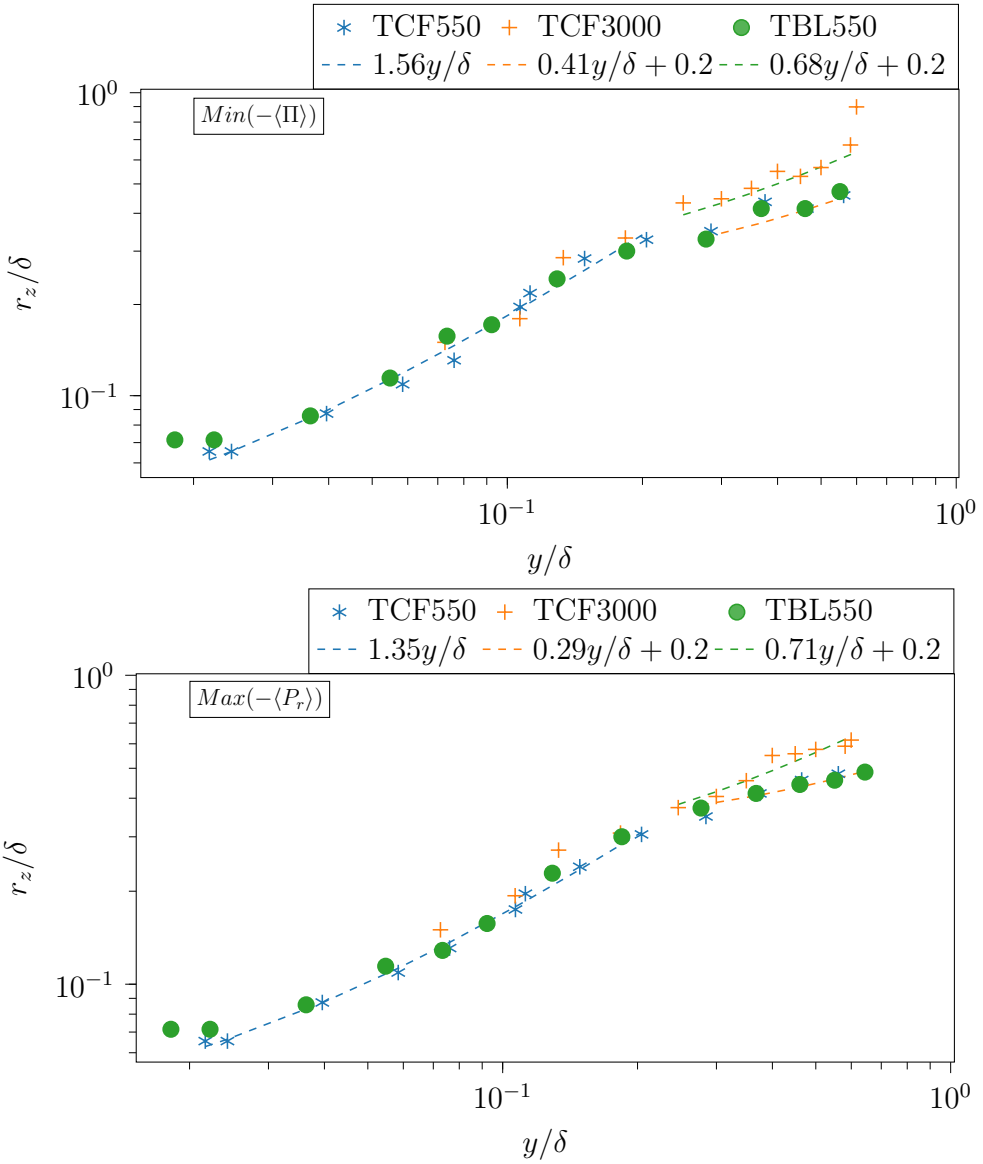

Figure 5.33: Peak value of $-\langle\Pi\rangle$ (top) and $-\langle P_r\rangle$ (bottom) in all three DNS datasets in the r_z direction at different wall distances. The wall distance and the x-axes are normalised by δ of each flow

5.5.1 Observation

From the results of the Spatio-temporal averaging of KHMH equation terms, it is observed that $-\langle\Pi\rangle$ and $-\langle P_r\rangle$ have negative and positive peaks respectively at the

same scales in the spanwise direction for various wall distances. And the scale at which the peaks occurred, increase with wall distance. This phenomenon suggests that the energy produced at the buffer layer tends to climb up the scale as the wall distance is increased to reach the turbulent core and eventually towards the centre-line of the channel flow, or the edge of the boundary layer. Cimarelli et al. [23] observed the same phenomenon in Turbulent Channel Flow where it is pointed out that a spatial reverse cascade occurs where the scale-energy ascends to the centre of the channel through a straight line in (r_y, r_z, y^+) space. This is confirmed in the last section that the energy produced in the buffer layer reaches a higher wall distance (inverse cascade) through the spanwise scales.

Figure 5.33 shows the scale position of the negative peak of $-\langle\Pi\rangle$ and the positive peak of $\langle P_r\rangle$. There are two distinct ranges observed in the plot : (a) $0.02 < y/\delta < 0.2$ and (b) $0.25 < y/\delta < 0.55$. In the first range, all the three DNS datasets tend to follow the same trend, which means that there is no effect of Reynolds number or the type of flow in this range near the wall. However, the second range is observed to have an effect of Reynolds number, in which both the TCF and TBL at $Re_\tau = 550$ belongs to one set of range and TCF at $Re_\tau = 3000$ belongs to a different range.

5.5.2 Discussion

From the analysis of the energy cascade phenomenon in the three wall-bounded turbulent flows, it is concluded that there is a strong inverse energy cascade in the buffer layer at small streamwise and spanwise scales, and from there, there is forward cascade into smaller scales and inverse cascade to the large scales of the flow. As the wall distance is increased the inverse cascade is present only for certain values of spanwise scales and for many values of streamwise scales.

By tracking the peak of the interscale energy transfer term and the production term, it is clear that the inverse energy cascade which moves the energy to larger scales as the wall distance is increased, and thereby is responsible for generating the Reynolds stress which results in an increase of the production term in the spanwise direction. This result is observed in the spanwise direction for $r_x^+ = 0$, and is almost not present in the streamwise direction for $r_z^+ = 0$. This is investigated by considering the value of these two terms normalised by the absolute value of $\langle\epsilon'^*\rangle$ in the $r_x - r_z$ plane, which shows that this phenomenon is also present in the streamwise direction for some non-zero values of r_z^+.

Hwang et al. [58] defines the wall-attached self-similar structures (WASS), which, in

the physical space, is closely related to the attached-eddy hypothesis introduced by Townsend [123] and later developed by Perry and Chong [91]. In this context, the WASS is defined as having length scales in the range $3Re_\tau^{\frac{1}{2}} \leq l_y^+ \leq 0.6\delta^+$. In addition, there is also another wall-attached u structures called buffer layer structures which are defined in the range $l_y^+ < 3Re_\tau^{\frac{1}{2}}$. Thus it can be concluded that the first part of the results where the peaks scale the same way for both the turbulent channel flows and the turbulent boundary layer flow is due to the buffer layer structures. And the second part of the results where the two turbulent channel flows and the turbulent boundary layer flow scales differently is due to WASS structures.

Part III

Overview of the PIV datasets and its analysis with KHMH equation

Chapter 6

PIV experiment

The primary goal of the present work is to solve the KHMH equation to obtain information about the scale-by-scale energy budget using experiments in the turbulent boundary layer. In this regard, it is necessary to know some information about the flow field beforehand such as the behaviour of the different terms of the KHMH equation, and for this reason, the analysis is started with a low Reynolds number ($Re_\tau = 550$) DNS of Turbulent Channel Flow. This DNS is chosen because it is closer to some related studies in the past[81,99], thereby validating the codes used for computation.

After validating the average behaviour of the KHMH equation terms with the studies from the past, the next step is to explore the physics behind the non-averaged part of the equation. This is studied by visualising the standard deviation. This is in turn followed by the computation of the correlation coefficient between the different terms of the KHMH equation. Since each term corresponds to a physical process in the energy cascade, any significant value of correlation coefficient between certain terms essentially reveals the correlation between physical processes associated with them.

After analysing the terms with the TCF at $Re_\tau = 550$, the next step was towards the objective to analyse the results at a higher Reynolds number. This is the reason behind choosing the DNS of TCF at $Re_\tau = 3000$ for the study. Various results so obtained from this flow is then compared with that of the previous DNS, by normalising the parameters accordingly *i.e.,* using wall distances normalised by wall-units for $y^+ < 200$, and using wall distance normalised by channel half-width for $y^+ > 200$.

It is known beforehand that the experiment will be performed on a ZPG TBL flow

in the wind tunnel. Hence to have a better idea of the type of results from the experiments, it is important to obtain the behaviour of the terms of instantaneous KHMH equation in the DNS of ZPG-TBL flow. This is made possible by the use of the DNS of ZPG-TBL at $Re_\tau = 550$, which corresponds to the same Re_τ of one of the lower Reynolds number DNS, which then helps to compare the results between them. This helps to identify the differences or similarities that occur between the two canonical wall-bounded turbulent flows.

The results obtained so far forms the base on which the PIV experiment on the ZPG TBL in LMFL is planned. The main results that would be obtained from the experiment are the Spatio-temporal averaged value of KHMH equation terms, the standard deviation and the correlation coefficient of the different terms in streamwise directions.

6.1 Particle Image Velocimetry

6.1.1 Planar PIV experiment

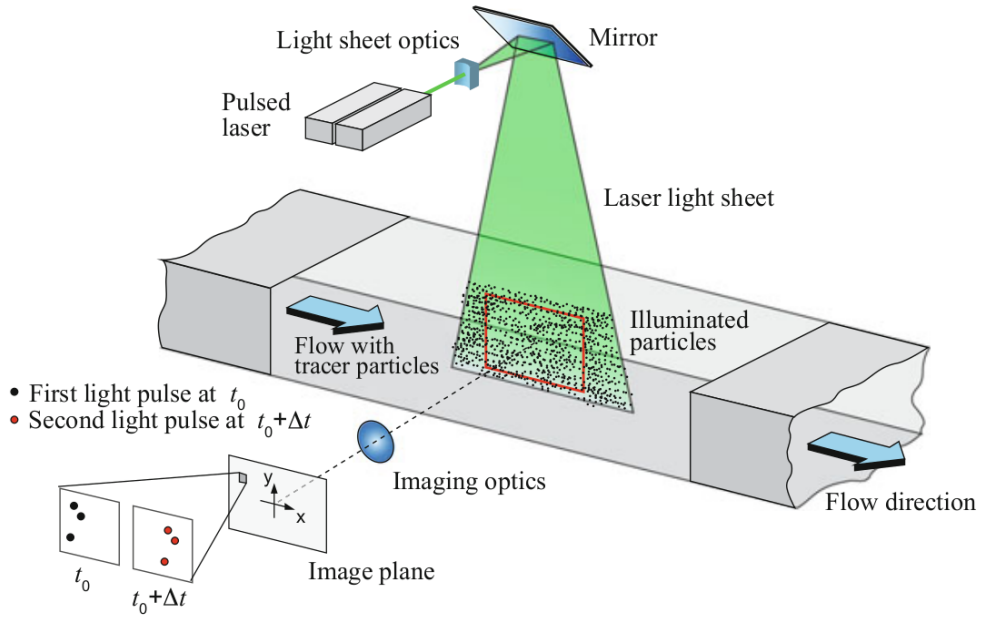

Figure 6.1: Experimental setup for Planar PIV (2C-2D) measurement

Particle Image Velocimetry (PIV) is an experimental technique used extensively in fluid mechanics research, which aims to obtain the velocity field in a plane or a volume of a fluid flow non-intrusively. For a Planar PIV measurement whose

experimental setup is given by Figure 6.1, the two components of velocity along a plane are measured which is made possible by a camera mounted orthogonal to the laser light sheet. The flow is seeded with tracer particle which is ideally the same density as the fluid itself, and so is expected to follow the fluid flow without any lag. This way of having neutrally buoyant tracers are possible in experiments in liquids flows where the many tracers available such as oils, oxygen bubbles, aluminium flakes, hollow glass spheres are used whose densities are approximately equal to that of water. For aerodynamic experiments, the closest to neutral buoyancy is achieved by the use of Helium-Filled-Soap-Bubbles (HFSB)[102]. Other commonly used tracers for airflows include oils, propylene glycols, glycerine water mixture, smoke, polystyrene etc, which aren't neutrally buoyant in air. To alleviate this problem of density difference, the particle sizes should be very small (of the order of μm) to ensure good flow tracing fidelity. However small particles scatter less light and it becomes difficult to distinguish between the particle and the background. Thus a compromise has to be reached between the two parameters. The motion of these particles is made visible by the illumination of a laser light sheet, which is obtained by expanding a laser light through an appropriate cylindrical lens. The images of the particles at specified time intervals are captured by the camera.

Before moving further into the discussion, it is important to discuss the imaging of the small tracer particles. When the light is scattered by the particle hits the circular aperture of the camera, it generates a far-field diffraction pattern which with the help of a lens gets imaged on the imaging sensor. Thus the image of the particle is recorded as a diffraction pattern, which cannot be changed even with a perfectly aberration-free lens[51]. The peak in the centre of the intensity distribution is called Airy's disk. This value of the radius of the Airy's disk is given by :

$$\frac{d_{diff} D_a}{2\lambda} = 1.22 \tag{6.1}$$

where 'd_{diff}' is the diffraction-limited image diameter, 'λ' is the wavelength of the light, 'D_a' is the diameter of the aperture. Considering the lens formula and substituting the definition of magnification factor, the diffraction-limited image diameter is given by:

$$d_{diff} = 2.44 f_{\#}(M+1)\lambda \tag{6.2}$$

where '$f_{\#}$' is the f-number of the lens, which is the ratio of focal length to the diameter of the aperture[47], 'M' is the magnification factor, which is the ratio of the object height to the image height. This diffraction-limited image diameter is relevant to particles at a small diameter. On the other hand, in experiments with

large particles, the geometric diameter of the particle is more dominant. Thus the following formula is a good estimate of the diameter of the particle[3]:

$$d_\tau = \sqrt{(M d_p)^2 + d_{diff}^2} \tag{6.3}$$

The use of PIV experiments for planar 2C-2D measurements has allowed studying complex flows due to its non-intrusive nature. However, having only two components of velocity in a plane seriously limits the number of spatial derivatives available from the experiments. To partially solve this problem, Stereoscopic PIV[7] is used. In this method, instead of one camera placed orthogonal to the laser light sheet, two cameras are placed at a certain angle to the light sheet and these images from both the cameras are then processed using stereoscopic cross-correlation methods to obtain all three components of velocity in a plane.

A calibration procedure is performed by using a calibration plate with crosses at known distances and is placed at the same place as the light sheet would be placed. The calibration plate is then translated in the plane perpendicular to the light sheet and the images are recorded by the cameras, to obtain the information in that direction. This process enables us to obtain the relation between physical distance in the object plane to distance in the image planes of the different cameras used in the experiment. The displacement of the particles between two successive time steps with the known time delay between the two images, and the information from the calibration helps to obtain the velocity vector field in a plane by using cross-correlation methods[63].

The spatial resolution of the vector field obtained from the cross-correlation method depends on the size of the interrogation window[61]. Thus decreasing the interrogation window size is a common procedure to increase the spatial resolution. However, this results in a reduction of the number of particles available for cross-correlation, thereby leading to random correlation peaks[62,93], random sub-pixel interpolation errors. On the other end, a large interrogation window provides a very accurate sub-pixel displacement and is robust provided the velocity gradient is small. With a large interrogation window, cross-correlation results in a smooth vector field, which has the possibility that the length scales corresponding to velocity fluctuations.

There have been many suggestions to improve the spatial resolution reported in the literature, which are the hybrid methods that combine the advantages of cross-correlation methods to obtain good pattern matching capabilities with very high particle yield. This is a common feature of PTV methods which involves tracking

individual particles in the flow. Keane et al.[61] proposed such a hybrid method with the name of super-resolution PIV, which has led to further development in this direction[25, 126, 59, 117, 131].

Scarano[100] implemented WIDIM (WIndow Deformation Iterative Multigrid) image distortion interrogation algorithm, which is based on the PID methodology proposed by Huang et al.[57], which is performed with the progressive refinement of interrogation window size. At first, PIV images are processed with cross-correlation with a large interrogation window size, which is usually based on some basic interrogation criteria such as the one-quarter rule. The result of this step is used as predictor displacement of all images. Based on the predictor, the two pairs of images are deformed. Each image is deformed for half of the displacement and so it is second-order accurate for the displacement in the intermediate position. Then based on the defined refinement step, the interrogation window size is reduced. The processing of the images then yields displacement with a fine spatial resolution, which allows obtaining the velocity vector field and this is then validated based on specified criteria. The resulting validated velocity vector field is either used as final output or as an iterative input to the previous steps where the interrogation process is repeated until the conditions for convergence are satisfied.

6.1.2 Tomographic Velocimetry measurement

In the preceding subsection, the progress of PIV experiments from Planar PIV which is a 2D-2C experiment to Stereoscopic PIV which returns a 2D-3C experiment is studied. Proceeding in this direction, the next step would be to have the information about the 3D flow field, which would enable to obtain all the possible derivatives of the velocity vector. This has been attempted in the past by Brücker[16] who used scanning light-sheet to reconstruct the 3D field around a short cylinder, by Maas et al.[79] who developed the digital 3D Particle Tracking Velocimetry (3D-PTV) method. This is followed by Tomographic PIV, introduced by Elsinga et al.[36, 101], as a solution to study the unsteady three-dimensional flows which are often found in turbulent flows. Relevant to the present work, there have been several studies in turbulent boundary layers by the Aerospace department in TU Delft, German company LaVision, German Aerospace Laboratory (DLR), the Fluid Mechanics lab of Lille in collaboration with Monash University (Elsinga et al.[32], Elsinga et al.[33], Elsinga and Marusic[34], Atkinson et al.[8], Schröder et al.[106], Schröder et al.[107], Schröder et al.[108]).

However, some disadvantages in using Tomo-PIV in obtaining the velocity field. As discussed previously, to achieve good spatial resolution, high seeding concentration

is necessary. This is possible in Tomo-PIV experiments, but the high concentration also results in ghost particles[35] during the reconstruction process. Additionally in Tomo-PIV, like that of planar PIV, the resulting vector field is always averaged value over the interrogation window (interrogation volume for Tomo PIV), and so it needs a bit of adaptation to account for the large gradients present in some regions of the flow[85]. The important and main drawback of Tomo-PIV is the high computation time and also the high volume of data stored during the acquisition.

These discussions point to the direction towards saving the position of the particles in time to obtain the velocity field directly without making any kind of spatial average. Thus it is the Lagrangian measurement, in which the computation time can be greatly reduced, which is the direct effect of the considerable reduction in the amount of data to be processed compared to the voxel space. This is the basis of the 3D Particle Tracking Velocimetry (3D PTV)[79], where particle positions are obtained by triangulation, and then to determine the matching particle in the next time-steps.

Schanz et al.[103] introduced the 'Shake The Box' (STB) method, which couples the IPR method[133] and an efficient way of using temporal information in a time-resolved PIV measurement. Thus this method combines the advantage of the IPR method, which is to processing highly seeded data and at the same time, tracking a large majority of real particles, at particle image densities higher than 0.1 particle-per-pixel (ppp). Schröder et al.[109] used the STB method to obtain all the components of Reynolds stress tensor close to the wall, and the instantaneous wall-shear stresses, which helps to prove the efficiency of this algorithm to capture the physics at regions with high velocity gradient. This method is extended in the direction of using multi-pulse measurements by Novara et al.[86], where it has been applied to the study of turbulent boundary layers[87], and has been used to study other flows such as flow over a laminar wing[42], subsonic jet at Mach number 0.84[80].

6.1.3 Two system S-PIV experiment

The present study requires an experiment of 4D (3D+time) velocity field and the pressure field to compute all the terms of the KHMH equation, which points towards a PTV experiment that is processed using the STB algorithm. However, there are some disadvantages of using the STB method for the present study. From the results from DNS, it is clear that the present study requires the accurate measurement of instantaneous values of velocity, to obtain the generalised KHMH equation terms. It is well known that noise appears in the PIV experiment data processing and it

affects the statistics concerning the fluctuations such as the variance and RMS values of velocity. It is more of a problem in a Tomographic (3D) experiment than in a planar experiment (2D) such as a planar or stereoscopic PIV experiment. The second concern with the Tomo-PTV with STB algorithm is that the measured data will be in the Lagrangian frame of reference, and the tool developed to compute the terms of the KHMH equation is in the Eulerian frame of reference. This would mean, either the tool to compute the KHMH equation term has to be modified to accommodate the velocity in the Lagrangian frame of reference or to use one of the transformation methods to convert the data to the Eulerian frame of reference[110]. It is possible to develop the necessary tools, however, the particles of a diameter of $1\mu m$ are well adapted for tomo PIV or PTV measurement when the third dimension is considerably smaller than the other two dimensions. Thus even if there is a possibility to obtain the velocity vector field in 3D using those measurements, the third direction is severely limited in terms of accessible length scales.

It is possible to mitigate the above-mentioned problems by using a planar measurement such as stereoscopic PIV which can provide the 3D velocity field in a plane. Thus as much as the above-mentioned problems of Lagrangian-to-Euler transformation is alleviated, a stereoscopic PIV measurement is still limited to measurements in a plane. In addition, the pressure term is not computed in the present experiment.

To decide between the different options for the plane of measurement in Stereoscopic PIV, the terms of KHMH equation are computed in DNS, by considering only the XY- plane ($\frac{\partial}{\partial x_3} = 0$), another computation by considering only the YZ- plane ($\frac{\partial}{\partial x_1} = 0$), and another computation by considering only the XZ- plane ($\frac{\partial}{\partial x_2} = 0$) . The Reynolds number (Re_τ) used in the experiments is 2270 and 3840, and so the computation is performed with DNS of TCF3000 because it is the DNS with closest Re_τ. In addition, it is possible to get terms $\frac{\partial u_1}{\partial x_1}$,$\frac{\partial u_2}{\partial x_2}$, $\frac{\partial u_3}{\partial x_3}$ using continuity equation from other two terms since the measurement is planar. To understand the effect of planar measurement on the results, there are different results to compare starting with the Spatio-temporal average values of the KHMH equation, the standard deviation of different terms, the correlation coefficient between different KHMH equation terms. The most important results which are sensitive to the fluctuating part of the datasets corresponds to the correlation coefficient between different terms. Of which the correlation coefficient of the pressure term with all the terms is not useful since there is no pressure term measured or computed from the experimental data. Hence the next result would be to plot the correlation coefficient of $A_t + A$ with

planar measurement terms.

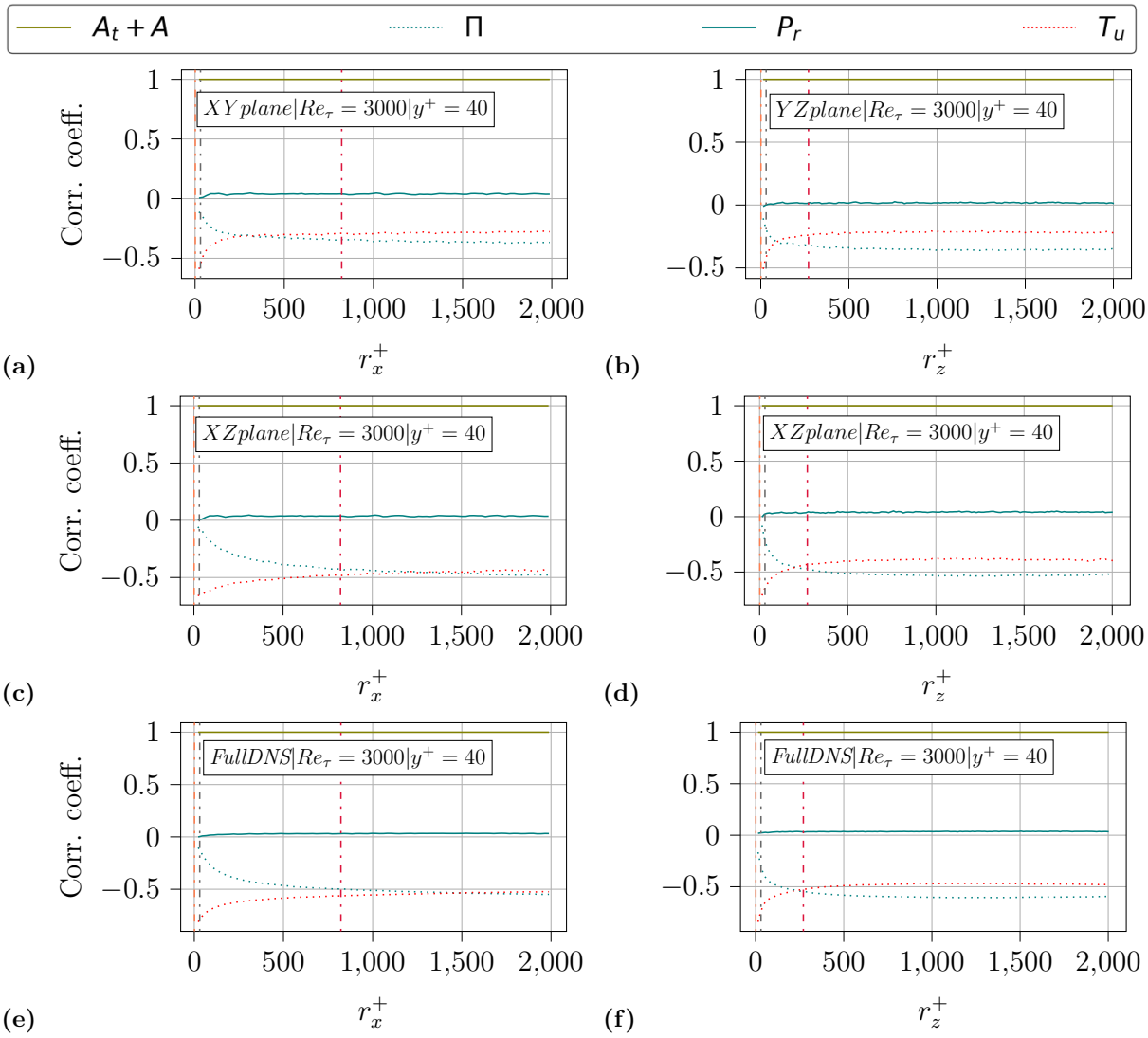

Figure 6.2: Correlation coefficient of $A_t + A$ with other terms of KHMH equation with only terms accessible in **(a)** XY- plane, **(b)** YZ- plane, **(c)**, **(d)** XZ- plane, **(e)**,**(f)** full DNS volume using dataset of TCF3000 at $y^+ = 40$

Figure 6.2 shows the correlation coefficient of $A_t + A$ with other terms of the KHMH equation using velocities and its derivatives available in XY-, YZ- and XZ planes. And the same result is plotted by full DNS data which takes into account the velocities and their derivatives in all three directions. When XY- plane is used, the result is only plotted for r_x direction, since there is no information about $\frac{\partial}{\partial x_3}$. When

the YZ- plane is used, the result is only plotted for r_z direction, since there is no information about $\frac{\partial}{\partial x_1}$. When XZ- plane is used, there is information about r_x and r_z direction since both $\frac{\partial}{\partial x_1}$ and $\frac{\partial}{\partial x_3}$ is available.

It is observed that when the full DNS dataset is used, the correlation coefficient between $A_t + A$ and the two energy transfer terms becomes slightly greater than 0.5 at all scales higher than the integral scale in this wall distance in both streamwise and spanwise direction. When the same computation is performed over data only from XY- plane, it is observed that the correlation coefficient between $A_t + A$ term and the two energy transfer terms is close to -0.3 at large scales. With the YZ-plane, the correlation coefficient between $A_t + A$ and the two energy transfer terms are also close to -0.3 at large scales. With the XZ- plane, the correlation coefficient between $A_t + A$ and the two energy transfer terms has a correlation coefficient close to 0.5 at large scales in both the r_x and r_z directions similar to the corresponding results from DNS.

There are some practical difficulties in making the Stereoscopic PIV in XZ- plane concerning the Laser light sheet in the measurement close to the wall and the measurement itself. For the present experiment, the frequency of the acquisition $f_s =$ 4.5kHz, the diameter of the particle is 1.8 pixels. The free-stream velocity used is 3 m/s. Thus the out-of-plane displacement is computed to be $45\mu m$. The light sheet thickness is computed such that there is less than one-quarter out-of-plane displacement. And the light sheet thickness is chosen as 500 μm, which gives 250 μm for the beam-waist (w_0). The magnification factor, $M = 0.26$, The parameters for the high-speed laser used in the experiment are as follows: $M^2 = 20$, $\lambda = 532nm$. Hence the angle of divergence at the field-of-view (θ_1) is computed as :

$$\theta_1 = \frac{\lambda M^2}{\pi w_0} = 13.5 \times 10^{-3} rad \tag{6.4}$$

To make the measurement parallel to the wall, the light sheet must come from the side of the wind tunnel, and since the wind tunnel is 2m wide, the field-of-view will be in the centre. Thus the light sheet has to travel at least 1 meter from the spherical lens with an angle of 13.54 $\times 10^{-3}$ rad, which means that the spherical lens must be at least 27.8 mm in length. And the measurement is close to the wall means that approximately half of the light-sheet goes below the wall and can result in problems such as multiple reflections from the glass surface. A better way to reduce these problems is to put the optics (prism) inside the wind tunnel on the side or downstream of the flow. And since the prism will be closer than 1m from the

field of view which would mean that the experiment will no longer be non-intrusive. Additionally, to study the variation with wall distance, it is necessary to repeat the experiments at different wall distances.

On the other hand, when an XY- plane or YZ- plane is studied, the light sheet is perpendicular to the wall, it can be implemented by bringing it from the bottom of the wind tunnel. This way, the beam-waist is at 1cm from the wall since the height of the FOV is approximately 2cm from the wall. Thus the light sheet travels approximately 5-10 cm from the spherical lens (which is placed just below the wind tunnel) before forming the beam waist. To obtain the behaviour of the terms at different wall distances, with XY- or YZ- plane, it will just be one experiment. The only disadvantage with XY- or YZ- plane is that it is possible to study either in the r_x direction or the r_z directions with either experiment. The XY- plane is chosen for the present Stereoscopic PIV experiment.

In the S-PIV measurements, there is the presence of noise and it does affect the statistics dependent on the fluctuations of velocity. In the present study, the correlation coefficient and the standard deviation of KHMH equation terms are dependent on the fluctuating part of the terms and hence will be greatly affected. To mitigate this problem, it was decided to use two independent Stereoscopic PIV systems which records the images at the same Field of View (FOV). This way, whenever there is a multiplication of terms, one part of the term could be used from the S-PIV system 1 and the other part of the term could be used from S-PIV system 2. This is illustrated below

$$\begin{aligned}\overline{u^2} = \overline{u_1 \times u_2} &= \overline{(u_{1_{true}} + \sigma_{u_1}) \times (u_{2_{true}} + \sigma_{u_2})} \\ &= \overline{u_{1_{true}} u_{2_{true}}} + \cancelto{0}{\overline{u_{2_{true}} \sigma_{u_1}}} + \cancelto{0}{\overline{\sigma_{u_2} u_{1_{true}}}} + \cancelto{0}{\overline{\sigma_{u_2} \sigma_{u_1}}} \\ &= \overline{u^2_{true}}\end{aligned} \tag{6.5}$$

where u_{true} is the true velocity component and σ_u is the noise associated with the velocity component. The first term on the right-hand side of Equation 6.5 is the true value of $\overline{u^2}$. Since the noise generated by both the systems are random, they don't correlate with the velocity fields of the second system, and so $\overline{u_{2true}\sigma_{u1}}$ and $\overline{\sigma_{u2}u_{1true}}$ are zero. Along with the same argument, the noise generated by both systems are random and hence doesn't result correlate with each other and so $\overline{\sigma_{u1}\sigma_{u2}}$ is equal to zero.

This way of removing the noise from the data works only when there is an average involved. However, it doesn't work for an instantaneous value of a variable. In the present study, the correlation coefficient values between different terms, and their

standard deviation depends on the instantaneous values of the terms and are affected by the noise. However, both these parameters are averaged over different points and time steps in the flow-field at each wall distance, and so the way of removing the noise explained above can help to remove the noise in the results.

6.2 Details of the experiment

6.2.1 The LMFL wind tunnel facility

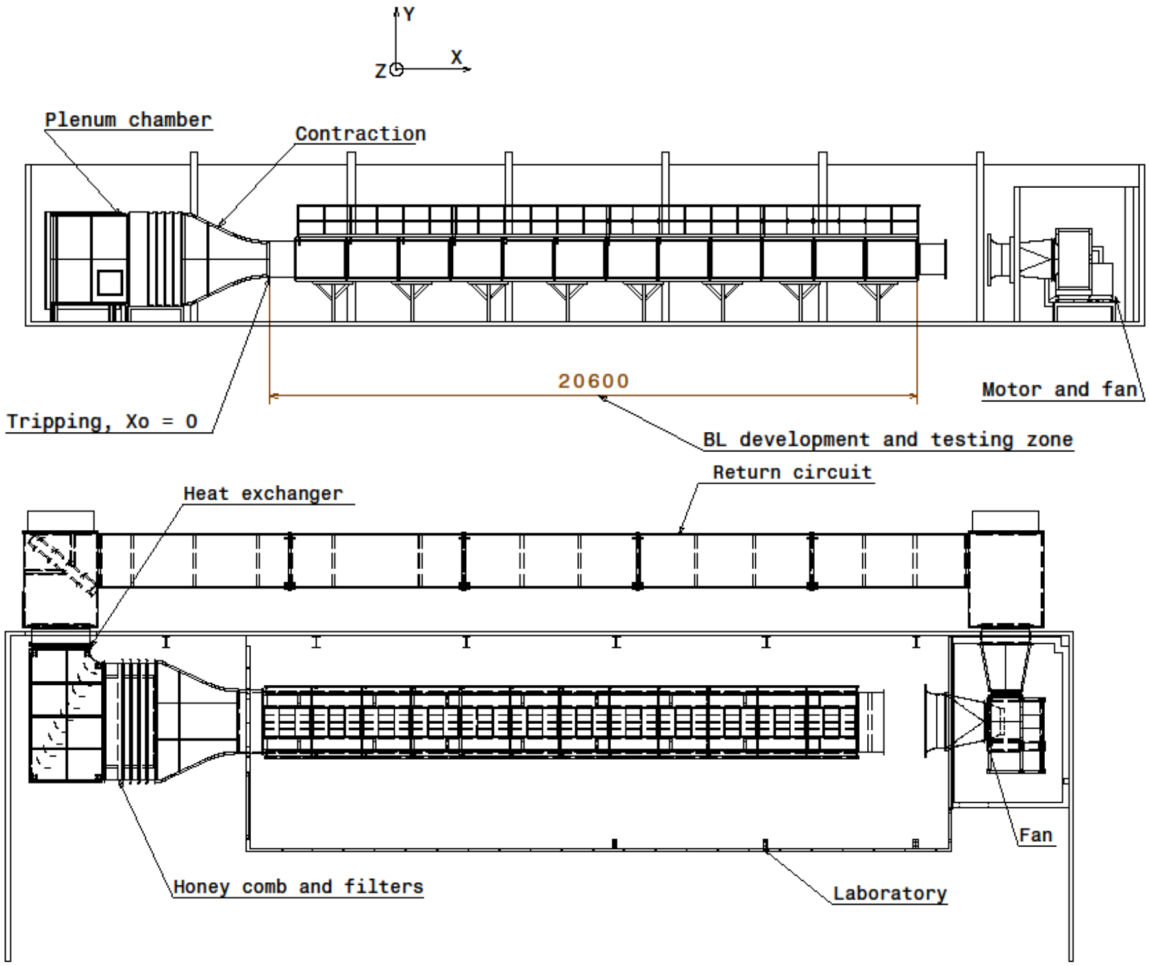

Figure 6.3: Sketch of the top view (top) and front view (bottom) of LMFL Turbulent boundary layer wind tunnel. Reproduced from Cuvier et al. [27]

The present PIV experiment is performed in the Laboratoire de Mécanique des Fluides de Lille (LMFL) boundary layer wind tunnel. Figure 6.3 shows the sketch of the top-view and the front-view of the wind tunnel respectively. The wind tunnel

is powered by a fan of a 37kW electric motor, with which it is possible to have a free-stream velocity from 3 m/s up to a maximum of 9.4 m/s measured at 100 mm downstream of the start of the test section, with a stability of less than 0.5%. The turbulence level is less than 0.3% and the temperature is regulated at $\pm 0.15°$C, which is made possible using a heat exchanger located at the plenum chamber. The test section is transparent with high quality 10 mm glass on all four sides along its entire length allowing for easy optical access to do PIV experiments. The test section is 20.6 m long in the streamwise direction (x-direction), with the cross-section of 2×1 m^2 along the spanwise (z-direction) and wall-normal direction (y-direction) respectively. This long test-section allows to reach Reynolds number based on momentum thickness, Re_θ up to 20,600 and the boundary layer thickness, δ of 0.24 m at 19.6 m from the tripping mechanism. Thus this facility enables us to make a detailed experimental investigation of near-wall physics.

The wind tunnel can be operated at the closed circuit with velocity and temperature regulation, or open to the outside. The boundary layer is tripped using a 4 mm cylinder fixed in the bottom wall with silicon along the spanwise direction and then a 93 mm of Grit 40 sandpaper (mean roughness of 425 μm). The top layer is tripped in the same way as the bottom plate but without the cylindrical rod. All the glass surfaces which cover the test section is mounted in such a way that the opposite faces are perfectly parallel (less than $\pm 0.1°$) to each other. Interested readers could refer to Carlier and Stanislas[18] for more details.

6.2.2 Stereoscopic PIV setup

For the present experimental campaign, the wind tunnel was used in the closed-circuit configuration. Figure 6.4 shows the schematic of the two sets of S-PIV (2D-3C) employing 4 cameras to capture a field of view illuminated by a laser light sheet in the streamwise-wall-normal plane. The present experimental campaign consists of performing S-PIV experiments at two free-stream velocities : (a) 3 m/s corresponding to a Reynolds number based on friction velocity $Re_\tau = 2220$, (b) 6m/s corresponding to a Reynolds number $Re_\tau = 3840$. The centre of the field of view in the streamwise directions is at 19.2 m from the inlet of the test section which corresponds to boundary layer thickness δ of 0.273 m, u_τ of 0.1207 m/s for Re_τ of 2220, and δ of 0.243 m, u_τ of 0.2337 m/s for Re_τ of 3840. The tracer for the experiment is a water-ethylene glycol mixture that is fully seeded in the entire closed circuit of the wind tunnel. The size of the droplets was estimated to be 1 μm and is expected to have a lifetime of 10 minutes.

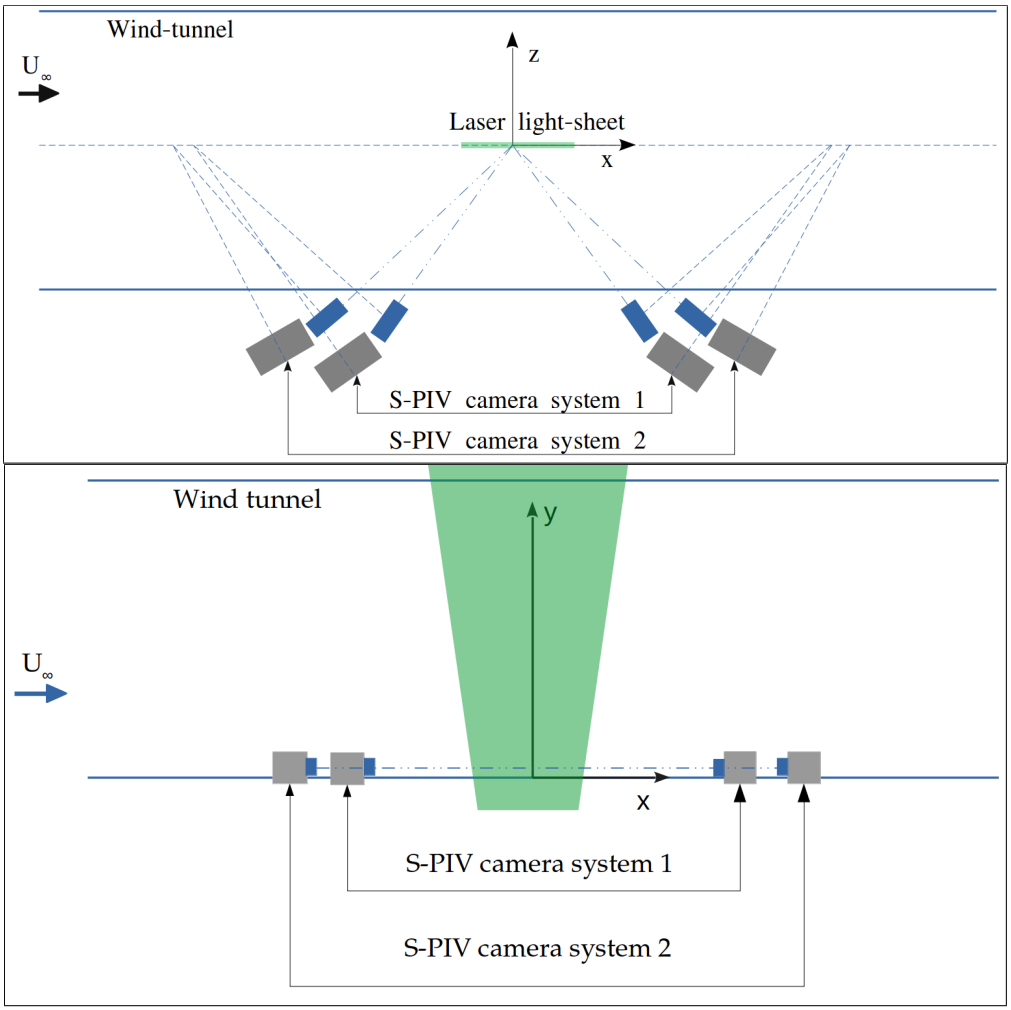

Figure 6.4: Schematic of two S-PIV systems experimental setup, showing the laser light sheet, the position of cameras, in top view (top) and front view (bottom)

The cameras and the Laser are synchronised by LaVision's High-Speed Controller, which is then used to acquire the images using Davis 8.4 software. For $Re_\tau = 2220$, the chip-size of the camera used were 1280×512 pixels which correspond to a Field-of-View of 60.4 × 18.4 mm^2, and in wall-units, this is $503^+ \times 153^+$. The acquisition frequency used is 4.5 kHz corresponding to 10 pixels displacement and the lasers are triggered at the same time with 10 mJ/pulse. For $Re_\tau = 3840$, the chip-size of the camera used was 640×512 pixels, which corresponds to a Field-of-View is 29.6 × 18.4 mm^2, and in wall-units, this is $493^+ \times 306^+$. The acquisition frequency used is 7.5 kHz corresponding to 14 pixels displacement and the lasers are triggered at 10.7 mJ/pulse. For both the Reynolds numbers, the magnification factor is 0.26,

and f-number, $f_{\#}$ of 8.

6.2.3 Method of data acquisition

The calculation of parameters of the S-PIV experiment is explained in this section. At first, it is important to choose the type of image acquisition for the PIV experiment. There are multiple possibilities concerning the frames and exposures in the PIV experiment, which are highly dependent on the needed results. For the present study, there are two ways of acquiring the data as shown in Figure 6.5: (a) High-speed PIV, (b) Time-resolved PIV.

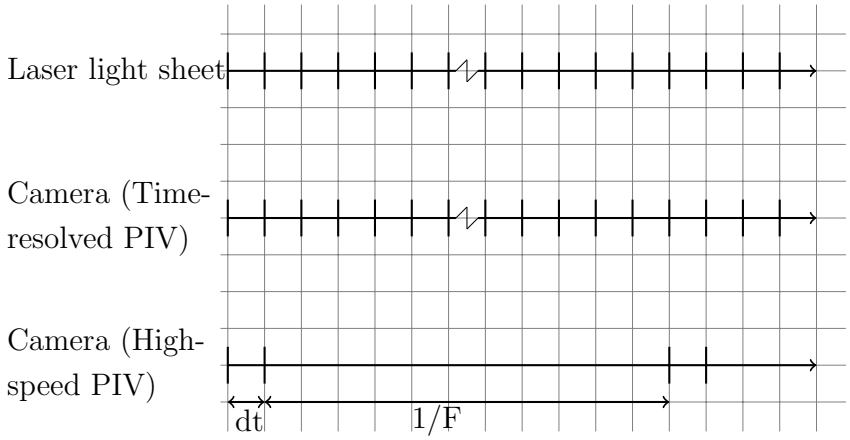

Figure 6.5: Schematic of image acquisition with time-resolved and high-speed PIV experiment

In a High-speed PIV experiment, the camera records two images with a given time delay. This time delay is only limited by the camera, and now there are cameras where it can be of the order of μs. These two images are then processed using cross-correlation methods to obtain the vector field. When the time between the first two images is as low as possible, the next image can be only captured after a certain time delay, which is determined by the frequency of the acquisition of the camera. This time delay value can be of the order of kHz for the full sensor of the camera. This method of obtaining the velocity vector field has the advantage that it is possible to converge the statistics with less amount of data since the datasets tend to be decorrelated if the time between the second frame of the first set of images and the first frame of the next two images is of the order of 2-3 integral time scales. This time between the second image of the first double-frame and the first image of the second double-frame is directly dependent on the size of the camera sensor, and so if this parameter is reduced, it is possible to reduce the time between the second

image of the first double-frame and the first image of the second double-frame. If the sensor size of the camera is so reduced that the time delay between the first two images are the same as the time delay between the second image of the first double-frame and the first image of the second double-frame, and this time delay is at least half the value of the characteristic time scale (Nyquist sampling theorem) to well-resolve the flow temporally, then it is called time-resolved PIV measurement.

Estimation of dt

To choose between the High-speed and Time-resolved PIV experiments, it is important to compute the characteristic time scales or the frequency associated with the flow. For the present experiment, characteristic frequency is:

$$\frac{\overline{u}}{\eta} = \frac{\overline{u}}{\left(\frac{\nu^3}{\epsilon}\right)^{\frac{1}{4}}} \tag{6.6}$$

where η is the Kolmogorov length scale, $\overline{u}$ is the mean-velocity, ϵ is the dissipation, ν is the kinematic viscosity.

For the PIV experiments, the maximum value of $\overline{u}/\eta$ near the buffer layer is of the order of 4.5 kHz, which is chosen as the sampling frequency for PIV at $Re_\tau = 2220$. This value of sampling frequency is higher than the frequency of the Miro camera used in the experiment, and this rules out the possibility of using High-speed PIV, in favour of Time-resolved PIV. This high frequency in time-resolved PIV is achieved by cropping the camera sensor.

Estimation of displacement between two frames

In PIV measurement, it is advisable to have 10 - 20 pixels displacement between two images of the experiment. For the present experiment, 10 pixels displacement is chosen for $Re_\tau = 2220$ and a 14 pixels displacement is chosen for $Re_\tau = 3840$.

For a 10 pixels mean displacement, the measurement uncertainty is $\sigma = 0.1$ pixels; assuming a standard deviation of 10% of mean velocity so $u_{RMS} = 1$ pixel, the error in the measurement of displacement is computed by

$$\frac{\sigma^2}{u_{RMS}^2} = \frac{0.1^2}{1^2} = 1\% \tag{6.7}$$

For a 14 pixels mean displacement, the measurement uncertainty is $\sigma = 0.1$ pixels; assuming a standard deviation of 10% of mean velocity so $u_{RMS} = 1.4$ pixels, the

error in the measurement of displacement is computed by

$$\frac{\sigma^2}{u_{RMS}^2} = \frac{0.1^2}{1.4^2} = 0.5\% \tag{6.8}$$

Estimation of the number of uncorrelated samples

To compute the terms of the KHMH equation, it is necessary to have the spatial and temporal derivatives of velocity. Hence a time-resolved stereoscopic PIV is employed here which is capable of producing a 2D-3C velocity field in an XY-plane, which provides all the derivatives in x- and y- directions and the time-derivatives of all three velocity components. With the help of the continuity equation, it is possible to obtain the $\frac{\partial w}{\partial z}$ term. If the entire experiment is performed in a time-resolved way, the resulting datasets will be correlated until the integral time scale, and therefore it requires a lot of data to converge the statistics. To tackle the limitation, it was decided to perform the time-resolved stereoscopic PIV for some time-steps and this is followed by approximately two integral time scales of no recording and then is followed the time-resolved stereoscopic PIV and so on, as shown in Figure 6.6. This way, it is possible to obtain the time-derivatives and is also possible to have converged statistics with less amount of data compared to full time-resolved experiments.

The number of uncorrelated samples is estimated from the corresponding value from the DNS of TCF3000. For this study, the integral scale value at the centre-line of the channel flow is used. From section 4.1.3 it is known that it gets difficult to converge quantities as the analysis moves closer to the centre-line of the channel flow. The integral scales of TCF3000 at x- and z- directions are given by $L_{11} = 0.27\delta$ and $L_{13} = 0.09\delta$ respectively. The computation domain in x- and z- directions are $6\pi\delta$ and $1.5\pi\delta$ respectively. This results in approximately 69 and 52 uncorrelated samples in each time-step and eight different time-steps which are far from each other are used. This gives approximately 29243 uncorrelated samples used in the computation of KHMH equation terms in the TCF3000.

In the present experiment at $Re_\tau = 2220$, the images were acquired in a time-resolved series of 5 images, and are then separated by two integral time scales (12 Hz) between each time-resolved acquisition, up to a total of 1803 sets of time-series images for each run of the experiment. A total of 35 runs were acquired, which results in 63105 uncorrelated samples. In the experiment at $Re_\tau = 3840$, time-resolved acquisition of 5 images, and separated by two integral time scales between each time-resolved acquisition, up to a total of 3606 sets of uncorrelated

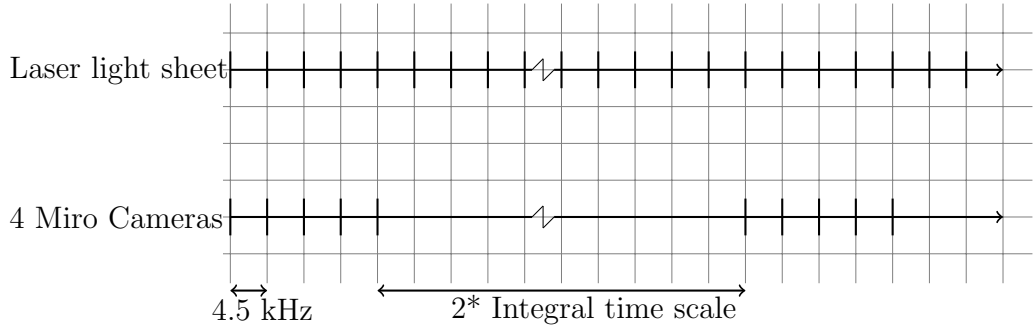

Figure 6.6: Schematic of image acquisition in the present PIV experiment

time series images are obtained for each run. A total of 30 runs were acquired, which corresponds to 108180 uncorrelated samples.

Processing of PIV datasets

The acquired data are then processed using a modified version of the MatPIV toolbox at LMFL. The experiment is calibrated by using a calibration plate that has crosses at known places and they are spaced equally between the known distance and this is captured by the cameras. Since it is a stereoscopic PIV experiment, which has the 3 velocity components, it is necessary to translate the calibration plate in the spanwise direction to a certain distance that is greater than the light sheet thickness. The images acquired by translation are fitted with a polynomial to estimate the mapping function. The order of the mapping function depends on the number of images obtained from translation. In the present experiment, the calibration plate is recorded in 11 spanwise positions. The mapping function for each camera enables us to obtain the 3C velocity field by reconstructing the images from the two cameras[114].

This calibration procedure is followed by self-calibration[132], where a disparity map is constructed from the cross-correlation of images from both cameras, which in-turn helps to verify if the laser light-sheet coincides with that of the calibration plate. Thus the disparity map allows to fit the true position of the light sheet in space and then the mapping functions are corrected accordingly. With this self-calibration procedure, it is possible to obtain the accurate mapping function even if the light-sheet and calibration plate don't coincide. This correlation maps also allows determining the different parameters of the light sheet such as their thickness, amount of overlap etc.

At first, the reflection of the wall from each camera is identified and is fitted with

a line. This is the reference of the first position for the wall-normal axis. And the mean background images were mapped using Soloff transformation. This enables us to build the mesh above the line (which is identified as the wall) with the mapped images and is then projected on each camera with the mapping function obtained by calibration.

The analysis is then performed with the projected grids. The images obtained were processed with cross-correlation PIV analysis[135,115] in 3 passes with interrogation window sizes from [(96×32), (32×32), (24×24)]. This is followed by image deformation[100,73], where bilinear interpolation is used for the displacement and b-spline cubic interpolation is used for the grey level, to improve the quality of the results. This is followed by the final pass cross-correlation PIV analysis with interrogation window size of (18×24), which corresponds to 0.97 × 0.97 mm^2, which is equivalent to $8^+ \times 8^+$ for $Re_\tau = 2220$, and $16^+ \times 16^+$ for $Re_\tau = 3840$. The effect of laser reflection and the camera noise is limited by the use of background division[94]. With an overlap of approximately 60%, the final field of XY- plane has 152 × 45 vectors with a spatial resolution of $3.3^+ \times 3.3^+$ for $Re_\tau = 2220$, and 75 × 45 vectors with a spatial resolution $6.6^+ \times 6.6^+$ for $Re_\tau = 3840$ experiment in the streamwise and the wall-normal direction respectively for both stereoscopic PIV systems. The computation of other parameters of S-PIV experiments are given in Appendix C.1.

Chapter 7

Results: PIV experiment

This chapter focuses on the results of S-PIV experiments, starting with the validation of PIV datasets in mean, variance and covariances of turbulent velocity fluctuation and by its comparison with DNS datasets of similar Re_τ. This is followed by the measurement uncertainty in the PIV dataset, computation of noise and computation of dissipation associated with each S-PIV system and at both Reynolds numbers. This is followed by the KHMH equation analysis which involves Spatio-temporal averaging of the terms, the standard deviation of the terms and correlation coefficient of $A_t + A$ with other terms. The effect of denoise is discussed for each subsection of the KHMH equation analysis. This is followed by the analysis of adding Additive Gaussian White Noise (AGWN) to DNS datasets to simulate the results from PIV experiments.

7.1 Validation of experiment

The current TBL datasets on PIV experiments are validated using different statistical quantities such as the mean, turbulence intensities velocity components. In the present experimental campaign, the datasets were obtained for two Reynolds numbers, $Re_\tau = 2220$ and $Re_\tau = 3840$. So the mean flow and turbulence quantities are then compared with the DNS dataset of the closest Reynolds numbers (Re_τ), to know the accuracy of the velocity components measured in the experiments. Thus for the PIV dataset of $Re_\tau = 2220$, the DNS dataset of ZPG-TBL of Borrell et al.[13,112,111] with $Re_\tau = 1989$ is used for comparison. And for the PIV dataset of $Re_\tau = 3840$, the DNS dataset of TCF of Hoyas and Jiménez[56] with $Re_\tau = 4200$ is used for comparison. In addition, the DNS dataset of TCF of Thais et al.[120] at $Re_\tau = 3000$ from the present work is also added in the comparison.

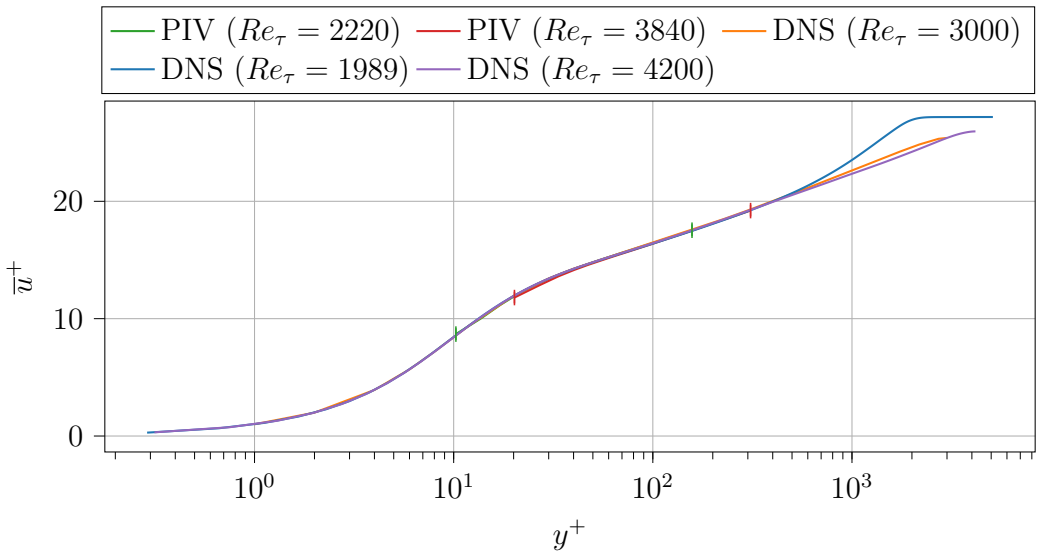

Figure 7.1: Comparison of average streamwise velocity normalised with inner coordinates $\overline{u}^+$ from the present PIV experiments at $Re_\tau = 2220$ and 3840 with DNS datasets of TCF at $Re_\tau = 1989, 3000, 4200$. The green vertical line shows the range of wall distances for the PIV experiment with $Re_\tau = 2220$, and the red vertical line shows the range of wall distances for the PIV experiment with $Re_\tau = 3840$

Figure 7.1 shows the mean ($\overline{u^+}$) profile from the present PIV experiments and their comparison with the same quantities in DNS datasets. The available wall distances in the PIV dataset with $Re_\tau = 2220$ are in the range $10.25 \leq y^+ \leq 157.31$, and for the PIV dataset with$Re_\tau = 3840$ is in the range $20.19 \leq y^+ \leq 309.6$. The limits of the wall distance values are marked by a vertical line of red and green colours for the higher and lower Reynolds number PIV experiments respectively. The mean velocity values ($\overline{u}^+$) shows a good agreement of the PIV experiment with that of the DNS dataset, for the wall distances measured from the experiments for both the Reynolds numbers.

Figure 7.2 shows the variance of turbulent velocity fluctuations of all three velocity components and $\overline{u'v'}^+$, along the wall-normal direction. The streamwise velocity fluctuations $\overline{u'^2}^+$ for both the PIV datasets don't agree well when $y^+ < 20$. At wall distances when $y^+ > 20$, the PIV dataset $Re_\tau = 2220$ tends to be between the two DNS datasets of $Re_\tau = 1989$ and $Re_\tau = 3000$. And the PIV dataset $Re_\tau = 3840$ seems to have a slight overprediction of this parameter. The spanwise velocity fluctuations $\overline{w'^2}^+$ has a peak close to $y^+ = 40$ in all datasets except for

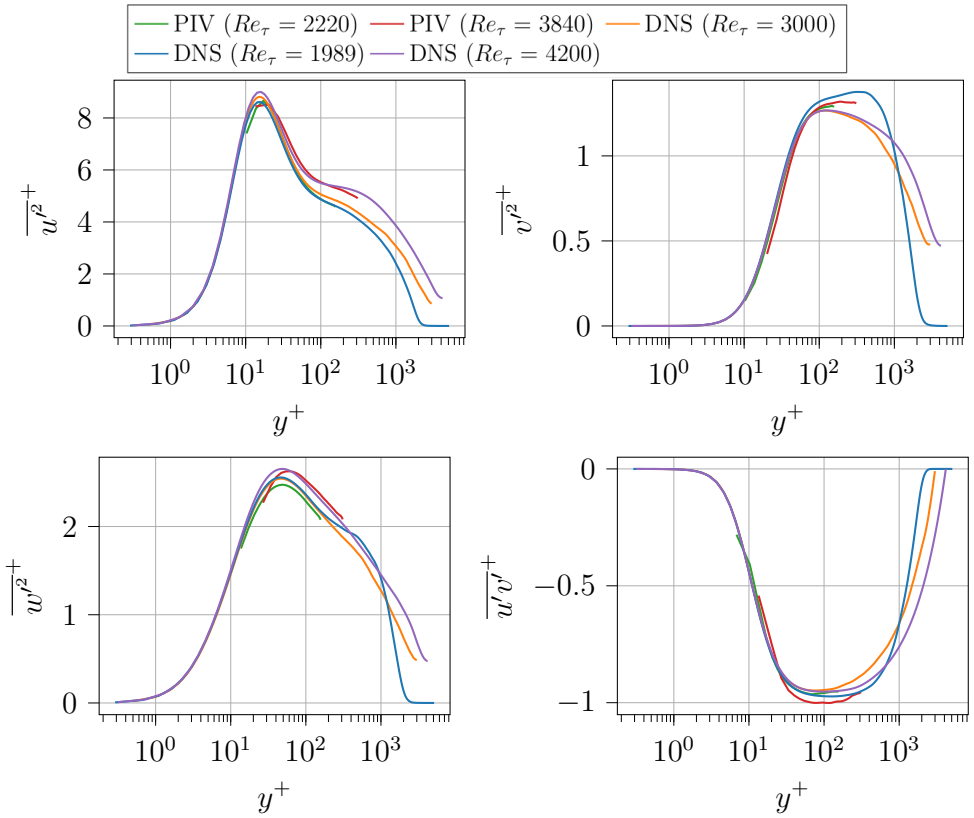

Figure 7.2: Comparison of variances and covariances of the streamwise, wall-normal and spanwise velocity components in the present PIV experiments at $Re_\tau = 2220$ and 3840 with DNS of TCF datasets at $Re_\tau = 1989, 3000$ and 4200

PIV with $Re_\tau = 3840$ for which the peak occurs close to $y^+ = 55$. Beyond the peak, PIV with $Re_\tau = 3840$ follows the TCF3000 with slight overprediction, and the PIV with $Re_\tau = 2220$ has consistently underpredicted this parameter than the DNS datasets. The wall-normal velocity fluctuation $\overline{v'^2}^+$ of both PIV follows the DNS after $y^+ = 20$, with a slight underprediction until $y^+ = 100$, and beyond that stays between the values of the three DNS datasets. The value of $\overline{u'v'}^+$ agrees well with the DNS above $y^+ = 20$ for both the PIV datasets, with overprediction of the peak in the DNS with higher Re_τ.

7.1.1 S-PIV measurement uncertainty

In addition to the validation of the results of PIV with that of DNS, it is important to compute the measurement uncertainty, to better assess the PIV experiment. In the past Kostas et al.[70], Herpin et al.[52], Srinath[116] computed the RMS of difference

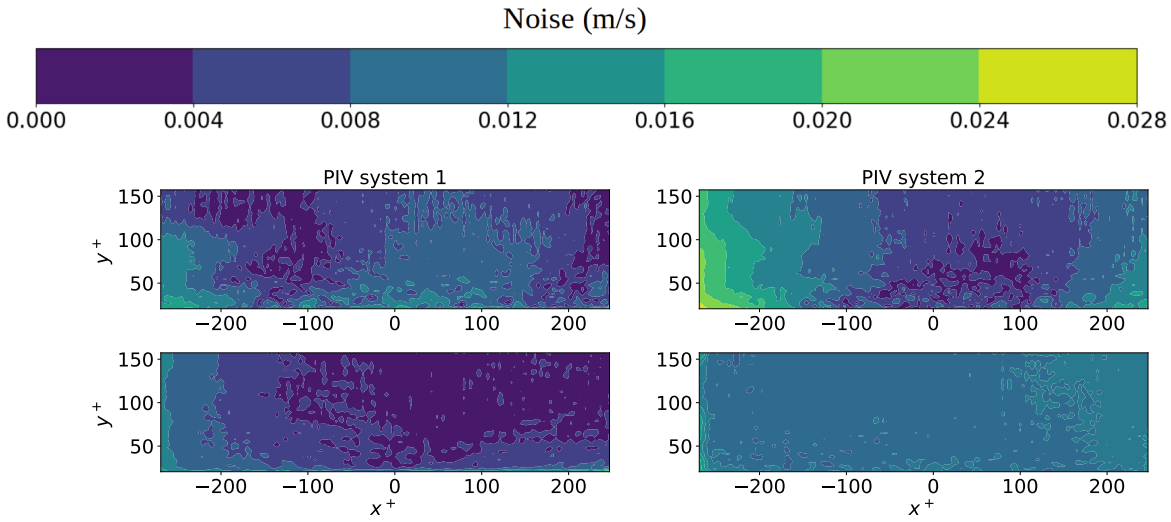

Figure 7.3: Measurement uncertainty in streamwise (top) and spanwise (bottom) components of velocity fluctuations in PIV systems '1' and '2' of PIV datasets at $Re_\tau = 2220$

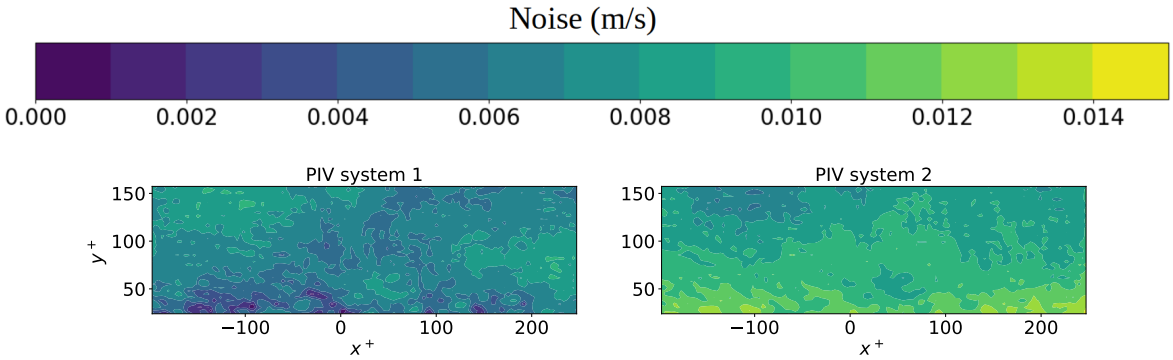

Figure 7.4: Measurement uncertainty in wall-normal components of velocity fluctuations in PIV systems '1' and '2' of PIV datasets at $Re_\tau = 2220$

of the three velocity components in the overlap regions of the FOV of their PIV experiments. This is made possible due to the small region on the edge of their field of view which was recorded simultaneously by two independent PIV systems. Thereby in the overlap region, the measurement uncertainty of the PIV experiment was computed by the difference of the RMS value of the velocity components, i.e., $\sigma_{u'} = \sqrt{(u'_{sys_a} - u'_{sys_b})^2}$, where '$u'$' is the velocity component and the subscript 'sys_a' and 'sys_b' denotes the two different PIV systems.

In the present experiment, however, the PIV uncertainty is quantified using the two PIV fields to obtain the denoised field and then to compute the uncertainty as

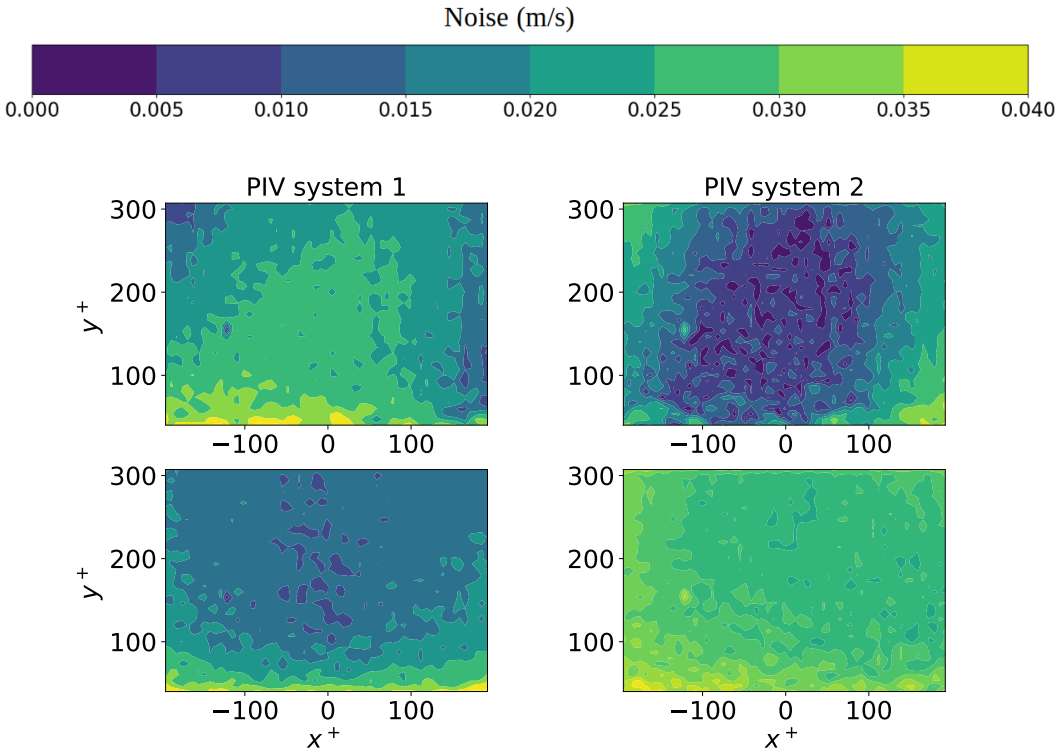

Figure 7.5: Measurement uncertainty in streamwise (top) and spanwise (bottom) components of velocity fluctuations in PIV systems '1' and '2' of PIV datasets at $Re_\tau = 3840$

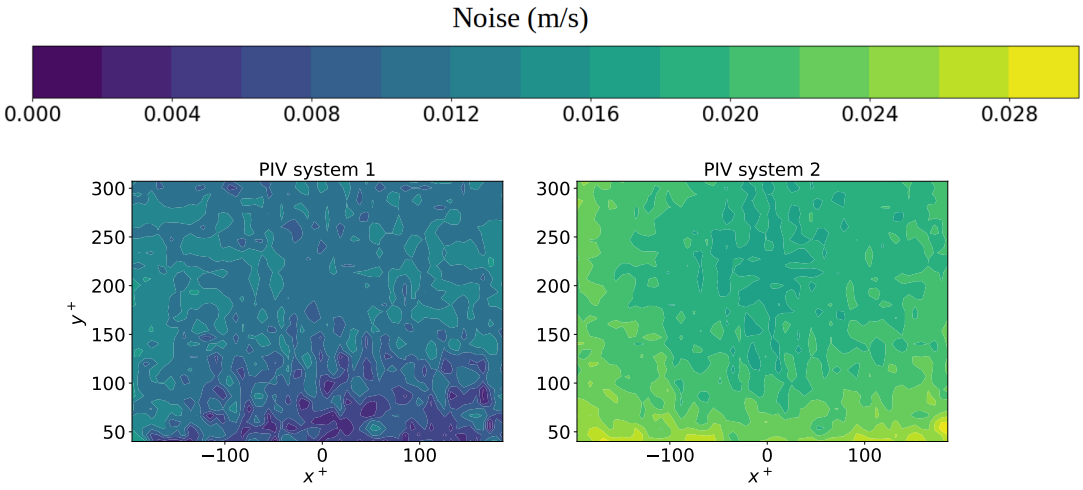

Figure 7.6: Measurement uncertainty in wall-normal components of velocity fluctuations in PIV systems '1' and '2' of PIV datasets at $Re_\tau = 3840$

the difference between the denoised and individual PIV system, which is given for

quantity 'u'' for system 'a' by the following equation:

$$\sigma_{u'} = \sqrt{u'_{sys_a} u'_{sys_b} - u'_{sys_a} u'_{sys_a}} \tag{7.1}$$

Since the two PIV system records the same field of view, it becomes possible to compute this measurement uncertainty for the entire field of view. Figures 7.3 and 7.4 shows the measurement uncertainty of PIV system 1 and 2 in (m/s) for $Re_\tau = 2220$ dataset. For this dataset, the wall distances closer to the wall where $y^+ < 20$ is not plotted. The maximum value of measurement uncertainty is 0.028 m/s for streamwise and spanwise velocity components, which is of the order of 0.93% of the freestream velocity. For the wall-normal velocity component, it is 0.014 m/s which is of the order of 0.4% of the freestream velocity. It is observed that the noise is higher close to the wall and along the sides. This is because there is a reflection of the laser sheet from the wall which leads to high intensity of noise signal close to the wall. And the laser light sheet is more powerful in the centre than in the sides and this leads to the drop of the intensity of particles along the sides, thereby reducing the signal-to-noise ratio along the boundaries of the Field of View.

Figures 7.5 and 7.6 shows the measurement uncertainty of the two S-PIV systems for the $Re_\tau = 3840$ datasets. For this dataset, the wall distance closer to the wall, when $y^+ < 40$ is not plotted. It is observed that the maximum value of the noise is approximately 0.04 m/s which is of the order of 0.6% of the free-stream velocity in the streamwise and spanwise direction. The maximum value of noise in the wall-normal direction is 0.03 m/s, which is of the order of 0.5% of the freestream velocity. The same observation as before that the noise is at its maximum along the boundaries of the Field-of-View holds at this Re_τ.

Determination of noise in the PIV dataset

The main objective behind using two S-PIV systems with the same field of view in this present experimental campaign is to compute the terms of the KHMH equation without the influence of noise present in the measurement of each variable in the PIV experiment on average. Thus any average over multiplication involving the same variable will result in multiplication of noise. This multiplication of noise is necessarily bad because, for the same variable, the noise is fully correlated. To get rid of this, it was decided that whenever there is a multiplication of the same variables, one instance of the variable is taken from S-PIV system 1 and the other instance is taken from the S-PIV system 2. This way the result will only involve the multiplication of variables with zero noise in the average given by Equation 7.1.

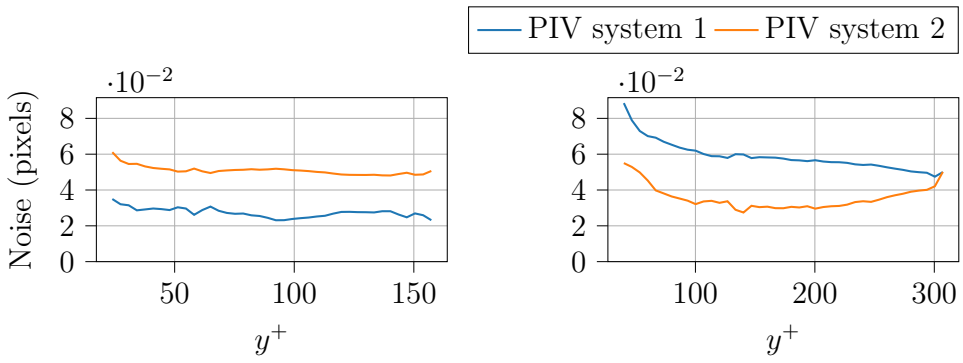

Figure 7.7: Noise value associated with streamwise velocity fluctuations (in pixels) for PIV dataset at $Re_\tau = 2220$ (left) and $Re_\tau = 3840$ (right)

The noise value associated with the individual PIV system in the measurement of the streamwise velocity is given in Figure 7.7 in pixels. For the lower Re_τ datasets, the value of error in pixel stays well below 0.06 pixels for both the PIV systems, when $y^+ > 20$, which agrees well with the widely accepted error value of 0.1 pixels[94]. For the higher Re_τ dataset, the error value for PIV system 1 stays under 0.08 pixels when $y^+ > 40$. For both the datasets, the noise value is higher than 0.1 pixels close to the wall and it decreases as the wall distance is increased consistent with the explanation in the last subsection.

Conclusion

This subsection can be concluded by the fact the variances and covariance of PIV datasets agree well with that of the comparable DNS datasets above the wall distance $y^+ = 20$ and $y^+ = 40$ for the PIV datasets with $Re_\tau = 2220$ and 3840 respectively. The measurement uncertainty associated with the velocity vector of the PIV datasets at both the Re_τ is less than 1% of the free-stream velocity for both the PIV datasets. The noise value is of the order 0.03-0.06 pixels for the dataset with $Re_\tau = 2220$, and between 0.04 to 0.08 pixels for the dataset with $Re_\tau = 3840$. This is true only when the values close to the wall and those along the boundaries of both the sides of the Field of View along the streamwise direction are removed from the analysis.

7.1.2 Computation of dissipation

The dissipation computed is essentially the pseudo-dissipation $\langle \tilde{\epsilon}' \rangle$[92] which is different from the true dissipation $\langle \epsilon' \rangle$, and is given by

$$\langle \tilde{\epsilon}' \rangle = \nu \left\langle \frac{\partial u_i'}{\partial x_j} \frac{\partial u_j'}{\partial x_i} \right\rangle = \langle \epsilon' \rangle - \nu \left\langle \frac{\partial u_i'}{\partial x_j} \frac{\partial u_j'}{\partial x_i} \right\rangle \tag{7.2}$$

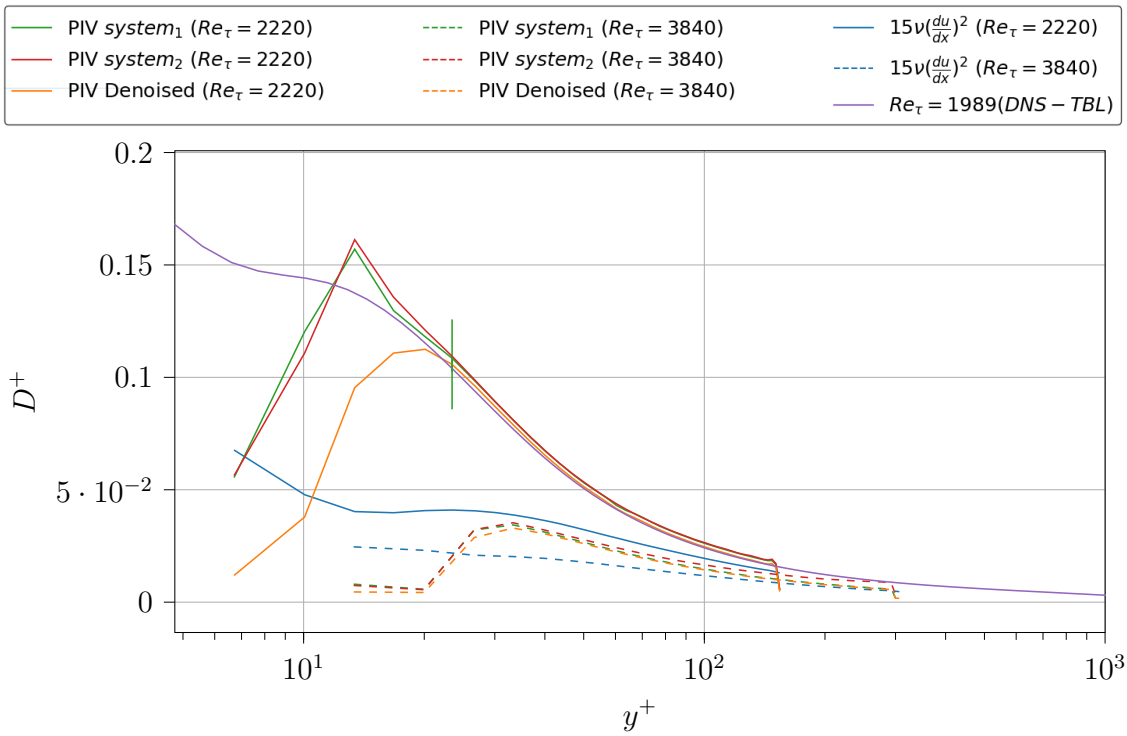

Figure 7.8: Computation of normalised dissipation D^+ with different methods in PIV datasets at $Re_\tau = 2220$ and 3840. This is then compared with the DNS of the TBL dataset at $Re_\tau = 1989$. A green vertical line shows the wall distances beyond which the axisymmetric assumptions holds good in the computation of dissipation

Pope [92] explains that the term $\nu\langle\frac{\partial u_i'}{\partial x_j}\frac{\partial u_j'}{\partial x_i}\rangle$ is at most a few percentages of ϵ, and therefore can be negligible in virtually all circumstances. And therefore in the present work, whenever dissipation is used, it is the pseudo dissipation. From the PIV experiment, it wasn't possible to obtain the two derivatives $\frac{\partial u_1'}{\partial x_3}$, $\frac{\partial u_2'}{\partial x_3}$. To alleviate for the missing terms, George and Hussein [43] presented a way of computing certain velocity derivatives which are usually not available in some experiments, and is valid away from the wall ($y^+ > 25$). For the present experiment, the two missing derivatives are computed by :

$$\left\langle \left(\frac{\partial u_1'}{\partial x_3}\right)^2 \right\rangle = \left\langle \left(\frac{\partial u_1'}{\partial x_2}\right)^2 \right\rangle \tag{7.3}$$

$$\left\langle \left(\frac{\partial u_2'}{\partial x_3}\right)^2 \right\rangle = \left\langle \left(\frac{\partial u_3'}{\partial x_2}\right)^2 \right\rangle \tag{7.4}$$

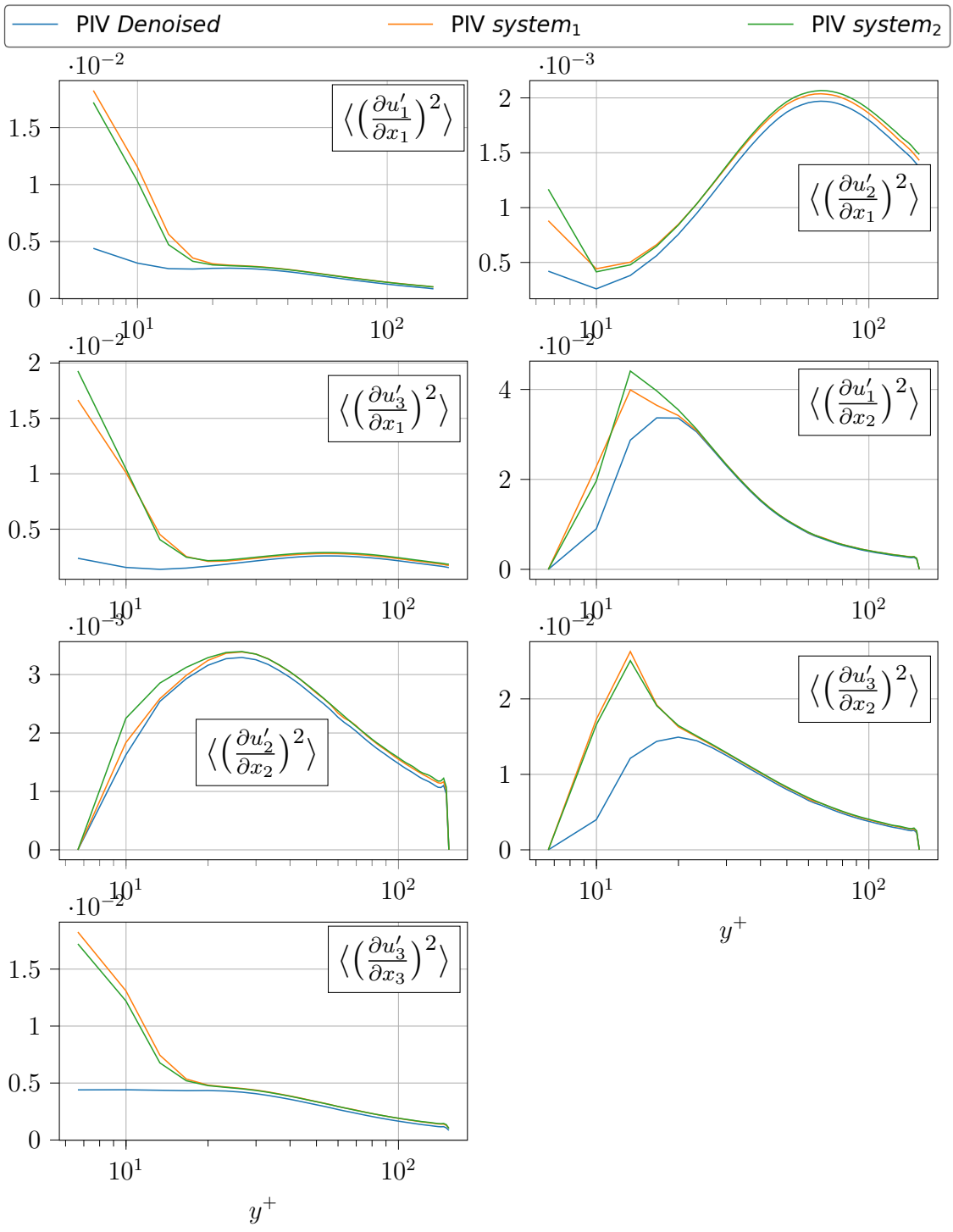

Figure 7.9: The individual terms of dissipation term for the S-PIV experiment at $Re_\tau = 2220$

Thus the dissipation in the present experiment is then obtained by

$$\langle \tilde{\epsilon}' \rangle = \nu \langle \Bigg[\left(\frac{\partial u_1'}{\partial x_1} \right)^2 + \left(\frac{\partial u_2'}{\partial x_1} \right)^2 + \left(\frac{\partial u_3'}{\partial x_1} \right)^2 + 2 \left(\frac{\partial u_1'}{\partial x_2} \right)^2 + \left(\frac{\partial u_2'}{\partial x_2} \right)^2 + 2 \left(\frac{\partial u_3'}{\partial x_2} \right)^2 + \left(\frac{\partial u_3'}{\partial x_3} \right)^2 \Bigg] \rangle \tag{7.5}$$

This value is given in Figure 7.8 by the PIV experiment denoised for both Re_τ values, and this is then compared with the same value computed from DNS of ZPG-TBL at $Re_\tau = 1989$. In addition, the computation of dissipation with the assumption of local isotropy is plotted for both PIV datasets and is observed to be the least accurate. For the lower Re_τ PIV datasets, above $y^+ = 25$ (marked by the vertical line), the dissipation values tend to follow that of the DNS. This is by the results in the previous subsection, from this dataset.

The dissipation value computed from the PIV at $Re_\tau = 3840$ is not comparable to that of the DNS or the PIV at $Re_\tau = 2220$. There is a possible explanation for this behaviour. The interrogation window size used for the processing of the PIV dataset at $Re_\tau = 3840$ is close to $14^+ \times 14^+$, and the Kolmogorov scale is of the order of $2.5^+ - 3^+$. Thus the resolution is of the order of $4.6\eta - 5.6\eta$. On the other hand, the resolution of the PIV dataset at $Re_\tau = 2220$, is of the order of $7^+ \times 7^+$, which corresponds to $2.3\eta - 2.8\eta$.

Figure 7.9 shows the value of each derivatives contributing to the value of dissipation from both PIV system '1', '2' and their corresponding denoised values. It is observed that the when $y^+ < 25$, the derivative values from the individual systems are much higher than the same that is denoised. All the terms except, $\frac{\partial u_1'}{\partial x_2}$ and $\frac{\partial u_3'}{\partial x_2}$ contribute the high value of noise in the computation of dissipation below $y^+ = 25$. And the peak value close to the wall of the dissipation from both the individual systems is due to the two derivatives $\frac{\partial u_1'}{\partial x_2}$ and $\frac{\partial u_3'}{\partial x_2}$, and due to the assumptions of George and Hussein [43] both these values are used two times for the computation. In addition, George et al. [44] showed that the local axisymmetry assumptions fail close to the wall, however, the wall distance up to which it is valid varies between different flows. In the present experiment in comparison to the dissipation value from DNS, it can be concluded that the local axisymmetry assumption is valid when $y^+ > 25$ for the PIV dataset at $Re_\tau = 2220$. This limiting value of $y^+ = 25$ is marked by a vertical line in Figure 7.8.

7.2 Spatio-temporal average value of KHMH equation terms

The datasets from both the PIV experiments are validated by comparing different statistics with that of DNS with comparable values of Re_τ. And this is followed by the computation of noise in each S-PIV system at both the Re_τ. The next part of the analysis is to obtain the averaged values of KHMH equation terms with PIV datasets, which is the focus of this section.

The PIV experiment is performed on an XY- plane, and so the derivatives in the spanwise direction are not available. With continuity equation, it is possible to obtain the $\frac{\partial u_3'}{\partial x_3}$ term. The PIV experiment doesn't have the pressure field and so the T_p term is not computed. In addition, the second-order derivatives such as the diffusion terms are also not computed. Thus the terms A_t, A, Π, T_u, P_r, ϵ^* and ϵ'^* of Equation 3.11 are only computed with the PIV datasets.

7.2.1 Effect of denoising the KHMH equation terms

The first step in this analysis is to observe the effect of denoising the velocity signals in the averaged values of the KHMH equation. The following are how the denoising is implemented in the terms of KHMH equation.

$$A_t = \frac{\partial}{\partial t}(\delta u_i')^2 = 2\delta u_i' \frac{\partial}{\partial t}(\delta u_i') = 2 \underbrace{\delta u_i'}_{system_a} \underbrace{\frac{\partial}{\partial t}(\delta u_i')}_{system_b} \tag{7.6}$$

$$\begin{aligned} \Pi = \delta u_j' \frac{\partial}{\partial r_j}(\delta u_i)^2 &= 2\delta u_i' \delta u_j' \frac{1}{2}\left(\left.\frac{\partial u_i'}{\partial x_j}\right|_2 + \left.\frac{\partial u_i'}{\partial x_j}\right|_1 \right) \\ &= \underbrace{\delta u_i'}_{system_a} \underbrace{\delta u_j'}_{system_b} \underbrace{\left(\left.\frac{\partial u_i'}{\partial x_j}\right|_2 + \left.\frac{\partial u_i'}{\partial x_j}\right|_1 \right)}_{system_a} \end{aligned} \tag{7.7}$$

$$\begin{aligned} P_r = 2\delta u_i' \delta u_j' \frac{\partial}{\partial r_j}(\delta \overline{u_i}) &= 2\delta u_i' \delta u_j' \frac{1}{2}\left(\left.\frac{\partial \overline{u_i}}{\partial x_j}\right|_2 + \left.\frac{\partial \overline{u_i}}{\partial x_j}\right|_1 \right) \\ &= \underbrace{\delta u_i'}_{system_a} \underbrace{\delta u_j'}_{system_b} \underbrace{\left(\left.\frac{\partial \overline{u_i}}{\partial x_j}\right|_2 + \left.\frac{\partial \overline{u_i}}{\partial x_j}\right|_1 \right)}_{system_a} \end{aligned} \tag{7.8}$$

$$\begin{aligned} A = \overline{u_j^*} \frac{\partial}{\partial x_j}(\delta u_i')^2 &= 2\delta u_i' \overline{u_j^*} \left(\left.\frac{\partial u_i'}{\partial x_j}\right|_2 - \left.\frac{\partial u_i'}{\partial x_j}\right|_1 \right) \\ &= 2 \underbrace{\delta u_i'}_{system_a} \underbrace{\overline{u_j^*}}_{system_b} \underbrace{\left(\left.\frac{\partial u_i'}{\partial x_j}\right|_2 - \left.\frac{\partial u_i'}{\partial x_j}\right|_1 \right)}_{system_a} \end{aligned} \tag{7.9}$$

$$T_u = u_j^{*'}\frac{\partial}{\partial x_j}(\delta u_i')^2 = 2\delta u_i' u_j^{*'}\left(\left.\frac{\partial u_i'}{\partial x_j}\right|_2 - \left.\frac{\partial u_i'}{\partial x_j}\right|_1\right)$$
$$= 2\underbrace{\delta u_i'}_{system_a}\underbrace{u_j^{*'}}_{system_b}\underbrace{\left(\left.\frac{\partial u_i'}{\partial x_j}\right|_2 - \left.\frac{\partial u_i'}{\partial x_j}\right|_1\right)}_{system_a} \tag{7.10}$$

This denoise method is based on two things : (a) product of a quantity with itself at the same physical point, results in the sum of the true value of the product and the product of noise; (b) product of quantity with its derivatives in space or time are denoised because the noise of a quantity and its derivative is not correlated.

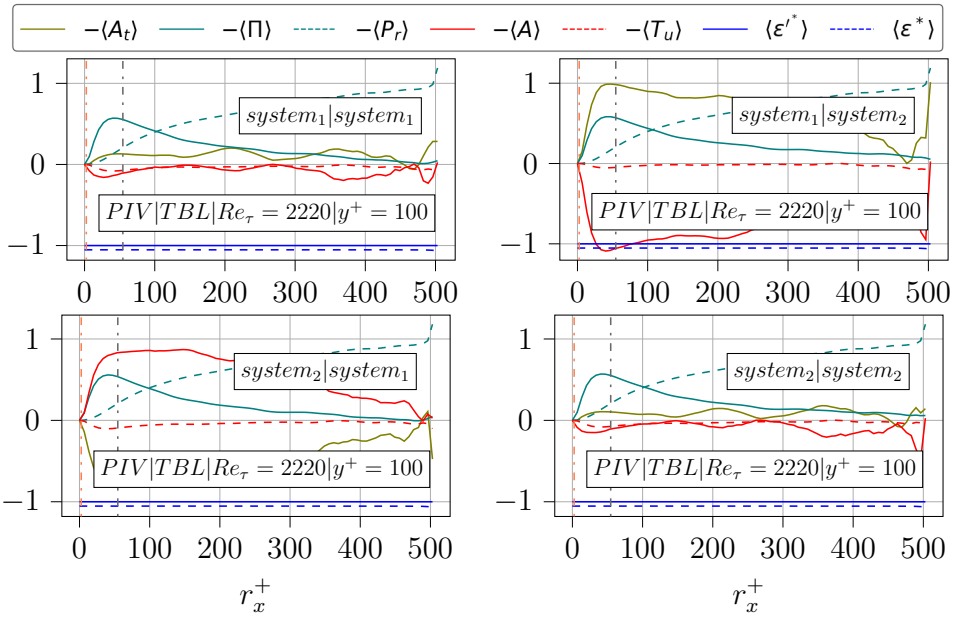

Figure 7.10: Spatio-temporal averaged values of KHMH equation terms from PIV datasets at $y^+ = 100$ in the r_x direction, using different combinations of two S-PIV systems at $Re_\tau = 2220$

Figure 7.10 shows the Spatio-temporal averaged values of KHMH equation terms obtained by the use of different combinations of S-PIV systems. It is observed that the terms $-\langle\Pi\rangle$, $-\langle P_r\rangle$, $\langle\epsilon^*\rangle$ and $\langle\epsilon'^*\rangle$ doesn't vary, with the use of different S-PIV systems in their computation. The terms $-\langle A_t\rangle$ and $-\langle A\rangle$ are observed to be less than $0.2\langle\epsilon'^*\rangle$ at all scales when computed using the same system. However, when different systems are used, their averages are of the order of $\langle\epsilon'^*\rangle$ at small and medium scales and approach zero approximately at $r_x^+ = 500$. This is investigated in detail and was found to have a bias error with the PIV measurement. More detail of this investigation is given in Appendix C.2.

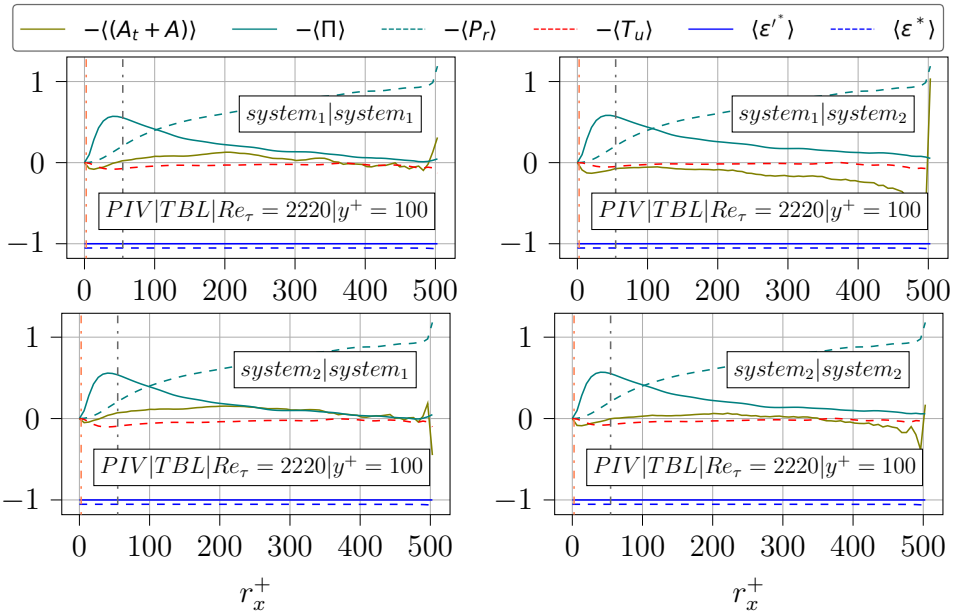

Figure 7.11: As Figure 7.10, but with the inclusion of $-\langle A_t + A\rangle$ term and the exclusion of $-\langle A_t\rangle$ and $-\langle A\rangle$ terms

Figure 7.11 shows the Spatio-temporal averaging of KHMH equation terms, where the terms $-\langle A_t\rangle$ and $-\langle A\rangle$ are added and are presented together. It can be observed that $\langle A_t + A\rangle$ with its computation in all combinations of two S-PIV systems. Thus it can be inferred that the bias error which was observed with $-\langle A_t\rangle$ and $-\langle A\rangle$ when they are computed from two different S-PIV systems is approximately equal and opposite and so they tend to nullify each other on $-\langle A_t + A\rangle$.

7.2.2 Comparison of averaged KHMH equation terms between PIV and DNS datasets

This subsection focuses on the Spatio-temporal average value of the KHMH equation terms at different wall distances in the PIV experiment of ZPG-TBL flow at $Re_\tau = 2220$ and $Re_\tau = 3840$. This is then compared with the results of DNS of TCF3000 computed without the $\frac{\partial u_1}{\partial x_3}$ and $\frac{\partial u_2}{\partial x_3}$ terms, to be compatible with that of PIV experiment. This is valid to all the terms except for the computation of the dissipation term, where the two missing spanwise direction derivatives are computed with the local axisymmetry assumption of George and Hussein [43].

Figures 7.12, 7.13 and 7.14 shows the Spatio-temporal average of the KHMH equation at different wall distances in streamwise direction with PIV experiments at two different Re_τ, compared with the same result from the DNS of TCF3000. The wall

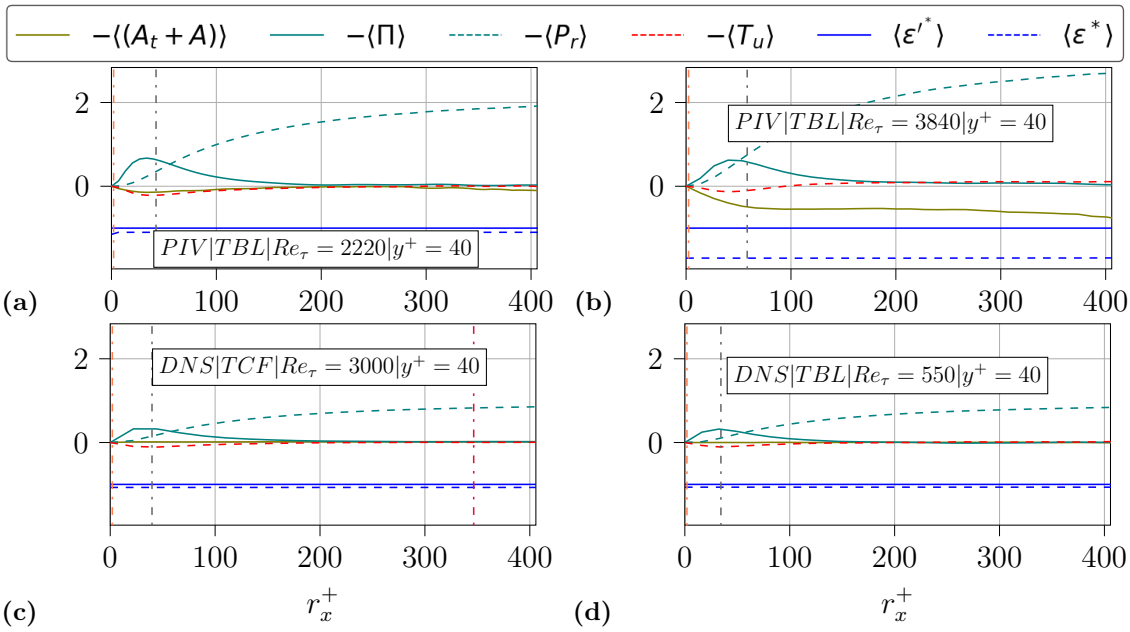

Figure 7.12: Spatio-temporal average value of the KHMH equation terms computed from PIV experiments at **(a)** Re_τ =2220, **(b)** Re_τ = 3840, and its comparison with **(c)** DNS of TCF3000 and **(d)** DNS of TBL550 in the streamwise direction at $y^+ = 40$

distances and the x-axes are all normalised by wall-units consistent with the similar results from the previous chapter. It is known from the PIV validation results that the dataset is not so trustworthy close to the wall, which is $y^+ < 25$ for $Re_\tau = 2220$ and $y^+ < 40$ for $Re_\tau = 3840$, and so only $y^+ = 40, 100, 140$ are considered for the analysis.

From the previous subsection, it is known that $-\langle A_t\rangle$ and $-\langle A\rangle$ are not converged enough when two S-PIV systems were used. However $-\langle A_t + A\rangle)$ is converged better than the individual terms. And also for the KHMH equation analysis in DNS datasets involved the $\langle A_t + A\rangle$ term to avoid the correlations due to the Taylor hypothesis.

On comparison of the results between the two PIV and two DNS datasets, it is observed that $-\langle\Pi\rangle$ is qualitatively the same between all the datasets. And between the two PIV datasets and TCF3000, $-\langle\Pi\rangle$ are similar quantitatively, and the peak value of this term is larger in PIV datasets than in the DNS datasets. The energy transfer in physical space is negligible at the wall distances studied in the present analysis. The difference between $\langle\epsilon^*\rangle$ and $\langle\epsilon'^*\rangle$ is approximately the same between the two DNS datasets and the PIV dataset at $Re_\tau = 2220$ at all the wall distances.

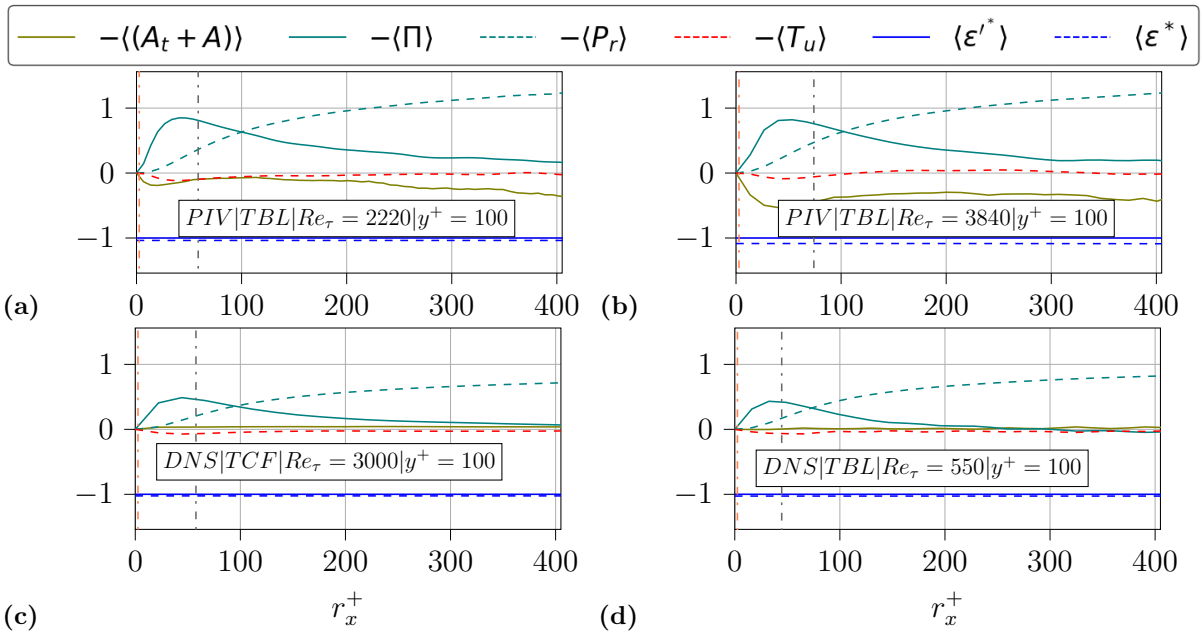

Figure 7.13: Spatio-temporal average value of the KHMH equation terms computed from PIV experiments at **(a)** Re_τ =2220, **(b)** Re_τ = 3840, and its comparison with **(c)** DNS of TCF3000 and **(d)** DNS of TBL550 in the streamwise direction at $y^+ = 100$

However in the PIV dataset at $Re_\tau = 3840$, the difference between $\langle\epsilon^*\rangle$ and $\langle\epsilon'^*\rangle$ are so high at $y^+ = 40$. At $y^+ = 100$ and 140, the difference is still higher than other datasets.

$-\langle P_r\rangle$ surpasses $\langle\epsilon'^*\rangle$ in the PIV datasets and the scale at which it surpasses increases with wall distance. This is not observed in the DNS datasets at the wall distances considered in the analysis. The $-\langle A_t + A\rangle$ term converges to a non-zero value at all scales in both PIV datasets, and the converged value is higher at $Re_\tau = 3840$ than at $Re_\tau = 2220$.

Conclusion

The $-\langle\Pi\rangle$ appears to be similar between all the datasets used in the analysis, however the peak of this term is overpredicted in the PIV datasets when compared to the same in DNS datasets. The $-\langle P_r\rangle$ surpasses $\langle\epsilon'^*\rangle$ at around the same scale in both the PIV datasets and this is not observed at any of the DNS datasets at this wall distance. From the previous subsection, it is known that $\langle\epsilon'^*\rangle$ is comparable to DNS with PIV at $Re_\tau = 2220$ when $y^+ > 25$. On the other hand, for PIV at $Re_\tau = 3840$, the normalised dissipation D^+ is approximately equal to that of DNS

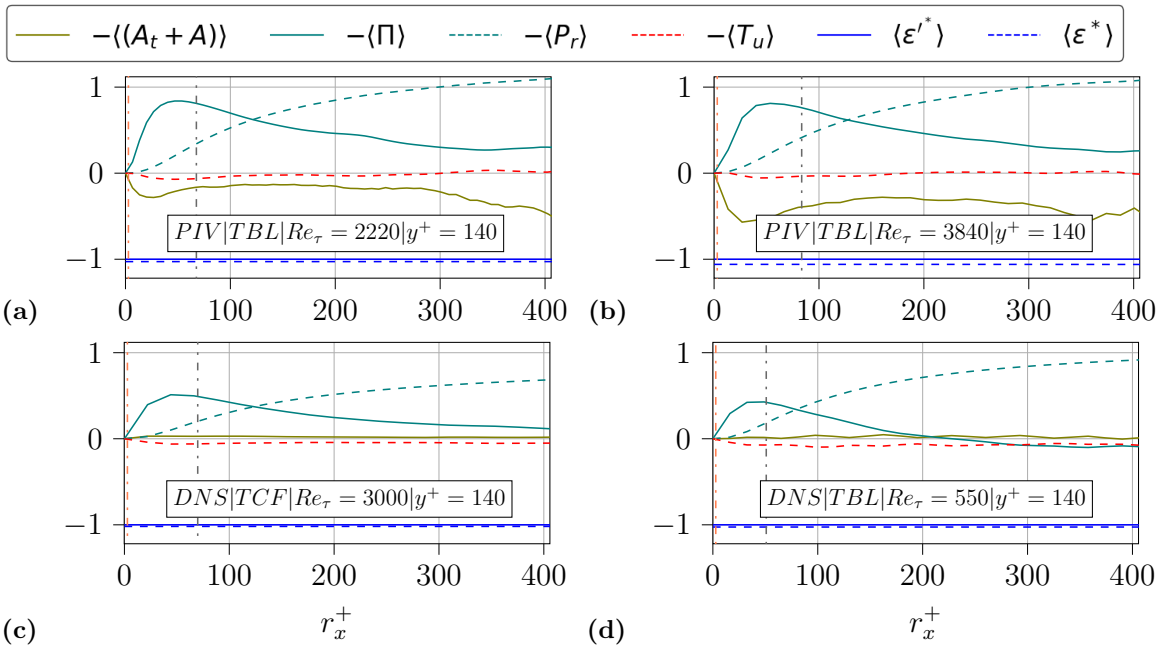

Figure 7.14: Spatio-temporal average value of the KHMH equation terms computed from PIV experiments at **(a)** Re_τ =2220, **(b)** Re_τ = 3840, and its comparison with **(c)** DNS of TCF3000 and **(d)** DNS of TBL550 in the streamwise direction at $y^+ = 140$

when $y^+ > 200$, which could explain the huge difference between $\langle\epsilon^*\rangle$ and $\langle\epsilon'^*\rangle$ with this dataset at $y^+ = 40$. At $y^+ = 100, 140$, the $\langle\epsilon^*\rangle$ and $\langle\epsilon'^*\rangle$ approximately resembles that of DNS and this could be attributed to the reduced difference between the normalised dissipation D^+ between the PIV and DNS datasets at those wall distances. The $\langle A_t + A\rangle$ converges to a non-zero value in both the PIV datasets and the value is higher at Re_τ = 3840, which could be attributed to the bias error in the measurement.

7.3 Instantaneous KHMH equation terms

After observing the Spatio-temporal average of the KHMH equation terms, the next step would be to quantify the instantaneous part of the same terms of the equation. One way to proceed in this direction is to observe the standard deviation of different terms normalised by the standard deviation of the dissipation term. This way it is possible to compare different datasets.

Figure 7.15 shows the instantaneous values of KHMH equation terms obtained from PIV at $Re_\tau = 2220$, which is then compared with that of DNS at $Re_\tau = 3000$. The

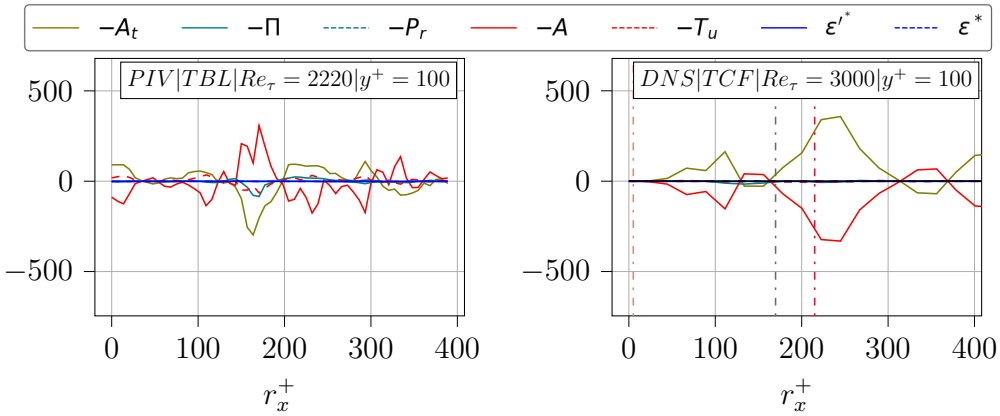

Figure 7.15: Instantaneous values of the KHMH equation terms normalised by the absolute value of ϵ'^* computed from PIV at $Re_\tau = 2220$ (left) and DNS of TCF3000 (right) in streamwise direction at $y^+ = 100$

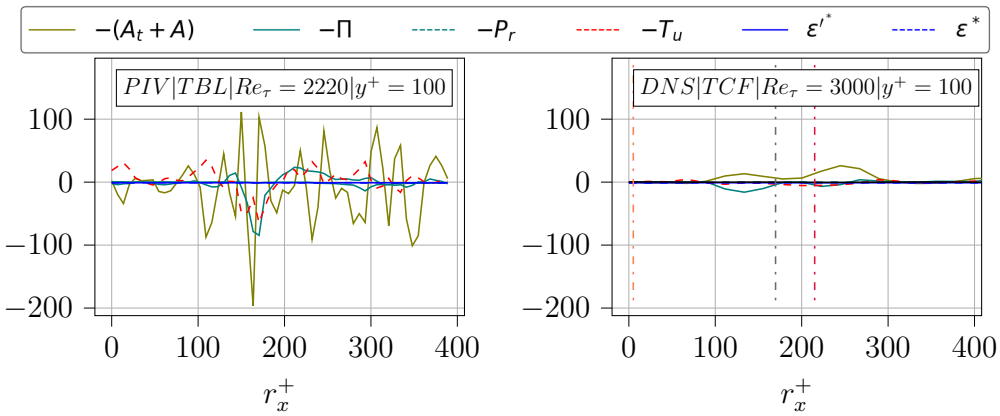

Figure 7.16: Instantaneous values of the KHMH equation terms normalised by the absolute value of ϵ'^* excluding A_t, A and including $A_t + A$, computed from PIV at $Re_\tau = 2220$ (left) and DNS of TCF3000 (right) in streamwise direction at $y^+ = 100$

high anti-correlation between the A_t and A terms are observed in both the datasets and it is known that this is due to the Taylor hypothesis. These two quantities are added together to obtain $A_t + A$, and this is then plotted with other instantaneous KHMH equation is shown in Figure 7.16 at $y^+ = 100$. It is observed that with PIV, the $A_t + A$ term fluctuates much higher than the energy transfer terms. On the other hand, $A_t + A$ fluctuates approximately of the same order as Π in the DNS datasets.

Effect of denoising the KHMH equation terms

Similar to the previous subsection, the denoising of the variables were performed in the computation of the standard deviation of the terms. There are two steps in performing this process. The first step is to denoise the computation of the KHMH terms using Equations 7.6, 7.7, 7.8, 7.9, 7.10. The second step is to compute the same terms by replacing system 1 for $system_a$ and system 2 for $system_b$ giving terms in '$system_{a|b}$'. The two systems are then swapped to giving the term with '$system_{b|a}$'. This results in two sets of terms which can be used with the following formula to obtain the denoised standard deviation for the term 'a' is computed by :

$$\sigma_a = \sqrt{\langle (\underbrace{a}_{system_{a|b}} - \underbrace{\langle a \rangle}_{system_{a|a}})(\underbrace{a}_{system_{b|a}} - \underbrace{\langle a \rangle}_{system_{b|b}}) \rangle} \tag{7.11}$$

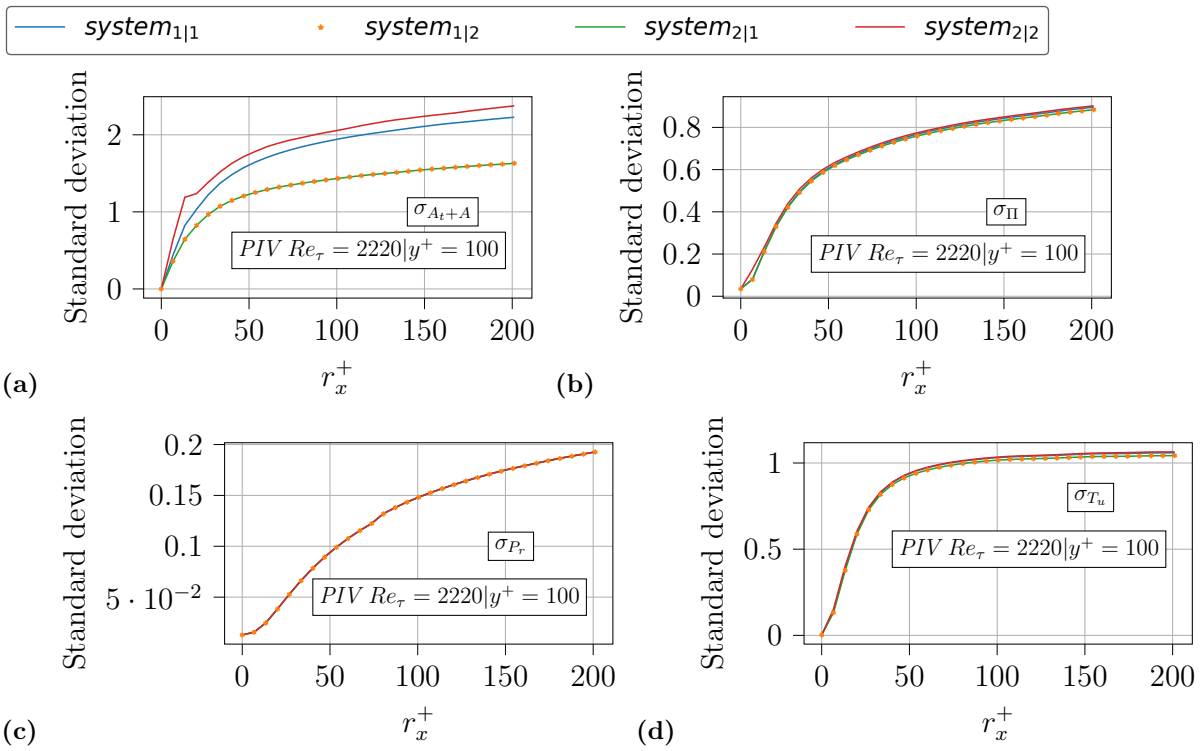

Figure 7.17: Standard deviation results of KHMH equation terms computed with different combinations of both S-PIV systems in the streamwise direction for the PIV dataset at $Re_\tau = 2220$

Figure 7.17 shows the standard deviation computed with different combinations of the two S-PIV systems in the PIV dataset at $Re_\tau = 2220$. It is observed that for all

the KHMH equation terms, the use of $system_{1|2}$ and $system_{2|1}$ has the same results for the standard deviation. And it is observed that only the standard deviation of $A_t + A$ has an appreciable difference when comparing the value using one S-PIV system and two S-PIV.

It is known that the multiplication of velocities at the same point in the velocity field results in the multiplication of noise. And so the use of two different systems provides a way to avoid this problem to some extent by using the velocity value from two different systems which have uncorrelated noise. From the results of the instantaneous values of KHMH equation terms, it is known that the highly fluctuating terms are A_t and A. After adding the two terms to get past the Taylor hypothesis, it was observed that $A_t + A$ is highly fluctuating compared to the other KHMH equation. And it was observed that the average values of Π, P_r and T_u are approximately the same irrespective of which combination of the two S-PIV systems are used. So this could explain that the effect of denoising strongly influences the results of the standard deviation of $A_t + A$ term.

7.3.1 Comparison of the averaged KHMH equation terms between PIV and DNS datasets

After observing the instantaneous KHMH equation terms behaviour with PIV datasets, followed by observing the effect of denoising in the standard deviation of the KHMH equation terms, the next step is to compare the denoised standard deviation from the two PIV datasets with that of DNS of TCF3000. The standard deviation of the KHMH equation terms are normalised by the standard deviation of Π.

Observation

Figure 7.18, 7.18 and 7.18 shows the standard deviation of KHMH equation terms $A_t + A$, Π, T_u and P_r in the two PIV datasets and the DNS of TCF3000 at $y^+ = 40$, 100 and 140. It is observed that the standard deviation of T_u is approximate of the same order as the standard deviation of Π at all wall distances in all three datasets. The production term has approximately the same standard deviation in all the three datasets at $y^+ = 100$ and 140. At $y^+ = 40$, however, the standard deviation of P_r is the highest in the PIV at $Re_\tau = 3840$, followed by PIV at $Re_\tau = 2220$ and then the DNS of TCF3000. The standard deviation of $A_t + A$ is similarly highest in PIV at $Re_\tau = 3840$, followed by PIV at $Re_\tau = 2220$ and then the DNS at $Re_\tau = 3000$ at all wall distances.

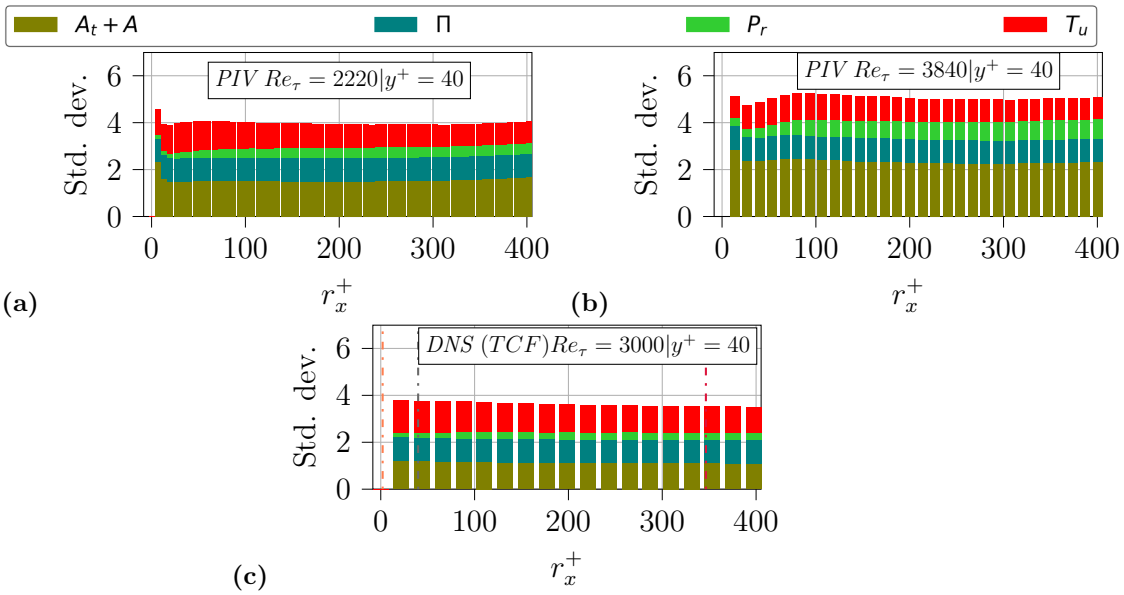

Figure 7.18: Standard deviation of KHMH equation terms at $y^+ = 40$, from **(a)** PIV at $Re_\tau = 2220$, **(b)** PIV at $Re_\tau = 3840$, **(c)** DNS of TCF3000. All terms of normalised by the standard deviation of Π

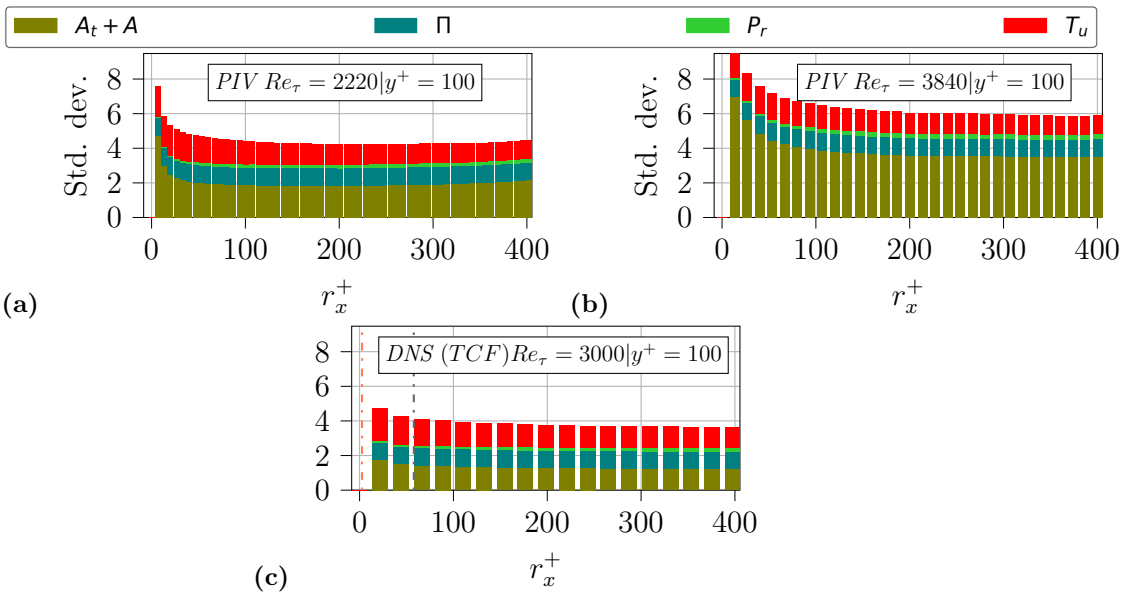

Figure 7.19: Standard deviation of KHMH equation terms at $y^+ = 100$, from **(a)** PIV at $Re_\tau = 2220$, **(b)** PIV at $Re_\tau = 3840$, **(c)** DNS of TCF3000. All terms of normalised by the standard deviation of Π

Discussion

The two energy transfer terms are the least affected by the noise of the data. This was also observed in their average values. The production term is not affected by

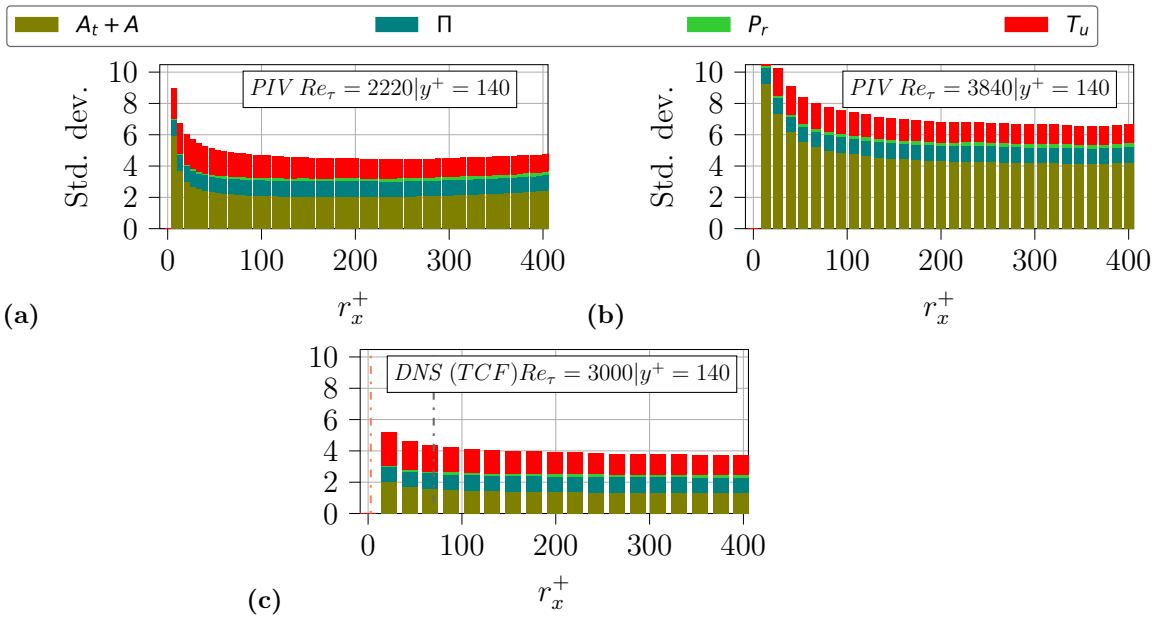

Figure 7.20: Standard deviation of KHMH equation terms at $y^+ = 140$, from **(a)** PIV at $Re_\tau = 2220$, **(b)** PIV at $Re_\tau = 3840$, **(c)** DNS of TCF3000. All terms of normalised by the standard deviation of Π

the noise in the average, however, the standard deviation of this term at $y^+ = 40$ is not comparable between the two PIV datasets. $A_t + A$ is the most affected term in terms of noise and the process of using two systems to denoise. This is also true with the average value of this term, on the other hand, it was observed that their average value resembled that of DNS when it was computed with only one system. The standard deviation did reduce its value with two systems when compared to the same value computed with one system alone. However, it is still not comparable to the DNS datasets, where $A_t + A$ is approximate of the order of standard deviation of Π at all wall distances.

7.4 Correlation coefficient of KHMH equation terms

The KMHH equation analysis of DNS datasets in the previous chapter started with the averaged values of KHMH equation terms, followed by the instantaneous behaviour of KHMH equation with the standard deviation of each term and is then followed by the correlation coefficient between $A_t + A$ and other terms of the KHMH equation, and then between T_p and other terms of the KHMH equation. In the

present KHMH equation analysis with PIV datasets, the pressure field is not available, and so the correlation coefficient between $A_t + A$ and other terms of the KHMH equation is focussed in this section.

Effect of denoising the KHMH equation terms

Before comparing the results between PIV and DNS datasets, it is important to observe the effect of denoise in the computation of the correlation coefficient with two S-PIV systems. Similar to previous sections, the effect of denoising is performed for the computation of correlation coefficients of KHMH equation terms. The individual terms are computed using Equations 7.6, 7.7, 7.8, 7.9, 7.10, and the standard deviation is computed using Equation 7.11. The correlation coefficient between term 'Q_1' and 'Q_2' is computed by :

$$corr(Q_1, Q_2) = \frac{(\langle \underbrace{Q_1}_{system_{a|b}} - \underbrace{\langle Q_1 \rangle}_{system_{a|a}})(\langle \underbrace{Q_2}_{system_{b|a}} - \underbrace{\langle Q_2 \rangle}_{system_{b|b}})}{\sqrt{(\underbrace{Q_1}_{system_{a|b}} - \underbrace{\langle Q_1 \rangle}_{system_{a|a}})(\underbrace{Q_1}_{system_{b|a}} - \underbrace{\langle Q_1 \rangle}_{system_{b|b}})} \sqrt{(\underbrace{Q_2}_{system_{a|b}} - \underbrace{\langle Q_2 \rangle}_{system_{a|a}})(\underbrace{Q_2}_{system_{b|a}} - \underbrace{\langle Q_2 \rangle}_{system_{b|b}})}} \tag{7.12}$$

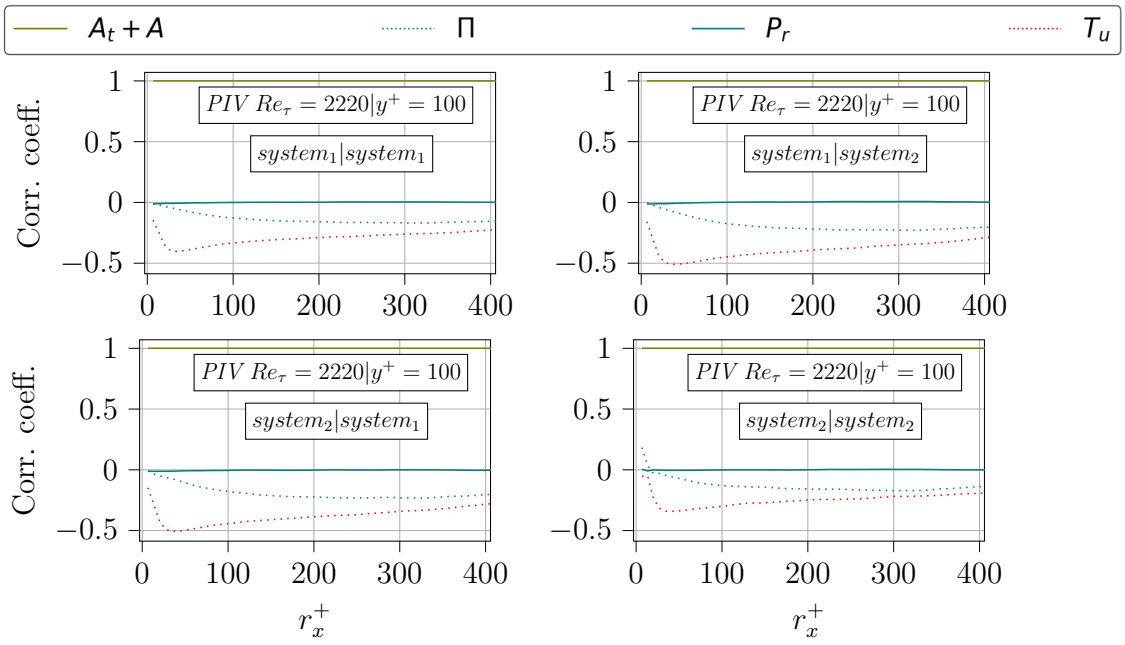

Figure 7.21: Correlation coefficient of KHMH equation terms with $A_t + A$ in streamwise direction separation of PIV at $Re_\tau = 2220$ by using a combination of two systems '1' and '2' at $y^+ = 100$

Figure 7.21 shows the correlation coefficient of $A_t + A$ with other terms of the KHMH equation with different combinations of two S-PIV systems at $y^+ = 100$. It is observed that the correlation coefficient values between $A_t + A$ and the two energy transfer terms Π and T_u have higher absolute values when the two independent systems are used. And it gives approximately the same results irrespective of using system 1 and system 2 or vice-versa, is used in place of the $system_a$ or $system_b$. This can be explained by the lower standard deviation of $A_t + A$ when two systems are used in their computation. It is beneficial to use the two S-PIV systems to compute the standard deviation value and in turn the correlation coefficient values. Hence the denoised correlation coefficient is used in both the PIV datasets to compare the results with that of DNS datasets.

7.4.1 Comparison of correlation coefficients between PIV and DNS datasets

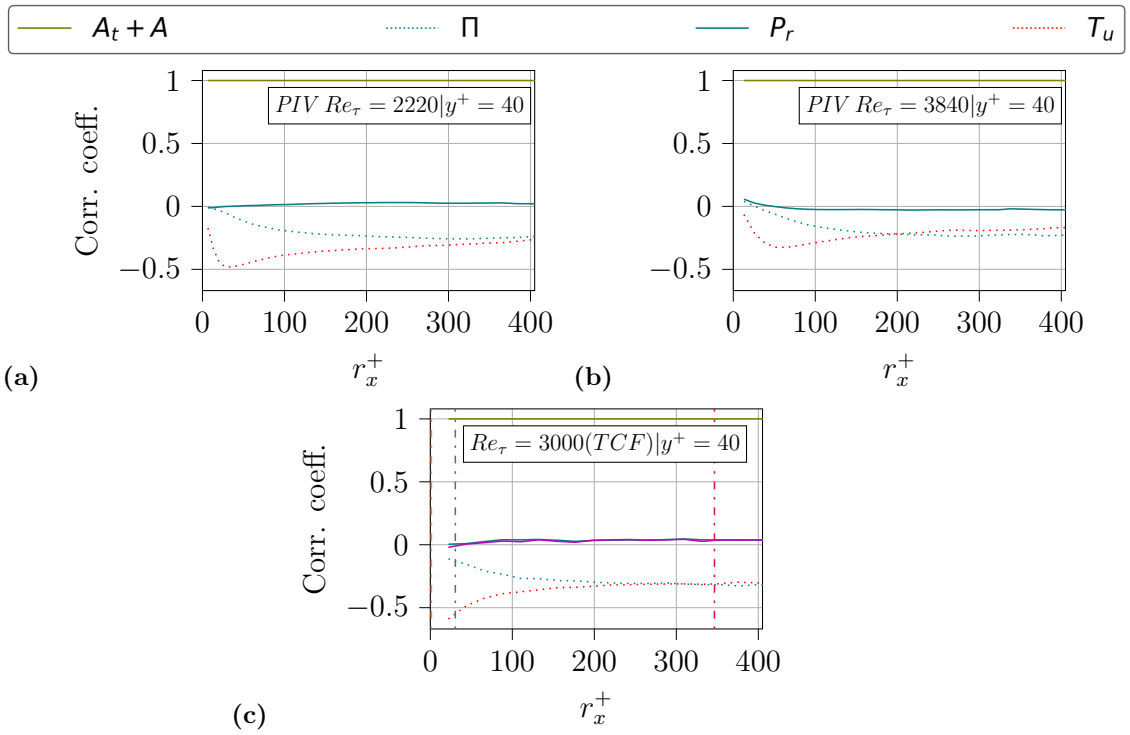

Figure 7.22: Correlation coefficient of the four KHMH terms with $A_t + A$ in streamwise direction separation of PIV at **(a)** $Re_\tau = 2220$, **(b)** $Re_\tau = 3840$ and is compared with the results of DNS of TCF at **(c)** $Re_\tau = 3000$ at $y^+ = 40$

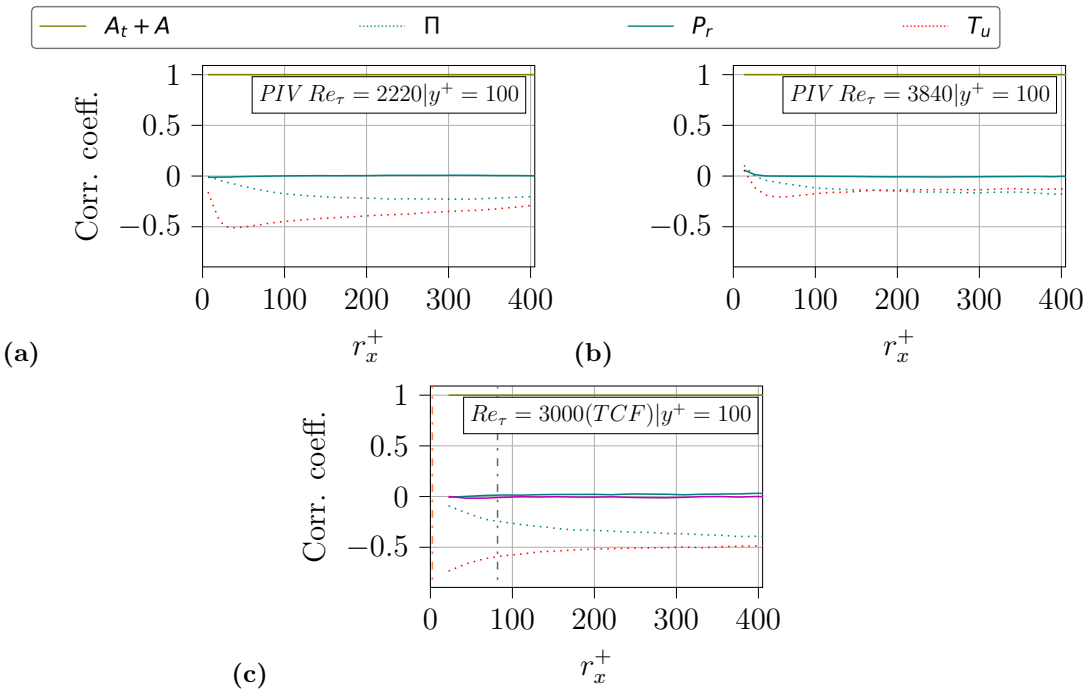

Figure 7.23: Correlation coefficient of the four KHMH terms with $A_t + A$ in streamwise direction separation of PIV at **(a)** $Re_\tau = 2220$, **(b)** $Re_\tau = 3840$ and is compared with the results of DNS of TCF at **(c)** $Re_\tau = 3000$ at $y^+ = 40$

Figures 7.22, 7.23 and 7.24 shows the correlation coefficient of $A_t + A$ with other terms of KHMH equation in streamwise direction at different wall distances with PIV datasets at $Re_\tau = 2220$ and $Re_\tau = 3840$, which is compared with the DNS of TCF3000. It is observed for the PIV dataset at $Re_\tau = 2220$, that the correlation coefficient between $A_t + A$ and Π at large scales is of the order of 0.2, between $A_t + A$ and T_u is of the order of 0.45 at large scales at all three wall distances. And it is observed for the PIV dataset at $Re_\tau = 3840$, that the correlation coefficient between $A_t + A$ and Π at large scales is of the order of 0.15, between $A_t + A$ and T_u is of the order of 0.35 at large scales at all three wall distances.

With the DNS datasets, the large scale correlation coefficient between $A_t + A$ and Π, $A_t + A$ and T_u are of the order of 0.3 at $y^+ = 40$, 0.45 at $y^+ = 100$, and 0.5 at $y^+ = 140$. From the previous subsection, it is known that the present correlation coefficient computed from two S-PIV systems is higher than that computed with one system only. The reduction in correlation coefficient when the Reynolds number is increased in PIV datasets could be due to the limited spatial resolution of the PIV dataset at $Re_\tau = 3840$. However, the reduced correlation coefficient between

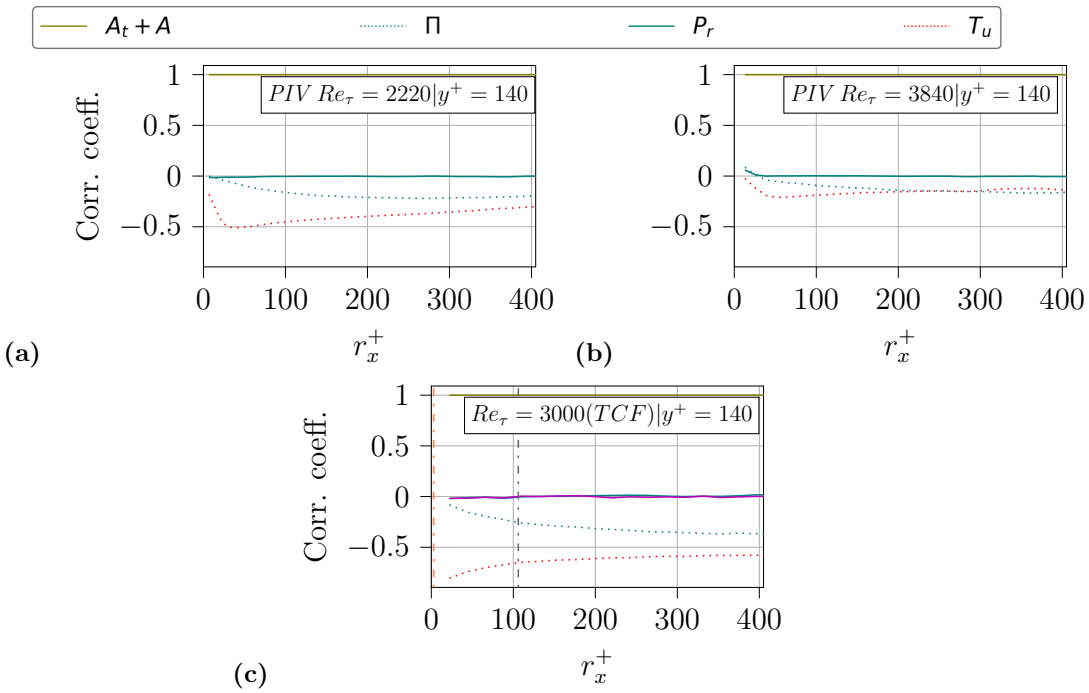

Figure 7.24: Correlation coefficient of the four KHMH terms with $A_t + A$ in streamwise direction separation of PIV at **(a)** $Re_\tau = 2220$, **(b)** $Re_\tau = 3840$ and is compared with the results of DNS of TCF at **(c)** $Re_\tau = 3000$ at $y^+ = 40$

DNS datasets and the PIV datasets could be due to the presence of noise in the instantaneous values of velocity signal.

To mitigate the problem of noise in PIV experiment, the two S-PIV system idea is used. Although the average values of the KHMH equation didn't have much influence on noise, the results were different for the standard deviation of the KHMH equation. In addition, the numerical scheme used for the computation of derivatives were optimised to have the least amount of noise. And the use of two S-PIV systems did indeed increase the correlation coefficient between the $A_t + A$ and the two energy transfer terms. However, all these methods of reduction of noise do reduce the noise when there is average involved. The noise in the instantaneous velocity signal is still present and this could be the reason for not having the same values of the correlation coefficient between the DNS and PIV experiments.

The correlation coefficient between $A_t + A$ and other KHMH equation terms is not the only result that could be obtained from experiments. There is a strong anti-correlation between A_t and A and this is observed in the instantaneous values of A_t

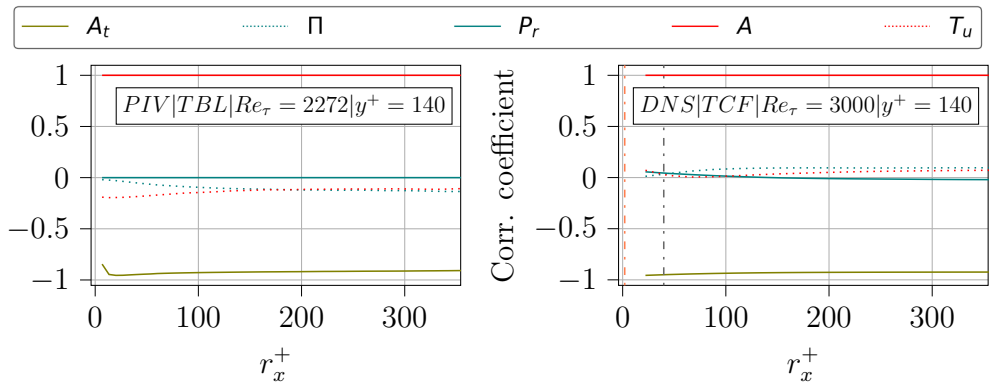

Figure 7.25: Correlation coefficient of advection term A with other terms of the KHMH equation in PIV experiments (left) and DNS of TCF3000 (right)

and A in both PIV and DNS datasets in Figure 7.15. Thus the correlation coefficient of advection term A is performed with both PIV at $Re_\tau = 2220$ and DNS dataset of TCF3000 is shown in Figure 7.25 at $y^+ = 140$. It can be observed that with the exception of the very small scales the high correlation coefficient between A_t and A are well computed with the PIV datasets and is nearly equal to the same computed from TCF3000.

It is known that the A_t and A have the highest fluctuation of all the KHMH equation terms, and so even with the presence of noise, the correlation coefficient is comparable between DNS and PIV datasets. On the other hand, with the term $A_t + A$ it becomes too difficult to find the correlation coefficient with other terms.

7.4.2 Addition of noise to the DNS datasets

In the previous section, the correlation coefficients of $A_t + A$ with other KHMH equation terms are studied. It is observed that the correlation coefficients computed by the PIV datasets are lower than those computed with the equivalent DNS datasets. To investigate this part further, it is decided to add noise to the TCF3000 dataset and compute the correlation coefficient of $A_t + A$ and the other terms of the KHMH equation.

To simulate the effect of noise, Additive Gaussian White Noise (AGWN) is added to the velocity field of TCF3000 and every KHMH equation term is computed. It is known that $\frac{\partial \boldsymbol{u'}}{\partial t}$ is computed by decomposing Navier-Stokes' equation in this dataset. And so computing $\frac{\partial \boldsymbol{u'}}{\partial t}$ after the noise is added to the velocity field results in a correlated noise between the time derivative and other terms. To avoid this

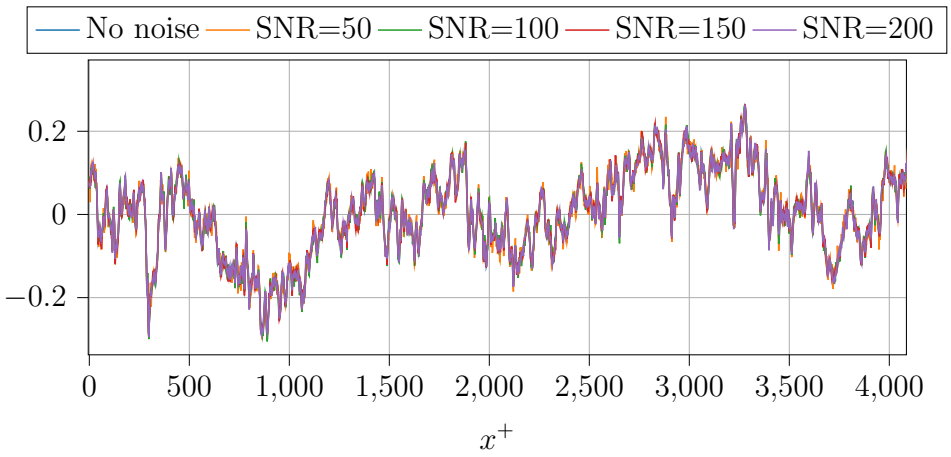

Figure 7.26: Instantaneous velocity signals with different intensities of adding Additive Gaussian White Noise (AGWN) for DNS of TCF3000 datasets

problem, the time derivative term is computed without the addition of noise. This is followed by the addition of noise to the velocity field

To study the influence of the intensity of noise in the correlation coefficient results, different levels of noise is added by adjusting the Signal-to-Noise Ratio (SNR) parameter for 50, 100, 150, 200. For the TCF3000 to resemble that of the experiment, the Least Square method is used for obtaining the derivatives.

The instantaneous velocity signal with different levels of noise is given in Figure 7.26. The corresponding correlation coefficient computed with different levels of noise is given in Figure 7.27. On comparing the correlation coefficient of $A_t + A$ computed with the use of only one S-PIV system, with that from DNS with added noise, the results with SNR = 150 matches approximately with the result. Thus it is shown that a noise that is 1/150 times the velocity signal results in the correlation coefficient comparable to that, obtained from S-PIV experiments. In addition, the reduction of the absolute correlation coefficient between $A_t + A$ and T_u at small scales is also replicated in the DNS with added noise. This could be attributed to the fact that when small scales are considered for $(\delta\mathbf{u})^2$, the two points considered are close together such that their difference is mostly dominated by the noise of the signal.

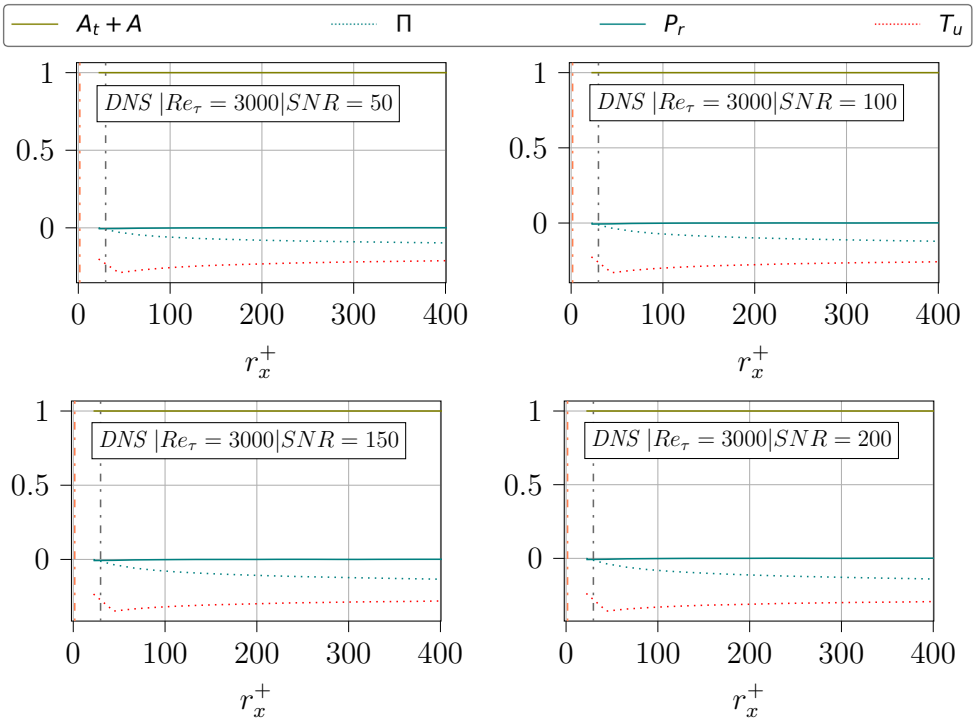

Figure 7.27: Correlation coefficient of $A_t + A$ and other KHMH equation terms in TCF3000 with different levels of noise

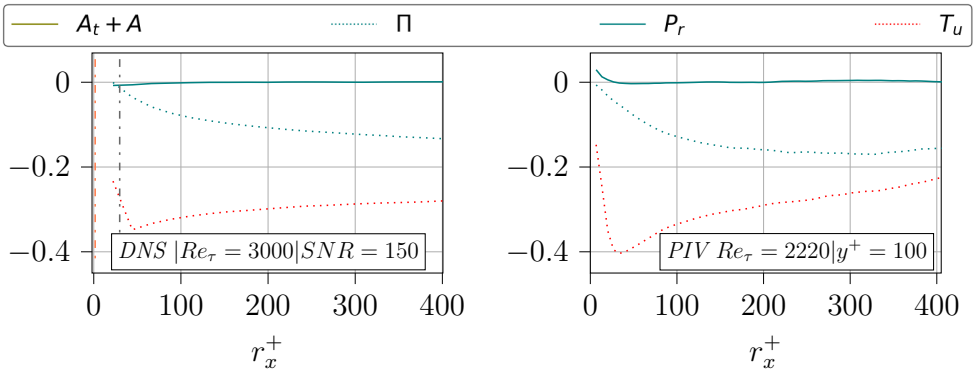

Figure 7.28: Correlation coefficient of $A_t + A$ term in DNS of TCF3000 with added noise (left) and PIV experiments (right)

Conclusion

With the use of the PIV dataset at $Re_\tau = 2220$, a high correlation coefficient of about -0.9 between A_t and A is replicated to high accuracy when compared to the same result with DNS of TCF3000. The large scale correlation coefficient of $A_t + A$ and the two energy transfer terms (Π, T_u) is of the order of -0.2 with PIV datasets with

one S-PIV system. When the PIV dataset is denoised by using two S-PIV systems, the large scale correlation coefficient between $A_t + A$ and two energy transfer terms (Π, T_u) improves to reach about -0.25. Thus the sweeping decorrelation hypothesis is observed in PIV datasets, although with a lower correlation coefficient of the individual terms.

With the use of the PIV dataset at $Re_\tau = 3840$, the correlation coefficient between $A_t + A$ and the two energy transfer terms (Π, T_u) is lower than that of the PIV dataset at $Re_\tau = 2220$. This can be explained considering the spatial resolution of the PIV dataset at $Re_\tau = 2220$ and $Re_\tau = 3840$ is of the order of $2.3\eta - 2.8\eta$ and $4.6\eta - 5.6\eta$ respectively. The better results of KHMH equation terms from PIV at $Re_\tau = 2220$ shows that the required spatial resolution to be the order of 2.3-2.8η. It is possible to increase the spatial resolution by zooming into the Field of View, however, this will result in the decrease of the r_x values obtainable from the PIV dataset.

The computation of the correlation coefficient of DNS datasets with the addition of noise to the DNS datasets revealed that the AGWN of SNR value of 150 replicates the correlation coefficient of $A_t + A$ with the two energy transfer terms in the PIV dataset at $Re_\tau = 2220$ with the use of one S-PIV system. This shows that the sensitivity of this particular correlation coefficient to the noise in the dataset. Such analysis can help to have an idea of the possible results that can be obtained from the PIV datasets thereby help to design better PIV experiments for the KHMH equation analysis.

Part IV

Conclusion

Chapter 8

Conclusion and Perspectives

The main objective of the present work is to investigate the process of the energy transfer occurring in wall-bounded turbulent flows at high Reynolds numbers. This is achieved by understanding the different terms of the Kármán-Howarth-Monin-Hill (KHMH) equation which pertains to different physical processes occurring in the flow. This knowledge would serve to improve the theory of turbulent flows and turbulence modelling.

The present work is broadly divided into two parts : (a) Analysis of the KHMH equation term in the DNS of Turbulent channel flows at $Re_\tau = 550$ and 3000, and in the DNS of Zero Pressure Gradient Turbulent Boundary Layer flow at $Re_\tau = 550$. (b) To design the PIV experiment in the ZPG Turbulent Boundary Layer wind tunnel at LMFL at $Re_\tau = 2220$ and 3840 based on the results from the DNS datasets.

The advantage of the KHMH equation is that it gives possibilities to study space and scale transfers at given locations with/without averaging, therefore both mean quantities and fluctuations. The uses of the KHMH equation to study the phenomenon of energy cascade in Turbulent Channel Flow and Turbulent Boundary Layer with both DNS and PIV experiments are two-fold : (a) The present tool and the analysis to study the KHMH equation can be extended to other different DNS datasets which would help to unravel the multitude of results of that particular DNS datasets, (b) the present PIV experiment shows the feasibility of computing different terms of KHMH equation in ZPG TBL flow, which would eventually help to design the experiments in Adverse Pressure Gradient (APG) TBL flow in the LMFL wind tunnel, and also serves to show the possibility of implementation of other PIV experiments in flow geometries for which the equivalent DNS datasets are difficult to perform or not available as of yet.

8.1 Summary of findings

8.1.1 Results from DNS datasets

The present work allows drawing various conclusions on the physics of wall-bounded turbulent flows based on the averaged and the instantaneous values of the terms of the KHMH equation and their evolution with different wall distances. The main conclusions are as follows.

Spatio-temporal average of KHMH equation terms

The Spatio-temporal averaged values of KHMH equation terms[54] in both TCF and TBL flows with zero or negligible averages are $-\langle A_t \rangle, -\langle A \rangle, \langle T_p \rangle$ and $\langle D_x \rangle$. And the dominant terms are $\langle D_{r2} \rangle$ near the Kolmogorov scale, $-\langle \Pi \rangle$ in the multiple ranges of scales dependent on wall distance, $-\langle P_r \rangle$ beyond the integral scale, $-\langle T_u \rangle$ near the centreline of the channel flow and the edge of the turbulent boundary layer, and the dissipation terms ($\langle \epsilon^* \rangle$, $\langle \epsilon'^* \rangle$) in all scales at all wall distances. In addition, near the edge of the boundary layer, $-\langle A \rangle$ and $\langle T_p \rangle$ are dominant in TBL550.

The $-\langle \Pi \rangle$ is dominant only at smaller scales in the buffer layer. With the increase of wall distance, $-\langle \Pi \rangle$ is dominant at larger scales. At the channel centreline and the edge of the boundary layer thickness, $-\langle \Pi \rangle$ is non-zero even at scales larger than δ. In TCF3000, $-\langle \Pi \rangle$ is approximately equal to $0.5\langle \epsilon'^* \rangle$ at $r_x = 9\delta$. A quick decomposition of the term revealed that the dominance of this term at very large scales is due to this term $\langle u_1' u_2' \frac{\partial u_1'}{\partial x_2} \rangle$, which is due to the correlation between the large and small scales of the flow[64].

The Spatio-temporal average values of the KHMH equation terms are different between the streamwise and spanwise directions. This is mainly observed between $-\langle \Pi \rangle$ and $-\langle P_r \rangle$. From the buffer layer, there are some scales in which production surpasses the $\langle \epsilon'^* \rangle$ and this positive peak of $-\langle P_r \rangle$ coincides with the negative peak of $-\langle \Pi \rangle$. The scales at which this peak occurs increases progressively with the increase of wall distance in the same way in all three DNS datasets when the wall distance is normalised by δ. Cimarelli et al.[23] observed this behaviour of $\langle \Pi \rangle$ in a DNS of TCF, to conclude that this is due to the spatial reverse cascade where the energy ascends towards the channel centreline in a straight line in (r_y, r_z, y) space.

A **modified Taylor microscale** derived for wall-bounded turbulent flows separately for the streamwise and spanwise direction is observed to scale the peak of $-\langle \Pi \rangle$ from outside the buffer layer until near the centreline of the channel flow

and the edge of turbulent boundary layer flow and is verified in all the three DNS datasets.

Instantaneous KHMH equation terms

The results of instantaneous behaviour of KHMH equation reveals another aspects of different terms which were masked in averages. The dominant terms in the instantaneous KHMH equation analysis are $A_t + A$, T_p, Π, T_u. And the fluctuations of these dominant terms are at least an order of magnitude higher than that of the fluctuation of the dissipation term (ϵ'^*), and it tends to increase with wall distance. The dominance of $A_t + A$, Π and T_u can be explained by the anti-alignment of the local and convective acceleration terms of turbulent channel flows. When the standard deviation of the terms are normalised by the standard deviation of Π, the magnitude of the standard deviation of all the terms are same between the TCF at different Reynolds number and the TBL flow.

A high correlation coefficient between $A_t + A$ and (Π, T_u) of the order of -0.5 from $y^+ = 12$ to $y/\delta = 1$ is observed in TCF550 and TBL550. And the correlation coefficient with $A_t + A$ is between 0.65 to 0.8 with $\Pi + T_u$ from $y^+ = 12$ to $y/\delta = 1$ in TCF550 and TBL550. Near the wall, this is explained by $A_t + A$ balancing the $\Pi + T_u$, and away from the wall, this could be due to the large scale structures sweeping the small scale structures (sweeping decorrelation hypothesis).

A high correlation coefficient is observed between $A_t + A$ and T_p only near the wall, of the order of 0.3 in all three DNS datasets. A correlation coefficient of the order of 0.35-0.45 is observed between T_p and the two energy transfer terms (Π, T_u). The correlation coefficient between T_p and $\Pi + T_u$ is of the order of 0.5 to 0.65. This high correlation coefficient of both the energy transfer terms with $A_t + A$ and T_p reflects the relation between the non-linear term and time derivative term, and non-linear term and pressure term in the Navier-Stokes' equation. This argument that the non-linear term is causing this correlation coefficient is solidified by the fact that the correlation coefficient between $A_t + A$ and T_p is negligible except near the wall.

The increase of Reynolds number increases the correlation coefficient between $A_t + A$ and $\Pi + T_u$, which is noticeable from $y^+ = 12$ till the centreline of the channel. On the other hand, the increase of Reynolds number results in a reduction of the correlation coefficient between T_p and $\Pi + T_u$ when $y^+ > 100$.

The high correlation coefficient of -0.5 is observed between $A_t + A$ and the two energy transfer terms does extend to scales of the order of 9δ value in the DNS of

TCF at $Re_\tau = 3000$. On decomposing both the energy transfer terms reveals that the terms δu_1 and $\frac{\partial}{\partial x_j}(\delta u_1)$ contributes the most, especially the $\delta u_1 \frac{\partial}{\partial x_1}(\delta u_1)$, to the correlation coefficient between Π and $A_t + A$, and between Π and T_p.

Scale-by-scale energy cascade

On observing the radial component of interscale energy transfer term (Π_ρ) and the scale energy flux ($\delta u_\rho \delta u_i^2$), it is revealed that there is an inverse energy cascade in the buffer layer at $y^+ = 12$, which coincides approximately with the observation by Cimarelli et al.[22] as the scale energy source, where the production surpasses the dissipation. With the increase of wall distance the inverse cascade moves to higher spanwise scales in all three DNS datasets. This is tracked by the negative peak value of $-\langle\Pi\rangle$ in r_z direction at different wall distances. This negative peak of $-\langle\Pi\rangle$ approximately coincides with the positive peak of $-\langle P_r\rangle$. The trend of the two peaks in r_z/δ is linear in y/δ. There is no effect of Re_τ, from $y/\delta = 0.01$ to 0.1 in the position of the two peaks, suggesting this is in the range of the buffer layer structures. In the range $0.1 < y/\delta < 0.4$, the peaks of the TCF and TBL at $Re_\tau = 550$ are together, and the peak of TCF3000 follows a different curve, and this is in the range of Wall-Attached Self-similar Structures (WASS).

8.1.2 Results from PIV experiments

Measurement uncertainty

The variances and covariance of PIV datasets agree well with that of DNS of similar Re_τ when $y^+ > 20$ and $y^+ > 40$ for PIV with $Re_\tau = 2220$ and 3840 respectively. The measurement uncertainty with both the PIV datasets are less than 1% of free-stream velocity for both PIV datasets. The noise value associated with the streamwise velocity fluctuations is of the order of 0.03-0.06 pixels and 0.04-0.08 pixels for the PIV dataset with $Re_\tau = 2220$ and 3840 respectively.

Computation of dissipation

The normalised dissipation rate D^+ computed with PIV dataset with $Re_\tau = 2220$, with replacing the missing derivatives with the axisymmetry assumption[43], agrees well with that of TBL DNS dataset $Re_\tau = 1989$ when $y^+ > 25$. This is verified for the computation from using S-PIV $system_1$, $system_2$ and a combination of two systems ($system_{1|2}$), and they all tend to agree well with the DNS datasets when $y^+ > 25$.

The normalised dissipation rate D^+ computed with the PIV dataset with $Re_\tau = 3840$ doesn't agree with that of the DNS dataset when $y^+ < 200$. This is attributed to the limited spatial resolution which is of the order of 4.6η - 5.6η. With the PIV at $Re_\tau = 2220$, the spatial resolution is of the order of 2.3η-2.8η, which helped in the computation that agrees with the DNS datasets.

Spatio-temporal average KHMH equation

The Spatio-temporal average of KHMH equation terms obtained from both PIV datasets, on comparison, revealed that $-\langle\Pi\rangle$ is qualitatively the same between the DNS and PIV datasets. However, their peak value is higher in both the PIV datasets compared to the DNS datasets. $-\langle P_r\rangle$ from both the PIV datasets surpasses $\langle\epsilon'^*\rangle$ at around the same scale, and it increases with the wall distance. In comparison, $-\langle P_r\rangle$ is always lower than $\langle\epsilon'^*\rangle$ at all r_x^+ values considered in the present analysis of DNS datasets. The use of two S-PIV systems in the computation results in bias error for $-\langle A_t\rangle$ and $\langle A\rangle$, however $-\langle A_t + A\rangle$ term is approximately the same irrespective of which system is used for the computation in the PIV with $Re_\tau = 2220$. The computation with PIV at $Re_\tau = 3840$ has a higher value for $-\langle A_t + A\rangle$ than all the other datasets. The modified Taylor microscale doesn't exactly scale the peak in both PIV and DNS datasets when considered to have terms only in XY- plane, and this could be due to the absence of $\frac{\partial u_1}{\partial x_3}$ and $\frac{\partial u_2}{\partial x_3}$ terms.

Instantaneous KHMH equation terms

The standard deviation of Π and T_u are of the same order in both PIV and DNS datasets, and hence these terms have the least effect of noise. P_r is not affected by the noise on average, however, its standard deviation at $y^+ = 40$ is not comparable to DNS datasets. At $y^+ = 100$ and 140, the standard deviation of P_r is approximately the same between PIV and DNS datasets. $A_t + A$ is the most affected term from the noise of PIV datasets. The use of two S-PIV systems had resulted in the reduction of this standard deviation, however, it is still higher in both the PIV dataset than that of the DNS dataset.

The correlation coefficient between $A_t + A$ and Π, T_u improves when two S-PIV systems are used. This could be explained by the lower standard deviation of $A_t + A$ term when two S-PIV systems are used. At $y^+ = 40$, this correlation coefficient from PIV at $Re_\tau = 2220$ is approximately the same as that of DNS datasets. However with the increase of wall distance this correlation coefficient increases in absolute value in DNS, and it remains the same in PIV with $Re_\tau = 2220$. The PIV with

$Re_\tau = 3840$, has the lowest correlation coefficient of the three datasets. This could be attributed to the limited spatial resolution in the dataset.

The effect of noise in the instantaneous signal is simulated with the DNS dataset by the addition of Additive Gaussian White Noise (AGWN) of different levels of Signal-to-Noise Ratio (SNR). It was found that when the SNR=150, the results of correlation coefficient from the DNS is approximately equal to that of PIV at $Re_\tau = 2220$. In addition the reduced absolute value of correlation coefficient between $A_t + A$ and T_u is produced in the DNS dataset with added AGWN, thereby showing the effect of noise in the small scales.

8.2 Perspectives

8.2.1 Study of KHMH equation terms with $r_y \neq 0$

The derivation of the KHMH Equation 3.11 used in the present work involved making $r_y = 0$, which reduce many terms to zero for the channel flows. This enabled us to understand the behaviour of different terms of the resulting KHMH equation in the r_x and r_z direction which are the homogeneous directions for the channel flows and quasi-homogeneous and homogeneous directions respectively for Turbulent Boundary Layer flow. The next step would be to use the KHMH equation with $r_y \neq 0$, this way the analysis can be extended to study the scale-space physics in the wall-normal direction which is the inhomogeneous direction in the wall-bounded turbulent flows.

The KHMH equation terms are a function of three scale-space variables and the wall-normal direction in the physical space. In the present study, when the behaviour in a particular scale direction is studied such as in r_x direction, $r_z = 0$ and vice-versa. Some results such as the one in Section 5.4 involved studying physics in the $r_x - r_z$ plane. When the equation is studied with $r_y \neq 0$, it allows performing the analysis in different combinations of available planes to give a better understanding of the flow[22, 83].

8.2.2 Correlation coefficient between terms at different physical position

It was observed in both averaged and instantaneous KHMH equation terms that some physical processes exist at length scales much larger than the characteristic length scale of the flow, such as the channel half-width or the boundary layer thick-

ness. In the present study, when the correlation coefficient is obtained for two terms, they always belong to the same physical position. The same analysis can be performed, when the two terms are at different physical positions.

To start with, the first position can be static and be placed near the wall and the second physical position can be moved and the correlation coefficient so computed, will enable to connect with the results of wall-attached eddies. This can be slowly improved upon until the correlation coefficient between any two physical positions in the flow can be computed.

Other forms of interscale energy transfers

In the present study, the interscale energy transfer Π and the scale energy flux $\delta u_k \delta u_i^2$ is compared to conclude it is a direct cascade when both terms are negative and inverse cascade when both the terms are positive. So the direct cascade will result in a reduction of size in scales, followed by the reduction of energy and vice-versa for the inverse cascade. However, there are physical positions where both terms have opposite signs, which would mean that there could be an increase of energy even when the scales are reducing and vice versa. The present analysis did show a significant presence of the other forms of energy cascade away from the wall. This will require a more detailed analysis to have a proper understanding of the phenomenon.

PIV/PTV experiments

It was noticed in the PIV experiment chapter that the XZ- plane gave a better result in terms of the correlation coefficient between $A_t + A$ and the two energy transfer terms. If the practical difficulty of implementation is solved, *e.g.,* by using a different laser with a lower M^2 value, which will enable to perform the same experiment with XZ- plane at multiple wall distances. In addition, it is always possible to do an L-shaped SPIV experiment with one XY- plane and one YZ- plane, which helps to obtain the derivatives of velocity in all three directions[38]. This helps to compute the KHMH terms and dissipation accurately.

It has been observed with the results of the PIV dataset at $Re_\tau = 2220$ that the average values of KHMH equation terms compare well with that of DNS datasets at the wall distances considered. The results of standard deviation and correlation coefficient of KHMH equation is reproduced to a greater extent in the PIV dataset at $Re_\tau = 2220$ than with the PIV dataset at $Re_\tau = 3840$. This was attributed to the limited spatial resolution of the $Re_\tau = 3840$ PIV dataset. Thus with a better

camera, the Field of View can be zoomed to obtain the same spatial resolution of PIV at $Re_\tau = 2220$, which in turn helps to obtain comparable results at higher Re_τ.

The next step would also be to perform the KHMH equation analysis in the APG TBL flow configuration, which is possible with the LMFL wind tunnel. This introduces a lot of parameters to manage in terms of planning the experiment. Performing the KHMH analysis with previously obtained data in APG configuration, in addition to the results of the KHMH equation obtained from the present work would help to design the experiment optimised for the best results.

With the rapid progress of Particle Tracking Velocimetry (PTV), velocimetry experiments with a large third dimension, and the possibility to obtain a 4D (3D+time) velocity field in the Lagrangian frame, which can be interpolated into the Eulerian frame of reference[110]. This opens up the possibility of performing the KHMH equation analysis in three-dimensional flows, which would help to improve the existing knowledge about complex flows.

Part V

Appendices

Appendix A

KHMH equation terms in original co-ordinates

A.1 Derivation of KHMH equation based on full velocity

Starting with Navier-Stokes' equation at point 1

$$\frac{\partial}{\partial t}(u_i\big|_1) + u_j \frac{\partial}{\partial x_j}(u_i)\bigg|_1 = -\frac{1}{\rho}\frac{\partial}{\partial x_i}(p)\bigg|_1 + \nu \frac{\partial^2}{\partial x_j^2}(u_i)\bigg|_1 \tag{A.1}$$

Similarly for point 2

$$\frac{\partial}{\partial t}(u_i\big|_2) + u_j \frac{\partial}{\partial x_j}(u_i)\bigg|_2 = -\frac{1}{\rho}\frac{\partial}{\partial x_i}(p)\bigg|_2 + \nu \frac{\partial^2}{\partial x_j^2}(u_i)\bigg|_2 \tag{A.2}$$

Subtracting equation A.1 from equation A.2

$$\begin{aligned}\frac{\partial}{\partial t}(u_i\big|_2 - u_i\big|_1) + u_j \frac{\partial}{\partial x_j}(u_i)\bigg|_2 - u_j \frac{\partial}{\partial x_j}(u_i)\bigg|_1 = &-\left(\frac{1}{\rho}\frac{\partial}{\partial x_i}(p)\bigg|_2 - \frac{1}{\rho}\frac{\partial}{\partial x_i}(p)\bigg|_1\right) \\ &+ \nu \frac{\partial^2}{\partial x_j^2}(u_i)\bigg|_2 - \nu \frac{\partial^2}{\partial x_j^2}(u_i)\bigg|_1\end{aligned} \tag{A.3}$$

With the assumption that derivatives of quantities in point 1 with respect to point 2 is zero

$$\frac{\partial}{\partial x_j}\bigg|_2 (u_i\big|_1) = 0 \tag{A.4}$$

Substituting $u_i\big|_2 - u_i\big|_1 = \delta u_i$ and implementing the above mentioned assumption

$$\begin{aligned}\frac{\partial}{\partial t}(\delta u_i) + u_j \frac{\partial}{\partial x_j}(\delta u_i)\bigg|_2 - u_j \frac{\partial}{\partial x_j}(\delta u_i)\bigg|_1 = &-\left(\frac{1}{\rho}\frac{\partial}{\partial x_i}(\delta p)\bigg|_2 - \frac{1}{\rho}\frac{\partial}{\partial x_i}(\delta p)\bigg|_1\right) \\ &+ \nu \frac{\partial^2}{\partial x_j^2}(\delta u_i)\bigg|_2 - \nu \frac{\partial^2}{\partial x_j^2}(\delta u_i)\bigg|_1\end{aligned} \tag{A.5}$$

Converting from physical space (point 1,2 etc) to midpoint and space of separation vector (X,r), with $X_i = x_i\big|_2 + x_i\big|_1$ and $r_i = x_i\big|_2 - x_i\big|_1$

$$\begin{aligned}\frac{\partial\phi}{\partial X_i} &= \frac{\partial\phi}{\partial x_i}\bigg|_2 + \frac{\partial\phi}{\partial x_i}\bigg|_1 \\ \frac{\partial\phi}{\partial r_i} &= \frac{1}{2}\left[\frac{\partial\phi}{\partial x_i}\bigg|_2 - \frac{\partial\phi}{\partial x_i}\bigg|_1\right]\end{aligned} \tag{A.6}$$

Transforming equation A.5 into (X,r) co-ordinates

$$\frac{\partial}{\partial t}(\delta u_i) + u_j^*\frac{\partial}{\partial X_j}(\delta u_i) + \delta u_j\frac{\partial}{\partial r_j}(\delta u_i) = -\frac{1}{\rho}\frac{\partial}{\partial X_i}(\delta p) + \frac{\nu}{2}\frac{\partial^2}{\partial X_j^2}(\delta u_i) + 2\nu\frac{\partial^2}{\partial r_j^2}(\delta u_i) \tag{A.7}$$

where $u_j^* = \frac{1}{2}(u_j\big|_1 + u_j\big|_2)$

Multiplying the above equation with δu_k

$$\begin{aligned}\delta u_k\frac{\partial}{\partial t}(\delta u_i) + u_j^*\delta u_k\frac{\partial}{\partial X_j}(\delta u_i) + \delta u_j u_k\frac{\partial}{\partial r_j}(\delta u_i) = &-\frac{1}{\rho}\delta u_k\frac{\partial}{\partial X_i}(\delta p) + \frac{\nu}{2}\delta u_k\frac{\partial^2}{\partial X_j^2}(\delta u_i) \\ &+ 2\nu\delta u_k\frac{\partial^2}{\partial r_j^2}(\delta u_i)\end{aligned} \tag{A.8}$$

Writing equation A.7 in terms of δu_k and multiplying δu_i

$$\begin{aligned}\delta u_i\frac{\partial}{\partial t}(\delta u_k) + u_j^*\delta u_i\frac{\partial}{\partial X_j}(\delta u_k) + \delta u_j u_i\frac{\partial}{\partial r_j}(\delta u_k) = &-\frac{1}{\rho}\delta u_i\frac{\partial}{\partial X_i}(\delta p) + \frac{\nu}{2}\delta u_i\frac{\partial^2}{\partial X_j^2}(\delta u_k) \\ &+ 2\nu\delta u_i\frac{\partial^2}{\partial r_j^2}(\delta u_k)\end{aligned} \tag{A.9}$$

Adding equation A.8 and A.9

$$\begin{aligned}&\frac{\partial}{\partial t}(\delta u_i\delta u_k) + u_j^*\frac{\partial}{\partial X_j}(\delta u_i\delta u_k) + \delta u_j\frac{\partial}{\partial r_j}(\delta u_i\delta u_k) \\ &= -\frac{1}{\rho}\delta u_k\frac{\partial}{\partial X_k}(\delta p) - \frac{1}{\rho}\delta u_i\frac{\partial}{\partial X_i}(\delta p) + \frac{\nu}{2}\left[\frac{\partial^2}{\partial X_j^2}(\delta u_i\delta u_k) - 2\left(\frac{\partial u_i}{\partial X_j}\right)\left(\frac{\partial u_k}{\partial X_j}\right)\right] \\ &+ 2\nu\left[\frac{\partial^2}{\partial r_j^2}(\delta u_i\delta u_k) - 2\left(\frac{\partial u_i}{\partial r_j}\right)\left(\frac{\partial u_k}{\partial r_j}\right)\right]\end{aligned} \tag{A.10}$$

Simplifying the last two terms

$$\begin{aligned}&\frac{\partial}{\partial t}(\delta u_i\delta u_k) + u_j^*\frac{\partial}{\partial X_j}(\delta u_i\delta u_k) + \delta u_j\frac{\partial}{\partial r_j}(\delta u_i\delta u_k) \\ &= -\frac{1}{\rho}\delta u_k\frac{\partial}{\partial X_k}(\delta p) - \frac{1}{\rho}\delta u_i\frac{\partial}{\partial X_i}(\delta p) + \frac{\nu}{2}\frac{\partial^2}{\partial X_j^2}(\delta u_i\delta u_k) \\ &+ 2\nu\frac{\partial^2}{\partial r_j^2}(\delta u_i\delta u_k) - 2\nu\left[\left(\frac{\partial u_i}{\partial u_j}\bigg|_1\right)^2 + \left(\frac{\partial u_i}{\partial u_j}\bigg|_2\right)^2\right]\end{aligned} \tag{A.11}$$

Taking the trace of the equation ie., i=k

$$\frac{\partial}{\partial t}|\delta u|^2 + \delta u_j \frac{\partial}{\partial r_j}|\delta u|^2 + u_j^* \frac{\partial}{\partial X_j}|\delta u|^2 = -\frac{2}{\rho}\delta u_i \frac{\partial}{\partial X_i}(\delta p) + 2\nu \frac{\partial^2}{\partial r_j^2}|\delta u|^2 + \frac{\nu}{2}\frac{\partial^2}{\partial X_j^2}|\delta u|^2 - 2\nu\left[\left(\frac{\partial u_i}{\partial x_j}\Big|_1\right)^2 + \left(\frac{\partial u_i}{\partial x_j}\Big|_2\right)^2\right] \tag{A.12}$$

where ν is the kinematic viscosity, ρ is the fluid density.

A.2 Computation of KHMH equation based on full velocity

In this section, the transformation of KHMH equation terms obtained without velocity decomposition, from (X_j, r_j) co-ordinates to $(x_j\big|_1, x_j\big|_2)$. This is achieved by using the following :

$$\frac{\partial \phi}{\partial X_j} = \frac{\partial \phi}{\partial x_j}\Big|_1 + \frac{\partial \phi}{\partial x_j}\Big|_2$$

$$\frac{\partial \phi}{\partial r_j} = \frac{1}{2}\left[\frac{\partial \phi}{\partial x_j}\Big|_2 - \frac{\partial \phi}{\partial x_j}\Big|_1\right]$$

$$\frac{\partial^2 \phi}{\partial X_j^2} = \frac{\partial^2 \phi}{\partial x_j^2}\Big|_1 + \frac{\partial^2 \phi}{\partial x_j^2}\Big|_2 + 2\frac{\partial}{\partial x_j}\left(\frac{\partial \phi}{\partial x_j}\Big|_2\right)\Big|_1$$

$$\frac{\partial^2 \phi}{\partial r_j^2} = \frac{1}{4}\left[\frac{\partial^2 \phi}{\partial x_j^2}\Big|_1 + \frac{\partial^2 \phi}{\partial x_j^2}\Big|_2 - \frac{1}{2}\frac{\partial}{\partial x_j}\left(\frac{\partial \phi}{\partial x_j}\Big|_2\right)\Big|_1\right]$$

KHMH equation is given by

$$\frac{\partial}{\partial t}|\delta u_i|^2 + \delta u_j \frac{\partial}{\partial r_j}|\delta u_i|^2 + u_j^* \frac{\partial}{\partial X_j}|\delta u_i|^2 = -\frac{2}{\rho}\delta u_i \frac{\partial}{\partial X_i}(\delta p) + 2\nu \frac{\partial^2}{\partial r_j^2}|\delta u_i|^2 + \frac{\nu}{2}\frac{\partial^2}{\partial X_j^2}|\delta u_i|^2 - 2\nu\left[\left(\frac{\partial u_i}{\partial x_j}\Big|_1\right)^2 + \left(\frac{\partial u_i}{\partial x_j}\Big|_2\right)^2\right] \tag{A.13}$$

Term-by-term conversion of Equation A.13 from (X_j, r_j) co-ordinates to $(x_j\big|_1, x_j\big|_2)$results in the following.

Time derivative term is the same in both co-ordinate space

Interscale energy transfer is given by

$$\delta u_j \frac{\partial}{\partial r_j}|\delta u_i|^2 = \frac{1}{2}\delta u_j\left[\frac{\partial |\delta u_i|^2}{\partial x_j}\Big|_2 - \frac{\partial |\delta u_i|^2}{\partial x_j}\Big|_1\right] = \frac{2}{2}\delta u_j \delta u_i\left[\frac{\partial \delta u_i}{\partial x_j}\Big|_2 - \frac{\partial \delta u_i}{\partial x_j}\Big|_1\right] = \delta u_j \delta u_i\left[\frac{\partial u_i}{\partial x_j}\Big|_2 + \frac{\partial u_i}{\partial x_j}\Big|_1\right]$$

Energy transfer in physical space is given by

$$u_j^* \frac{\partial}{\partial X_j}|\delta u_i|^2 = 2u_j^* \delta u_i \left[\frac{\partial \delta u_i}{\partial x_j}\bigg|_2 + \frac{\partial \delta u_i}{\partial x_j}\bigg|_1\right] = 2u_j^* \delta u_i \left[\frac{\partial u_i}{\partial x_j}\bigg|_2 - \frac{\partial u_i}{\partial x_j}\bigg|_1\right]$$

Pressure velocity term is given by

$$-\frac{2}{\rho}\delta u_i \frac{\partial}{\partial X_i}(\delta p) = -\frac{2}{\rho}\delta u_i \left[\frac{\partial \delta p}{\partial x_i}\bigg|_2 + \frac{\partial \delta p}{\partial x_i}\bigg|_1\right] = -\frac{2}{\rho}\delta u_i \left[\frac{\partial p}{\partial x_i}\bigg|_2 - \frac{\partial p}{\partial x_i}\bigg|_1\right]$$

Diffusion in physical scale is given by

$$\begin{aligned}\frac{\nu}{2}\frac{\partial^2}{\partial X_j^2}|\delta u_i|^2 &= \frac{\nu}{2}\left[\frac{\partial^2|\delta u_i|^2}{\partial x_j^2}\bigg|_2 + \frac{\partial^2|\delta u_i|^2}{\partial x_j^2}\bigg|_1 + 2\frac{\partial}{\partial x_j}\left(\frac{|\delta u_i|^2}{\partial x_j}\bigg|_2\right)\bigg|_1\right] \\ &= 2\frac{\nu}{2}\left[\left(\frac{\partial u_i}{\partial x_j}\bigg|_2\right)^2 + \left(\frac{\partial u_i}{\partial x_j}\bigg|_1\right)^2 + \delta u_i\left(\frac{\partial^2 u_i}{\partial x_j^2}\bigg|_2 - \frac{\partial^2 u_i}{\partial x_j^2}\bigg|_1\right) - 2\frac{\partial u_i}{\partial x_j}\bigg|_1 \frac{\partial u_i}{\partial x_j}\bigg|_2\right]\end{aligned}$$

Diffusion in scale space is given by

$$\begin{aligned}2\nu\frac{\partial^2}{\partial r_j^2}|\delta u_i|^2 &= 2\nu\left[\frac{1}{4}\frac{\partial^2|\delta u_i|^2}{\partial x_j^2}\bigg|_2 + \frac{1}{4}\frac{\partial^2|\delta u_i|^2}{\partial x_j^2}\bigg|_1 - \frac{1}{2}\frac{\partial}{\partial x_j}\left(\frac{\partial|\delta u_i|^2}{\partial x_j}\bigg|_2\right)\bigg|_1\right] \\ &= 2\nu\frac{1}{4}\left[\frac{\partial^2|u_i|^2}{\partial x_{j2}^2} + \frac{\partial^2|u_i|^2}{\partial x_{j1}^2} - 2\frac{\partial}{\partial x_j}\left(\frac{\partial|\delta u_i|^2}{\partial x_j}\bigg|_2\right)\bigg|_1\right] \\ &= \frac{\nu}{2}\times 2\left[\left(\frac{\partial u_i}{\partial x_j}\bigg|_1\right)^2 + \left(\frac{\partial u_i}{\partial x_j}\bigg|_2\right)^2 + \delta u_i\left(\frac{\partial^2 u_i}{\partial x_j^2}\bigg|_2 - \frac{\partial^2 u_i}{\partial x_j^2}\bigg|_1\right) + 2\frac{\partial u_i}{\partial x_j}\bigg|_1 \frac{\partial u_i}{\partial x_j}\bigg|_2\right]\end{aligned}$$

Dissipation term is the same in both the equations.

A.3 Computation of KHMH equation based on decomposed velocity

In this section, the terms of the KHMH equation which is obtained by decomposition of velocity into mean and fluctuations are transformed from their (X_j, r_j) co-ordinates to $(x_j\big|_1, x_j\big|_2)$ co-ordinates.

KHMH equation before velocity decomposition is given by:

$$\begin{aligned}\frac{\partial}{\partial t}|\delta u_i|^2 + \delta u_j\frac{\partial}{\partial r_j}|\delta u_i|^2 + u_j^*\frac{\partial}{\partial X_j}|\delta u_i|^2 = &-\frac{2}{\rho}\delta u_i\frac{\partial}{\partial X_i}(\delta p) + 2\nu\frac{\partial^2}{\partial r_j^2}|\delta u_i|^2 + \frac{\nu}{2}\frac{\partial^2}{\partial X_j^2}|\delta u_i|^2 \\ &- 2\nu\left[\left(\frac{\partial u_i}{\partial x_j}\bigg|_1\right)^2 + \left(\frac{\partial u_i}{\partial x_j}\bigg|_2\right)^2\right]\end{aligned} \tag{A.14}$$

The decomposition of velocity of time derivative term leads to

$$\frac{\partial}{\partial t}(\delta\overline{u_i}+\delta u_i')^2 = \underbrace{\frac{\partial}{\partial t}(\delta u_i')^2}_{A_t} + \frac{\partial}{\partial t}(\delta\overline{u_i})^2 + 2\delta u_i'\frac{\partial}{\partial t}(\delta\overline{u_i}) + 2\delta\overline{u_i}\frac{\partial}{\partial t}(\delta u_i') \tag{A.15}$$

The time derivative remains the same in both co-ordinate space

$$A_t = \frac{\partial}{\partial t}(\delta u_i')^2 = 2\delta u_i'\frac{\partial}{\partial t}(\delta u_i')$$

$$\frac{\partial}{\partial t}(\delta\overline{u_i})^2 = 2\delta\overline{u_i}\frac{\partial}{\partial t}(\delta\overline{u_i}) = 0$$

$$2\delta\overline{u_i}\frac{\partial}{\partial t}(\delta u_i')$$

$$2\delta u_i'\frac{\partial}{\partial t}(\delta\overline{u_i})^2 = 0$$

The interscale energy transfer term (T_r) after decomposition is given by

$$\begin{aligned}(\delta\overline{u_j}+\delta u_j')\frac{\partial}{\partial r_j}(\delta\overline{u_i}+\delta u_i') = {} & \delta\overline{u_j}\frac{\partial}{\partial r_j}(\delta\overline{u_i})^2 + \delta\overline{u_j}\frac{\partial}{\partial r_j}(\delta u_i')^2 + 2\delta\overline{u_j}\delta\overline{u_i}\frac{\partial}{\partial r_j}(\delta u_i') \\ & + 2\delta\overline{u_j}\delta u_i'\frac{\partial}{\partial r_j}(\delta\overline{u_i}) + \delta u_j'\frac{\partial}{\partial r_j}(\delta\overline{u_i})^2 + \delta u_j'\frac{\partial}{\partial r_j}(\delta u_i')^2 \\ & + 2\delta u_j'\delta\overline{u_i}\frac{\partial}{\partial r_j}(\delta u_i') + 2\delta u_j'\delta u_i'\frac{\partial}{\partial r_j}(\delta\overline{u_i})\end{aligned} \tag{A.16}$$

This is represented as

$$T_r = T_{r1} + T_{r2} + T_{r3} + T_{r4} + T_{r5} + \Pi + T_{r7} + P_r$$

The transformation to original co-ordinates is given by

$$\begin{aligned}T_{r1} = \delta\overline{u_j}\frac{\partial}{\partial r_j}(\delta\overline{u_i})^2 &= 2\delta\overline{u_i}\delta\overline{u_j}\frac{\partial}{\partial r_j}(\delta\overline{u_i}) \\ &= 2\delta\overline{u_i}\delta\overline{u_j}\frac{1}{2}\left[\left.\frac{\partial\delta\overline{u_i}}{\partial x_j}\right|_2 - \left.\frac{\partial\delta\overline{u_i}}{\partial x_j}\right|_1\right] \\ &= \delta\overline{u_i\delta u_j}\left[\left.\frac{\partial\overline{u_i}}{\partial x_j}\right|_2 + \left.\frac{\partial\overline{u_i}}{\partial x_j}\right|_1\right]\end{aligned}$$

$$\begin{aligned}T_{r2} = \delta\overline{u_j}\frac{\partial}{\partial r_j}(\delta u_i')^2 &= 2\delta u_i'\delta\overline{u_j}\frac{\partial}{\partial r_j}(\delta u_i') \\ &= 2\delta u_i'\delta\overline{u_j}\frac{1}{2}\left[\left.\frac{\partial\delta u_i'}{\partial x_j}\right|_2 - \left.\frac{\partial\delta u_i'}{\partial x_j}\right|_1\right] \\ &= \delta u_i'\delta\overline{u_j}\left[\left.\frac{\partial u_i'}{\partial x_j}\right|_2 + \left.\frac{\partial u_i'}{\partial x_j}\right|_1\right]\end{aligned}$$

$$T_{r3} = 2\delta\overline{u_i}\delta\overline{u_j}\frac{\partial}{\partial r_j}(\delta u_i') = 2\delta\overline{u_i}\delta\overline{u_j}\frac{\partial}{\partial r_j}(\delta u_i')$$
$$= 2\delta\overline{u_i}\delta\overline{u_j}\frac{1}{2}\left[\left.\frac{\partial\delta u_i'}{\partial x_j}\right|_2 - \left.\frac{\partial\delta u_i'}{\partial x_j}\right|_1\right]$$
$$= \delta\overline{u_i}\delta\overline{u_j}\left[\left.\frac{\partial u_i'}{\partial x_j}\right|_2 + \left.\frac{\partial u_i'}{\partial x_j}\right|_1\right]$$

$$T_{r4} = 2\delta u_i'\delta\overline{u_j}\frac{\partial}{\partial r_j}(\delta\overline{u_i}) = 2\delta u_i'\delta\overline{u_j}\frac{\partial}{\partial r_j}(\delta\overline{u_i})$$
$$= 2\delta u_i'\delta\overline{u_j}\frac{1}{2}\left[\left.\frac{\partial\delta\overline{u_i}}{\partial x_j}\right|_2 - \left.\frac{\partial\delta\overline{u_i}}{\partial x_j}\right|_1\right]$$
$$= \delta u_i'\delta\overline{u_j}\left[\left.\frac{\partial\overline{u_i}}{\partial x_j}\right|_2 + \left.\frac{\partial\overline{u_i}}{\partial x_j}\right|_1\right]$$

$$T_{r5} = \delta u_j'\frac{\partial}{\partial r_j}(\delta\overline{u_i})^2 = 2\delta u_j'\delta\overline{u_i}\frac{\partial}{\partial r_j}(\delta\overline{u_i})$$
$$= 2\delta u_j'\delta\overline{u_i}\frac{1}{2}\left[\left.\frac{\partial\delta\overline{u_i}}{\partial x_j}\right|_2 - \left.\frac{\partial\delta\overline{u_i}}{\partial x_j}\right|_1\right]$$
$$= \delta u_j'\delta\overline{u_i}\left[\left.\frac{\partial\overline{u_i}}{\partial x_j}\right|_2 + \left.\frac{\partial\overline{u_i}}{\partial x_j}\right|_1\right]$$

$$\Pi = \delta u_j'\frac{\partial}{\partial r_j}(\delta u_i')^2 = 2\delta u_i'\delta u_j'\frac{\partial}{\partial r_j}(\delta u_i')$$
$$= 2\delta u_i'\delta u_j'\frac{1}{2}\left[\left.\frac{\partial\delta u_i'}{\partial x_j}\right|_2 - \left.\frac{\partial\delta u_i'}{\partial x_j}\right|_1\right]$$
$$= \delta u_i'\delta u_j'\left[\left.\frac{\partial u_i'}{\partial x_j}\right|_2 + \left.\frac{\partial u_i'}{\partial x_j}\right|_1\right]$$

$$T_{r7} = 2\delta u_j'\delta\overline{u_i}\frac{\partial}{\partial r_j}(\delta u_i') = 2\delta u_j'\delta\overline{u_i}\frac{\partial}{\partial r_j}(\delta u_i')$$
$$= 2\delta u_j'\delta\overline{u_i}\frac{1}{2}\left[\left.\frac{\partial\delta u_i'}{\partial x_j}\right|_2 - \left.\frac{\partial\delta u_i'}{\partial x_j}\right|_1\right]$$
$$= \delta u_j'\delta\overline{u_i}\left[\left.\frac{\partial u_i'}{\partial x_j}\right|_2 + \left.\frac{\partial u_i'}{\partial x_j}\right|_1\right]$$

$$P_r = 2\delta u_i'\delta u_j'\frac{\partial}{\partial r_j}(\delta\overline{u_i}) = 2\delta u_i'\delta u_j'\frac{\partial}{\partial r_j}(\delta\overline{u_i})$$
$$= 2\delta u_i'\delta u_j'\frac{1}{2}\left[\left.\frac{\partial\delta\overline{u_i}}{\partial x_j}\right|_2 - \left.\frac{\partial\delta\overline{u_i}}{\partial x_j}\right|_1\right]$$
$$= \delta u_i'\delta u_j'\left[\left.\frac{\partial\overline{u_i}}{\partial x_j}\right|_2 + \left.\frac{\partial\overline{u_i}}{\partial x_j}\right|_1\right]$$

The energy transfer in physical space term (T_x) after decomposition is given by

$$\begin{aligned}(\overline{u_j}+u_j')^*\frac{\partial}{\partial X_j}(\delta\overline{u_i}+\delta u_i') = \overline{u_j}^*\frac{\partial}{\partial X_j}(\delta\overline{u_i})^2 + \overline{u_j}^*\frac{\partial}{\partial X_j}(\delta u_i')^2 + 2\overline{u_j}^*\delta\overline{u_i}\frac{\partial}{\partial X_j}(\delta u_i') \\ + 2\overline{u_j}^*\delta u_i'\frac{\partial}{\partial X_j}(\delta\overline{u_i}) + u_j'^*\frac{\partial}{\partial X_j}(\delta\overline{u_i})^2 + u_j'^*\frac{\partial}{\partial X_j}(\delta u_i')^2 \\ + 2u_j'^*\delta\overline{u_i}\frac{\partial}{\partial X_j}(\delta u_i') + 2u_j'^*\delta u_i'\frac{\partial}{\partial X_j}(\delta\overline{u_i})\end{aligned} \tag{A.17}$$

This is represented as

$$T_x = T_{x1} + A + T_{x3} + T_{x4} + T_{x5} + T_u + T_{x7} + T_{x8}$$

The transformation to original co-ordinates is given by

$$\begin{aligned}T_{x1} = \overline{u_j}^*\frac{\partial}{\partial X_j}(\delta\overline{u_i})^2 &= 2\overline{u_j}^*\delta\overline{u_i}\frac{\partial}{\partial X_j}(\delta\overline{u_i}) \\ &= 2\overline{u_j}^*\delta\overline{u_i}\left[\frac{\partial\delta\overline{u_i}}{\partial x_j}\bigg|_2 + \frac{\partial\delta\overline{u_i}}{\partial x_j}\bigg|_1\right] \\ &= 2\overline{u_j}^*\delta\overline{u_i}\left[\frac{\partial\overline{u_i}}{\partial x_j}\bigg|_2 - \frac{\partial\overline{u_i}}{\partial x_j}\bigg|_1\right]\end{aligned}$$

$$\begin{aligned}A = \overline{u_j^*}\frac{\partial}{\partial X_j}(\delta u_i')^2 &= 2\delta u_i'\overline{u_j^*}\frac{\partial}{\partial X_j}(\delta u_i') \\ &= 2\delta u_i'\overline{u_j^*}\left[\frac{\partial\delta u_i'}{\partial x_j}\bigg|_2 + \frac{\partial\delta u_i'}{\partial x_j}\bigg|_1\right] \\ &= 2\delta u_i'\overline{u_j^*}\left[\frac{\partial u_i'}{\partial x_j}\bigg|_2 - \frac{\partial u_i'}{\partial x_j}\bigg|_1\right]\end{aligned}$$

$$\begin{aligned}T_{x3} = 2\overline{u_j}^*\delta\overline{u_i}\frac{\partial}{\partial X_j}(\delta u_i') &= 2\overline{u_j}^*\delta\overline{u_i}\frac{\partial}{\partial X_j}(\delta u_i') \\ &= 2\overline{u_j}^*\delta\overline{u_i}\left[\frac{\partial\delta u_i'}{\partial x_j}\bigg|_2 + \frac{\partial\delta u_i'}{\partial x_j}\bigg|_1\right] \\ &= 2\overline{u_j}^*\delta\overline{u_i}\left[\frac{\partial u_i'}{\partial x_j}\bigg|_2 - \frac{\partial u_i'}{\partial x_j}\bigg|_1\right]\end{aligned}$$

$$\begin{aligned}T_{x4} = 2\delta u_i'\overline{u_j}^*\frac{\partial}{\partial X_j}(\delta\overline{u_i}) &= 2\delta u_i'\overline{u_j}^*\frac{\partial}{\partial X_j}(\delta\overline{u_i}) \\ &= 2\delta u_i'\overline{u_j}^*\left[\frac{\partial\delta\overline{u_i}}{\partial x_j}\bigg|_2 + \frac{\partial\delta\overline{u_i}}{\partial x_j}\bigg|_1\right] \\ &= 2\delta u_i'\overline{u_j}^*\left[\frac{\partial\overline{u_i}}{\partial x_j}\bigg|_2 - \frac{\partial\overline{u_i}}{\partial x_j}\bigg|_1\right]\end{aligned}$$

$$T_{x5} = u_j^{'*}\frac{\partial}{\partial X_j}(\delta\overline{u_i})^2 = 2u_j^{'*}\delta\overline{u_i}\frac{\partial}{\partial X_j}(\delta\overline{u_i})$$
$$= 2u_j^{'*}\delta\overline{u_i}\left[\left.\frac{\partial\delta\overline{u_i}}{\partial x_j}\right|_2 + \left.\frac{\partial\delta\overline{u_i}}{\partial x_j}\right|_1\right]$$
$$= 2u_j^{'*}\delta\overline{u_i}\left[\left.\frac{\partial\overline{u_i}}{\partial x_j}\right|_2 - \left.\frac{\partial\overline{u_i}}{\partial x_j}\right|_1\right]$$

$$T_u = u_j^{'*}\frac{\partial}{\partial X_j}(\delta u_i')^2 = 2u_j^{'*}\delta u_i'\frac{\partial}{\partial X_j}(\delta u_i')$$
$$= 2u_j^{'*}\delta u_i'\left[\left.\frac{\partial\delta u_i'}{\partial x_j}\right|_2 + \left.\frac{\partial\delta u_i'}{\partial x_j}\right|_1\right]$$
$$= 2u_j^{'*}\delta u_i'\left[\left.\frac{\partial u_i'}{\partial x_j}\right|_2 - \left.\frac{\partial u_i'}{\partial x_j}\right|_1\right]$$

$$T_{x7} = 2u_j^{'*}\delta\overline{u_i}\frac{\partial}{\partial X_j}(\delta u_i') = 2u_j^{'*}\delta\overline{u_i}\frac{\partial}{\partial X_j}(\delta u_i')$$
$$= 2u_j^{'*}\delta\overline{u_i}\left[\left.\frac{\partial\delta u_i'}{\partial x_j}\right|_2 + \left.\frac{\partial\delta u_i'}{\partial x_j}\right|_1\right]$$
$$= 2u_j^{'*}\delta\overline{u_i}\left[\left.\frac{\partial u_i'}{\partial x_j}\right|_2 - \left.\frac{\partial u_i'}{\partial x_j}\right|_1\right]$$

$$T_{x8} = 2u_j^{'*}\delta u_i'\frac{\partial}{\partial X_j}(\delta\overline{u_i}) = 2u_j^{'*}\delta u_i'\frac{\partial}{\partial X_j}(\delta\overline{u_i})$$
$$= 2u_j^{'*}\delta u_i'\left[\left.\frac{\partial\delta\overline{u_i}}{\partial x_j}\right|_2 + \left.\frac{\partial\delta\overline{u_i}}{\partial x_j}\right|_1\right]$$
$$= 2u_j^{'*}\delta u_i'\left[\left.\frac{\partial\overline{u_i}}{\partial x_j}\right|_2 - \left.\frac{\partial\overline{u_i}}{\partial x_j}\right|_1\right]$$

The pressure term is given by

$$(\delta\overline{u_i} + \delta u_i')\frac{\partial}{\partial X_i}(\delta p) = \delta\overline{u_i}\frac{\partial}{\partial X_i}(\delta p) + \delta u_i'\frac{\partial}{\partial X_i}(\delta p) \tag{A.18}$$

The transformation to original co-ordinates is given by

$$\delta\overline{u_i}\frac{\partial}{\partial X_i}(\delta p) = \delta\overline{u_i}\left[\left.\frac{\partial\delta p}{\partial x_i}\right|_2 + \left.\frac{\partial\delta p}{\partial x_i}\right|_1\right]$$
$$= \delta\overline{u_i}\left[\left.\frac{\partial p}{\partial x_i}\right|_2 - \left.\frac{\partial p}{\partial x_i}\right|_1\right]$$

$$T_p = \delta u_i'\frac{\partial}{\partial X_i}(\delta p) = \delta u_i'\left[\left.\frac{\partial\delta p}{\partial x_i}\right|_2 + \left.\frac{\partial\delta p}{\partial x_i}\right|_1\right]$$
$$= \delta u_i'\left[\left.\frac{\partial p}{\partial x_i}\right|_2 - \left.\frac{\partial p}{\partial x_i}\right|_1\right]$$

The interscale diffusion term is given by

$$2\nu\frac{\partial^2}{\partial r_j^2}(\delta\overline{u_i}+\delta u_i')^2 = 2\nu\frac{\partial^2}{\partial r_j^2}\left[(\delta\overline{u_i})^2+(\delta u_i')^2+(2\delta\overline{u_i}\delta u_i')\right] \tag{A.19}$$

The transformation to original co-ordinate system is given by

$$\begin{aligned}
D_{r1} = 2\nu\frac{\partial^2}{\partial r_j^2}(\delta\overline{u_i})^2 &= 2\nu\left[\frac{2}{4}\left(\frac{\partial\delta\overline{u_i}}{\partial x_j}\bigg|_2\right)^2+\frac{2}{4}\left(\frac{\partial\delta\overline{u_i}}{\partial x_j}\bigg|_1\right)^2+\frac{1}{2}\delta\overline{u_i}\left(\frac{\partial^2\delta\overline{u_i}}{\partial x_j^2}\bigg|_2+\frac{\partial^2\delta\overline{u_i}}{\partial x_j^2}\bigg|_1\right)\right.\\
&\quad\left.-\frac{1}{2}\frac{\partial}{\partial x_j}\left(\frac{\partial\delta\overline{u_i}}{\partial x_j}\bigg|_2\right)\bigg|_1\right]\\
&= 2\nu\left[\frac{2}{4}\left(\frac{\partial\overline{u_i}}{\partial x_j}\bigg|_2\right)^2+\frac{2}{4}\left(\frac{\partial\overline{u_i}}{\partial x_j}\bigg|_1\right)^2\right.\\
&\quad+\frac{1}{2}\delta\overline{u_i}\left(\frac{\partial^2\overline{u_i}}{\partial x_j^2}\bigg|_2-\frac{\partial^2\overline{u_i}}{\partial x_j^2}\bigg|_1\right)+\frac{\partial\overline{u_i}}{\partial x_j}\bigg|_2\frac{\partial\overline{u_i}}{\partial x_j}\bigg|_1\Bigg]\\
&= \nu\left[\left(\frac{\partial\overline{u_i}}{\partial x_j}\bigg|_2\right)^2+\left(\frac{\partial\overline{u_i}}{\partial x_j}\bigg|_1\right)^2+\delta\overline{u_i}\left(\frac{\partial^2\overline{u_i}}{\partial x_j^2}\bigg|_2-\frac{\partial^2\overline{u_i}}{\partial x_j^2}\bigg|_1\right)\right.\\
&\quad\left.+2\frac{\partial\overline{u_i}}{\partial x_j}\bigg|_2\frac{\partial\overline{u_i}}{\partial x_j}\bigg|_1\right]
\end{aligned}$$

$$\begin{aligned}
D_{r2} = 2\nu\frac{\partial^2}{\partial r_j^2}(\delta u_i')^2 &= 2\nu\left[\frac{2}{4}\left(\frac{\partial\delta u_i'}{\partial x_j}\bigg|_2\right)^2+\frac{2}{4}\left(\frac{\partial\delta u_i'}{\partial x_j}\bigg|_1\right)^2+\frac{1}{2}\delta u_i'\left(\frac{\partial^2\delta u_i'}{\partial x_j^2}\bigg|_2+\frac{\partial^2\delta u_i'}{\partial x_j^2}\bigg|_1\right)\right.\\
&\quad\left.-\frac{1}{2}\frac{\partial}{\partial x_j}\left(\frac{\partial\delta u_i'}{\partial x_j}\bigg|_2\right)\bigg|_1\right]\\
&= 2\nu\left[\frac{2}{4}\left(\frac{\partial u_i'}{\partial x_j}\bigg|_2\right)^2+\frac{2}{4}\left(\frac{\partial u_i'}{\partial x_j}\bigg|_1\right)^2\right.\\
&\quad+\frac{1}{2}\delta u_i'\left(\frac{\partial^2 u_i'}{\partial x_j^2}\bigg|_2-\frac{\partial^2 u_i'}{\partial x_j^2}\bigg|_1\right)+\frac{\partial u_i'}{\partial x_j}\bigg|_2\frac{\partial u_i'}{\partial x_j}\bigg|_1\Bigg]\\
&= \nu\left[\left(\frac{\partial u_i'}{\partial x_j}\bigg|_2\right)^2+\left(\frac{\partial u_i'}{\partial x_j}\bigg|_1\right)^2\right.\\
&\quad\left.+\delta u_i'\left(\frac{\partial^2 u_i'}{\partial x_j^2}\bigg|_2-\frac{\partial^2 u_i'}{\partial x_j^2}\bigg|_1\right)+2\frac{\partial u_i'}{\partial x_j}\bigg|_2\frac{\partial u_i'}{\partial x_j}\bigg|_1\right]
\end{aligned}$$

$$
\begin{aligned}
D_{r3} = 2\nu\frac{\partial^2}{\partial r_j^2}(2\delta\overline{u_i}\delta u_i') &= 2\nu\left[\frac{1}{4}\frac{\partial^2(2\delta\overline{u_i}\delta u_i')}{\partial x_j}\bigg|_2 + \frac{1}{4}\frac{\partial^2(2\delta\overline{u_i}\delta u_i')}{\partial x_j}\bigg|_1 - \frac{1}{2}\frac{\partial}{\partial x_j}\left(\frac{\partial(2\delta\overline{u_i}\delta u_i')}{\partial x_j}\bigg|_2\right)\bigg|_1\right] \\
&= 2\nu\left[\frac{1}{2}\delta\overline{u_i}\frac{\partial^2\delta u_i'}{\partial x_j^2}\bigg|_2 + \frac{1}{2}\delta u_i'\frac{\partial^2\delta\overline{u_i}}{\partial x_j^2}\bigg|_2 + \frac{\partial\delta u_i'}{\partial x_j}\bigg|_2\frac{\partial\delta\overline{u_i}}{\partial x_j}\bigg|_2 - \frac{1}{2}\delta\overline{u_i}\frac{\partial^2\delta u_i'}{\partial x_j^2}\bigg|_1\right. \\
&\quad - \frac{1}{2}\delta u_i'\frac{\partial^2\delta\overline{u_i}}{\partial x_j^2}\bigg|_1 + \frac{\partial\delta u_i'}{\partial x_j}\bigg|_1\frac{\partial\delta\overline{u_i}}{\partial x_j}\bigg|_1 + \frac{\partial\delta\overline{u_i}}{\partial x_j}\bigg|_1\frac{\partial\delta u_i'}{\partial x_j}\bigg|_2 + \frac{\partial\delta u_i'}{\partial x_j}\bigg|_1\frac{\partial\delta\overline{u_i}}{\partial x_j}\bigg|_2\Bigg] \\
&= \nu\left[\delta\overline{u_i}\frac{\partial^2 u_i'}{\partial x_j^2}\bigg|_2 + \delta u_i'\frac{\partial^2\overline{u_i}}{\partial x_j^2}\bigg|_2 + 2\frac{\partial u_i'}{\partial x_j}\bigg|_2\frac{\partial\overline{u_i}}{\partial x_j}\bigg|_2 - \delta\overline{u_i}\frac{\partial^2 u_i'}{\partial x_j^2}\bigg|_1 - \delta u_i'\frac{\partial^2\overline{u_i}}{\partial x_j^2}\bigg|_1\right. \\
&\quad + 2\frac{\partial u_i'}{\partial x_j}\bigg|_1\frac{\partial\overline{u_i}}{\partial x_j}\bigg|_1 + 2\frac{\partial\overline{u_i}}{\partial x_j}\bigg|_1\frac{\partial u_i'}{\partial x_j}\bigg|_2 + 2\frac{\partial u_i'}{\partial x_j}\bigg|_1\frac{\partial\overline{u_i}}{\partial x_j}\bigg|_2\Bigg]
\end{aligned}
$$

The diffusion in physical space term (D_x) is given by

$$
\frac{\nu}{2}\frac{\partial^2}{\partial X_j^2}(\delta\overline{u_i} + \delta u_i')^2 = \frac{\nu}{2}\frac{\partial^2}{\partial X_j^2}\left[(\delta\overline{u_i})^2 + (\delta u_i')^2 + (2\delta\overline{u_i}\delta u_i')\right]
$$

This is represented as

The transformation to original co-ordinate system is given by

$$
\begin{aligned}
D_{x1} = \frac{1}{2}\nu\frac{\partial^2}{\partial X_j^2}(\delta\overline{u_i})^2 &= \frac{1}{2}\nu\left[2\left(\frac{\partial\delta\overline{u_i}}{\partial x_j}\bigg|_2\right)^2 + 2\left(\frac{\partial\delta\overline{u_i}}{\partial x_j}\bigg|_1\right)^2 + 2\delta\overline{u_i}\left(\frac{\partial^2\delta\overline{u_i}}{\partial x_j^2}\bigg|_2 + \frac{\partial^2\delta\overline{u_i}}{\partial x_j^2}\bigg|_1\right)\right. \\
&\quad \left. + 2\frac{\partial}{\partial x_j}\left(\frac{\partial\delta\overline{u_i}}{\partial x_j}\bigg|_2\right)\bigg|_1\right] \\
&= \frac{1}{2}\nu\left[2\left(\frac{\partial\overline{u_i}}{\partial x_j}\bigg|_2\right)^2 + 2\left(\frac{\partial\overline{u_i}}{\partial x_j}\bigg|_1\right)^2 + 2\delta\overline{u_i}\left(\frac{\partial^2\overline{u_i}}{\partial x_j^2}\bigg|_2 - \frac{\partial^2\overline{u_i}}{\partial x_j^2}\bigg|_1\right) - 4\frac{\partial\overline{u_i}}{\partial x_j}\bigg|_2\frac{\partial\overline{u_i}}{\partial x_j}\bigg|_1\right] \\
&= \nu\left[\left(\frac{\partial\overline{u_i}}{\partial x_j}\bigg|_2\right)^2 + \left(\frac{\partial\overline{u_i}}{\partial x_j}\bigg|_1\right)^2 + \delta\overline{u_i}\left(\frac{\partial^2\overline{u_i}}{\partial x_j^2}\bigg|_2 - \frac{\partial^2\overline{u_i}}{\partial x_j^2}\bigg|_1\right) - 2\frac{\partial\overline{u_i}}{\partial x_j}\bigg|_2\frac{\partial\overline{u_i}}{\partial x_j}\bigg|_1\right]
\end{aligned}
$$

$$
\begin{aligned}
D_x = \frac{1}{2}\nu\frac{\partial^2}{\partial X_j^2}(\delta u_i')^2 &= \frac{1}{2}\nu\left[2\left(\frac{\partial\delta u_i'}{\partial x_j}\bigg|_2\right)^2 + 2\left(\frac{\partial\delta u_i'}{\partial x_j}\bigg|_1\right)^2 + 2\delta u_i'\left(\frac{\partial^2\delta u_i'}{\partial x_j^2}\bigg|_2 + \frac{\partial^2\delta u_i'}{\partial x_j^2}\bigg|_1\right)\right. \\
&\quad \left. + 2\frac{\partial}{\partial x_j}\left(\frac{\partial\delta u_i'}{\partial x_j}\bigg|_2\right)\bigg|_1\right] \\
&= \frac{1}{2}\nu\left[2\left(\frac{\partial u_i'}{\partial x_j}\bigg|_2\right)^2 + 2\left(\frac{\partial u_i'}{\partial x_j}\bigg|_1\right)^2 + 2\delta u_i'\left(\frac{\partial^2 u_{i2}'}{\partial x_j^2}\bigg|_2 - \frac{\partial^2 u_i'}{\partial x_j^2}\bigg|_1\right) - 4\frac{\partial u_i'}{\partial x_j}\bigg|_2\frac{\partial u_i'}{\partial x_j}\bigg|_1\right] \\
&= \nu\left[\left(\frac{\partial u_i'}{\partial x_j}\bigg|_2\right)^2 + \left(\frac{\partial u_i'}{\partial x_j}\bigg|_1\right)^2 + \delta u_i'\left(\frac{\partial^2 u_i'}{\partial x_j^2}\bigg|_2 - \frac{\partial^2 u_i'}{\partial x_j^2}\bigg|_1\right) - 2\frac{\partial u_i'}{\partial x_j}\bigg|_2\frac{\partial u_i'}{\partial x_j}\bigg|_1\right]
\end{aligned}
$$

$$
\begin{aligned}
D_{x3} = \frac{1}{2}\nu\frac{\partial^2}{\partial X_j^2}(2\delta\overline{u_i}\delta u_i') &= \frac{1}{2}\nu\left[\frac{\partial^2(2\delta\overline{u_i}\delta u_i')}{\partial x_j}\bigg|_2 + \frac{\partial^2(2\delta\overline{u_i}\delta u_i')}{\partial x_j}\bigg|_1 + 2\frac{\partial}{\partial x_j}\left(\frac{\partial(2\delta\overline{u_i}\delta u_i')}{\partial x_j}\bigg|_2\right)\bigg|_1\right] \\
&= \frac{1}{2}\nu\left[2\delta\overline{u_i}\frac{\partial^2\delta u_i'}{\partial x_j^2}\bigg|_2 + 2\delta u_i'\frac{\partial^2\delta\overline{u_i}}{\partial x_j^2}\bigg|_2 + 4\frac{\partial\delta u_i'}{\partial x_j}\bigg|_2\frac{\partial\delta\overline{u_i}}{\partial x_j}\bigg|_2 - 2\delta\overline{u_i}\frac{\partial^2\delta u_i'}{\partial x_j^2}\bigg|_1\right. \\
&\quad \left. - 2\delta u_i'\frac{\partial^2\delta\overline{u_i}}{\partial x_j^2}\bigg|_1 + 4\frac{\partial\delta u_i'}{\partial x_j}\bigg|_1\frac{\partial\delta\overline{u_i}}{\partial x_j}\bigg|_1 + 4\frac{\partial\delta\overline{u_i}}{\partial x_j}\bigg|_1\frac{\partial\delta u_i'}{\partial x_j}i\bigg|_2 + 4\frac{\partial\delta u_i'}{\partial x_j}\bigg|_1\frac{\partial\delta\overline{u_i}}{\partial x_j}\bigg|_2\right] \\
&= \nu\left[\delta\overline{u_i}\frac{\partial^2 u_i'}{\partial x_j^2}\bigg|_2 + \delta u_i'\frac{\partial^2\overline{u_i}}{\partial x_j^2}\bigg|_2 - 2\frac{\partial u_i'}{\partial x_j}\bigg|_2\frac{\partial\overline{u_i}}{\partial x_j}\bigg|_2 - \delta\overline{u_i}\frac{\partial^2 u_i'}{\partial x_j^2}\bigg|_1 - \delta u_i'\frac{\partial^2\overline{u_i}}{\partial x_j^2}\bigg|_1\right. \\
&\quad \left. - 2\frac{\partial u_i'}{\partial x_j}\bigg|_1\frac{\partial\overline{u_i}}{\partial x_j}\bigg|_1 - 2\frac{\partial\overline{u_i}}{\partial x_j}\bigg|_1\frac{\partial u_i'}{\partial x_j}\bigg|_2 - 2\frac{\partial u_i'}{\partial x_j}\bigg|_1\frac{\partial\overline{u_i}}{\partial x_j}\bigg|_2\right]
\end{aligned}
$$

The dissipation term (ϵ) is given by

$$
\begin{aligned}
2\nu\left[\left(\frac{\partial(\overline{u_i}+u_i')}{\partial x_j}\bigg|_1\right)^2 + \left(\frac{\partial(\overline{u_i}+u_i')}{\partial x_j}\bigg|_2\right)^2\right] &= 2\nu\left[\left(\frac{\partial\overline{u_i}}{\partial x_j}\bigg|_1\right)^2 + \left(\frac{\partial u_i'}{\partial x_j}\bigg|_1\right)^2 + 2\frac{\partial\overline{u_i}}{\partial x_j}\bigg|_1\frac{\partial u_i'}{\partial x_j}\bigg|_1\right] \\
&\quad + 2\nu\left[\left(\frac{\partial\overline{u_i}}{\partial x_j}\bigg|_2\right)^2 + \left(\frac{\partial u_i'}{\partial x_j}\bigg|_2\right)^2 + 2\frac{\partial\overline{u_i}}{\partial x_j}\bigg|_2\frac{\partial u_i'}{\partial x_j}\bigg|_2\right]
\end{aligned} \tag{A.20}
$$

There is no transformation for dissipation term, since it is already in the $(x_j\big|_1, x_j\big|_2)$ co-ordinate system

Appendix B

Results from DNS datasets

B.1 Computation of integral scales

The integral length scale defined on the basis of the velocity in a turbulent flow refers to correlation length that exists in a velocity signal in particular direction. It is used as the characteristic large scale in a turbulent flow where it becomes difficult to define a large length scale based on physical constraints of the flow domain[55]. In the present work the integral scale is defined by :

$$L_{jk} = \int_0^\infty R_{ii}(r,t)\,\mathrm{d}r. \tag{B.1}$$

where 'j' refers to the direction of velocity vector, 'k' refers to direction of integration and 'ii' refers to the *auto*correlation function which is defined by :

$$R_{ii}(r) = \frac{\langle u_i(x_i,t)u_i(x_i+r,t)\rangle}{\langle u_i^2\rangle} \tag{B.2}$$

The computation of the integral scale is not straight-forward to compute from Equation B.1. The *auto*correlation curve generally decreases fast to its first zero crossing, and thereafter may become negative or continue to oscillate about zero. O'Neill et al.[90] investigated the computation of the veloctity integral scale using different methods and concludes that the method of integrating upto the first zero crossing to be well defined and suitable for many flows.

Figure B.1 shows the zero crossing in the autocorrelation R_{11}, which is due to the streamwise velocity component in the streamwise direction of flow in TCF3000. The integral scale is computed from integrating the autocorrelation function upto the zero crossing. Figure B.2 shows the integral scales L_{11} and L_{13} which are due to the streamwise velocity in streamwise and spanwise directions respectively.

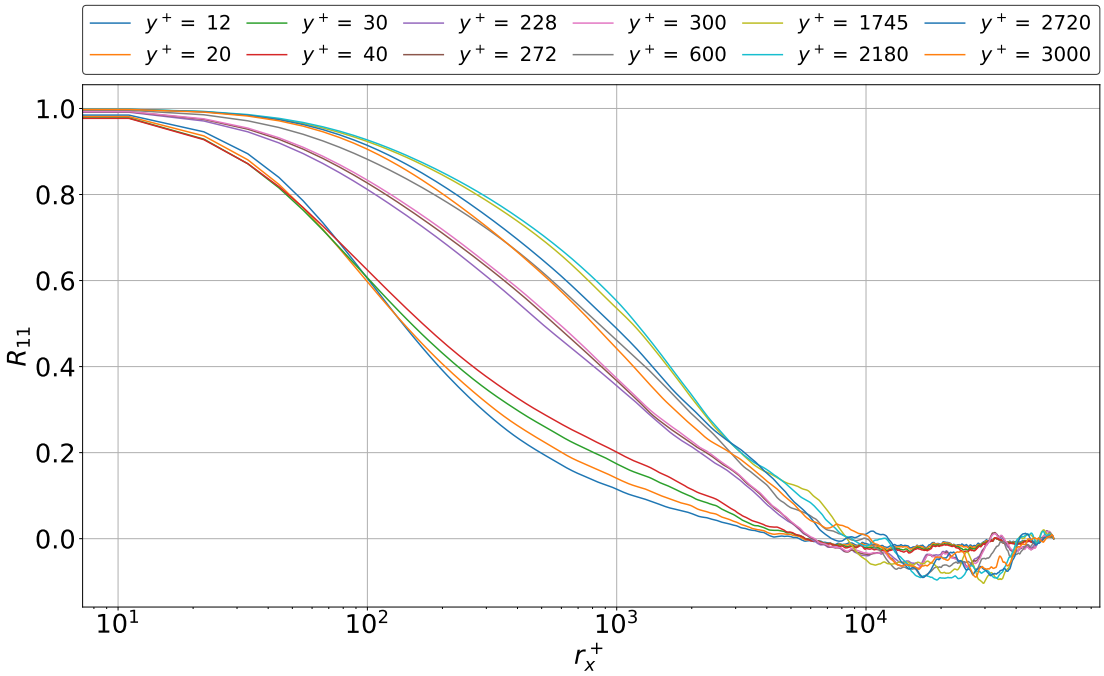

Figure B.1: Autocorrelation of the streamwise velocity component in the streamwise direction in TCF3000

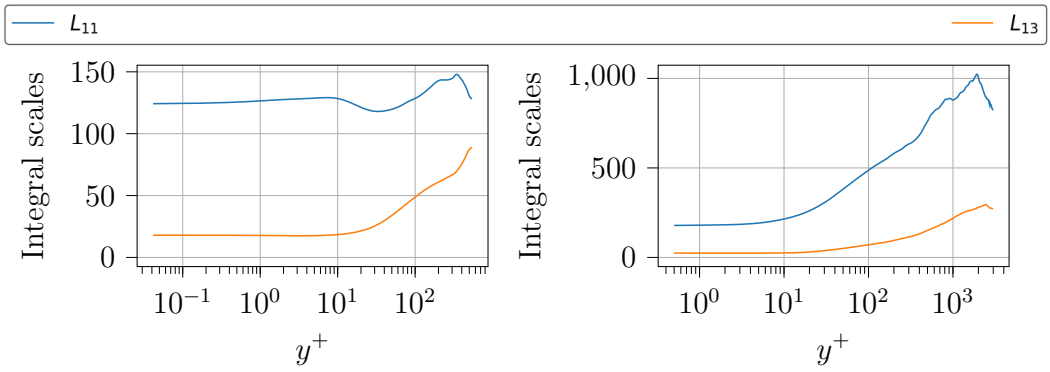

Figure B.2: Integral scales L_{11}, L_{13} in TCF550 (left) and TCF3000 (right)

B.2 Comparison of statistics of DNS datasets

Figure B.3 and B.4 shows the mean velocity, and the statistics of variances and co-variances of the velocity fluctuations in wall-units of TCF550 and TCF3000, which is then compared with DNS datasets with $Re_\tau = 1989$ and 4200. It is observed that the mean velocity profile matches exactly for all the DNS datasets. The variance and the co-variance statistics agree well between the DNS at $Re_\tau = 1989, 3000$ and 4200. This is could be explained by the huge difference between the Re_τ values

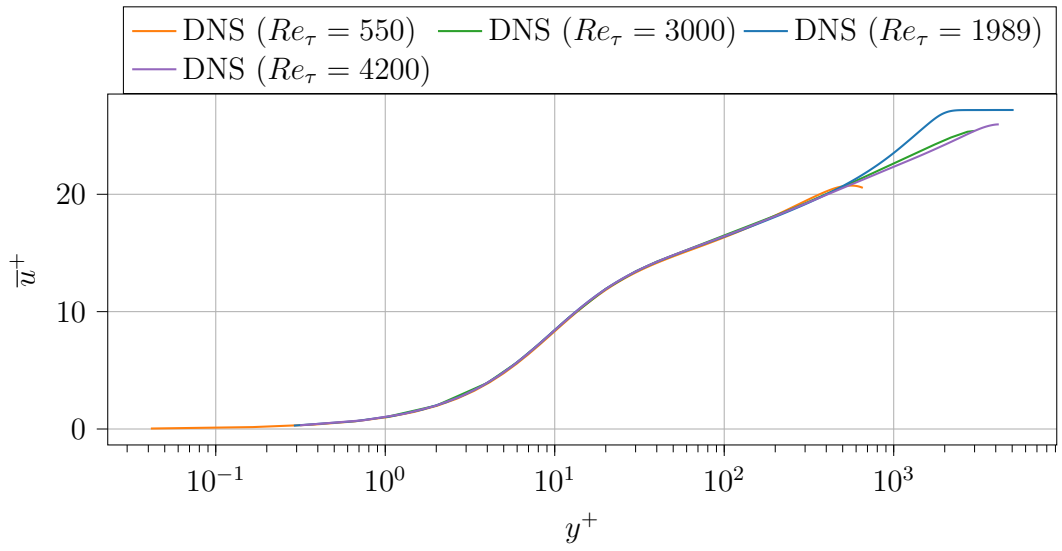

Figure B.3: Mean velocity statistics of DNS datasets at different Re_τ, in wall-units

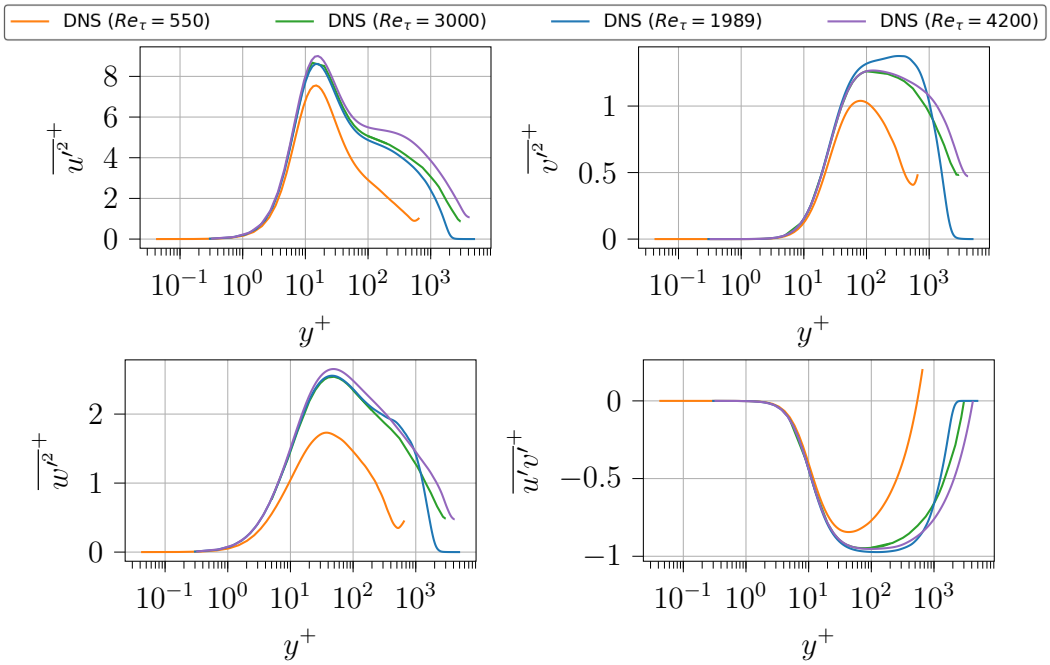

Figure B.4: Variances and co-varianceof DNS datasets at different Re_τ, in wall-units

between TCF550 and the other DNS datasets used for the comparison.

B.3 Average value of interscale energy transfer at large scales

The average value of $\langle\Pi\rangle$ at large scales is approximately equal to $0.5\langle\epsilon'\rangle$ and it is valid till $r^+ = 9\delta$. This is investigated further by decomposing Π into nine terms (a_{11} to a_{33}), which showed that $a_{21} = \langle u_1' u_2' \partial_2 u_1' \rangle$ contributes most to high average value of $-\langle\Pi\rangle$. Following the work of Kholmyansky and Tsinober[64], where they derived the following result

$$\langle u_2' \partial_2 u_1' \rangle = -\langle u_2' \omega_3' - u_3' \omega_2' \rangle \tag{B.3}$$

This Equation B.3 relates the product of velocity and velocity derivative to correlation coefficient between large and small scales of the flow. This section focuses on deriving similar relation for a_{21} term.

Starting with the vector identity

$$\boldsymbol{(u'.\nabla)u'} = \frac{1}{2}\boldsymbol{\nabla(u'.u')} - \boldsymbol{u'} \times \boldsymbol{(\nabla \times u')}$$

$$(u_1'\partial_1 u_1' + u_2'\partial_2 u_1' + u_3'\partial_3 u_1')\vec{\imath} + (u_1'\partial_1 u_2' + u_2\partial_2 u_2' + u_3'\partial_3 u_2')\vec{\jmath} + (u_1'\partial_1 u_3' + u_2'\partial_2 u_3' + u_3'\partial_3 u_3')\vec{k}$$
$$= [(\partial_1\vec{\imath} + \partial_2\vec{\jmath} + \partial_3\vec{k})(u_1'^2 + u_2'^2 + u_3'^2)] - [(u_2'\omega_3' - u_3'\omega_2')\vec{\imath} - (u_1'\omega_3' - u_3'\omega_2')\vec{\jmath} + (u_1'\omega_2 - u_2'\omega_1)\vec{k}]$$

Equating the $\vec{\imath}$ components and multiplying the resulting equation by u_1 to get the equation in terms of a_{21},

$$u_1'u_1'\partial_1 u_1' + u_1'u_2'\partial_2 u_1' + u_1'u_3'\partial_3 u_1' = u_1'(\partial_1)(u_1'^2 + u_2'^2 + u_3'^2) - u_1'(u_2'\omega_3' - u_3'\omega_2')$$

Averaging the above equation gives

$$\langle u_1'\partial_1 u_1' + u_2'\partial_2 u_1' + u_3'\partial_3 u_1' \rangle = \langle u_1'(\partial_1)(u_1'^2 + u_2'^2 + u_3'^2)\rangle - \langle u_1'(u_2'\omega_3' - u_3'\omega_2')\rangle$$

First term on the right hand side is non-zero only for the derivative in the wall-normal direction $[\partial_2(..)]$

$$\langle u_1'u_1'\partial_1 u_1' + u_1'u_2'\partial_2 u_1' + u_1'u_3'\partial_3 u_1' \rangle = -\langle (u_1'u_2'\omega_3' - u_1'u_3'\omega_2')\rangle$$

$$\langle u_1'u_1'\partial_1 u_1' + \partial_2(\frac{u_1'u_1'u_2'}{2}) - \frac{u_1'u_1'}{2}\partial_2 u_2' + \partial_3(\frac{u_1'u_1'u_3'}{2}) - \frac{u_1'u_1'}{2}\partial_3 u_3' \rangle = -\langle (u_1'u_2'\omega_3' - u_1'u_3'\omega_2')\rangle$$

The third and the fifth term on the left hand side can be simplified using continuity equation for incompressible flows

$$\langle \frac{3}{2}(u_1'u_1'\partial_1 u_1') + \partial_2(\frac{u_1'u_1'u_2'}{2}) + \partial_3(\frac{u_1'u_1'u_3'}{2})\rangle = -\langle (u_1'u_2'\omega_3' - u_1'u_3'\omega_2')\rangle$$

$$\langle \partial_1(\frac{u_1' u_1' u_1'}{2}) + \partial_2(\frac{u_1' u_1' u_2'}{2}) + \partial_3(\frac{u_1' u_1' u_3'}{2}) \rangle = -\langle (u_1' u_2' \omega_3' - u_1' u_3' \omega_2') \rangle$$

The second term on the left hand side is the only non-zero term, because it is in the wall-normal direction. The other terms on the left hand side of the equation are zero.

$$\langle \partial_2(\frac{u_1' u_1' u_2'}{2}) \rangle = -\langle (u_1' u_2' \omega_3' - u_1' u_3' \omega_2') \rangle$$

$$\langle \frac{u_1' u_1'}{2} \partial_2 u_2' \rangle + \underbrace{\langle u_1' u_2' \partial_2 u_1' \rangle}_{a_{21}} = -\langle (u_1' u_2' \omega_3' - u_1' u_3' \omega_2') \rangle$$

The term a_{21} shows the correlation of a Reynolds stress term and a vorticity which in-turn suggests the correlation coefficient between the large and small scales of the flow.

B.4 Standard deviation of KHMH equation terms

B.4.1 Comparison of TCF at different Re_τ

Figure B.5 shows the standard deviation of KHMH equation terms in streamwise direction at different wall-distances in TCF550 and TCF3000. The normalisation of the standard deviations of the terms are by $\frac{u_\tau^4}{\nu}$ between $y^+ = 12$ and $y^+ = 100$, and by $\frac{U_{max}^3}{\delta}$ ofr $y/\delta = 0.72, 1$.

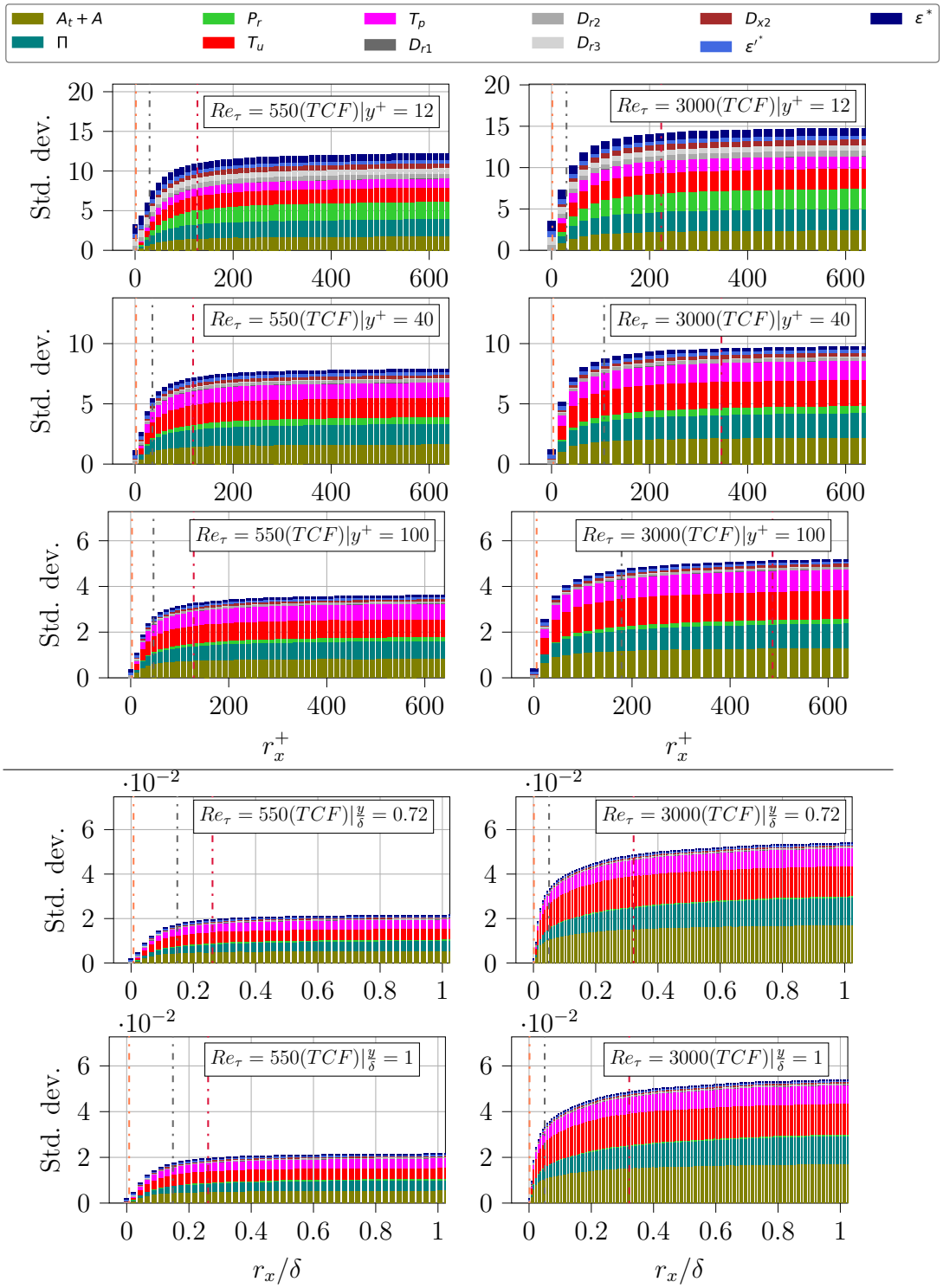

Figure B.5: Standard deviation of KHMH terms in streamwise direction separation of TCF at $Re_\tau = 550$ (left) and TCF at $Re_\tau = 3000$ (right)

B.4.2 Comparison of TCF550 and TBL550

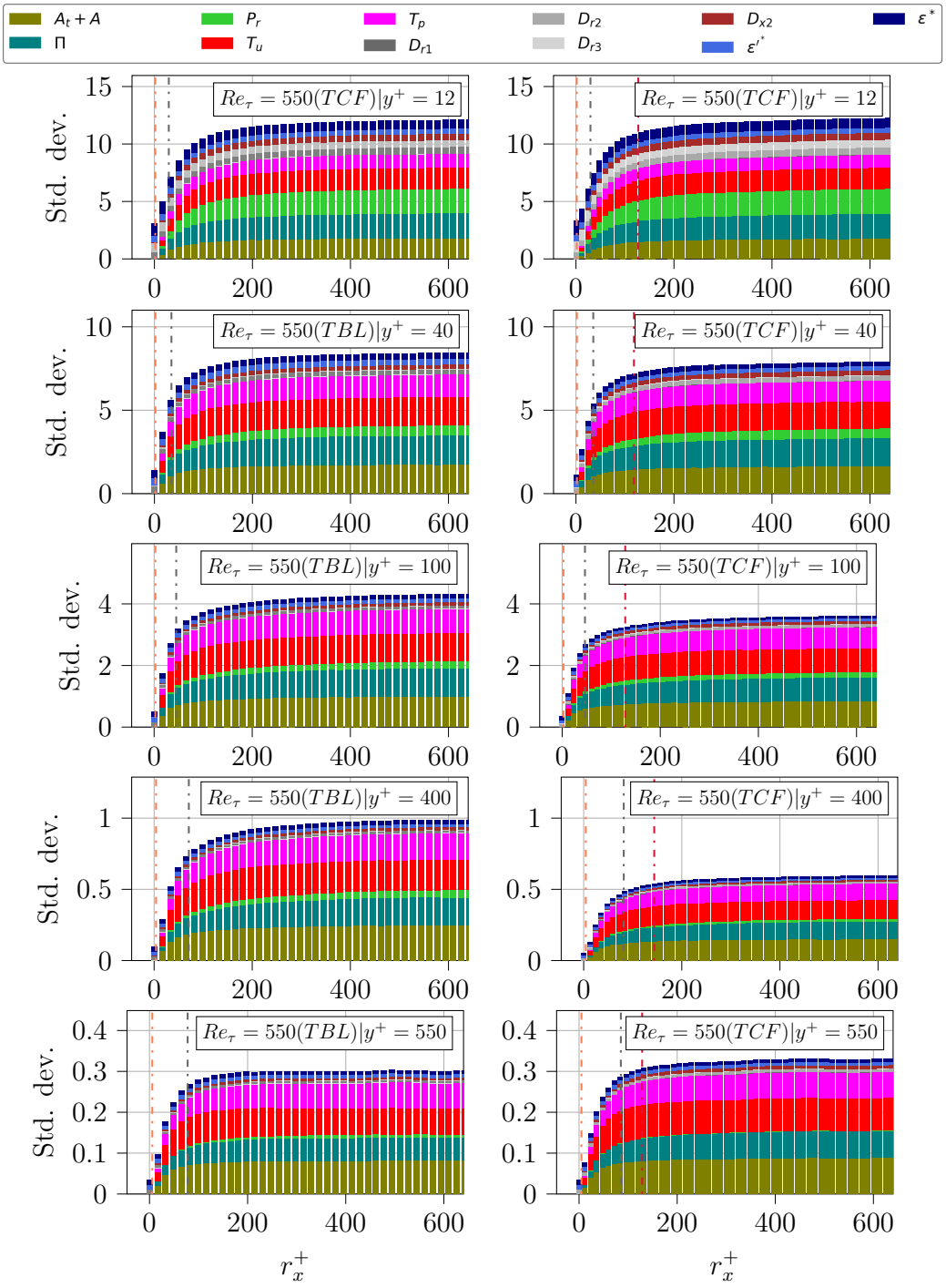

Figure B.6: Standard deviation of KHMH terms in streamwise direction separation of TBL at $Re_\tau = 550$(left) and TCF at $Re_\tau = 550$ (right)

Figure B.6 shows the standard deviation of KHMH equation terms in streamwise

direction at different wall-distances in TCF550 and TBL550. The normalisation of the standard deviations of the terms are by $\frac{u_\tau^4}{\nu}$ at all wall-distances.

Appendix C

Computation of S-PIV parameters

C.1 Computation of S-PIV parameters

The diameter of the particle (ϕ_d) is computed for magnification factor, M = 0.26, f-number $f_\# = 8$ as :

$$\phi_d = 2.44 f_\# (1 + M)\lambda = 1.3 \times 10^{-5} m = 1.3 pixels \tag{C.1}$$

The out-of-plane velocity is computed for u_∞ = 3m/s as :

$$w_{rms} = \frac{u_{rms}}{1.5} = \frac{0.1 u_\infty}{1.5} = \frac{0.3}{1.5} = 0.2 m/s \tag{C.2}$$

The out-of-plane displacement for sampling frequency, f_s =4.6 kHz is computed as :

$$\delta_z = w_{rms} \times \Delta t = \frac{w_{rms}}{f_s} = \frac{0.2}{4.6 \times 10^3} = 43.4 \mu m \tag{C.3}$$

The thickness of light sheet has an upper limit, so that there is less averaging in that direction. The light-sheet should have equal distribution of energy of the laser all along the thickness to ensure high SNR value, and also that it is sufficiently smaller than the interrogation window. However for the lower end is defined by the fact that the out-of-plane displacement should be limited to one-quarter of the ligh-sheet thickness. Thus for the present experiment the out-of-plane displacement is 0.043 mm, interrogation window is 1mm, and so a trade-off value of light sheet thickness of 0.5mm is chosen for the experiment.

The angle of divergence from the beam-waist at the field-of-view (θ_1) is computed by Equation 6.4 as 13.54×10^{-3} rad. The Rayleigh length z_r, which is defined as the distance along the propogation direction in which the area of cross-section doubles from the beam-waist. This is computed by :

$$z_r = \frac{\pi w_0^2}{\lambda M^2} = 18mm \tag{C.4}$$

This length corresponds to approximately the length of the field-of-view along the wall-normal direction which is 20mm. The laser beam is a diverging beam, which has an angle of 4.4 $\times10^{-3}$ rad, which is then made parallel by the use of 1000 mm lens. The radius of the laser beam which is parallel is given by 4.44 mm. The light-sheet thickness is decided to 0.5 mm, and so the angle of divergence at field-of-view is 13.54 $\times10^{-3}$ rad, and so the focal length of the spherical lens to be used is computed by :

$$f = 4.44/tan(13.54 \times 10^{-3}) = 327mm \tag{C.5}$$

Since the laser beam is parallel before the spherical lens, it will converge at the focus which is 327 mm according to our requirements. The closest available spherical lens is 400 mm, and is therefore used in the experiment.

In order to decide the cylindrical lens for illuminating the field-of-view of 70 mm in length, it is decided to produce a light sheet of 180 mm. This high value is chosen because, the high value of $M^2 = 20$ for the laser means that the beam is more concentrated and powerful in the center and it is important that this region covers the entire field-of-view. For the computation of angle of divergence for cylindrical lens (θ_2)

$$\theta_2 = tan^{-1}(90/400) = 0.221rad \tag{C.6}$$

For the computation of focal length of the cylindrical lens,

$$f_1 = 4.44/tan(0.221) = 20.06mm \tag{C.7}$$

The closest value of cylindrical lens is 22 mm and is used in the experiment to create the light-sheet.

C.2 Effect of Denoise in average KHMH terms

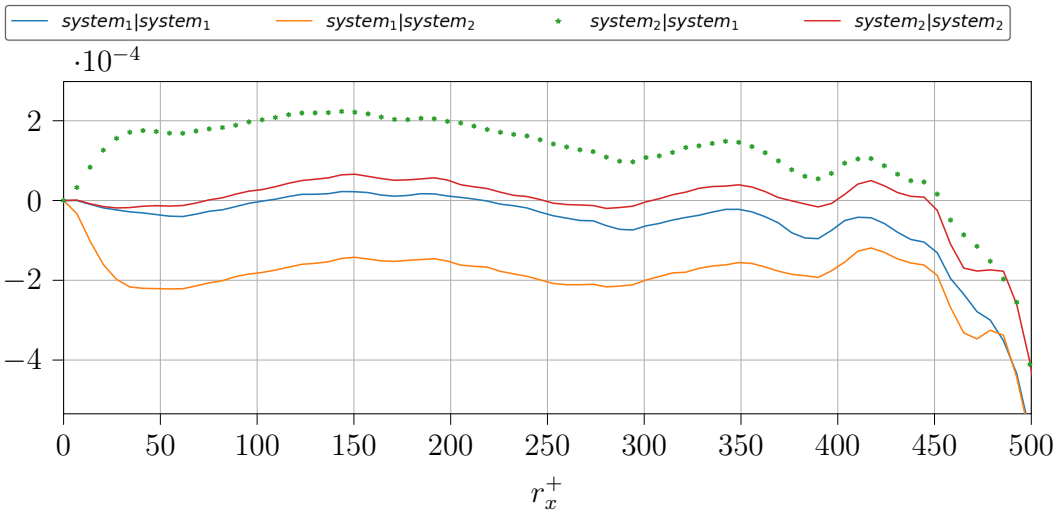

Figure C.1: Computation of time derivative ($A_t \times (10\Delta t)$) from different combination of systems

This section focuses on the effect of denoise in the average value of the time derivative term A_t, given by:

$$A_t = \frac{\partial}{\partial t}(\delta \boldsymbol{u_i})^2 = \delta \boldsymbol{u_i} \frac{\partial \delta \boldsymbol{u_i}}{\partial t} \tag{C.8}$$

Computing the term using Least square method

$$\begin{aligned} A_t &= (u_2 - u_1)(\frac{\partial u_2}{\partial t} - \frac{\partial u_1}{\partial t}) \\ &= u_2 \frac{\partial u_2}{\partial t} - u_2 \frac{\partial u_1}{\partial t} - u_1 \frac{\partial u_2}{\partial t} + u_1 \frac{\partial u_1}{\partial t} \\ &= u_2^t \left(\frac{2u_2^{t+2} + u_2^{t+1} - u_2^{t-1} - 2u_2^{t-2}}{10\Delta t} \right) - u_2^t \left(\frac{2u_1^{t+2} + u_1^{t+1} - u_1^{t-1} - 2u_1^{t-2}}{10\Delta t} \right) \\ &- u_1^t \left(\frac{2u_2^{t+2} + u_2^{t+1} - u_2^{t-1} - 2u_2^{t-2}}{10\Delta t} \right) + u_1^t \left(\frac{2u_1^{t+2} + u_1^{t+1} - u_1^{t-1} - 2u_1^{t-2}}{10\Delta t} \right) \end{aligned} \tag{C.9}$$

$$\begin{aligned} (A_t)(10\Delta t) &= u_2^t(2u_2^{t+2} + u_2^{t+1} - u_2^{t-1} - 2u_2^{t-2}) - u_2^t(2u_1^{t+2} + u_1^{t+1} - u_1^{t-1} - 2u_1^{t-2}) \\ &- u_1^t(2u_2^{t+2} + u_2^{t+1} - u_2^{t-1} - 2u_2^{t-2}) + u_1^t(2u_1^{t+2} + u_1^{t+1} - u_1^{t-1} - 2u_1^{t-2}) \\ &= \underbrace{2u_2^t u_2^{t+2}}_{a_1} + \underbrace{u_2^t u_2^{t+1}}_{a_2} - \underbrace{u_2^t u_2^{t-1}}_{a_3} - \underbrace{2u_2^t u_2^{t-2}}_{a_4} - \underbrace{2u_2^t u_1^{t+2}}_{a_5} - \underbrace{u_2^t u_1^{t+1}}_{a_6} + \underbrace{u_2^t u_1^{t-1}}_{a_7} + \underbrace{2u_2^t u_1^{t-2}}_{a_8} \\ &- \underbrace{2u_1^t u_2^{t+2}}_{a_9} - \underbrace{u_1^t u_2^{t+1}}_{a_{10}} + \underbrace{u_1^t u_2^{t-1}}_{a_{11}} + \underbrace{2u_1^t u_2^{t-2}}_{a_{12}} + \underbrace{2u_1^t u_1^{t+2}}_{a_{13}} + \underbrace{u_1^t u_1^{t+1}}_{a_{14}} - \underbrace{u_1^t u_1^{t-1}}_{a_{15}} - \underbrace{2u_1^t u_1^{t-2}}_{a_{16}} \end{aligned} \tag{C.10}$$

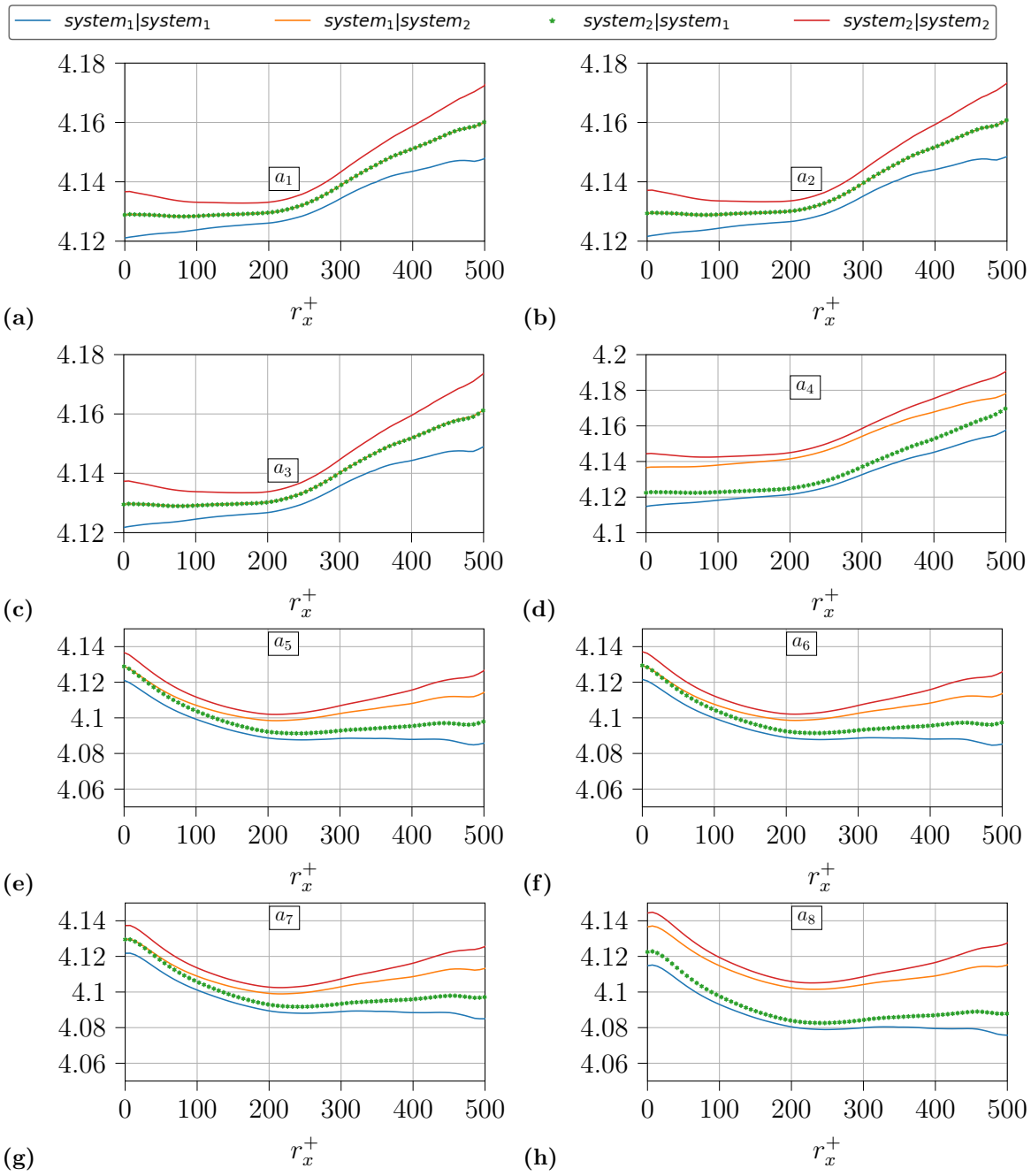

Figure C.2: Computation of individual terms (a_1 to a_8) from different combination of systems

Figure C.1, shows $\langle A_t \rangle \times 10\Delta t$ which is numerator of the time derivative term of KHMH equation. It can be observed that the error between the computation of this value is of the order of 10^{-4}. In order to investigate further, this term is decomposed into its individual components, and the average value of all the individual terms are

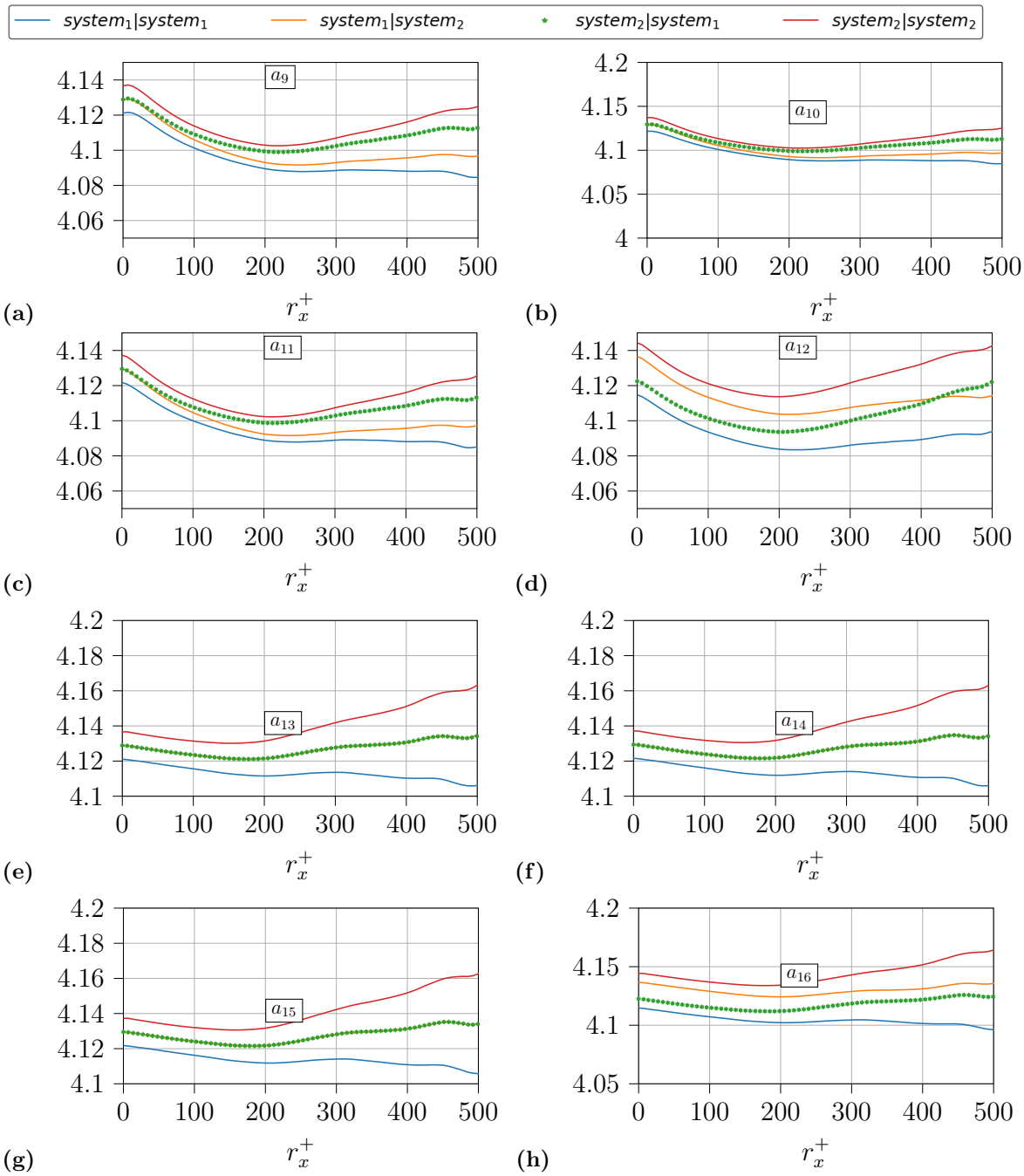

Figure C.3: Computation of individual terms (a_9 to a_{16}) from different combination of systems

shown in Figure C.2, C.2. The individual terms are subtracted or added to obtain $\langle A_t \rangle$. When the individual terms are studied, it can be observed that the denoised values of each of those terms are always between the values of the two systems. For many individual terms, both the denoise values are the same. However when

the addition/subtraction of terms are performed, somehow the A_t with individual systems are near zero and the one with denoised is away from zero.

C.3 Numerical scheme used for time and space derivatives in PIV datasets

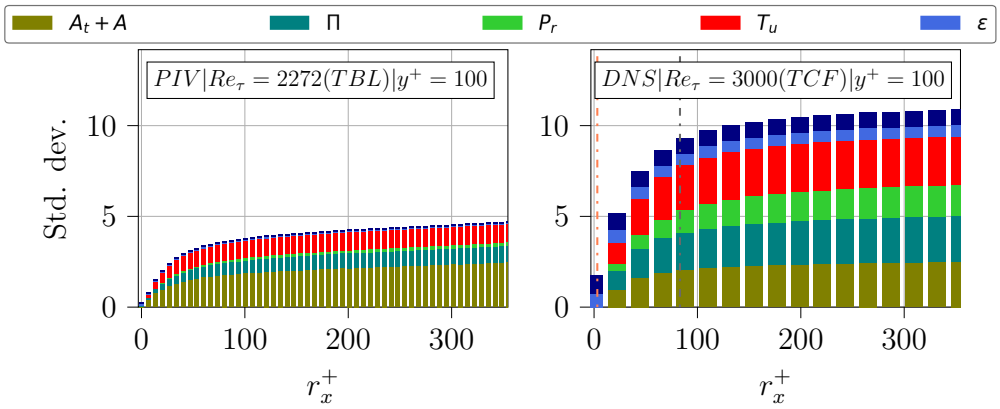

Figure C.4: Standard deviation of KHMH terms computed from PIV experiments at $Re_\tau = 2220$ (left) and TCF3000 DNS (right) in streamwise direction at $y^+ = 100$. The standard deviations of all the terms are normalised by $\frac{u_\tau^4}{\nu^3}$

Figure C.4 shows the standard deviation of different terms of KHMH equation between the PIV dataset at $Re_\tau = 2220$ and the DNS datasets. The main observation is that $A_t + A$ has high standard deviation compared to interscale energy transfer term in the PIV datasets. However in the DNS dataset, both the $A_t + A$ and the interscale energy transfer terms have approximately the same standard deviation. This higher standard deviation could be explained by the fact the noise present in the PIV experiment has more influence on the quantities associated with the fluctuation of velocity.

The terms of the KHMH equation contains both the velocity vectors and their derivatives. And so it is important to understand the effect of the noise, so as to find a way to reduce it without losing the physics of the flow. The terms considered here has both time and space derivative. It is true that the velocity vector in the PIV experiment is filtered in space due to the averaging of the velocity vector in the interrogation window. However the time derivative has no such filter and so it is important to address the noise in the time-derivative term.

The time-derivative in the present experiment is obtained by second-order central

difference scheme, which is given by :

$$\left.\frac{\partial u}{\partial t}\right|_i = \frac{u_{i+1} - u_{i-1}}{2\Delta t} \tag{C.11}$$

If the noise is assumed to be correlated to a certain length scale, then the adjacent points are highly correlated than the points away from it. Hence it is possible to reduce the noise by obtaining the derivative from points next to the immediate neighbours. This will be addressed as central difference (skipped). This is given by :

$$\left.\frac{\partial u}{\partial t}\right|_i = \frac{u_{i+2} - u_{i-2}}{4\Delta t} \tag{C.12}$$

Foucaut and Stanislas[39] observed that the Least-Square method (LS)[94], to obtain the derivative has smaller noise amplification coefficient than the central difference schemes, and still maintains the second-order scheme. So, this method is optimized to reduce the effect of noise in the computation of derivatives. This LS scheme is given by:

$$\left.\frac{\partial u}{\partial t}\right|_i = \frac{-2u_{i-2} - u_{i-1} + u_{i+1} + 2u_{i-2}}{10\Delta t} \tag{C.13}$$

Figure C.5 shows the standard deviation of $A_t + A$ term from using different methods to obtain time-derivative. It can be observed that the second-order central difference scheme has the highest standard deviation followed by second order central difference scheme (skipped), where the next set of points are used and is followed by linear regression method. The least standard deviation of all 4 methods is obtained by the least square fit which is slmost equal to that of linear regresssion. In addition to time-derivative, there is also a space derivative in the $A_t + A$ and so the least-square method is used for the space derivative and this plotted as 'least square (space+time)' in Figure C.5. It is observed that the standard deviation is reduced when both the space and time derivatives are obtained using least-square method. Hence this method is used to obtain the derivatives of velocity in the PIV datasets.

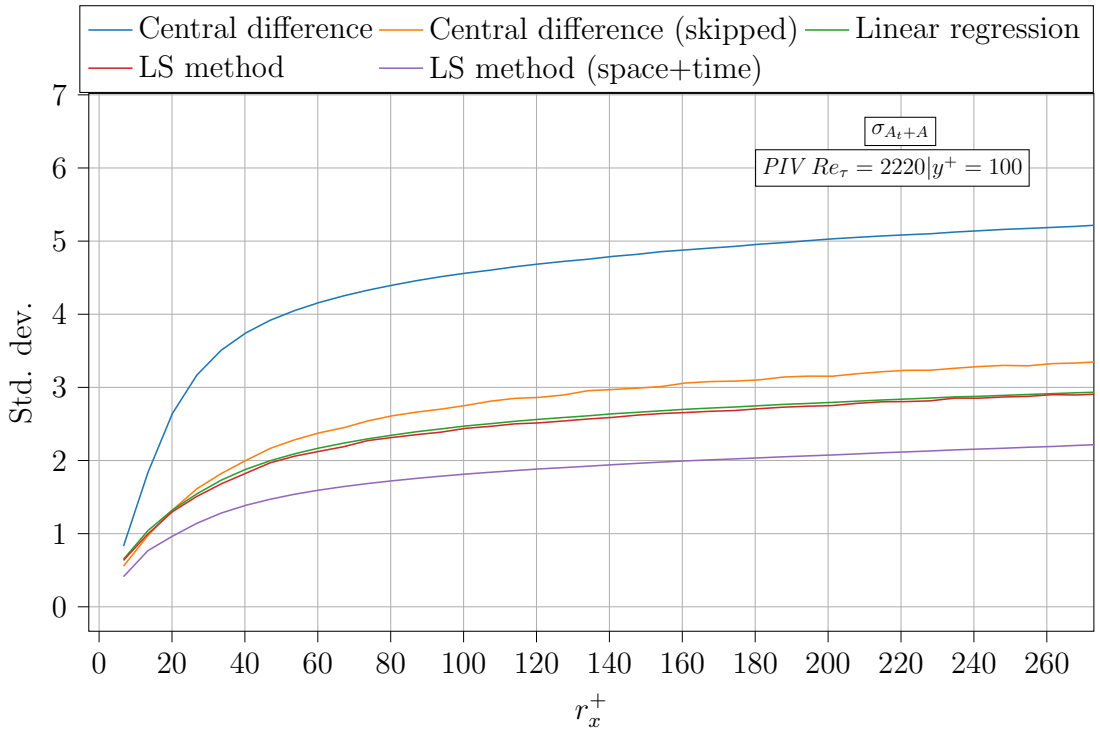

Figure C.5: Standard deviation of modified time-derivative term computed from different methods to obtain derivatives

Bibliography

[1] Adrian, R. J. (2007). Hairpin vortex organization in wall turbulence. *Physics of Fluids*, 19(4):041301.

[2] Adrian, R. J. and Moin, P. (1988). Stochastic estimation of organized turbulent structure: homogeneous shear flow. *Journal of Fluid Mechanics*, 190:531–559.

[3] Adrian, R. J. and Yao, C.-S. (1985). Pulsed laser technique application to liquid and gaseous flows and the scattering power of seed materials. *Applied optics*, 24(1):44–52.

[4] Alves Portela, F., Papadakis, G., and Vassilicos, J. (2017). The turbulence cascade in the near wake of a square prism. *Journal of Fluid Mechanics*, 825:315–352.

[5] Antonia, R., Ould-Rouis, M., Anselmet, F., and Zhu, Y. (1997). Analogy between predictions of kolmogorov and yaglom. *Journal of Fluid Mechanics*, 332:395–409.

[6] Aragón, J. L., Naumis, G. G., Bai, M., Torres, M., and Maini, P. K. (2008). Turbulent luminance in impassioned van gogh paintings. *Journal of Mathematical Imaging and Vision*, 30(3):275–283.

[7] Arroyo, M. and Greated, C. (1991). Stereoscopic particle image velocimetry. *Measurement science and technology*, 2(12):1181.

[8] Atkinson, C., Coudert, S., Foucaut, J.-M., Stanislas, M., and Soria, J. (2011). The accuracy of tomographic particle image velocimetry for measurements of a turbulent boundary layer. *Experiments in fluids*, 50(4):1031–1056.

[9] Bakewell Jr, H. P. and Lumley, J. L. (1967). Viscous sublayer and adjacent wall region in turbulent pipe flow. *The Physics of Fluids*, 10(9):1880–1889.

[10] Batchelor, G. (1947). Kolmogoroff's theory of locally isotropic turbulence. In *Mathematical Proceedings of the Cambridge Philosophical Society*, volume 43, pages 533–559. Cambridge University Press.

[11] Beattie, J. and Kriel, N. (2019). Is the starry night turbulent? *arXiv preprint arXiv:1902.03381*.

[12] Bernard, P. S. and Handler, R. A. (1990). Reynolds stress and the physics of turbulent momentum transport. Technical report, NAVAL RESEARCH LAB WASHINGTON DC.

[13] Borrell, G., Sillero, J. A., and Jiménez, J. (2013). A code for direct numerical simulation of turbulent boundary layers at high reynolds numbers in bg/p supercomputers. *Computers & Fluids*, 80:37–43.

[14] Brodkey, R. S., Wallace, J. M., and Eckelmann, H. (1974). Some properties of truncated turbulence signals in bounded shear flows. *Journal of Fluid Mechanics*, 63(2):209–224.

[15] Brown, G. L. and Roshko, A. (1974). On density effects and large structure in turbulent mixing layers. *Journal of Fluid Mechanics*, 64(4):775–816.

[16] Brücker, C. (1995). Digital-particle-image-velocimetry (dpiv) in a scanning light-sheet: 3d starting flow around a short cylinder. *Experiments in Fluids*, 19(4):255–263.

[17] Cantwell, B. J. (1981). Organized motion in turbulent flow. *Annual review of fluid mechanics*, 13(1):457–515.

[18] Carlier, J. and Stanislas, M. (2005). Experimental study of eddy structures in a turbulent boundary layer using particle image velocimetry. *Journal of Fluid Mechanics*, 535:143.

[19] Casciola, C., Gualtieri, P., Benzi, R., and Piva, R. (2003). Scale-by-scale budget and similarity laws for shear turbulence. *Journal of Fluid Mechanics*, 476:105–114.

[20] Chen, L., Coleman, S. W., Vassilicos, J. C., and Hu, Z. (2010). Acceleration in turbulent channel flow.

[21] Cimarelli, A. and De Angelis, E. (2014). The physics of energy transfer toward improved subgrid-scale models. *Physics of Fluids*, 26(5):055103.

[22] Cimarelli, A., De Angelis, E., and Casciola, C. (2013). Paths of energy in turbulent channel flows. *Journal of Fluid Mechanics*, 715:436–451.

[23] Cimarelli, A., De Angelis, E., Jimenez, J., and Casciola, C. M. (2016). Cascades and wall-normal fluxes in turbulent channel flows. *Journal of Fluid Mechanics*, 796:417–436.

[24] Corino, E. R. and Brodkey, R. S. (1969). A visual investigation of the wall region in turbulent flow. *Journal of Fluid Mechanics*, 37(1):1–30.

[25] Cowen, E. and Monismith, S. (1997). A hybrid digital particle tracking velocimetry technique. *Experiments in fluids*, 22(3):199–211.

[26] Cuvier, C., Foucaut, J.-M., Braud, C., and Stanislas, M. (2014). Characterisation of a high reynolds number boundary layer subject to pressure gradient and separation. *Journal of Turbulence*, 15(8):473–515.

[27] Cuvier, C., Srinath, S., Stanislas, M., Foucaut, J.-M., Laval, J.-P., Kähler, C., Hain, R., Scharnowski, S., Schröder, A., Geisler, R., et al. (2017). Extensive characterisation of a high reynolds number decelerating boundary layer using advanced optical metrology. *Journal of Turbulence*, 18(10):929–972.

[28] Danaila, L., Anselmet, F., and Zhou, T. (2004). Turbulent energy scale-budget equations for nearly homogeneous sheared turbulence. *Flow, turbulence and combustion*, 72(2-4):287–310.

[29] Danaila, L., Anselmet, F., Zhou, T., and Antonia, R. (1999). A generalization of yaglom's equation which accounts for the large-scale forcing in heated decaying turbulence. *Journal of Fluid Mechanics*, 391:359–372.

[30] Danaila, L., Krawczynski, J., Thiesset, F., and Renou, B. (2012). Yaglom-like equation in axisymmetric anisotropic turbulence. *Physica D: Nonlinear Phenomena*, 241(3):216–223.

[31] De Karman, T. and Howarth, L. (1938). On the statistical theory of isotropic turbulence. *Proceedings of the Royal Society of London. Series A-Mathematical and Physical Sciences*, 164(917):192–215.

[32] Elsinga, G., Adrian, R., van Oudheusden, B., and Scarano, F. (2007a). Tomographic-piv investigation of a high reynolds number turbulent boundary layer 7th int. In *Symp. on PIV, Rome, Italy*.

[33] Elsinga, G., Kuik, D., Van Oudheusden, B., and Scarano, F. (2007b). Investigation of the three-dimensional coherent structures in a turbulent boundary layer. In *Forty-fifth AIAA Aerospace Sciences Meeting, Reno, NV, AIAA-2007-1305*.

[34] Elsinga, G. and Marusic, I. (2010). Evolution and lifetimes of flow topology in a turbulent boundary layer. *Physics of Fluids*, 22(1):015102.

[35] Elsinga, G., Van Oudheusden, B., and Scarano, F. (2006a). Experimental assessment of tomographic-piv accuracy. In *13th international symposium on applications of laser techniques to fluid mechanics, Lisbon, Portugal, paper*, volume 20.

[36] Elsinga, G. E., Scarano, F., Wieneke, B., and van Oudheusden, B. W. (2006b). Tomographic particle image velocimetry. *Experiments in fluids*, 41(6):933–947.

[37] Falco, R. E. (1977). Coherent motions in the outer region of turbulent boundary layers. *The Physics of Fluids*, 20(10):S124–S132.

[38] Foucaut, J.-M., Cuvier, C., Stanislas, M., and George, W. K. (2016). Quantification of the full dissipation tensor from an l-shaped spiv experiment in the near wall region. In *Progress in Wall Turbulence 2*, pages 429–439. Springer.

[39] Foucaut, J. M. and Stanislas, M. (2002). Some considerations on the accuracy and frequency response of some derivative filters applied to particle image velocimetry vector fields. *Measurement Science and Technology*, 13(7):1058–1071.

[40] Frisch, U. and Kolmogorov, A. N. (1995). *Turbulence: the legacy of AN Kolmogorov*. Cambridge university press.

[41] Gatti, D., Remigi, A., Chiarini, A., Cimarelli, A., and Quadrio, M. (2019). An efficient numerical method for the generalised kolmogorov equation. *Journal of Turbulence*, 20(8):457–480.

[42] Geisler, R., Novara, M., and Schröder, A. (2016). Volumetric multi-pulse particle tracking measurement for separated laminar transitional flow investigations. In *18th international symposium on applications of laser techniques to fluid mechanics*, pages 4–7.

[43] George, W. K. and Hussein, H. J. (1991). Locally axisymmetric turbulence. *Journal of Fluid Mechanics*, 233:1–23.

[44] George, W. K., Stanislas, M., Foucaut, J.-M., Laval, J.-P., and Cuvier, C. (2020). Velocity derivatives in turbulent boundary layers. part ii: Statistical properties. *arXiv preprint arXiv:2010.09348*.

[45] Gersten, K. and Herwig, H. (1992). Strömungsmechanik. grundlagen der impuls. *Wärme-und Stoffübertragung aus asymptotischer Sicht*, 6.

[46] Gomes-Fernandes, R., Ganapathisubramani, B., and Vassilicos, J. (2015). The energy cascade in near-field non-homogeneous non-isotropic turbulence. *Journal of Fluid Mechanics*, 771:676–705.

[47] Goodman, J. W. (2005). *Introduction to Fourier optics*. Roberts and Company Publishers.

[48] Guezennec, Y. (1989). Stochastic estimation of coherent structures in turbulent boundary layers. *Physics of Fluids A: Fluid Dynamics*, 1(6):1054–1060.

[49] Hagen, G. (1839). Ueber die bewegung des wassers in engen cylindrischen röhren. *Annalen der Physik*, 122(3):423–442.

[50] Head, M. and Bandyopadhyay, P. (1981). New aspects of turbulent boundary-layer structure. *Journal of fluid mechanics*, 107:297–338.

[51] Hecht, E. and Zajac, A. (1974). Optics addison-wesley. *Reading, Mass*, 19872:350–351.

[52] Herpin, S., Wong, C. Y., Stanislas, M., and Soria, J. (2008). Stereoscopic piv measurements of a turbulent boundary layer with a large spatial dynamic range. *Experiments in fluids*, 45(4):745.

[53] Hill, R. J. (1997). Applicability of kolmogorov's and monin's equations of turbulence. *Journal of Fluid Mechanics*, 353:67–81.

[54] Hill, R. J. (2002). Exact second-order structure-function relationships. *Journal of Fluid Mechanics*, 468:317–326.

[55] Hinze, J. (1975). *Turbulence*. McGraw-Hill classic textbook reissue series. McGraw-Hill.

[56] Hoyas, S. and Jiménez, J. (2008). Reynolds number effects on the reynolds-stress budgets in turbulent channels. *Physics of Fluids*, 20(10):101511.

[57] Huang, H., Dabiri, D., and Gharib, M. (1997). On errors of digital particle image velocimetry. *Measurement Science and Technology*, 8(12):1427.

[58] Hwang, J., Lee, J. H., and Sung, H. J. (2020). Statistical behaviour of self-similar structures in canonical wall turbulence. *arXiv preprint arXiv:2009.08686*.

[59] Ishikawa, M., Murai, Y., Wada, A., Iguchi, M., Okamoto, K., and Yamamoto, F. (2000). A novel algorithm for particle tracking velocimetry using the velocity gradient tensor. *Experiments in Fluids*, 29(6):519–531.

[60] Jiménez, J. (1999). The physics of wall turbulence. *Physica A: Statistical Mechanics and its Applications*, 263(1-4):252–262.

[61] Keane, R., Adrian, R., and Zhang, Y. (1995). Super-resolution particle imaging velocimetry. *Measurement Science and Technology*, 6(6):754.

[62] Keane, R. D. and Adrian, R. J. (1990). Optimization of particle image velocimeters. i. double pulsed systems. *Measurement science and technology*, 1(11):1202.

[63] Keane, R. D. and Adrian, R. J. (1992). Theory of cross-correlation analysis of piv images. *Applied scientific research*, 49(3):191–215.

[64] Kholmyansky, M. and Tsinober, A. (2000). On the origins of intermittency in real turbulent flows. *Intermittency in Turbulent Flows*, page 183.

[65] Kim, J. and Moin, P. (1986). The structure of the vorticity field in turbulent channel flow. part 2. study of ensemble-averaged fields. *Journal of Fluid Mechanics*, 162:339–363.

[66] Kline, S. J., Reynolds, W. C., Schraub, F., and Runstadler, P. (1967). The structure of turbulent boundary layers. *Journal of Fluid Mechanics*, 30(4):741–773.

[67] Kolmogorov, A. N. (1941a). Dissipation of energy in locally isotropic turbulence. In *Dokl. Akad. Nauk SSSR*, volume 32, pages 16–18.

[68] Kolmogorov, A. N. (1941b). The local structure of turbulence in incompressible viscous fluid for very large reynolds numbers. In *Dokl. Akad. Nauk SSSR*, volume 30, pages 299–303.

[69] Kolmogorov, A. N. (1941c). On degeneration (decay) of isotropic turbulence in an incompressible viscous liquid. In *Dokl. Akad. Nauk SSSR*, volume 31, pages 538–540.

[70] Kostas, J., Foucaut, J., and Stanislas, M. (2005). Application of double spiv on the near wall turbulence structure of an adverse pressure gradient turbulent boundary layer. In *6th International Symposium on PIV, Pasadena, California*, pages 21–23.

[71] Laizet, S. and Lamballais, E. (2009). High-order compact schemes for incompressible flows: A simple and efficient method with quasi-spectral accuracy. *Journal of Computational Physics*, 228(16):5989–6015.

[72] Landau, L. and Lifshitz, E. (1987). Fluid mechanics 2nd edition pergamon press.

[73] Lecordier, B. and Trinite, M. (2004). Advanced piv algorithms with image distortion validation and comparison using synthetic images of turbulent flow. In *Particle Image Velocimetry: Recent Improvements*, pages 115–132. Springer.

[74] Lindborg, E. (1996). On kolmogorov's third order structure function law, the local isotropy hypothesis and the pressure-velocity correlation. In *Advances in Turbulence VI*, pages 247–250. Springer.

[75] Lindborg, E. (1999). Correction to the four-fifths law due to variations of the dissipation. *Physics of Fluids*, 11(3):510–512.

[76] Lozano-Durán, A., Flores, O., and Jiménez, J. (2012). The three-dimensional structure of momentum transfer in turbulent channels. *Journal of Fluid Mechanics*, 694:100.

[77] Lozano-Durán, A. and Jiménez, J. (2014). Time-resolved evolution of coherent structures in turbulent channels: characterization of eddies and cascades. *Journal of fluid mechanics*, 759:432.

[78] Lundgren, T. S. (2003). Kolmogorov turbulence by matched asymptotic expansions. *Physics of fluids*, 15(4):1074–1081.

[79] Maas, H., Gruen, A., and Papantoniou, D. (1993). Particle tracking velocimetry in three-dimensional flows. *Experiments in Fluids*, 15(2):133–146.

[80] Manovski, P., Mohan, N. K. D., Geisler, R., Novara, M., Schanz, D., Agocs, J., Ahlefeldt, T., Spehr, C., and Schröder, A. (2016). 3d lagrangian particle tracking using 4-pulse shake-the-box synchronised with microphone measurements on a subsonic jet at mach 0.9.

[81] Marati, N., Casciola, C., and Piva, R. (2004). Energy cascade and spatial fluxes in wall turbulence. *Journal of Fluid Mechanics*, 521:191–215.

[82] Millikan, C. B. (1939). A critical discussion of turbulent flow in channels and circular tubes. In *Proc. 5th Int. Congress on Applied Mechanics (Cambridge, MA, 1938)*, pages 386–392. Wiley.

[83] Mollicone, J.-P., Battista, F., Gualtieri, P., and Casciola, C. (2018). Turbulence dynamics in separated flows: the generalised kolmogorov equation for inhomogeneous anisotropic conditions. *Journal of Fluid Mechanics*, 841:1012–1039.

[84] Monin, A. and Yaglom, A. (1975). Statistical fluid mechanics: Mechanics of turbulence, vol. 2, 874 pp.

[85] Novara, M., Ianiro, A., and Scarano, F. (2012). Adaptive interrogation for 3d-piv. *Measurement Science and Technology*, 24(2):024012.

[86] Novara, M., Schanz, D., Gesemann, S., Lynch, K., and Schröder, A. (2016a). Lagrangian 3d particle tracking for multi-pulse systems: performance assessment and application of shake-the-box.

[87] Novara, M., Schanz, D., Reuther, N., Kähler, C. J., and Schröder, A. (2016b). Lagrangian 3d particle tracking in high-speed flows: Shake-the-box for multi-pulse systems. *Experiments in Fluids*, 57(8):128.

[88] Obligado, M. and Vassilicos, J. C. (2019). The non-equilibrium part of the inertial range in decaying homogeneous turbulence. *EPL (Europhysics Letters)*, 127(6):64004.

[89] Oboukhov, A. (1941). On the distribution of energy in the spectrum of turbulent flow. In *Dokl. Akad. Nauk SSSR*, volume 32, pages 22–24.

[90] O'Neill, P. L., Nicolaides, D., Honnery, D., Soria, J., et al. (2004). Autocorrelation functions and the determination of integral length with reference to experimental and numerical data. In *15th Australasian fluid mechanics conference*, volume 1, pages 1–4. Univ. of Sydney Sydney, NSW, Australia.

[91] Perry, A. and Chong, M. (1982). On the mechanism of wall turbulence. *Journal of Fluid Mechanics*, 119:173–217.

[92] Pope, S. (2000). Turbulent flows, 771 pp.

[93] Prasad, A., Adrian, R., Landreth, C., and Offutt, P. (1992). Effect of resolution on the speed and accuracy of particle image velocimetry interrogation. *Experiments in Fluids*, 13(2-3):105–116.

[94] Raffel, M., Willert, C. E., Scarano, F., Kähler, C. J., Wereley, S. T., and Kompenhans, J. (2018). *Particle image velocimetry: a practical guide*. Springer.

[95] Reynolds, O. (1883). Xxix. an experimental investigation of the circumstances which determine whether the motion of water shall be direct or sinuous, and of the law of resistance in parallel channels. *Philosophical Transactions of the Royal society of London*, (174):935–982.

[96] Reynolds, O. (1895). Iv. on the dynamical theory of incompressible viscous fluids and the determination of the criterion. *Philosophical transactions of the royal society of london.(a.)*, (186):123–164.

[97] Richardson, L. (1922). Weather prediction by numerical process (cambridge u. press).

[98] Robinson, S. K. (1991). Coherent motions in the turbulent boundary layer. *Annual Review of Fluid Mechanics*, 23(1):601–639.

[99] Saikrishnan, N., De Angelis, E., Longmire, E. K., Marusic, I., Casciola, C. M., and Piva, R. (2012). Reynolds number effects on scale energy balance in wall turbulence. *Physics of Fluids*, 2(1):015101.

[100] Scarano, F. (2001). Iterative image deformation methods in piv. *Measurement science and technology*, 13(1):R1.

[101] Scarano, F. (2012). Tomographic piv: principles and practice. *Measurement Science and Technology*, 24(1):012001.

[102] Scarano, F., Ghaemi, S., Caridi, G. C. A., Bosbach, J., Dierksheide, U., and Sciacchitano, A. (2015). On the use of helium-filled soap bubbles for large-scale tomographic piv in wind tunnel experiments. *Experiments in Fluids*, 56(2):42.

[103] Schanz, D., Schröder, A., Gesemann, S., Michaelis, D., and Wieneke, B. (2013). Shake the box: a highly efficient and accurate tomographic particle tracking velocimetry (tomo-ptv) method using prediction of particle positions.

[104] Schlatter, P. and Örlü, R. (2012). Turbulent boundary layers at moderate reynolds numbers: inflow length and tripping effects. *Journal of Fluid Mechanics*, 710:5–34.

[105] Schlichting, H. and Gersten, K. (2016). *Boundary-layer theory*. Springer.

[106] Schröder, A., Geisler, R., Elsinga, G., Scarano, F., and Dierksheide, U. (2005). Investigation of a turbulent spot using time-resolved tomographic piv.

[107] Schröder, A., Geisler, R., Elsinga, G. E., Scarano, F., and Dierksheide, U. (2008). Investigation of a turbulent spot and a tripped turbulent boundary layer flow using time-resolved tomographic piv. *Experiments in Fluids*, 44(2):305–316.

[108] Schröder, A., Geisler, R., Staack, K. é. a. a., Elsinga, G., Scarano, F., Wieneke, B., Henning, A., Poelma, C., and Westerweel, J. (2011). Eulerian and lagrangian views of a turbulent boundary layer flow using time-resolved tomographic piv. *Experiments in fluids*, 50(4):1071–1091.

[109] Schröder, A., Schanz, D., Geisler, R., Novara, M., and Willert, C. (2015a). Near-wall turbulence characterization using 4d-ptv "shake-the-box".

[110] Schröder, A., Schanz, D., Michaelis, D., Cierpka, C., Scharnowski, S., and Kähler, C. J. (2015b). Advances of piv and 4d-ptv" shake-the-box" for turbulent flow analysis–the flow over periodic hills. *Flow, Turbulence and Combustion*, 95(2):193–209.

[111] Sillero, J. A., Jiménez, J., and Moser, R. D. (2013). One-point statistics for turbulent wall-bounded flows at reynolds numbers up to $\delta+ \approx 2000$. *Physics of Fluids*, 25(10):105102.

[112] Simens, M. P., Jiménez, J., Hoyas, S., and Mizuno, Y. (2009). A high-resolution code for turbulent boundary layers. *Journal of Computational Physics*, 228(11):4218–4231.

[113] Solak, I. (2018). *Simulation numérique directe et analyse des grandes échelles d'une couche limite turbulente*. PhD thesis, Lille 1.

[114] Soloff, S. M., Adrian, R. J., and Liu, Z. C. (1997). Distortion compensation for generalized stereoscopic particle image velocimetry. *Measurement Science and Technology*, 8(12):1441–1454.

[115] Soria, J. (1996). An investigation of the near wake of a circular cylinder using a video-based digital cross-correlation particle image velocimetry technique. *Experimental Thermal and Fluid Science*, 12(2):221–233.

[116] Srinath, S. (2017). *Modeling and prediction of near wall turbulent flows*. PhD thesis, Ecole Centrale de Lille.

[117] Takehara, K., Adrian, R., Etoh, G., and Christensen, K. (2000). A kalman tracker for super-resolution piv. *Experiments in Fluids*, 29(1):S034–S041.

[118] Tennekes, H. (1975). Eulerian and lagrangian time microscales in isotropic turbulence. *Journal of Fluid Mechanics*, 67(3):561–567.

[119] Tennekes, H., Lumley, J. L., Lumley, J. L., et al. (1972). *A first course in turbulence*. MIT press.

[120] Thais, L., Tejada-Martı, A. E., Gatski, T. B., Mompean, G., et al. (2011). A massively parallel hybrid scheme for direct numerical simulation of turbulent viscoelastic channel flow. *Computers & fluids*, 43(1):134–142.

[121] Theodorsen, T. (1955). The structure of turbulence. In *50 Jahre Grenzschichtforschung*, pages 55–62. Springer.

[122] Thiesset, F., Danaila, L., Antonia, R., and Zhou, T. (2011). Scale-by-scale energy budgets which account for the coherent motion. In *Journal of Physics: Conference Series*, volume 318, page 052040. IOP Publishing.

[123] Townsend, A. (1980). *The structure of turbulent shear flow*. Cambridge university press.

[124] Tsinober, A., Vedula, P., and Yeung, P. (2001). Random taylor hypothesis and the behavior of local and convective accelerations in isotropic turbulence. *Physics of Fluids*, 13(7):1974–1984.

[125] Valente, P. and Vassilicos, J. (2015). The energy cascade in grid-generated non-equilibrium decaying turbulence. *Physics of Fluids*, 27(4):045103.

[126] Van der Plas, G. and Bastiaans, R. (1998). Accuracy and resolution of a fast ptv-algorithm suitable for hires-pv. In *International symposium on flow visualization (ISFV), 8th: 1998 Sep: Sorrento, Italy*, pages 87–1.

[127] Van Gogh, V. and Irwin, B. (1975). *Starry night*. Athena Reproductions.

[128] Von Kármán, T. (1930). Mechanische änlichkeit und turbulenz. *Nachrichten von der Gesellschaft der Wissenschaften zu Göttingen, Mathematisch-Physikalische Klasse*, 1930:58–76.

[129] Wallace, J. M. (2016). Quadrant analysis in turbulence research: history and evolution. *Annual Review of Fluid Mechanics*, 48:131–158.

[130] Wallace, J. M., Eckelmann, H., and Brodkey, R. S. (1972). The wall region in turbulent shear flow. *Journal of Fluid Mechanics*, 54(1):39–48.

[131] Wernet, M. (2001). New insights into particle image velocimetry data using fuzzy-logic-based correlation/particle tracking processing. *Experiments in fluids*, 30(4):434–447.

[132] Wieneke, B. (2005). Stereo-PIV using self-calibration on particle images. *Experiments in Fluids*, 39(2):267–280.

[133] Wieneke, B. (2012). Iterative reconstruction of volumetric particle distribution. *Measurement Science and Technology*, 24(2):024008.

[134] Willert, C. E., Cuvier, C., Foucaut, J.-M., Klinner, J., Stanislas, M., Laval, J.-P., Srinath, S., Soria, J., Amili, O., Atkinson, C., et al. (2018). Experimental evidence of near-wall reverse flow events in a zero pressure gradient turbulent boundary layer. *Experimental Thermal and Fluid Science*, 91:320–328.

[135] Willert, C. E. and Gharib, M. (1991). Digital particle image velocimetry. *Experiments in Fluids*, 10(4):181–193.

[136] Willmarth, W. and Lu, S. (1972). Structure of the reynolds stress near the wall. *Journal of Fluid Mechanics*, 55(1):65–92.

[137] Yasuda, T. and Vassilicos, J. C. (2018). Spatio-temporal intermittency of the turbulent energy cascade. *Journal of Fluid Mechanics*, 853:235–252.

Analyse de la cascade d'énergie dans une couche limite turbulente

Ce travail consiste à étudier la cascade d'énergie échelle par échelle dans les écoulements turbulents limités par des parois. L'équation de Karman-Howarth-Monin-Hill (KHMH) est une équation d'évolution de $\delta \boldsymbol{u}^2$, qui est directement liée au contenu énergétique dans l'espace des échelles et intégre différents processus associés aux transferts d'énergie dans l'espace physique et l'espace d'échelle (cascade). Le pic de la moyenne spatio-temporelle du terme cascade se met à l'échelle avec la micro-échelle de Taylor modifiée dans une région éloignée de la paroi. Le terme de dérivée temporelle modifiée instantanée et le terme de pression sont fortement corrélés avec les deux termes de transfert d'énergie. Une valeur positive de la moyenne spatio-temporelle du terme de cascade observée au niveau de la zone tampon se déplace vers des échelles plus élevées dans le sens de l'envergure à mesure que la distance à la paroi augmente, ce qui suggère une combinaison de cascade inverse et de tourbillon attaché à la paroi dans la physique de l'écoulement. L'utilisation d'une expérience de double PIV stéréoscopiques indépendantes a permis de débruiter les statistiques, ce qui a aidé à calculer certaines parties des termes de l'équation KHMH dans l'expérience des flux ZPG-TBL, permettant ainsi des mesures près de la paroi à des nombres de Reynolds plus élevés.

Mots clés: Turbulence, écoulement en canal, écoulement en couche limite, transfert d'énergie échelle par échelle, vélocimétrie par image de particules (PIV), nombre de Reynolds.

Analysis of energy cascade in wall-bounded turbulent flows

This work aims to investigate the scale-by-scale energy cascade in wall-bounded turbulent flows. Karman-Howarth-Monin-Hill (KHMH) equation is an evolution equation of $\delta \boldsymbol{u}^2$, which is directly linked to energy content in the scale space and incorporates different processes associated with energy transfers in both physical and scale-space (cascade). The peak of the Spatio-temporal average of cascade term scales with the modified Taylor microscale in the region away from the wall. The instantaneous modified time derivative term and pressure term correlates strongly with the two energy transfer terms. A positive value of the Spatio-temporal average of cascade term observed at the buffer layer moves to higher spanwise scales as the wall distance increases, suggesting a combination of inverse cascade and wall-attached eddy in the physics of the flow. The use of two independent Stereoscopic PIV experiments allowed to denoise the statistics, which helped to compute some parts of KHMH equation terms in the ZPG-TBL flows experiment, thereby enabling measurements close to the wall at higher Reynolds numbers.

Keywords : Turbulence, Channel Flow, Boundary Layer Flow, Scale-by-scale energy transfer, Particle Image Velocimetry (PIV), Reynolds number.